Nonlinear subgrid finite element models for low Mach number flows coupled with radiative heat transfer

Matias Avila

Advisor: **Ramon Codina**
Co Advisor: **Javier Principe**

**Escola Tècnica Superior d'Enginyers
de Camins, Canals i Ports de Barcelona**

Universitat Politècnica de Catalunya

September 2012

Acknowledgements

Miro para atras, y han pasado mas de cinco anos desde que comence esta tesis, ha sido una etapa enriquecedora en mi vida, que comence por amor (a la ciencia), sin mayores deseos que aprender y ensenar, y con mucha ilusion. A lo largo de estos aos mi ilusion ha ido mermando y renaciendo, pasando por momentos criticos. Mi camino se ha hecho mas facil y ameno gracias a las personas que me acompanaron y dieron su cario y compartieron sus consejos, tanto en el ambito personal como profesional, endulzandome la vida con su compania. Ellos me han dado energia suficiente para continuar y terminar este camino.

En primer lugar gracias a Ramon Codina, por confiar en mi, y ofrecerme una beca para realizar la tesis con el. Le agradezco su buena disposicion para resolver mis cuestiones dentro y fuera del ambito academico. Por sus consejos enriquecedores cada vez que tenia una duda, agradezco su rigurosidad en las respuestas y su exigencia en la formulacion de mis preguntas. Ya lo estoy extraando, sin duda una gran persona.

Muchisimas gracias a Javier Prncipe por responderme cientos de preguntas, aportando siempre nuevos puntos de vista, por sus consejos y por sus explicaciones una y otra vez, por ser un cuestionador y discutidor insaciable. Gracias Javier por tu cercania, por tu amistad y por tu empuje. Sin vos esta tesis hubiera sido distinta.

Gracias al personal de Quantech, por acompanarme en esa maravillosa empresa donde trabaje durante seis anos. Maravillosa por lo que aprendi y por la gente tan especial que conoc alli dentro. Gracias a Javier Marcipar por confiar en mi, por motivarme constantemente, por hacerme sentir til y querido, y por facilitarme a emprender mi doctorado. Gracias a Martin Solina por su amistad y por las risas en el despacho (Que pasa locoooo???). Gracias a Annelys por endulzarme la vista dia tras dia en la oficina, por las lindas charlas, por su gran amistad y por su amor. Gracias a Fernando Rastellini por ser tan buen loco... y su agradable compania. Gracias a Gerardo Socorro, mielmano, por que cuando el esta todo es mas sencillo, por su amistad y por ser la persona maravillosa que es, por todos los rones compartidos y regalados. Gracias a Luis, por todo, por su excelente onda, por ayudarme siempre en los asados, y su compaia en los buenos y malos momentos. Gracias a Laurentiu por su risa estridente, risa que me hacia reir, por las charlas en las comidas y por su apoyo siempre. Gracias a Herbert por su buena onda, por todo lo que me enseno y me ayudo, y por recomendarme a Ramon. Gracias a Lupe, por su pequea gran belleza, y ser esa gran persona cariosa y cercana. Gracias a Marina por su sonrisa de piano. Gracias a Xantuli por hacernos reir tanto en las comidas. Gracias a Elisenda, muacs, por venir a mis obras de teatro, y... sus conjuntos...

Gracias a mis companeros de piso brasilenos Neto y Serginho por la alegria que me hacian sentir cada dia cuando volvia a casa. Gracias a Daniel por dejar que le rompiera su casa en Badalona durante casi dos anos. Gracia a Nelly, por su confianza, calidez, paciencia, y excelente compaia.

Gracias a todos los companeros de teatro, con los que comparti tantas risas, esfuerzos, llantos, golpes, abrazos, cantos, saltos y bailes. Porque hicieron que me olvidara de mi tesis cada vez que estaba con ellos, oxigenandome el cerebro durante horas y dias. Gracias a Tamara por su enorme amistad, por las charlas interminables donde por fin alguien hablaba tanto como yo, por ser Sevillana y por hacerme sentir como un sevillano mas. Gracias a Francesca, por las risas dentro y fuera del teatro, por ser tan bella y autentica. Gracias a Gustavo por sus canciones, sus asados, los viajes en velero, y por su amistad. Gracias a Laia por querer tanto a Gustavo, y por su buena onda y compaia. Gracias a Olga por su carino, a Mariano por ser tan copado y tan cercano, alguien de quien siempre se aprende. Gracias a Monica, a Mireia, etc... Gracias a la Vaneeee!!!! Gracias a Kandarp, por su paz, escucha, y por aprender tanto de el... Gracias a las chicas de la cafeteria del Pol, sobretodo a Lorena (de Pitalito) por los buenos momentos.

Gracias a mi hermano Adriel por recibirme siempre con los brazos tan abiertos en Salou, y su enorme energia positiva. Gracias a mi madre por su motivacion constante, y acogerme en su casa siempre que quise. Gracias a mi hermanita penelope, por su frescura, y por ser tan linda.

Gracias a Pakop y Emily, por recibirme en su casa de Mollet casi cada noche y por su amistad.

Gracias a los chicos de la oficina. A Joan por estar frente a mi, por su intensidad y capacidad de trabajo, algo que se aprende y contagia. Gracias a Cristian por su amabilidad, su tranquilidad, y su compana. Gracias a FERMIIIIN por todos esos mates compartidos por la manana, por los fernets, por su buena onda y por su amistad. Gracias a Ester por esa tan linda charla. Gracias a Hector y a Pablo Mata.

Gracias al DEO: Martini, Oriol, Xavi, Pasqui y Toni, por las pelis, las pizzas, el bara, los viajes, la amistad y hacerme sentir mas catalan dia tras dia. Visca Catalunya. Gracias a mis amigos de Argentina, Martin, Igor, Montanes, Nasa, Ale, Macarena por estar siempre conmigo, desde la distancia. Macarena sos muy hermosa!

Between the beginning of October and the end of December of 2011 Professor Ruben Sevilla received me for a stay in the *Computational and Civil Engineering College* at the *Swansea University* in Wales, United Kingdom. Thanks to Dr. Ruben Sevilla, Dr Oubay Hassan for all the support, and for make me feel so welcome. During this period the development and implementation of higher order elements, described in chapter 3 of this thesis, was done. I specially appreciate Ruben's help, patience and fruitful discussions. I would like to thank to all the group for their very warm reception and friendship, specially to Miquel Aguirre, Aurelio Arranz , Rihannon, Alejandro Diaz, Maria, Mauro Innocente, Rocio Pascual, Antonio Gil, ...

The financial support received from the*Centre Internacional de Mètodes Numèrics a l'Enginyeria* is acknowledged.

The work in radiation has been partially supported by project FITUN, ref. TRA2008-05162, from the Spanish Ministry of Science and Innovation. Financial support provided by the International Center For Mechanical Sciences (CISM) and Autostrada del Brennero S.p.A., from Italy, is also acknowledged.

Abstract

The general description of a fluid flow involves the solution of the compressible Navier-Stokes equations, a very complex problem whose mathematical structure is not well understood. It is widely accepted that these equations provide an accurate description of any problem in fluid mechanics which may present many different nonlinear physical mechanisms. Depending on the physics of the problem under consideration, different simplified models neglecting some physical mechanisms can be derived from asymptotic analysis. On the other hand, radiative heat transfer can strongly interact with convection in high temperature flows, and neglecting its effects may have significant consequences in the overall predictions. Problems as fire scenarios emphasized the need for an evaluation of the effect of radiative heat transfer. This work is directed to strongly thermally coupled low Mach number flows with radiative heat transfer.

The complexity of these mathematical problem makes their numerical solution very difficult. Despite the important difference in the treatment of the incompressibility, the low Mach number equations present the same mathematical structure as the incompressible Navier-Stokes equations, in the sense that the mechanical pressure is determined from the mass conservation constraint. Consequently the same type of numerical instabilities can be found, namely, the problem of compatibility conditions between the velocity and pressure finite element spaces, and the instabilities due to convection dominated flows. These instabilities can be avoided by the use of stabilization techniques. Many stabilization techniques used nowadays are based on the variational multiscale method, in which a decomposition of the approximating space into a coarse scale resolvable part and a fine scale subgrid part is performed. The modeling of the subgrid scale and its influence leads to a modified coarse scale problem providing stability. The quality of the final approximation (accuracy, efficiency) depends on the particular model.

The extension of these techniques to nonlinear and coupled problems is presented. The distinctive features of our approach are to consider the subscales as transient and to keep the scale splitting in all the nonlinear terms appearing in the finite element equations and in the subgrid scale model. The first ingredient permits to obtain an improved time discretization scheme (higher accuracy, better stability). The second ingredient permits to prove global conservation properties, being also responsible of the higher accuracy of the method. This ingredient is intimately related to the problem of thermal turbulence modeling from a strictly numerical point of view. The capability for the simulation of turbulent flows is a measure of the ability of modeling the effect of the subgrid flow structures over the coarser ones. The performance of the model in predicting the behavior of turbulent flows is demonstrated.

The radiation transport equation has been also approximated within the variational multiscale framework, the design and analysis of stabilized finite element methods is presented.

Contents

Chapter 1

Introduction

We know from everyday observation that liquids and gases in motion behave in very varied and often complicated ways. When one observes them in the controlled conditions of a laboratory, one finds that the variety and complexity of flow patterns arise even if the arrangement is quite simple. Fluid dynamics is the study of these phenomena. The general description of a fluid flow involves the solution of the compressible Navier Stokes equations. It is widely accepted that these equations provide an accurate description of any problem in fluid mechanics which may present many different nonlinear physical mechanisms. This set of equations is highly nonlinear, the mathematical formulation of the physical principles of mass , momentum and energy conservation coupled with a state equation, is very complex and very little is known about its mathematical structure. Results on the boundary conditions that make the problem well posed, and on the existence of a unique solution can be found in [63]. The mathematical complexity of the problem is the manifestation of the also complex physical behavior of these flows. Many different nonlinear physical mechanisms are coupled in fluid mechanics problems. For these reasons, depending on the physics of the problem under consideration, different models can be derived from the compressible Navier Stokes equations, whose mathematical structure is better understood [64]. The derivation of these reduced sets of equations is based on some assumptions on the problem, usually made in terms of some dimensionless parameters that measure the relative importance of different physical processes, like the Mach or Reynolds numbers.

The most important of these simplified models is described by the incompressible Navier Stokes equations. This set of equations is smaller than the compressible one and its mathematical structure is much better understood. However many important flows cannot be considered as incompressible due to the presence of thermal effects. The most widely used model in the context of thermally coupled flows is the so called Boussinesq approximation proposed in [10]. This model treats the flow as incompressible being useful in natural convection problems with small density variations. A formal justification for the Boussinesq approximation can be found in [80] and references therein.

Flow problems whith strong thermal coupling such as fires, combustion problems, gas turbines, ovens, etc... cannot be modeled by the Boussinesq approximation because the large variations of density and temperature. In most of these problems the flow velocity is much smaller than the velocity of the sound in the medium. These kind of flows are known as “low speed flows” and can be modeled appropriately by the low Mach number approximation model. A formal justification of this model can be found in [80] and references therein. The low Mach number model leads to a removal of the acoustic modes (involving fast time scales) but large density and temperature gradients are allowed, which cannot be modeled by the Boussinesq approximation. Despite this important difference in the treatment of the incompressibility, the low Mach number equations present the same mathematical structure as the incompressible Navier-Stokes equations, in the sense that the mechanical pressure is determined from the mass conservation constraint. Consequently the same type of numerical instabilities can be found.

In high temperature flows thermal radiation can be an important mechanism of heat transfer, having direct effects on many industrial applications such as fires, combustion problems, furnaces, gas turbines, etc. Radiative heat transfer can strongly interact with convective flows and neglecting its effects may have significant consequences in the overall predictions. Therefore in high temperature flows an accurate calculation of radiative transfer is of crucial importance for the prediction of the thermal performance. The radiative intensity field depends on the position and on the propagating direction, being determined from the integro-differential radiative heat transfer equation. The natural approach to account for radiation is to simplify the radiative transfer equation, considering directional discretizations that transforms the integro-differential RTE into a set of coupled differential equations. The modeling of radiative heat transfer increases the computational work and involves tedious mathematics due to the directional nature of the intensity radiation field. Moreover the coupling between the radiative transfer and the energy equations is highly nonlinear, and an iterative process needs to be done.

The finite element method is a tool very often employed to deal with the numerical simulation of multiphysics problems. The complexity of the mathematical problems found in fluid mechanics makes their numerical solution very difficult. Special techniques are needed because when the standard Galerkin method is used, numerical instabilities appear. In the incompressible case, two well known sources of numerical instabilities are the incompressibility constraint and the presence of dominant convective terms. The convective instability is also present in the convection diffusion reaction problem (CDR) and was early understood as a lack of diffusion of the discrete problem. The first attempts to remedy the situation consisted in the addition of an extra stabilizing term of diffusive type and were called artificial viscosity methods. These methods are not consistent, i.e. the exact solution of the continuous problem does not satisfy the perturbed equation, what results in a loss of accuracy. The first consistent method, the streamline upwind Petrov Galerkin method (SUPG), was developed in the late seventies [11]. This method and many of its successors consist then in the addition of a stabilizing term to the original Galerkin formulation which is proportional to the residual and we refer to [16] for a comparison of different methods of this type.

The incompressibility constraint gives rise to a instability of the pressure, being also found in the Stokes problem. The standard Galerkin method applied to solve this problem is stable provided the Ladyzhenskaya-Babuska-Brezzi (LBB) condition is satisfied, which requires a compatibility of the spaces where the velocity and pressure belong. In particular, equal order interpolations do not satisfy this condition for Galerkin problem. Stabilized finite element methods (FEM) have been initially developed for the convection diffusion reaction (CDR) and Stokes problems. It is important to mention that the incompressible Navier Stokes equations can be written as a system of linearized convection diffusion reaction (CDR) equations and that the pressure gradient and incompressibility appear in the first order convective term. This observation was exploited in [50] to apply a technique similar to SUPG to obtain a stabilized formulation allowing the use of equal order interpolations.

The way of understanding these methods has changed since the introduction of the variational multiscale method (VMM) in [49]. This method is based on the split of the unknown into a coarse scale resolvable part and a fine scale subgrid part. This split corresponds to a decomposition of the functional space in which the solution of the problem is sought as a direct sum of a finite dimensional coarse scale space and a infinite dimensional fine scale one. The coarse scale space is the one induced by the discretization of the domain and the fine scale space is any complement to yield the continuous space. In this way, the problem is decomposed into a resolvable coarse scale problem induced by the discretization and a small scale problem that cannot be exactly solved because it is as complex as the original continuous problem. Modeling the subscale and taking into account its effect on the coarse scale problem results in a stable formulation for linear problems. This technique has been extended to incompressible Navier Stokes equations (see for example [18, 54]) and has been used to solve many different kind of problems as the low Mach approximation [79] but the nonlinearity of the problem was still not considered in their design.

The design of stabilization techniques considering the transient and nonlinear nature of the incompresible Navier Stokes problems began with the introduction of dynamic nonlinear subscales in [19, 27], developed in the context of the variational multiscale concept. With respect to classical multiscale-based stabilization techniques, the idea is to consider the subgrid scale time dependent and to consider its effect on the nonlinear convective term. Important improvements in the discrete formulation of the incompressible Navier-Stokes problem have been observed. From a theoretical point of view, the use of transient subgrid scales explains how the stabilization parameter should depend on the time step size and makes space and time discretizations commutative. The tracking of the subscales along the nonlinear process provides global momentum conservation for incompressible flows. From a practical point of view, the use of time dependent nonlinear subscales results in a more robust and more accurate method (an unusual combination) as shown by numerical experiments [19, 27, 47]. It has been observed in those experiments that the convection tracking notably improves the solution, gaining accuracy on coarse meshes and for high Reynolds numbers. The tracking in time results in a smooth pressure evolution, eliminating time-step to time-step oscillations observed in some cases with standard methods.

These developments also opened the door to the use of numerical techniques to cope with the potential instabilities and to model turbulence at the same time, as pointed out in [19, 27]. This is a natural step as turbulence is originated by the presence of the nonlinear convective term, as it is well known. The idea of modeling turbulence using the VMS framework goes back to [19], and it was fully developed for incompressible flows in [5]. The dissipative structure of the nonlinear and dynamic subscale model has been analyzed in [81], where it is compared the dissipation introduced by the numerical discretization of the problem with the diffusion introduced by a large eddy simulation model.

There are important open questions in the dynamic and nonlinear subscale model. The importance of the subgrid scale model is a subject that still needs more research. It is known that to evaluate the nonlinear effects in the subgrid scale models leads to better solutions, and it was observed in [47] that it is important to have the subgrid scale well converged in order to obtain a good global convergence. However, robust linearization schemes are still needed to assure convergence of the subgrid scale when coarse grids are used.

The objective of the present thesis is to develop a dynamic and nonlinear subgrid scale stabilized finite element formulation for the Boussinesq and low Mach approximations equations with radiative heat transfer. The low Mach equations form a highly nonlinear system, and we aim to model the involved nonlinear subgrid mechanisms with the sole use of nonlinear stabilization methods, dealing with thermal turbulence modeling from a strictly numerical point of view. We will extend the proposed nonlinear stabilized formulation to radiative flows, expecting to capture the subgrid nonlinear coupling between radiation and temperature.

The low Mach number approximation forms a higly nonlinear system of equations. Therefore, iterative schemes for the tracking of the subscales along the nonlinear process are expected to be complicated, being a subject that has not been exploited in the literature. We propose a formulation where the subgrid scale will be considered as time dependent and its effect will be considered on *all the nonlinear terms* of the finite element formulation. We expect to obtain improvements in the stable discrete formulation, more accurate solutions, and to be capable of modeling turbulence from a strictly numerical point of view for the kind of problems we are considering.

Let us close the introduction describing the organization of the work.

In chapter 2 we describe a variational multiscale finite element approximation for the incompressible Navier-Stokes equations using the Boussinesq approximation to model thermal coupling. The main feature of the formulation in contrast to other stabilized methods is that we consider the subscales as nonlinear, transient and orthogonal to the finite element space. We keep the effect of the subscales both in the nonlinear convective terms of the momentum and temperature equations and, if required, in the thermal coupling term of the momentum equation. This strategy allows us to approach the problem of dealing with thermal turbulence from a strictly numerical point of view and discuss important issues, such as the relationship between the turbulent mechanical dissipation and the turbulent thermal dissipation.

In chapter 3 we propose a variational multiscale finite element approximation for the low Mach number equations. The distinctive features of the formulation are to consider the subscales as transient and to keep the scale splitting in all the nonlinear terms. The first ingredient permits to obtain an improved time discretization scheme (higher accuracy, better stability, no restrictions on the time step size). The second ingredient permits to prove global conservation properties. The orthogonal subgrid scale method, which gives high improvement for incompressible flows, is now developed in the context of variable density flows, and its performance is studied. Several subgrid scale models are compared, obtaining important conclusions about the importance of the nonlinear models in the subscale equations, and the design of the numerical parameters. Numerical tests show that nonlinear and dynamic subscales give more accurate solutions than classical stabilized methods as SUPG. The efficiency of the numerical scheme (error vs. cpu time) is compared against the SUPG method when using linear, quadratic and cubic elements.

In chapter 4 we present solutions of the turbulent channel flow with large temperature differences, using the dynamic and nonlinear finite element approximation for the low Mach number equations introduced in chapter 3. The subgrid models are evaluated without the use of a physical model for the turbulent effects. A careful analysis of the dissipative structure of the method is presented, showing the physical interpretation of the subgrid scales. The design of stabilization parameters is also investigated in terms of the numerical dissipation.

The obtained numerical solutions are compared against DNS results, showing that the obtained results are as accurate as those obtained in the literature using advanced LES models on the same computational grid.

In chapter 5 a mathematical description of the radiative transfer equation is given, explaining the physical mechanisms of radiative propagation. After the radiative heat transfer equation is introduced and analyzed inside its mathematical framework , the most used models to obtain an approximate solution to the radiative heat transfer equation are introduced. A stabilized finite element method to discretize in space the monochromatic radiation transport equation is proposed, based on the decomposition of the unknowns into resolvable and subgrid scales parts, where the subgrid scales are considered orthogonal to the finite element space. A numerical analysis of the *spatial* approximation using SUPG, orthogonal subgrid scale formulations is performed, showing that they are both stable and optimally convergent in the same mesh-dependent norm. A comparison against the behavior of the Galerkin method, for which a non-standard numerical analysis is done, is also presented.

In chapter 6 the finite element approximation proposed in chapter 3 for the low Mach number equations is extended to consider the coupling with the radiative heat transfer equations to the flow problem through energy equation. The coupling terms are highly nonlinear, depending on the fourth power of temperature. The subgrid effect of this highly nonlinear coupling term is modeled using the nonlinear variational multiscale method, being related to turbulence radiation interaction concepts. Nonlinear schemes are proposed for the coupling between radiation and temperature. Numerical results show that the method gives more accurate results.

We close the work with chapter 7, where conclusions and further possible research lines are summarized. Let us finally mention that chapters are quite self contained even if it implies the need of repeating some information. This is because each chapter is an elaboration of the material in a publication as follows

- Chapter 2: “Finite element approximation of turbulent thermally coupled incompressible flows with numerical sub-grid scale modelling”, R. Codina, J. Principe and M. Avila. International Journal of Numerical Methods for Heat & Fluid Flow. Vol. 20 No. 5 (2010) 492-516

- Chapter 3: “A finite element dynamical nonlinear subscale approximation for the low Mach number flow equations”, M. Avila, R. Codina and J. Principe. Journal of Computational Physics Vol. 230 (2011) 7988–8009.

- Chapter 4:“Large eddy simulation of low Mach number flows using a dynamical and nonlinear finite element subgrid scale modeling”, In preparation.

- Chapter 5: “Spatial approximation of the radiation transport equation using a subgrid-scale finite element method”,M. Avila, J. Principe and R. Codina. Computer Methods in Applied Mechanics and Engineering, 2011, vol. 200: 425-438.

Chapter 2

Subgrid scale modeling for the Boussinesq approximation equations

This chapter is an elaboration of the material in

R. Codina, J. Principe and M. Avila. Finite element approximation of turbulent thermally coupled incompressible flows with numerical sub-grid scale modelling. International Journal of Numerical Methods for Heat & Fluid Flow. Vol. 20 No. 5 (2010) 492-516

The objective of this chapter is to describe a variational multiscale finite element approximation for the incompressible Navier-Stokes equations using the Boussinesq approximation to model thermal coupling. The main feature of the formulation in contrast to other stabilized methods is that we consider the subscales as transient and orthogonal to the finite element space. These subscales are solution of a differential equation in time that needs to be integrated. Likewise, we keep the effect of the subscales both in the nonlinear convective terms of the momentum and temperature equations and, if required, in the thermal coupling term of the momentum equation. This strategy allows us to approach the problem of dealing with thermal turbulence from a strictly numerical point of view and discuss important issues, such as the relationship between the turbulent mechanical dissipation and the turbulent thermal dissipation.

2.1 Introduction

Let $\Omega \subset \mathbb{R}^d$, with $d = 2, 3$, be the computational domain in which the flow takes place during the time interval $[0, T_{\text{end}}]$, and let Γ be its boundary. The initial and boundary value problem to be considered consists in finding a velocity field $\boldsymbol{u}$, a pressure field p and a temperature field

T such that

$$\begin{aligned}
\partial_t \boldsymbol{u} + \boldsymbol{u}\cdot\nabla\boldsymbol{u} - \nu\Delta\boldsymbol{u} + \nabla p + \alpha\boldsymbol{g}T &= \boldsymbol{f} + \alpha\boldsymbol{g}T_0 && \text{in } \Omega,\ t\in(0,T_{\text{end}}), && (2.1)\\
\nabla\cdot\boldsymbol{u} &= 0 && \text{in } \Omega,\ t\in(0,T), && (2.2)\\
\partial_t T + \boldsymbol{u}\cdot\nabla T - \kappa\Delta T &= Q && \text{in } \Omega,\ t\in(0,T_{\text{end}}), && (2.3)\\
\boldsymbol{u} &= 0 && \text{on } \Gamma,\ t\in(0,T_{\text{end}}), && (2.4)\\
\boldsymbol{u} &= \boldsymbol{u}^0 && \text{in } \Omega,\ t=0, && (2.5)\\
T &= 0 && \text{on } \Gamma,\ t\in(0,T_{\text{end}}), && (2.6)\\
T &= T^0 && \text{in } \Omega,\ t=0. && (2.7)
\end{aligned}$$

In these equations, ν is the kinematic viscosity, κ the thermal diffusivity, α the thermal expansion coefficient, $\boldsymbol{f}$ the external body forces, T_0 the reference temperature, $\boldsymbol{g}$ the gravity acceleration vector, Q the heat source and $\boldsymbol{u}^0$ and T^0 the initial conditions for velocity and temperature, respectively.

The literature on the finite element approximation of problem (2.1)-(2.7) is vast (see for example the introductory text [84]). The spatial discretization suffers from the well known problems of compatibility conditions between the velocity and pressure finite element spaces as well as the instabilities due to convection dominated flows, in this case both in the momentum equation (2.1) and the heat equation (2.3).

Apart from numerical difficulties, the physics modeled by (2.1)-(2.7) is extremely complex. In particular, turbulence should be in principle modeled by this system of equations. Since it is commonly accepted that turbulent scales cannot be captured in most applications, turbulence models of different complexity have been developed (see [97, 44] for background).

In recent years, the idea of using numerical techniques able to cope with the potential instabilities *and* to model turbulence at the same time has gained adepts, in particular within the variational multiscale concept introduced by Hughes in [55, 49]. The original motivation of this type of formulations was to justify the so called *stabilized finite element methods*. The possibility to model turbulence was remarked by Codina in [19] in contrast is the option adopted by Hughes in [51] to add a large-eddy-simulation (LES) type model for the subgrid scales (see Remark 6 in [19] and, for background on LES models, [77]). In [5] the possibility to model turbulence using only numerical ingredients within the variational multiscale context is fully and successfully exploited. The role of numerical stabilization terms to model turbulence had also been envisaged in [31, 45], for example. For similar ideas using other numerical formulations, see [9, 86] and references therein.

The purpose of this chapter is to give an overview of the finite element model proposed in [19, 27, 41, 81, 24] and to present a complete description of its main properties, including the latest results obtained. It turns out that these properties support our view of modeling thermal turbulence from a strictly numerical point of view. Our formulation is reviewed in Section 2.2, where some additional developments concerning the modeling of the subgrid scales are included. Section 2.3 contains a thorough discussion about the conservation properties of the scheme and the energy transfer mechanisms, which are relevant to model turbulent flows. In particular, we show how the numerical model we propose allows for a natural scale splitting in the energy balance, both in the mechanical and in the thermal problems. Likewise, the relationship with the dissipation introduced by classical LES models is described. Section 2.4 presents the results of two numerical examples, one of them showing the transition to turbulence as the Rayleigh number increases and the other showing the results of a numerical simulation of a turbulent flow. Conclusions and final remarks close the chapter in Section 2.5.

2.2 Finite element approximation

2.2.1 Variational formulation

To define the functional setting, let $H^1(\Omega)$ be the space of functions such that they and their first derivatives belong to $L^2(\Omega)$ (that is, they are square integrable), and let $H_0^1(\Omega)$ be the subspace of functions in $H^1(\Omega)$ vanishing on the boundary. Let also $\boldsymbol{V}_{\rm st} = H_0^1(\Omega)^d$, $Q_{\rm st} = L^2(\Omega)/\mathbb{R}$, $\Psi_{\rm st} = H_0^1(\Omega)$ and define $\boldsymbol{V} = \boldsymbol{L}^2(0,T;\boldsymbol{V}_{\rm st})$, $Q = L^1(0,T;Q_{\rm st})$ (for example) and $\Psi = L^2(0,T;\Psi_{\rm st})$, where $L^p(0,T;X)$ stands of the space of functions such that their X norm in the spatial argument is an $L^p(0,T)$ function in time, that is, its p-th power is integrable if $1 \leq p < \infty$ or bounded if $p = \infty$.

The weak form of the problem consists in finding $(\boldsymbol{u}, p, T) \in \boldsymbol{V} \times Q \times \Psi$ such that

$$(\partial_t \boldsymbol{u}, \boldsymbol{v}) + \langle \boldsymbol{u} \cdot \nabla \boldsymbol{u}, \boldsymbol{v} \rangle + \nu(\nabla \boldsymbol{u}, \nabla \boldsymbol{v}) - (p, \nabla \cdot \boldsymbol{v}) + \alpha(\boldsymbol{g}T, \boldsymbol{v}) = \langle \boldsymbol{f}, \boldsymbol{v} \rangle + \alpha(\boldsymbol{g}T_0, \boldsymbol{v}), \quad (2.8)$$

$$(q, \nabla \cdot \boldsymbol{u}) = 0, \quad (2.9)$$

$$(\partial_t T, \psi) + \langle \boldsymbol{u} \cdot \nabla T, \psi \rangle + \kappa(\nabla T, \nabla \psi) = \langle Q, \psi \rangle, \quad (2.10)$$

for all $(\boldsymbol{v}, q, \psi) \in \boldsymbol{V}_{\rm st} \times Q_{\rm st} \times \Psi_{\rm st}$, where $(\cdot,\cdot)$ denotes the $L^2(\Omega)$ inner product and $\langle f, g \rangle := \int_\Omega fg$ whenever functions f and g are such that the integral is well defined.

The dimensionless numbers relevant in this problem are

$$\mathrm{Re} := \frac{LU}{\nu}, \qquad \text{Reynolds number,} \quad (2.11a)$$

$$\mathrm{Pe} := \frac{LU}{\kappa}, \qquad \text{Péclet number,} \quad (2.11b)$$

$$\mathrm{Pr} := \frac{\nu}{\kappa} \qquad \text{Prandtl number,} \quad (2.11c)$$

$$\mathrm{Ra} := \frac{\alpha|\boldsymbol{g}|L^3\delta T}{\nu\kappa} \qquad \text{Rayleigh number.} \quad (2.11d)$$

where L is a characteristic length of the problem, U a characteristic velocity and δT a characteristic temperature difference, usually computed from temperature boundary values when these are not zero. When U cannot be determined by the boundary conditions, for example because zero velocities are prescribed, $U = \nu/L$ can be taken, which corresponds to choose $\mathrm{Re} = 1$ and gives $\mathrm{Pe} = \mathrm{Pr}$.

2.2.2 Scale splitting

Let us consider a finite element partition $\{K\}$ with $n_{\rm e}$ elements of the computational domain Ω, from which we can construct finite element spaces for the velocity, pressure and temperature in the usual manner. We will assume that they are all built from continuous piecewise polynomials of the same degree k.

The basic idea of the multiscale approach we will follow [49] is to split the continuous unknowns as

$$\boldsymbol{u} = \boldsymbol{u}_h + \tilde{\boldsymbol{u}}, \tag{2.12}$$

$$p = p_h + \tilde{p}, \tag{2.13}$$

$$T = T_h + \tilde{T}, \tag{2.14}$$

where the components with subscript h belong to the corresponding finite element spaces. The components with a tilde belong to any space such that its direct sum with the finite element space yields the functional space where the unknown is sought. For the moment, we leave it undefined. These additional components are what we will call *subscales*. Each particular variational multiscale method will depend on the way the subscales are approximated. Our main focus in this chapter is to explain the consequences *of considering these subscales time dependent*, and therefore requiring to be integrated in time. Likewise, we will keep the previous decomposition (2.12)-(2.14) in *all the terms of the variational equations of the problem.* As we shall see, this has important consequences in the modeling of thermally coupled turbulent flows. The only approximation we will make for the moment is to assume that the subscales vanish on the interelement boundaries, $\partial\Omega_e$. This happens for example if one assumes that their Fourier modes correspond to high wave numbers, as it is explained in [19], but can be relaxed using the approach proposed in [26].

From the previous splitting two sets of equations can be obtained. The first is the projection of the original equations onto the finite element spaces of velocity, pressure and temperature. On the other hand, the equations for the subscales are obtained by projecting onto their corresponding spaces, that is, by taking the test function $\tilde{\boldsymbol{v}}$ in the space of subscales instead of in the finite element space. If $\tilde{P}$ denotes the projection onto any of the subscale spaces (for velocity, pressure or temperature), these equations are

$$\tilde{P}[\partial_t \tilde{\boldsymbol{u}} + (\boldsymbol{u}_h + \tilde{\boldsymbol{u}}) \cdot \nabla \tilde{\boldsymbol{u}} - \nu \Delta \tilde{\boldsymbol{u}} + \nabla \tilde{p} + \alpha \boldsymbol{g} \tilde{T}] = \tilde{P}(\boldsymbol{R}_u), \tag{2.15}$$

$$\tilde{P}(\nabla \cdot \tilde{\boldsymbol{u}}) = \tilde{P}(R_p), \tag{2.16}$$

$$\tilde{P}[\partial_t \tilde{T} + (\boldsymbol{u}_h + \tilde{\boldsymbol{u}}) \cdot \nabla \tilde{T} - \kappa \Delta \tilde{T}] = \tilde{P}(R_T), \tag{2.17}$$

where

$$\begin{aligned}
\boldsymbol{R}_u &= \boldsymbol{f} + \alpha \boldsymbol{g} T_0 - [\partial_t \boldsymbol{u}_h + (\boldsymbol{u}_h + \tilde{\boldsymbol{u}}) \cdot \nabla \boldsymbol{u}_h - \nu \Delta_h \boldsymbol{u}_h + \nabla p_h + \alpha \boldsymbol{g} T_h], \\
R_p &= -\nabla \cdot \boldsymbol{u}_h, \\
R_T &= Q - [\partial_t T_h + (\boldsymbol{u}_h + \tilde{\boldsymbol{u}}) \cdot \nabla T_h - \kappa \Delta_h T_h],
\end{aligned}$$

are the residuals of the finite element unknowns in the momentum, continuity and heat equation, respectively. Equations (2.15)-(2.17) need to be solved within each element and, as we have assumed, considering homogeneous velocity and temperature Dirichlet boundary conditions.

2.2.3 Approximation of the subscales I: general procedure

In this subsection we present a general procedure to approximate the subscales in problem (2.15)-(2.17) and, in particular, of the *spatial differential operators* applied to the subgrid scales. To this end, let us consider an element K of the finite element partition and a problem of the form

$$\mathcal{L}u' = r_h \quad \text{in } K, \tag{2.18}$$

which needs to be completed with boundary conditions. As indicated previously, $u' = 0$ on ∂K is a possibility. In the model problem (2.18), the unknown u' is assumed to have a vector character, although no particular notation will be used to specify it. Likewise, the forcing term r_h is also a vector. The number of components of both u' and r_h will be denoted by n.

Our objective is to obtain a $n \times n$ *diagonal* matrix τ such that

$$u' \approx \tau\, r_h \quad \text{in each } K, \tag{2.19}$$

so that $\tau \approx \mathcal{L}^{-1}$ with the appropriate boundary conditions. In the following subsection, this approximation will be used for the spatial operator arising from the linearization of the left-hand-side in (2.15)-(2.17), now u' being composed of the velocity components, the pressure and the temperature.

In order to obtain (2.19), we use a heuristic Fourier analysis, introduced in [19] and extended in [23], for example. Let us denote the Fourier transform by $\widehat{\ }$. Let $\boldsymbol{k}/h$ be the wave number, with $\boldsymbol{k}$ dimensionless. The basic heuristic assumption is that u' is highly fluctuating, and therefore dominated by high wave numbers. As a consequence, we may assume that

- Values of u' on ∂K can be neglected to approximate u' in the interior of K.
- The Fourier transform can be evaluated as for functions vanishing on ∂K (and extended to $\mathbb{R}^d$ by zero).

The Fourier-transformed equation for the subscales will be

$$\hat{\mathcal{L}}(\boldsymbol{k})\hat{u}'(\boldsymbol{k}) = \hat{r}_h(\boldsymbol{k})$$

Before proceeding, it is crucial to discuss the proper scaling of this problem. Let u be an element in the domain of $\mathcal{L}$ and f an element in its range. Suppose that $\mathcal{L}u = f$ is written in such a way that $f^{\mathrm{t}}u = \sum_{i=1}^{n} f_i u_i$ is dimensionally well defined. In general, if $f, g \in \operatorname{range}\mathcal{L}$ and $u, v \in \operatorname{dom}\mathcal{L}$,

$$f^{\mathrm{t}}g = \sum_{i=1}^{n} f_i g_i, \quad u^{\mathrm{t}}v = \sum_{i=1}^{n} u_i v_i$$

may not be dimensionally meaningful. This is the case for example when the unknowns are $u = (\boldsymbol{u}, p, T)$, as in our case.

Let M be a scaling matrix, diagonal and with positive diagonal entries, that makes the products $f^{\mathrm{t}}Mg$ and $u^{\mathrm{t}}M^{-1}v$ dimensionally consistent. Let also

$$\begin{aligned} |f|_M^2 &:= f^{\mathrm{t}}Mf \quad M\text{-norm of } f \\ |u|_{M^{-1}}^2 &:= u^{\mathrm{t}}M^{-1}u \quad M^{-1}\text{-norm of } u \\ \|f\|_{L_M^2(K)} &:= \int_K |f|_M^2 \end{aligned}$$

A simple stability analysis dictates that matrix τ *must be such that* $\|\mathcal{L}\|_{L^2_M(K)} \leq \|\tau^{-1}\|_{L^2_M(K)}$. This will be the basic approximation condition of $\mathcal{L}$ by a *diagonal* matrix. In order to devise a way to satisfy it, let us note that

$$\begin{aligned}
\|\mathcal{L}u\|^2_{L^2_M(K)} &= \int_K |\mathcal{L}u|^2_M \mathrm{d}\boldsymbol{x} \\
&\approx \int_{\mathbb{R}^d} |\widehat{\mathcal{L}}(\boldsymbol{k})\widehat{u}(\boldsymbol{k})|^2_M \mathrm{d}\boldsymbol{k} \\
&\leq \int_{\mathbb{R}^d} |\widehat{\mathcal{L}}(\boldsymbol{k})|^2_M |\widehat{u}(\boldsymbol{k})|^2_{M^{-1}} \mathrm{d}\boldsymbol{k} \\
&= |\widehat{\mathcal{L}}(\boldsymbol{k}^0)|^2_M \int_{\mathbb{R}^d} |\widehat{u}(\boldsymbol{k})|^2_{M^{-1}} \mathrm{d}\boldsymbol{k} \\
&\approx |\widehat{\mathcal{L}}(\boldsymbol{k}^0)|^2_M \|u\|^2_{L^2_{M^{-1}}(K)},
\end{aligned}$$

where the first approximation comes from the fact that boundary values of u' have been discarded and $\boldsymbol{k}^0$ is a wave number whose existence follows from the mean value theorem. From the previous development we have that $\|\mathcal{L}\|_{L^2_M(K)} \leq |\widehat{\mathcal{L}}(\boldsymbol{k}^0)|_M$. *Our proposal is to choose* τ *diagonal and such that* $|\widehat{\mathcal{L}}(\boldsymbol{k}^0)|_M = |\tau^{-1}|_M$. A particular way to achieve this is the following: let

$$\lambda_{\max}(\boldsymbol{k}^0) = \max \operatorname{spec}_{M^{-1}}(\widehat{\mathcal{L}}(\boldsymbol{k}^0)^* M \widehat{\mathcal{L}}(\boldsymbol{k}^0)), \tag{2.20}$$

where $\lambda \in \operatorname{spec}_{M^{-1}} A$ if there exists x such that $Ax = \lambda M^{-1} x$. Then, we may require that $\tau^{-1} M \tau^{-1} = \lambda_{\max} M^{-1}$, that is to say $M\tau^{-1} = \lambda^{1/2}_{\max}(\boldsymbol{k}^0) I$, from where

$$\tau = \lambda^{-1/2}_{\max}(\boldsymbol{k}^0) M. \tag{2.21}$$

The components of $\boldsymbol{k}^0$ have to be understood as algorithmic constants.

2.2.4 Approximation of the subscales II: application to thermally coupled flows

Let us apply the previous ideas to the spatial differential operator appearing in (2.15)-(2.17). If we call $\boldsymbol{a} = \boldsymbol{u}_h + \tilde{\boldsymbol{u}}$ and consider it given as linearization strategy, and constant to allow the approximation of the Fourier transform, in the two-dimensional case it is found that

$$\hat{\mathcal{L}}(\boldsymbol{k}) = \begin{bmatrix} \nu|\boldsymbol{k}|^2 + \mathrm{i}a_j k_j & 0 & \mathrm{i}k_1 & \alpha g_1 s_T \\ 0 & \nu|\boldsymbol{k}|^2 + \mathrm{i}a_j k_j & \mathrm{i}k_2 & \alpha g_2 s_T \\ \mathrm{i}k_1 & \mathrm{i}k_2 & 0 & 0 \\ 0 & 0 & 0 & s_T(\kappa|\boldsymbol{k}|^2 + \mathrm{i}a_j k_j) \end{bmatrix}, \tag{2.22}$$

where $\mathrm{i} = \sqrt{-1}$ and s_T is a scaling factor for the temperature such that $\boldsymbol{f} \cdot \boldsymbol{u}$ and $s_T^{-1} QT$ have the same dimensions, that is to say, the dimensions of s_T must be [Temperature]^2[Velocity]$^{-2}$. It could be for example $s_T = \delta T^2 U^{-2}$, where δT and U are the characteristic values for temperature and velocity to define the dimensionless numbers in (2.11). The superscript in the wave number in (5.14) has been omitted.

Let us introduce the *stabilization* parameters τ_1, τ_2 and τ_3, computed as

$$\tau_1 = \left[\left(c_1 \frac{\nu}{h^2} \right)^2 + \left(c_2 \frac{|\boldsymbol{u}_h + \tilde{\boldsymbol{u}}|}{h} \right)^2 \right]^{-1/2}, \tag{2.23}$$

$$\tau_2 = \frac{h^2}{c_1 \tau_1}, \tag{2.24}$$

$$\tau_3 = \left[\left(c_1 \frac{\kappa}{h^2} \right)^2 + \left(c_2 \frac{|\boldsymbol{u}_h + \tilde{\boldsymbol{u}}|}{h} \right)^2 \right]^{-1/2}, \tag{2.25}$$

where h is the element size and c_1 and c_2 are algorithmic constants (we have adopted $c_1 = 4$ and $c_2 = 2$ in the numerical experiments) that approximate $h^2|\boldsymbol{k}|^2$ and $h|\boldsymbol{k}|$ multiplied by the cosine of the angle formed by $\boldsymbol{k}$ with $\boldsymbol{u}_h + \tilde{\boldsymbol{u}}$.

A possible scaling matrix in this particular problem (in 2D) is

$$M = \mathrm{diag}(\tau_1, \tau_1, \tau_2, \tau_3 s_T^{-1}).$$

If this matrix is used to solve the eigenvalue problem in (2.20), with $\hat{\mathcal{L}}(\boldsymbol{k})$ given by (5.14), it is found that

$$\lambda_{\max} = \frac{3}{2} + \frac{1}{2}\omega + \frac{1}{2}\sqrt{5 + 6\omega + \omega^2}, \quad \omega := \tau_1 \tau_3 \alpha^2 |\boldsymbol{g}|^2 s_T.$$

Suppose that the problem has a characteristic velocity U. Let us identify with a subscript h the analogous of the dimensionless numbers defined in (2.11) evaluated with the element size instead of L. If $s_T = \delta T^2 U^{-2}$, as explained above, it may be readily seen that

$$\omega \sim \mathrm{Ra}_h^2 \mathrm{Pe}_h^{-1} \mathrm{Re}_h^{-1} (1 + \mathrm{Pe}_h)^{-1} (1 + \mathrm{Re}_h)^{-1},$$

where $\sim$ stands for equality up to constants.

If the Boussinesq assumption is valid we may assume ω small, expand $\lambda_{\max}$ and keep only the lower order terms. However, our systematic approach will yield in this case a conservative value of $\lambda_{\max}^{-1/2}$. For example, for $\omega = 0$ we would find $\lambda_{\max} = \frac{3}{2} + \frac{\sqrt{5}}{2}$, whereas when there is no coupling $\lambda_{\max} = 1$ could be taken.

In the following analysis we will consider the simplest approximation $\lambda_{\max}^{-1/2} = 1$. Therefore, our *final approximation for the subgrid scales will be*

$$\partial_t \tilde{\boldsymbol{u}} + \frac{1}{\tau_1} \tilde{\boldsymbol{u}} = \tilde{P}(\boldsymbol{R}_u), \tag{2.26}$$

$$\frac{1}{\tau_2} \tilde{p} = \tilde{P}(R_p + \tau_1 \partial_t R_p), \tag{2.27}$$

$$\partial_t \tilde{T} + \frac{1}{\tau_3} \tilde{T} = \tilde{P}(R_T), \tag{2.28}$$

When the time derivative of the subscales is neglected, we will call them *quasi-static*, whereas otherwise we will call them *dynamic*.

2.2.5 Final approximate problem in space

Substituting (2.12)-(2.14) into (2.8)-(2.10), taking the test functions in the corresponding finite element spaces and integrating some terms by parts, and using the fact that $\boldsymbol{u} = \boldsymbol{u}_h + \tilde{\boldsymbol{u}}$ is divergence free, it is found that

$$
\begin{aligned}
&(\partial_t \boldsymbol{u}_h, \boldsymbol{v}_h) + \langle \boldsymbol{u}_h \cdot \nabla \boldsymbol{u}_h, \boldsymbol{v}_h \rangle + \nu(\nabla \boldsymbol{u}_h, \nabla \boldsymbol{v}_h) - (p_h, \nabla \cdot \boldsymbol{v}_h) + \alpha(\boldsymbol{g} T_h, \boldsymbol{v}_h) \\
&\qquad - \langle \tilde{\boldsymbol{u}}, \nu \Delta_h \boldsymbol{v}_h + \boldsymbol{u}_h \cdot \nabla \boldsymbol{v}_h \rangle \\
&\qquad + (\partial_t \tilde{\boldsymbol{u}}, \boldsymbol{v}_h) + \langle \tilde{\boldsymbol{u}} \cdot \nabla \boldsymbol{u}_h, \boldsymbol{v}_h \rangle - \langle \tilde{\boldsymbol{u}}, \tilde{\boldsymbol{u}} \cdot \nabla \boldsymbol{v}_h \rangle \\
&\qquad - (\tilde{p}, \nabla \cdot \boldsymbol{v}_h) + \alpha(\boldsymbol{g} \tilde{T}, \boldsymbol{v}_h) = \langle \boldsymbol{f}, \boldsymbol{v}_h \rangle + \alpha(\boldsymbol{g} T_0, \boldsymbol{v}_h), && (2.29) \\
&(q_h, \nabla \cdot \boldsymbol{u}_h) - (\tilde{\boldsymbol{u}}, \nabla q_h) = 0, && (2.30) \\
&(\partial_t T_h, \psi_h) + \langle \boldsymbol{u}_h \cdot \nabla T_h, \psi_h \rangle + \kappa(\nabla T_h, \nabla \psi_h) \\
&\qquad - \langle \tilde{T}, \kappa \Delta_h \psi_h + \boldsymbol{u}_h \cdot \nabla \psi_h \rangle \\
&\qquad + (\partial_t \tilde{T}, \psi_h) + \langle \tilde{\boldsymbol{u}} \cdot \nabla T_h, \psi_h \rangle - \langle \tilde{T}, \tilde{\boldsymbol{u}} \cdot \nabla \psi_h \rangle = \langle Q, \psi_h \rangle, && (2.31)
\end{aligned}
$$

which must hold for all test functions $(\boldsymbol{v}_h, q_h, \psi_h) \in \boldsymbol{V}_h \times Q_h \times \Psi_h$. The subindex h in the Laplacian denotes that it is evaluated elementwise. The subscales in these equations are obtained from (2.26)-(2.28).

The first approximation involved in the previous equations is to assume that the subscales vanish at the interelement boundaries. The final numerical scheme is obtained by approximating these subscales in the element interiors, in our case by means of (2.26)-(2.28). These equations however still require the definition of the projections $\tilde{P}$. Classical stabilized finite element methods correspond to taking $\tilde{P} = I$ (identity) when applied to the corresponding finite element residual. Our proposal however is to take $\tilde{P} = P_h^{\perp} = I - P_h$, where P_h is the L^2 projection onto the finite element space (see [19] and, for an analysis of the method for a stationary and linearized problem, [20]). This leads to what we call *orthogonal subscale stabilization* (OSS). When this is used in (2.29)-(2.31) one gets

$$
\begin{aligned}
&(\partial_t \boldsymbol{u}_h, \boldsymbol{v}_h) + \langle \boldsymbol{u}_h \cdot \nabla \boldsymbol{u}_h, \boldsymbol{v}_h \rangle + \nu(\nabla \boldsymbol{u}_h, \nabla \boldsymbol{v}_h) - (p_h, \nabla \cdot \boldsymbol{v}_h) + \alpha(\boldsymbol{g} T_h, \boldsymbol{v}_h) \\
&\qquad - \langle \tilde{\boldsymbol{u}}, \nu \Delta_h \boldsymbol{v}_h + \boldsymbol{u}_h \cdot \nabla \boldsymbol{v}_h \rangle + \langle \tilde{\boldsymbol{u}} \cdot \nabla \boldsymbol{u}_h, \boldsymbol{v}_h \rangle - \langle \tilde{\boldsymbol{u}}, \tilde{\boldsymbol{u}} \cdot \nabla \boldsymbol{v}_h \rangle - (\tilde{p}, \nabla \cdot \boldsymbol{v}_h) \\
&\qquad = \langle \boldsymbol{f}, \boldsymbol{v}_h \rangle + \alpha(\boldsymbol{g} T_0, \boldsymbol{v}_h), && (2.32) \\
&(q_h, \nabla \cdot \boldsymbol{u}_h) - (\tilde{\boldsymbol{u}}, \nabla q_h) = 0, && (2.33) \\
&(\partial_t T_h, \psi_h) + \langle \boldsymbol{u}_h \cdot \nabla T_h, \psi_h \rangle + \kappa(\nabla T_h, \nabla \psi_h) \\
&\qquad - \langle \tilde{T}, \kappa \Delta_h \psi_h + \boldsymbol{u}_h \cdot \nabla \psi_h \rangle + \langle \tilde{\boldsymbol{u}} \cdot \nabla T_h, \psi_h \rangle - \langle \tilde{T}, \tilde{\boldsymbol{u}} \cdot \nabla \psi_h \rangle = \langle Q, \psi_h \rangle. && (2.34)
\end{aligned}
$$

Note that $(\partial_t \tilde{\boldsymbol{u}}, \boldsymbol{v}_h)$ and $\alpha(\boldsymbol{g}\tilde{T}, \boldsymbol{v}_h)$ vanish in (2.29) and $(\partial_t \tilde{T}, \psi_h)$ vanishes in (2.31) because of the choice $\tilde{P} = P_h^{\perp}$.

Any time discretization can now be applied to obtain a fully discrete problem.

2.2.6 Main properties of the formulation

The first and most important point to be considered is the effect of considering the subscales dynamic, and therefore to deal with their time variation. Some of these properties are:

- The effect of the time integration is now clear. Certainly, when the time discretization is introduced the effective stabilization parameters have to be modified (as it is done for example in [5, 88, 91]), but when the steady-state is reached the subscale $\tilde{\boldsymbol{u}}$ that is obtained as solution to (2.26) satisfies $\tilde{\boldsymbol{u}} = \tau_1 \tilde{P}(\boldsymbol{R}_u)$, so that the usual expression employed for stationary problems is recovered.

- Suppose for example that the backward Euler scheme is used to integrate (2.26). From the point of view of the algebraic solver, the factor $\left(\frac{1}{\delta t} + \frac{1}{\tau_1}\right)^{-1}$ instead of τ_1 multiplying $\tilde{P}(\boldsymbol{R}_u)$ is crucial for the conditioning of the system matrix. If τ_1 is used as stabilization factor, when $\delta t \to 0$ (and thus the leading terms are those coming from the discretization of the time derivative) both the Galerkin and stabilizing terms could lead to matrix terms of the same order and the condition number of the matrix of the Galerkin method could be deteriorated.

- It is clear that space discretization (understood as scale splitting) and time discretization commute, that is *time discretization + stabilization (scale splitting) = stabilization (scale splitting) + time discretization.*

- Numerical experiments show that the temporal time integration is significantly improved:

  - Oscillations originated by initial transients are eliminated.
  - The numerical dissipation is minimized.

  For the numerical results that demonstrate this fact we refer to [27, 24]. This is also observed in the numerical experiments of Section 2.4.

- The numerical analysis shows optimal stability without any restriction between τ_1 and δt. Contrary to classical stabilized methods, anisotropic space-time discretizations are allowed [7]. See [27] for a stability analysis of the linearized Navier-Stokes equations and [3] for a complete stability and convergence analysis for the Stokes problem.

Another very important issue of the formulation presented is the possibility to model turbulent flows. The terms involving the velocity subgrid scale arising from the convective term in the Navier-Stokes equations are $\langle \tilde{\boldsymbol{u}}, \tilde{\boldsymbol{u}} \cdot \nabla \boldsymbol{v}_h \rangle = \langle \nabla \boldsymbol{v}_h, \tilde{\boldsymbol{u}} \otimes \tilde{\boldsymbol{u}} \rangle$, which can be understood as the contribution from *the Reynolds tensor* an LES approach, and $-\langle \tilde{\boldsymbol{u}}, \boldsymbol{u}_h \cdot \nabla \boldsymbol{v}_h \rangle + \langle \tilde{\boldsymbol{u}} \cdot \nabla \boldsymbol{u}_h, \boldsymbol{v}_h \rangle$, which can be understood as the contribution from *the cross stresses*. Therefore, we may expect that, in some sense, *modeling* $\tilde{\mathbf{u}}$ *implies to model the subgrid scale tensor*. The question is how good this model will be. The numerical models proposed here yield two possibilities depending on the projection chosen, but others can be devised.

Related to the way turbulence is modeled, the numerical formulation proposed has an inherent turbulent Prandtl number. In other words, it is not necessary to specify which is the amount of turbulent thermal dissipation, but emanates directly from the formulation. This issue is further discussed later on.

2.3 Conservation properties and energy transfer mechanisms

In this section we discuss some conservation properties and the dissipative structure of the formulation proposed which are relevant for the numerical modeling of thermally coupled turbulent flows. In order to simplify a bit the exposition, we will consider the parameter $\tau_2 = 0$, that is to say, $\tilde{p} = 0$ in (2.27).

Another important remark is that the expression used for the convective term might not be the most convenient one. For divergence free velocity fields vanishing on the domain boundary, we have that

$$\langle \boldsymbol{u} \cdot \nabla \boldsymbol{u}, \boldsymbol{v} \rangle = -\langle \boldsymbol{u} \otimes \boldsymbol{u}, \nabla \boldsymbol{v} \rangle = \frac{1}{2}\langle \boldsymbol{u} \cdot \nabla \boldsymbol{u}, \boldsymbol{v} \rangle - \frac{1}{2}\langle \boldsymbol{u} \otimes \boldsymbol{u}, \nabla \boldsymbol{v} \rangle.$$

Any of these expressions can be used in the convective term of the approximate Navier-Stokes equations without altering the consistency. However, the discrete problem has different properties, as we will see. Thus, given a vector field $\boldsymbol{a}$ we introduce

$$c_u(\boldsymbol{a}; \boldsymbol{u}, \boldsymbol{v}) = \begin{cases} c_u^{\text{nc}}(\boldsymbol{a}; \boldsymbol{u}, \boldsymbol{v}) = \langle \boldsymbol{a} \cdot \nabla \boldsymbol{u}, \boldsymbol{v} \rangle & \text{Non conservative form} \\ c_u^{\text{c}}(\boldsymbol{a}; \boldsymbol{u}, \boldsymbol{v}) = -\langle \boldsymbol{a} \otimes \boldsymbol{u}, \nabla \boldsymbol{v} \rangle & \text{Conservative form} \\ c_u^{\text{ss}}(\boldsymbol{a}; \boldsymbol{u}, \boldsymbol{v}) = \frac{1}{2}\langle \boldsymbol{a} \cdot \nabla \boldsymbol{u}, \boldsymbol{v} \rangle - \frac{1}{2}\langle \boldsymbol{a} \otimes \boldsymbol{u}, \nabla \boldsymbol{v} \rangle & \text{Skew-symmetric form} \end{cases} \tag{2.35}$$

Similarly, for the temperature equation we introduce

$$c_T(\boldsymbol{a}; T, \psi) = \begin{cases} c_T^{\text{nc}}(\boldsymbol{a}; T, \psi) = \langle \boldsymbol{a} \cdot \nabla T, \psi \rangle & \text{Non-conservative form} \\ c_T^{\text{c}}(\boldsymbol{a}; T, \psi) = -\langle \boldsymbol{a} T, \nabla \psi \rangle & \text{Conservative form} \\ c_T^{\text{ss}}(\boldsymbol{a}; T, \psi) = \frac{1}{2}\langle \boldsymbol{a} \cdot \nabla T, \psi \rangle - \frac{1}{2}\langle \boldsymbol{a} T, \nabla \psi \rangle & \text{Skew-symmetric form} \end{cases} \tag{2.36}$$

The terms “conservative” and “non-conservative” are classical in the CFD community. The term “skew-symmetric” refers to the fact that

$$c_u^{\text{ss}}(\boldsymbol{a}; \boldsymbol{u}, \boldsymbol{u}) = 0, \quad c_T^{\text{ss}}(\boldsymbol{a}; T, T) = 0,$$

even if $\boldsymbol{a}$ is *not* divergence free.

In order to study the conservation properties of the scheme, we consider the extended problem which includes the boundary fluxes $B_{R,u}(\boldsymbol{v}_h)$ and $B_{R,T}(\psi_h)$ in the Navier Stokes and heat equations [56]. These fluxes may include contributions from the convective term when $\boldsymbol{a}$ is not divergence free, which may change according to the form used for this term (non conservative, conservative or skew symmetric). This problem can be understood locally in a region R formed by an arbitrary set of elements [81, 56], case in which boundary contributions come from the fluxes exchanged with the rest of the computational domain.

Using the approximation $\tau_2 = 0$, defining $\boldsymbol{a} = \boldsymbol{u}_h + \tilde{\boldsymbol{u}}$ (which is solenoidal prior to the approximation of the subscales), introducing the possibilities for the convective term described and accounting for the boundary fluxes, problem (2.32)-(2.34) can be reformulated as:

$$\begin{aligned}
&(\partial_t \boldsymbol{u}_h, \boldsymbol{v}_h) + c_u(\boldsymbol{a}; \boldsymbol{u}_h, \boldsymbol{v}_h) + \nu(\nabla \boldsymbol{u}_h, \nabla \boldsymbol{v}_h) - (p_h, \nabla \cdot \boldsymbol{v}_h) + \alpha(\boldsymbol{g} T_h, \boldsymbol{v}_h) \\
&\qquad - \langle \tilde{\boldsymbol{u}}, \nu \Delta_h \boldsymbol{v}_h + \boldsymbol{a} \cdot \nabla \boldsymbol{v}_h \rangle = \langle \boldsymbol{f}, \boldsymbol{v}_h \rangle + \alpha(\boldsymbol{g} T_0, \boldsymbol{v}_h) + B_{R,u}(\boldsymbol{v}_h), && (2.37) \\
&(q_h, \nabla \cdot \boldsymbol{u}_h) - (\tilde{\boldsymbol{u}}, \nabla q_h) = 0, && (2.38) \\
&(\partial_t T_h, \psi_h) + c_T(\boldsymbol{a}; T_h, \psi_h) + \kappa(\nabla T_h, \nabla \psi_h) \\
&\qquad - \langle \tilde{T}, \kappa \Delta_h \psi_h + \boldsymbol{a} \cdot \nabla \psi_h \rangle = \langle Q, \psi_h \rangle + B_{R,T}(\psi_h). && (2.39)
\end{aligned}$$

As mentioned earlier, we may understand that this problem is posed in a region $R \subset \Omega$ formed by an arbitrary union of elements K of the finite element partition. When $R = \Omega$, $B_{\Omega,u}(\boldsymbol{v}_h) = 0$ and $B_{\Omega,T}(\psi_h) = 0$ with homogeneous boundary conditions. Otherwise, these boundary terms may depend on the way the convective term is written, but in any case they will be due to the action exerted by the fluid outside R on its boundary.

2.3.1 Conservation

Different conservation statements can be obtained by taking appropriate test functions in the discrete variational problems (2.37)-(2.39). They all hold at the continuous level, but not at the discrete one, since $\boldsymbol{a}$ will not be exactly divergence free. In what follows, R is considered strictly contained in Ω to allow us taking constant test functions in R. Otherwise, if $R = \Omega$ the homogeneous Dirichlet conditions have to be replaced by the appropriate fluxes.

Conservation of linear momentum and heat

Let $\boldsymbol{e}_k$ be the vector of $\mathbb{R}^d$ with the k-th component equal to 1 and the rest equal to 0. Taking $\boldsymbol{v}_h = \boldsymbol{e}_k$ in (2.37) it follows that

$$\frac{\mathrm{d}}{\mathrm{d}t} \int_R u_{h,k} + c_u(\boldsymbol{a}; \boldsymbol{u}_h, \boldsymbol{e}_k) = \int_R [f_k + \alpha g_k (T_0 - T_h)] + B_{R,u}(\boldsymbol{e}_k).$$

This equation can be understood as a conservation of linear momentum in a region R *provided* $c_u(\boldsymbol{a}; \boldsymbol{u}_h, \boldsymbol{e}_k) = 0$ *or has only contributions on* ∂R. If the conservative form of the convective term is used it is obvious that $c_u^{\mathrm{c}}(\boldsymbol{a}; \boldsymbol{u}_h, \boldsymbol{e}_k) = 0$ (see (2.35)), so that *the conservative form always conserves linear momentum.* On the other hand, it is immediately checked that

$$c_u^{\mathrm{nc}}(\boldsymbol{a}; \boldsymbol{u}_h, \boldsymbol{e}_k) = -\int_R u_{h,k} \nabla \cdot \boldsymbol{u}_h + \int_R \tilde{\boldsymbol{u}} \cdot \nabla u_{h,k} + \int_{\partial R} (\boldsymbol{n} \cdot \boldsymbol{u}_h) u_{h,k},$$

where $\boldsymbol{n}$ is the unit normal exterior to ∂R. From (2.38) it follows that the first two terms in this equation are zero, provided we can take $q_h = u_{h,k}$. Thus, *the non-conservative form conserves linear momentum if equal velocity-pressure interpolations are used.* Note that this would not be possible using the Galerkin method. This fact was already noticed in [56].

From the expression of the skew-symmetric form of the convective term it is clear that it has the same properties as the non-conservative form, since now

$$c_u^{\mathrm{ss}}(\boldsymbol{a}; \boldsymbol{u}_h, \boldsymbol{e}_k) = -\frac{1}{2} \int_R u_{h,k} \nabla \cdot \boldsymbol{u}_h + \frac{1}{2} \int_R \tilde{\boldsymbol{u}} \cdot \nabla u_{h,k} + \frac{1}{2} \int_{\partial R} (\boldsymbol{n} \cdot \boldsymbol{u}_h) u_{h,k}.$$

A similar analysis can be undertaken for the heat equation. If $\psi_h = 1$ in (2.39) it follows that

$$\frac{\mathrm{d}}{\mathrm{d}t}\int_R T_h + c_T(\boldsymbol{a}; T_h, 1) = \int_R Q + B_{R,T}(1).$$

This equation can be understood as a conservation of heat in a region R *provided* $c_T(\boldsymbol{a}; T_h, 1) = 0$ *or contributes only with terms defined on* ∂R. Once again, if the conservative form of the convective term is used, $c_T^{\mathrm{c}}(\boldsymbol{a}; T_h, 1) = 0$ (see (2.36)), so that *the conservative form always conserves heat*. On the other hand,

$$c_T^{\mathrm{nc}}(\boldsymbol{a}; T_h, 1) = -\int_R T_h \nabla \cdot \boldsymbol{u}_h + \int_R \tilde{\boldsymbol{u}} \cdot \nabla T_h + \int_{\partial R} (\boldsymbol{n} \cdot \boldsymbol{u}_h) T_h.$$

From (2.38) it follows that the first two terms in this equation are zero, provided we can take $q_h = T_h$. Thus, *the non-conservative form conserves heat if equal temperature-pressure interpolations are used*. As for the Navier-Stokes equations, the same conclusion applies to the skew-symmetric form of the convective term in the heat equation.

Conservation of angular momentum

Conservation of angular momentum for the continuous version of (2.37) is obtained by taking $\boldsymbol{v} = \boldsymbol{e}_k \times \boldsymbol{x}$, where $\boldsymbol{x}$ is the position vector. For all vectors $\boldsymbol{w}$ it follows that $\boldsymbol{w} \cdot \boldsymbol{v} = \boldsymbol{x} \times \boldsymbol{w}|_k$ (the k-th component of $\boldsymbol{x} \times \boldsymbol{w}$). Note also that $\nabla \cdot (\boldsymbol{e}_k \times \boldsymbol{x}) = 0$.

If we take $\boldsymbol{v}_h = \boldsymbol{e}_k \times \boldsymbol{x}$, a necessary condition to have a global angular momentum conservation statement is that the viscous term vanishes. It is readily checked that

$$\nu(\nabla \boldsymbol{u}_h, \nabla(\boldsymbol{e}_k \times \boldsymbol{x})) = \nu \int_R \nabla \times \boldsymbol{u}_h|_k,$$

which is in general not zero. Let ∇^S be the symmetrical gradient operator. The viscous term at the continuous level could also be written as $2\nu(\nabla^S \boldsymbol{u}, \nabla^S \boldsymbol{v})$. Since $\nabla^S(\boldsymbol{e}_k \times \boldsymbol{x}) = 0$, we conclude that *the viscous term has to be written as* $2\nu(\nabla^S \boldsymbol{u}_h, \nabla^S \boldsymbol{v}_h)$ to allow global conservation of angular momentum. However, writing the viscous term this way is obviously not enough. The convective term must also vanish when $\boldsymbol{v}_h = \boldsymbol{e}_k \times \boldsymbol{x}$ (or lead only to boundary contributions). If the non-conservative form is used we have that

$$c_u^{\mathrm{nc}}(\boldsymbol{a}; \boldsymbol{u}_h, \boldsymbol{e}_k \times \boldsymbol{x}) = -\int_R (\nabla \cdot \boldsymbol{u}_h) \boldsymbol{x} \times \boldsymbol{u}_h|_k + \int_R \tilde{\boldsymbol{u}} \cdot \nabla(\boldsymbol{x} \times \boldsymbol{u}_h|_k) + \int_{\partial R} (\boldsymbol{n} \cdot \boldsymbol{u}_h) \boldsymbol{x} \times \boldsymbol{u}_h|_k. \tag{2.40}$$

We could guarantee that the first two terms vanish only if we could take $q_h = \boldsymbol{x} \times \boldsymbol{u}_h|_k$, which would be possible only if the pressure interpolation is of one order higher than the velocity interpolation. This does not make sense for the approximation of the Navier-Stokes equations, and therefore we consider not possible to have angular momentum conservation using the non-conservative form of the convective term. However, we can take $q_h = P_h(\boldsymbol{x} \times \boldsymbol{u}_h|_k)$ in (2.38), and therefore (2.40) reduces to

$$\begin{aligned} c_u^{\mathrm{nc}}(\boldsymbol{a}; \boldsymbol{u}_h, \boldsymbol{e}_k \times \boldsymbol{x}) = &-\int_R (\nabla \cdot \boldsymbol{u}_h) P_h^{\perp}(\boldsymbol{x} \times \boldsymbol{u}_h|_k) + \int_R \tilde{\boldsymbol{u}} \cdot \nabla P_h^{\perp}(\boldsymbol{x} \times \boldsymbol{u}_h|_k) \\ &+ \int_{\partial R} (\boldsymbol{n} \cdot \boldsymbol{u}_h) \boldsymbol{x} \times \boldsymbol{u}_h|_k, \end{aligned}$$

and, formally, $P_h^\perp(\boldsymbol{x} \times \boldsymbol{u}_h|_k)$ is of order $r + 1$, r being the interpolation order. Thus, the error involved in the approximation of the angular momentum will be small. Concerning the contribution from the velocity subscales in (2.37), it holds

$$-\langle \tilde{\boldsymbol{u}}, \boldsymbol{a} \cdot \nabla(\boldsymbol{e}_k \times \boldsymbol{x})\rangle = -\int_R \tilde{\boldsymbol{u}} \times \boldsymbol{u}_h|_k, \tag{2.41}$$

which is zero if the subscales are L^2 orthogonal to the finite element space. Clearly, the same comments apply to the skew-symmetric form of the convective term.

Let us move our attention to the conservative form defined in (2.35). It is readily checked that

$$c_u^{\mathrm{c}}(\boldsymbol{a}; \boldsymbol{u}_h, \boldsymbol{e}_k \times \boldsymbol{x}) = \int_R \tilde{\boldsymbol{u}} \times \boldsymbol{u}_h|_k, \tag{2.42}$$

This, together with (2.41), yields

$$c_u^{\mathrm{c}}(\boldsymbol{a}; \boldsymbol{u}_h, \boldsymbol{e}_k \times \boldsymbol{x}) - \langle \tilde{\boldsymbol{u}}, \boldsymbol{a} \cdot \nabla(\boldsymbol{e}_k \times \boldsymbol{x})\rangle = 0,$$

so that we obtain the statement of angular momentum conservation

$$\frac{\mathrm{d}}{\mathrm{d}t} \int_R \boldsymbol{x} \times \boldsymbol{u}_h = \int_R \boldsymbol{x} \times [\boldsymbol{f} + \alpha \boldsymbol{g}(T_0 - T_h)] + B_{R,u}(\boldsymbol{e}_k \times \boldsymbol{x}).$$

when the conservation form of the convective term is employed, independently of whether the velocity subscales are orthogonal or not to the finite element space.

Conservation of kinetic energy and heat energy

The last conservation statements we wish to discuss are those of kinetic energy for the Navier-Stokes equations and of heat energy for the heat equation. By "energy" we mean simply the L^2 norm of the velocity or the temperature, although in particular the L^2 norm of the temperature, that we call "heat energy", is not a physical energy. For the continuous problem, conservation of these quantities is obtained by taking the test functions equal to the velocity and the temperature, respectively, and using in a crucial manner the fact that the velocity is solenoidal to conclude that the convective terms in the corresponding equations do not contribute.

In the discrete case, we need to have $c_u(\boldsymbol{a}; \boldsymbol{u}_h, \boldsymbol{u}_h) = 0$ and $c_T(\boldsymbol{a}; T_h, T_h) = 0$. This is automatically satisfied for the skew-symmetric forms of these convective terms (this leads in fact to their definition), but not for the conservative or non-conservative forms. Therefore, *only the skew-symmetric expressions in (2.35) and (2.36) may lead to conservation of kinetic energy and of heat energy, respectively.*

When obtaining energy balance statements is when the importance of orthogonal and dynamic subgrid scales is more evident. To this end, it is enlightening not only to take $\boldsymbol{v}_h = \boldsymbol{u}_h$, $q_h = p_h$ and $\psi_h = T_h$ (for each $t \in (0, T)$), but also to test the equations for the subscales (2.26) and (2.28) (recall that we are assuming $\tau_2 = 0$) by $\tilde{\boldsymbol{u}}$ and $\tilde{T}$, respectively. If this is done, we get:

$$\frac{1}{2}\frac{\mathrm{d}}{\mathrm{d}t}\|\boldsymbol{u}_h\|_R^2 + \nu\|\nabla\boldsymbol{u}_h\|_R^2 - \sum_{K\subset R}\left\langle\tilde{\boldsymbol{u}}, \tilde{P}(\nu\Delta_h\boldsymbol{u}_h + \boldsymbol{a}\cdot\nabla\boldsymbol{u}_h + \nabla p_h)\right\rangle_K = W_h, \tag{2.43}$$

$$\frac{1}{2}\frac{\mathrm{d}}{\mathrm{d}t}\|\tilde{\boldsymbol{u}}\|_R^2 + \tau_1^{-1}\|\tilde{\boldsymbol{u}}\|_R^2 - \sum_{K\subset R}\left\langle\tilde{\boldsymbol{u}}, \tilde{P}(\nu\Delta_h\boldsymbol{u}_h - \boldsymbol{a}\cdot\nabla\boldsymbol{u}_h - \nabla p_h)\right\rangle_K = \tilde{W}, \tag{2.44}$$

$$\frac{1}{2}\frac{\mathrm{d}}{\mathrm{d}t}\|T_h\|_R^2 + \kappa\|\nabla T_h\|_R^2 - \sum_{K\subset R}\left\langle\tilde{T}, \tilde{P}(\kappa\Delta_h T_h + \boldsymbol{a}\cdot\nabla T_h)\right\rangle_K = H_h, \tag{2.45}$$

$$\frac{1}{2}\frac{\mathrm{d}}{\mathrm{d}t}\|\tilde{T}\|_R^2 + \tau_3^{-1}\|\tilde{T}\|_R^2 - \sum_{K\subset R}\left\langle\tilde{T}, \tilde{P}(\kappa\Delta_h T_h - \boldsymbol{a}\cdot\nabla T_h)\right\rangle_K = \tilde{H}. \tag{2.46}$$

In these expressions, $\|\cdot\|_R$ is the L^2 norm in R, $\langle f,g\rangle_K = \int_K fg$, W_h is the total mechanical power on R due to $\boldsymbol{u}_h$ (including the contribution from the Boussinesq model), $\tilde{W}$ the total mechanical power on R due to $\tilde{\boldsymbol{u}}$, H_h the total heat power on R due to T_h and $\tilde{H}$ the total heat power on R due to $\tilde{T}$. Here and in what follows we have assumed the stabilization parameters τ_1 and τ_3 constant in region R.

It is obvious from (2.43)-(2.46) that *there is no balance statement* for the kinetic energy of $\boldsymbol{u}_h$ or the heat energy of T_h *alone*, in the form of time variation plus dissipation equal to external input. However, these balance statements can indeed be found when the contributions from the finite element components and the subscales are added up. We will further elaborate this point in the following subsection, but we may already notice that

$$\frac{1}{2}\frac{\mathrm{d}}{\mathrm{d}t}\|\boldsymbol{u}_h\|_R^2 + \frac{1}{2}\frac{\mathrm{d}}{\mathrm{d}t}\|\tilde{\boldsymbol{u}}\|_R^2 + \nu\|\nabla\boldsymbol{u}_h\|_R^2 + \tau_1^{-1}\|\tilde{\boldsymbol{u}}\|_R^2 - 2\sum_{K\subset R}\left\langle\tilde{\boldsymbol{u}}, \tilde{P}(\nu\Delta_h\boldsymbol{u}_h)\right\rangle_K = W_h + \tilde{W}, \tag{2.47}$$

$$\frac{1}{2}\frac{\mathrm{d}}{\mathrm{d}t}\|T_h\|_R^2 + \frac{1}{2}\frac{\mathrm{d}}{\mathrm{d}t}\|\tilde{T}\|_R^2 + \kappa\|\nabla T_h\|_R^2 + \tau_3^{-1}\|\tilde{T}\|_R^2 - 2\sum_{K\subset R}\left\langle\tilde{T}, \tilde{P}(\kappa\Delta_h T_h)\right\rangle_K = H_h + \tilde{H}. \tag{2.48}$$

The second order derivatives can be neglected for linear interpolations (they identically zero) or when $\tilde{P}$ is taken as the L^2 projection to the space orthogonal to the corresponding finite element space (of velocities or of temperatures) *without* boundary conditions. In any case, from the expression of the stabilization parameters and some simple inverse estimates it can be shown that

$$\nu\|\nabla\boldsymbol{u}_h\|_R^2 + \tau_1^{-1}\|\tilde{\boldsymbol{u}}\|_R^2 - 2\sum_{K\subset R}\left\langle\tilde{\boldsymbol{u}}, \tilde{P}(\nu\Delta_h\boldsymbol{u}_h)\right\rangle_K \geq C\left(\nu\|\nabla\boldsymbol{u}_h\|_R^2 + \tau_1^{-1}\|\tilde{\boldsymbol{u}}\|_R^2\right),$$

for a constant $C > 0$, and similarly for the heat equation. Therefore, (2.47)-(2.48) *do have* the structure of time variation of energy plus dissipation equal to external input. In equations (2.43)-(2.46) there are some additional terms that can be understood as transfer of energy between scales, as explained in Subsection 2.3.2 below.

Convective term	Linear momentum	Angular momentum	Kinetic energy
Conservative	Yes	Yes	No
Non-conservative	Yes With equal $\boldsymbol{u}$-p interpolation	No	No
Skew-symmetric	Yes With equal $\boldsymbol{u}$-p interpolation	No	Yes

Table 2.1: Conservation properties for the Navier-Stokes equations depending on the expression of the convective term

Convective term	Heat	Heat energy
Conservative	Yes	No
Non-conservative	Yes With equal p-T interpolation	No
Skew-symmetric	Yes With equal p-T interpolation	Yes

Table 2.2: Conservation properties for the heat equation depending on the expression of the convective term

Summary

The results obtained in this subsection are collected in Table 2.1 for the Navier-Stokes equations and in Table 2.2 for the heat equation. As we have seen, the crucial point to obtain these results is the way in which the convective term is written.

Concerning the conservation of energy, it has to be understood that this refers to a balance in the sense described above, that is, including a positive dissipative term. As we have seen, this applies to the sum of the finite element component and the subscales (of velocity and of temperature), whereas the rest of conservation statements apply to the finite element component only. In fact, from the expression of the approximate equations for the subscales, (2.26) and (2.28), it can be seen that neither linear momentum nor angular momentum can be conserved for $\tilde{\boldsymbol{u}}$ (both will always decrease) and heat cannot be conserved for $\tilde{T}$ (it will also decrease).

2.3.2 Energy transfer terms

Let us take a closer look at the energy conservation equations (2.43)-(2.46). Introducing the definitions of Table 2.3, these equations can be written as

$$\begin{aligned}
\frac{\mathrm{d}}{\mathrm{d}t}\mathcal{E}_h^u + \mathcal{D}_h^u + \mathcal{C}^u + \mathcal{T}^u &= W_h,\\
\frac{\mathrm{d}}{\mathrm{d}t}\tilde{\mathcal{E}}^u + \tilde{\mathcal{D}}^u + \mathcal{C}^u - \mathcal{T}^u &= \tilde{W},\\
\frac{\mathrm{d}}{\mathrm{d}t}\mathcal{E}_h^T + \mathcal{D}_h^T + \mathcal{C}^T + \mathcal{T}^T &= H_h,\\
\frac{\mathrm{d}}{\mathrm{d}t}\tilde{\mathcal{E}}^T + \tilde{\mathcal{D}}^T + \mathcal{C}^T - \mathcal{T}^T &= \tilde{H}.
\end{aligned}$$

Note that with the Boussinesq model there is an energy input in the Navier-Stokes equations in the form of external power, in our case contained in the term W_h, that is not reflected in the heat equation.

Several remarks are in order:

- The dissipation terms are strictly positive. They contribute to decrease the energy of the variable whose balance is expressed in the equation where they appear.

- The cross scale dissipation terms defined in Table 2.3 appear in both the equation for the finite element scale and for the subscale (in either the Navier-Stokes or the heat equation). As explained earlier, they can be absorbed by the dissipation of *both* the finite element scale and the subscale, but not by any of them independently. Therefore, the cross scale dissipation terms *couple* the energy balance of the two scales of the problem. However, these terms *vanish* as $\nu \to 0$ and $\kappa \to 0$, and are otherwise active when viscosity and conductivity are high. In this case it is known that there is no scale separation, because the flow is completely resolved, i.e. direct numerical simulation (DNS) resolution has been reached.

- The transfer terms appear with an opposite sign in the energy equation for the finite element component and the subscale component. Thus, they certainly represent *transfer of energy between scales*. This, together with the fact that the cross scale dissipation terms vanish for vanishing viscosity and conductivity, leads us to conclude that in this situation *there is a scale separation between the finite element components and the subscales*. To arrive to this conclusion, it is essential to consider the subscales dynamic and orthogonal to the finite element space.

2.3.3 Numerical dissipation

To conclude this section, let us discuss the concept of numerical dissipation of the algorithm, both for the Navier-Stokes and the heat equation, and the possibility to model turbulence using this dissipation.

Equation	Energy	Dissipation
$\boldsymbol{u}_h$	$\mathcal{E}_h^u = \frac{1}{2}\Vert\boldsymbol{u}_h\Vert_R^2$	$\mathcal{D}_h^u = \nu\Vert\nabla\boldsymbol{u}_h\Vert_R^2$
$\tilde{\boldsymbol{u}}$	$\tilde{\mathcal{E}}^u = \frac{1}{2}\Vert\tilde{\boldsymbol{u}}\Vert_R^2$	$\tilde{\mathcal{D}}^u = \tau_1^{-1}\Vert\tilde{\boldsymbol{u}}\Vert_R^2$
T_h	$\mathcal{E}_h^T = \frac{1}{2}\Vert T_h\Vert_R^2$	$\mathcal{D}_h^T = \kappa\Vert\nabla T_h\Vert_R^2$
$\tilde{T}$	$\tilde{\mathcal{E}}^T = \frac{1}{2}\Vert\tilde{T}\Vert_R^2$	$\tilde{\mathcal{D}}^T = \tau_3^{-1}\Vert\tilde{T}\Vert_R^2$
Equation	Cross scale dissipation	Transfer term
$\boldsymbol{u}_h$	$\mathcal{C}^u = -\sum_{K\subset R}\left\langle\tilde{\boldsymbol{u}}, \tilde{P}(\nu\Delta_h\boldsymbol{u}_h)\right\rangle_K$	$\mathcal{T}^u = -\sum_{K\subset R}\left\langle\tilde{\boldsymbol{u}}, \tilde{P}(\boldsymbol{a}\cdot\nabla\boldsymbol{u}_h + \nabla p_h)\right\rangle_K$
$\tilde{\boldsymbol{u}}$	$\mathcal{C}^u$	$-\mathcal{T}^u$
T_h	$\mathcal{C}^T = -\sum_{K\subset R}\left\langle\tilde{T}, \tilde{P}(\kappa\Delta_h T_h)\right\rangle_K$	$\mathcal{T}^T = -\sum_{K\subset R}\left\langle\tilde{T}, \tilde{P}(\boldsymbol{a}\cdot\nabla T_h)\right\rangle_K$
$\tilde{T}$	$\mathcal{C}^T$	$-\mathcal{T}^T$

Table 2.3: Energy transfer terms

One can consider as numerical dissipation the one that affects the finite element component alone. If we write the subscales emanating from (2.26) and (2.28) as

$$\begin{aligned}\tilde{\boldsymbol{u}} &= \tau_1\left(\tilde{P}(\boldsymbol{R}_u) - \partial_t\tilde{\boldsymbol{u}}\right),\\ \tilde{T} &= \tau_3\left(\tilde{P}(R_T) - \partial_t\tilde{T}\right),\end{aligned}$$

we may write the total dissipation of the finite element scales as

$$\varepsilon_{\text{num}}^u := -\tau_1\sum_{K\subset R}\left\langle\tilde{P}(\boldsymbol{R}_u) - \partial_t\tilde{\boldsymbol{u}}, \tilde{P}(\nu\Delta_h\boldsymbol{u}_h + \boldsymbol{a}\cdot\nabla\boldsymbol{u}_h + \nabla p_h)\right\rangle_K, \tag{2.49}$$

$$\varepsilon_{\text{num}}^T := -\tau_3\sum_{K\subset R}\left\langle\tilde{P}(R_T) - \partial_t\tilde{T}, \tilde{P}(\kappa\Delta_h T_h - \boldsymbol{a}\cdot\nabla T_h)\right\rangle_K. \tag{2.50}$$

There are two main properties of $\varepsilon_{\text{num}}^u$ that are of paramount importance in the modeling of turbulent flows:

- For quasi-static subscales, it is shown in [41] that $\varepsilon_{\text{num}}^u$ behaves as the molecular dissipation of the continuous problem when the assumptions of classical statistical fluid mechanics apply and the mesh size h belongs to the inertial range of the Kolmogorov spectrum. This is precisely the requirement posed by Lilly to LES models [62], and thus *it poses the question of whether additional LES modeling is required or not in our pure numerical approach*. Our claim is that the answer is no.

- For quasi-static subscales, $\boldsymbol{f} = 0$ (or it is a finite element function) and $\nu \to 0$ and, $\varepsilon_{\text{num}}^u$ is non-negative at each point and at each time instant. However, for dynamic subscales this cannot be guaranteed a priori. In fact, numerical experiments show that $\varepsilon_{\text{num}}^u$ can be negative at some points and some time instants [81], that is to say, *dynamic subscales allow for backscatter*.

When applicable, similar concepts can be applied to the dissipation of the heat equation, $\varepsilon_{\mathrm{num}}^T$. However, in this case there is an additional issue to consider, namely, which is the ratio between $\varepsilon_{\mathrm{num}}^u$ and $\varepsilon_{\mathrm{num}}^T$, after appropriate scaling. This is what can be considered *the turbulent Prandtl number*. In usual LES models it needs to be assumed a priori. In our case it is an outcome of the numerical model.

If we introduce the effective turbulent viscosity and turbulent thermal conductivity

$$\nu_{\mathrm{tur}} = \frac{\varepsilon_{\mathrm{num}}^u}{\|\nabla \boldsymbol{u}_h\|^2}, \qquad \kappa_{\mathrm{tur}} = \frac{\varepsilon_{\mathrm{num}}^T}{\|\nabla T_h\|^2},$$

the turbulent Prandtl number may be defined as

$$\mathrm{Pr}_{\mathrm{tur}} := \frac{\nu_{\mathrm{tur}}}{\kappa_{\mathrm{tur}}} = \frac{\varepsilon_{\mathrm{num}}^u}{\|\nabla \boldsymbol{u}_h\|^2} \frac{\|\nabla T_h\|^2}{\varepsilon_{\mathrm{num}}^T}. \tag{2.51}$$

In view of expressions (2.49) and (2.50), if for $\nu \to 0$ and $\kappa \to 0$ we neglect the influence of the pressure gradient and assume that the gradients of velocity and temperature form the same angle with $\boldsymbol{a}$, we may estimate

$$\mathrm{Pr}_{\mathrm{tur}}^2 \sim \frac{\tau_1^2}{\tau_3^2} = \frac{c_1^2\kappa^2 + c_2^2|\boldsymbol{a}|^2 h^2}{c_1^2\nu^2 + c_2^2|\boldsymbol{a}|^2 h^2} = \frac{1 + \frac{c_2^2}{c_1^2}\mathrm{Pe}_h^2}{\mathrm{Pr}^2 + \frac{c_2^2}{c_1^2}\mathrm{Pe}_h^2}, \tag{2.52}$$

where

$$\mathrm{Pe}_h := \frac{|\boldsymbol{a}|h}{\kappa}, \tag{2.53}$$

is the element Péclet number. From (2.52) it follows that

$$\mathrm{Pr}_{\mathrm{tur}} \sim \begin{cases} \frac{1}{\mathrm{Pr}} & \text{if } \mathrm{Pe}_h \to 0 \\ 1 & \text{if } \mathrm{Pe}_h \to \infty \end{cases}$$

These limiting situations cannot be assumed in general turbulent flows. In a numerical example we will show that in fact the effective turbulent Prandtl number departs significantly from $\mathrm{Pr}_{\mathrm{tur}} = 1$, which is the value usually adopted when modeling turbulent thermal flows.

2.4 Numerical examples

2.4.1 Flow in a differentially heated cavity with aspect ratio 8

As a first example of application of the formulation presented, we have modeled the flow in a differentially heated cavity with aspect ratio 8. The data of the problem can be found in [15]. The interest of this problem in that it displays transition to chaos as the Rayleigh number is increased.

Three different Rayleigh numbers will be considered: $\mathrm{Ra} = 3.45\ 10^5$, where it is known that a Hopf bifurcation has occurred and the flow is oscillatory, $\mathrm{Ra} = 10^6$ and $\mathrm{Ra} = 10^7$.

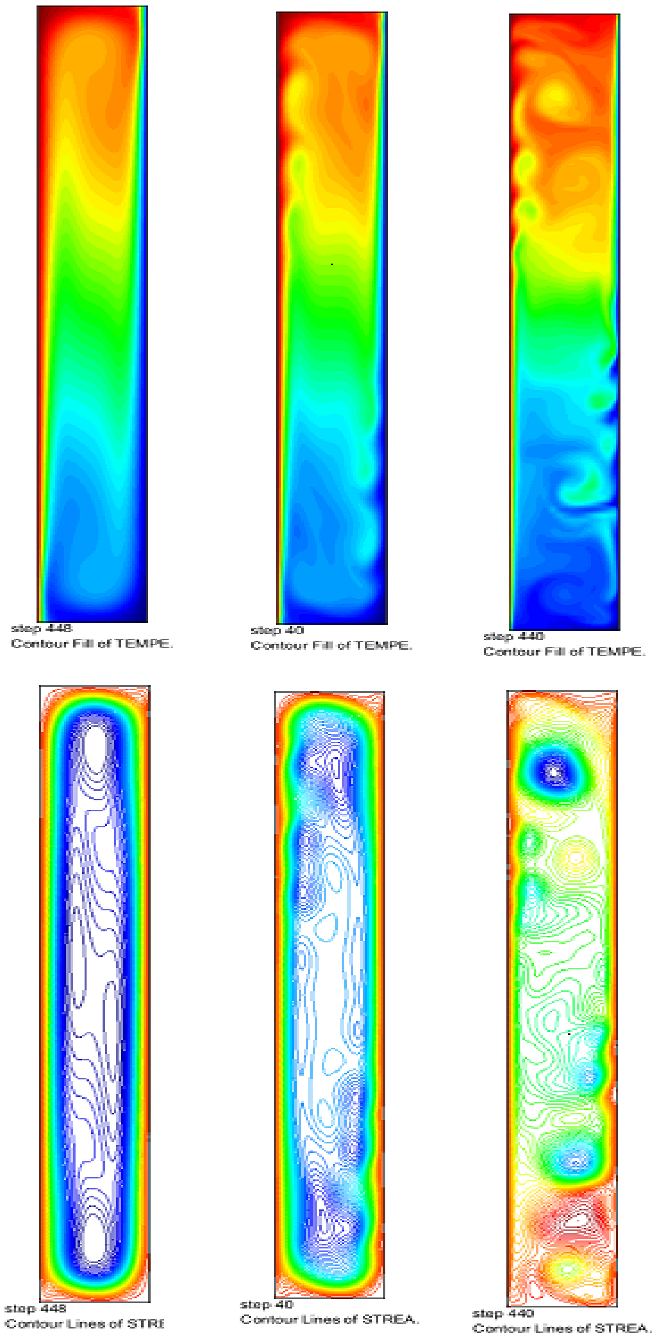

Figure 2.1: Temperature contours (top) and streamlines (bottom) for the three different Rayleigh numbers: $\mathrm{Ra} = 3.45\,10^5$, $\mathrm{Ra} = 10^6$ and $\mathrm{Ra} = 10^7$.

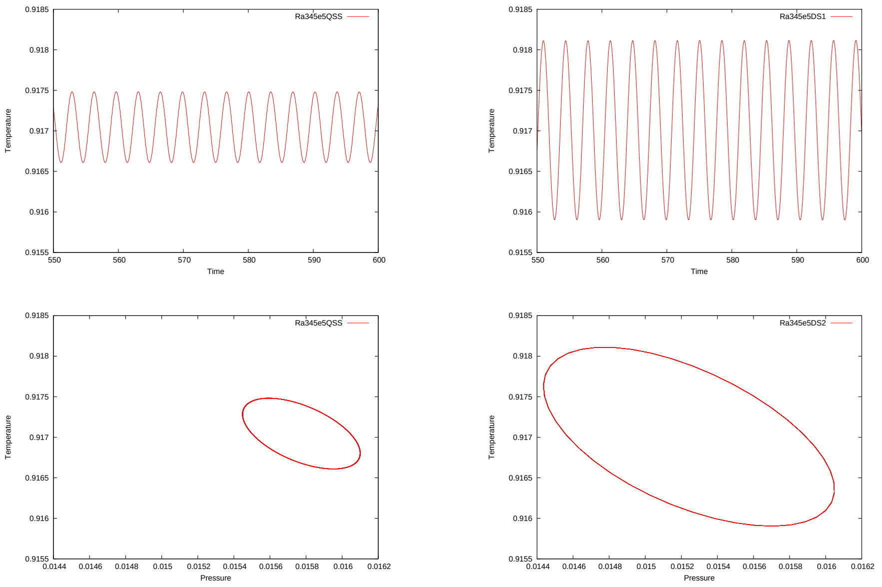

Figure 2.2: Results for $\mathrm{Ra} = 3.45\,10^5$. Left: QSS; right: DS; top: temperature evolution; bottom: pressure-temperature cycle.

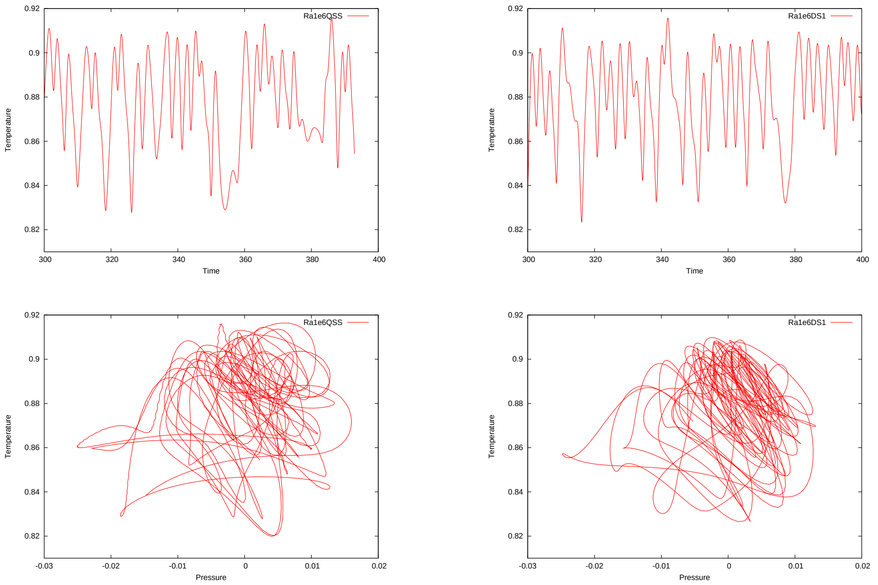

Figure 2.3: Results for $\mathrm{Ra} = 10^6$. Left: QSS; right: DS; top: temperature evolution; bottom: pressure-temperature cycle.

Chaotic behavior is expected in the last two cases, which is fully developed for the highest Rayleigh number.

In Fig. 2.1 snapshots of temperature contours and streamlines at a certain time step and for the three Rayleigh numbers are shown, with the only purpose to have an impression of the flow

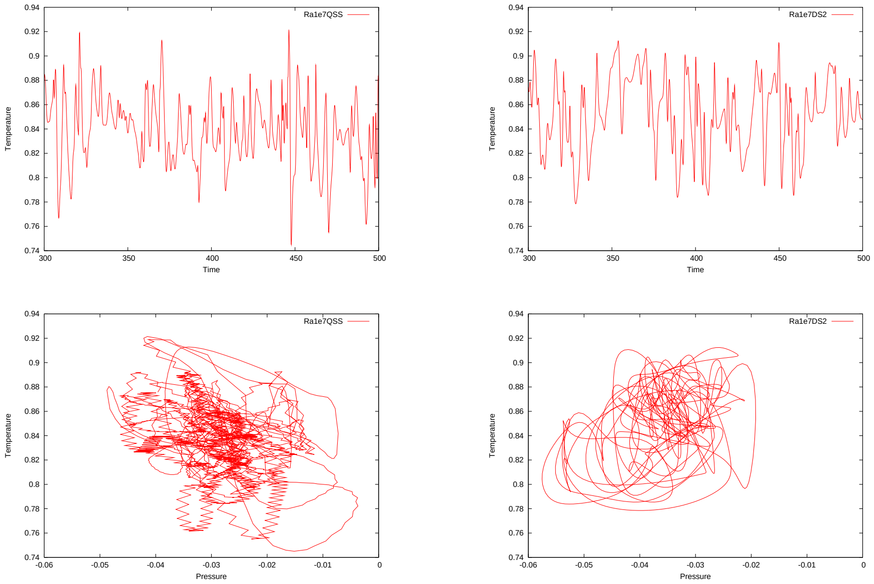

Figure 2.4: Results for $\mathrm{Ra} = 10^7$. Left: QSS; right: DS; top: temperature evolution; bottom: pressure-temperature cycle.

pattern. These and the following results have been obtained on a mesh of 10721 nodal points and 10500 bilinear quadrilateral elements. A second order BDF time integration scheme has been used for the Navier-Stokes and heat equation, whereas the subscales have been integrated using a backward Euler scheme. The time step size used is 0.08.

It is not our purpose here to compare the results obtained against others than can be found in the literature, but to see the effect of considering the subscales time-dependent. In this case we will label the resulting formulation DS, for dynamic subscales. When the time derivative of the subscales is neglected *and* $\boldsymbol{a} \approx \boldsymbol{u}_h$ is used as advection velocity, we will label the method as QSS, for quasi-static subscales.

To analyze the dynamical response of the formulation, we have plotted the temperature evolution at the point in the middle of the cavity, as well as the pressure-temperature cycle. Results are shown in Fig. 2.2 to Fig. 2.4. The conclusions that may be drawn from these pictures are:

- For $\mathrm{Ra} = 3.45\ 10^5$, both DS and QSS show the expected oscillatory behavior. However, DS has a wider p-T cycle, indicating less dissipation.

- For $\mathrm{Ra} = 10^6$ results obtained using DS and QSS are very similar. They both display chaos, as it can be observed from the p-T cycle.

- For $\mathrm{Ra} = 10^7$ the solution obtained is fully chaotic. A very important point to notice is that QSS has some oscillations in time, particularly visible in the p-T cycle, that do not appear using DS. We have observed the same behavior in other problems [27, 24].

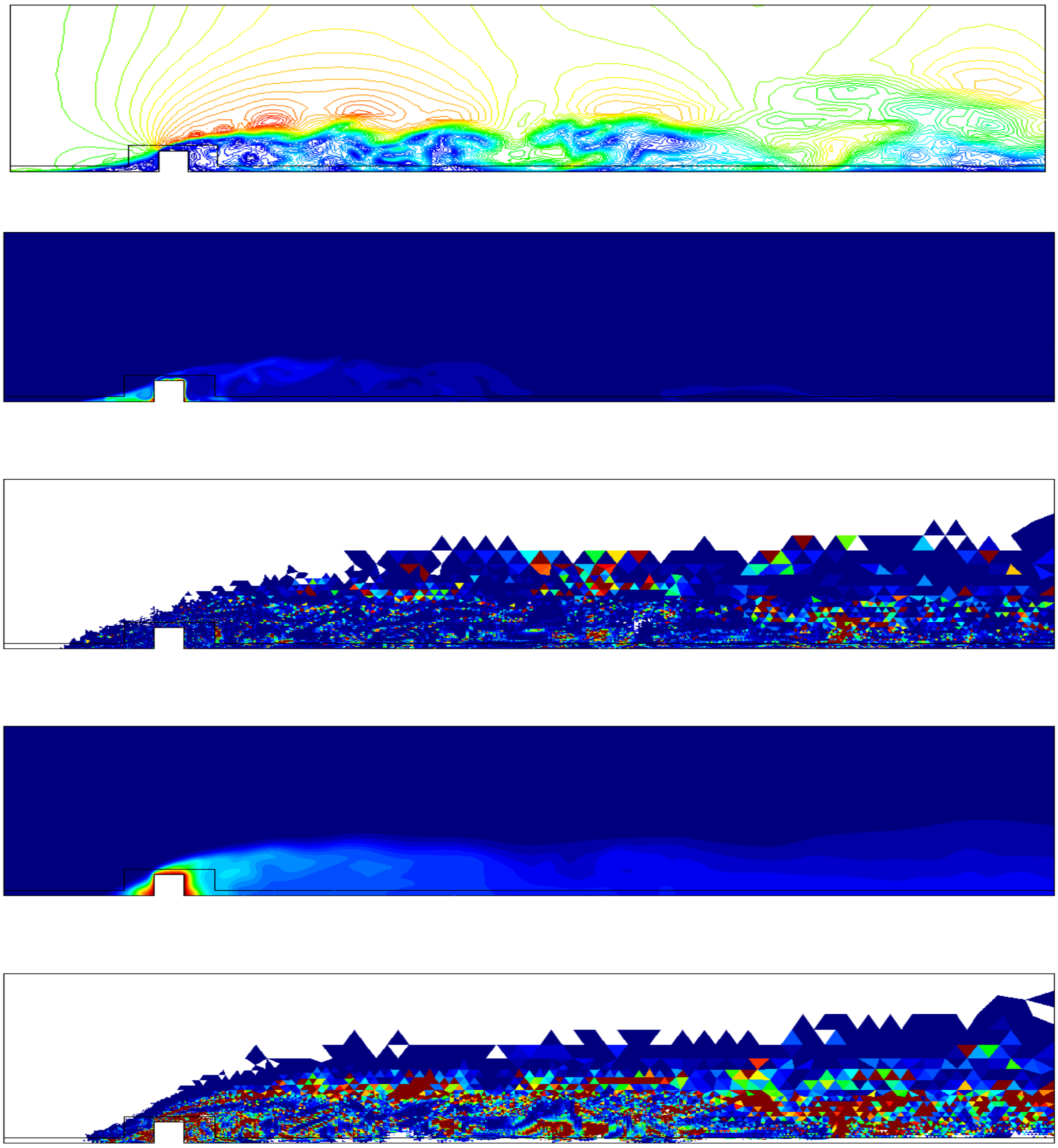

Figure 2.5: Results for the flow over a surface mounted obstacle in the mid section of the channel (at a certain time instant). From the top to the bottom: (1) Instantaneous velocity contours. (2) Instantaneous temperature contours for $\mathrm{Pr} = 1$. Maximum = 1 (red), minimum = 0 (blue). (3) Effective turbulent Prandtl number for $\mathrm{Pr} = 1$. Cut-off at 10 (red). (4) Instantaneous temperature contours for $\mathrm{Pr} = 100$. Maximum = 1 (red), minimum = 0 (blue). (5) Effective turbulent Prandtl number for $\mathrm{Pr} = 100$. Cut-off at 10 (red).

2.4.2 Flow over a surface mounted obstacle

In this subsection we present a numerical experiment showing the relationship between the mechanical and the thermal dissipation associated to the numerical model we propose. This example is taken from [81], to where the reader is referred for details of the calculation.

The problem consists in modeling the flow over a surface mounted obstacle, consisting in a cylinder of square cross section. The domain is discretized using a finite element mesh of around 2.2 million linear tetrahedral elements. Just to have a feeling of the flow, the instantaneous velocity contours (at a certain time instant) in the mid section of the channel where the flow takes place are plotted in the top picture of Fig. 2.5. Velocity boundary conditions are prescribed on the left boundary, whereas zero velocity is fixed on the bottom surface and zero normal velocity on the top boundary of the computational domain. The outflow (right boundary) is left free.

Concerning the setting for the thermal analysis, only the temperature on the obstacle is fixed to 1, whereas the rest of the boundary is assumed adiabatic. The thermal expansion coefficient is $\alpha = 0$ (no Boussinesq coupling) and two Prandtl numbers have been considered, namely, $\mathrm{Pr} = 1$ and $\mathrm{Pr} = 100$.

The interesting fact of this numerical simulation is to see which are the values obtained for the turbulent Prandtl number associated to the formulation as given by (2.51) (with $c_1 = 4$ and $c_2 = 2$, the numerical parameters we use in the calculations with linear elements). In Fig. 2.5 we have plotted the temperature contours at a certain time instant and the turbulent Prandtl number for $\mathrm{Pr} = 1$ and $\mathrm{Pr} = 100$. The conclusion is clear: since the dissipations in (2.51) (or the local Péclet number in estimate (2.53)) change from point to point, so does the turbulent Prandtl number. In Fig. 2.5 the local Péclet number has been computed with a characteristic velocity per element, and it is therefore constant within each element of the finite element mesh. It is observed that there are many elements in which the turbulent Prandtl number is far from the value $\mathrm{Pr}_{\mathrm{tur}} = 1$ usually adopted in LES models.

2.5 Conclusions

The purpose of this chapter has been to give a complete overview of a finite element formulation for thermally coupled incompressible whose intention is to go beyond stabilized finite element methods and, more precisely, to allow to simulate turbulent flows. The main aspects of the proposed method have been touched, namely:

- Its derivation through a scale splitting in the variational multiscale context.
- The definition of the stabilization parameters through an approximate Fourier analysis of the problem from a procedure applicable to general systems of equations.
- The possibility of considering dynamic subscales.
- The choice of the space of subscales as orthogonal to the finite element space.

Relevant to the possibility of simulating thermally coupled turbulent flows, we have analyzed:

- The conservation properties of the formulation in terms of the expression of the convective term.
- The dissipative structure, identifying the energy transfer terms and the possibility to have scale separation and to model backscatter.
- The numerical dissipation for both the Navier-Stokes and the heat equation, introducing a unambiguous numerical definition for the turbulent Prandtl number.

Even though there are many questions left open, we believe that the material presented here is a clear indication of the potential of the approach we propose to model turbulence, particularly in the case of thermally coupled flows. In the following chapters it will be derived a finite element formulation for low Mach number flows on the variational multiscale context. The main aspects touched in this chapter are treated exhaustively in the following chapters, with the difficulty of dealing with variable density flows. The dissipative structure and the possibility of simulating thermally coupled variable density flows are treated in chapter 4.

Chapter 3

Nonlinear subgrid scale approximation for the low Mach number flow equations

This chapter is an elaboration of the material in

M. Avila, R. Codina and J. Principe. A finite element dynamical nonlinear subscale approximation for the low Mach number flow equations. Journal of Computational Physics Vol. 230 (2011) 7988–8009.

In this chapter we propose a variational multiscale finite element approximation of thermally coupled low speed flows. The physical model is described by the low Mach number equations, which are obtained as a limit of the compressible Navier-Stokes equations in the small Mach number regime. In contrast to the commonly used Boussinesq approximation, this model permits to take volumetric deformation into account. Although the former is more general than the latter, both systems have similar mathematical structure and their numerical approximation can suffer from the same type of instabilities.

The proposed stabilized finite element approximation is based on the variational multiscale method, in which a decomposition of the approximating space into a coarse scale resolvable part and a fine scale subgrid part is performed. Modeling the subscale and taking its effect on the coarse scale problem into account results in a stable formulation. The quality of the final approximation (accuracy, efficiency) depends on the particular model.

The distinctive features of our approach are to consider the subscales as transient and to keep the scale splitting in all the nonlinear terms. The first ingredient permits to obtain an improved time discretization scheme (higher accuracy, better stability, no restrictions on the time step size). The second ingredient permits to prove global conservation properties. It also allows us to approach the problem of dealing with thermal turbulence from a strictly numerical point of view.

Numerical tests show that nonlinear and dynamic subscales give more accurate solutions than classical stabilized methods. The formulation is also tested using elements of second and third order. Numerical examples will show if the formulation is competitive using higher order methods, that is to say, if the associated increased computational complexity is worth affording compared to lower order methods, and compared to usual stabilization methods, such as SUPG.

3.1 Introduction

Computational fluid dynamics has become a key technology in industrial development, such aerodynamic design, turbines, combustion processes, owens, fire scenarios, etc.

The general description of a fluid flow involves the solution of the compressible Navier-Stokes Equations. It is widely accepted that these equations provide an accurate description of any problem in fluid mechanics which may present many different nonlinear physical mechanisms. Depending on the physics of the problem under consideration, different simplified models describing some of these mechanisms can be derived from the compressible Navier-Stokes equations.

Our application is directed to low speed strongly thermally coupled flows which are described by the compressible Navier-Stokes equations in the low-Mach number limit. This limit is derived by an asymptotic expansion of the problem variables as power series of the small parameter $\gamma \mathrm{Ma}^2 \ll 1$, where γ denotes the specific heat ratio and Ma the Mach number of the problem. For details of this asymptotic expansion procedure, see [80, 67, 64]. As a particular result of this process, the total pressure is split into two parts, the thermodynamic part $p^{\mathrm{th}}\left(t\right)$ which is uniform in space, and the hydrodynamic part $p\left(\boldsymbol{x},t\right)$ which is several orders of magnitude smaller than p^{th} and is therefore omitted in the state and energy equations. This leads to a removal of the acoustic modes but large variations of density due to temperature variations are allowed. This system of equations is commonly used to describe problems of combustion in the form of deflagrations (i.e., flames at low speed).

Despite this important difference in the treatment of the incompressibility, the low Mach number equations present the same mathematical structure as the incompressible Navier-Stokes equations, in the sense that the mechanical pressure is determined from the mass conservation constraint. Consequently the same type of numerical instabilities can be found, namely the problem of compatibility conditions between the velocity and pressure finite element spaces, and the instabilities due to convection dominated flows. These instabilities can be avoided by the use of stabilization techniques. A Galerkin finite element method can be used with mixed LBB stable elements, avoiding stabilization techniques when convection is not dominant [68, 43]. Stabilized finite element methods (FEM) have been initially developed for the Stokes [50] and for the convection diffusion reaction (CDR) problems [16]. Later they have been extended to incompressible Navier-Stokes equations [18, 54], and for the low Mach approximation [79] but the nonlinearity of the problem was not considered in their design. These extensions were essentially the application to nonlinear transient problems of a technique developed for linear steady ones.

The design of stabilization techniques considering the transient nonlinear nature of the problems began with the introduction of dynamic nonlinear subscales in [19, 27]. Developed in the context of the variational multiscale (VMS) concept introduced by Hughes [49], the idea is to consider the subgrid scale time dependent and to consider its effect on all the nonlinear terms, resulting in extra terms in the final discrete scheme. Important improvements in the discrete formulation of the incompressible Navier-Stokes problem have been observed. From a theoretical point of view, the use of transient subgrid scales explains how the stabilization parameter should depend on the time step size and makes space and time discretizations commutative. The tracking of the subscales along the nonlinear process provides global momentum conservation for incompressible flows. From a practical point of view, the use of time dependent nonlinear subscales results in a more robust and more accurate method (an unusual combination) as shown by numerical experiments [19, 27].

These developments also opened the door to the use of numerical techniques to cope with the potential instabilities and to model turbulence at the same time, as pointed out in [19, 27]. This is a natural step as turbulence is originated by the presence of the nonlinear convective term, as it is well known. The idea of modeling turbulence using only numerical ingredients actually goes back at least to [8], and the possibility to use the VMS framework for that purpose to [19]. It was fully developed for incompressible flows in [5] and for low Mach number flows recently in [39], where quantitative comparisons against direct numerical simulations are presented. It is important to point out, however, that not all the terms arising from the nonlinear scale splitting are considered in these works. Apart from these results, a careful analysis of the dissipative structure of the variational multiscale method with nonlinear time dependent subscales was presented in [41, 81], showing the physical interpretation of the method. This analysis was extended to thermally coupled flows using the Boussinesq approximation in chapter 2 and [25].

In this chapter we consider time dependent subscales and their effect in *all* the nonlinear terms in the low Mach number flow equations. It is shown that the method does not only provide the necessary stabilization of the formulation but also enables to obtain more accurate solutions than the classical linear approach for an equivalent mesh as it happened for incompressible flows. It is also shown that global conservation properties for mass, momentum and energy are obtained from the final discrete scheme.

Since a few years, there has been a renew of the interest in high order schemes for compressible fluid dynamics for steady and unsteady problems. The development of higher-order methods for Navier-Stokes equations has been a hot research topic all over the world. The goal of these researches is to design cheaper and more efficient numerical methods able to handle very large and very complex problems. An study of the accuracy and efficiency of the nonlinear stabilized finite element when using quadratic and cubic elements will be presented. It is known that significantly fewer degrees of freedom are required for higher-order methods than for classical second-order schemes to reach the same level of accuracy [66]. Also higher order methods deal much better with complex geometries, representing better the curved boundaries and boundary conditions [87]. However, the use of higher order methods increases the computer memory demand, and better linear solvers are needed to solve the algebraical systems of equations.

The chapter is organized as follows. In Section 3.2, the Low Mach number equations and their variational formulation are given. Afterwards the VMS formulation through dynamic scale splitting is derived in Section 3.3. It is shown in Section 3.4 that this formulation provides global mass, momentum and energy conservation when using equal interpolation spaces for the velocity, pressure and temperature equations. Time integration schemes are discussed in Section 3.5. The treatment of the nonlinear terms is described in detail in Section 3.6. The formulation is tested for both stationary and dynamic problems in Section 3.8 using linear and higher order methods. That is to say, if the associated increased computational complexity is worth affording compared to lower order methods, and compared to usual stabilization methods, such as SUPG. Conclusions are drawn in Section 3.9.

3.2 The low Mach number equations

3.2.1 Initial and boundary value problem

Let $\Omega \subset \mathbb{R}^d$,with $d = 2, 3$, be the computational domain in which the flow takes place during the time interval $[0, t_{\text{end}}]$, and let $\partial\Omega$ be its boundary. The initial and boundary value problem to be considered consists of finding a velocity field $\boldsymbol{u}$, a hydrodynamic pressure field p, a temperature field T, and the thermodynamic pressure p^{th} such that

$$\begin{aligned}
\frac{\partial \rho}{\partial t} + \nabla \cdot (\rho \boldsymbol{u}) &= 0 \quad \text{in}\, \Omega,\ t \in (0, t_{\text{end}}) && (3.1)\\
\rho\frac{\partial \boldsymbol{u}}{\partial t} + \rho \boldsymbol{u} \cdot \nabla \boldsymbol{u} - \nabla \cdot (2\mu \boldsymbol{\varepsilon}'(\boldsymbol{u})) + \nabla p &= \rho \boldsymbol{g} \ \text{in}\, \Omega,\ t \in (0, t_{\text{end}}) && (3.2)\\
\rho c_p \frac{\partial T}{\partial t} + \rho c_p \boldsymbol{u} \cdot \nabla T - \nabla \cdot (k \nabla T) - \alpha T \frac{dp^{\text{th}}}{dt} &= Q \quad \text{in}\, \Omega,\ t \in (0, t_{\text{end}}) && (3.3)
\end{aligned}$$

where ρ denotes the density, μ the viscosity, $\boldsymbol{\varepsilon}'(\boldsymbol{u}) = \boldsymbol{\varepsilon}(\boldsymbol{u}) - \frac{1}{3}(\nabla \cdot \boldsymbol{u})\boldsymbol{I}$ the deviatoric part of the rate of deformation tensor $\boldsymbol{\varepsilon}(\boldsymbol{u}) = \nabla^s \boldsymbol{u} = \frac{1}{2}\left(\nabla \boldsymbol{u} + \nabla \boldsymbol{u}^T\right)$, $\boldsymbol{I}$ the identity tensor, $\boldsymbol{g}$ the gravity force vector, c_p the specific heat coefficient at constant pressure, k the thermal conductivity, Q the heat source, and $\alpha = -\frac{1}{\rho}\frac{\partial \rho}{\partial T}|_p$ the thermal expansion coefficient. Equations (3.1)-(3.3) represent the mass, momentum and energy conservation respectively. Additionally the system must be closed by a state equation relating density ρ, thermodynamic pressure p^{th} and temperature T of the form

$$\rho = \rho\left(T, p^{\text{th}}\right) \tag{3.4}$$

These equations must be supplied with initial and boundary conditions. Initial conditions are

$$\begin{aligned}
\boldsymbol{u} &= \boldsymbol{u}_0 \ \text{in}\, \Omega,\ t = 0\\
T &= T_0 \ \text{in}\, \Omega,\ t = 0\\
p^{\text{th}} &= p_0^{\text{th}} \ \text{in}\, \Omega,\ t = 0
\end{aligned}$$

whereas Dirichlet and Neumann boundary conditions for Eqs. (3.2) and (3.3) are

$$\begin{aligned}
\boldsymbol{u} &= \widehat{\boldsymbol{u}} \ \text{on}\ \Gamma_D^{\boldsymbol{u}}\\
T &= \widehat{T} \ \text{on}\ \Gamma_D^{T}\\
(-p\boldsymbol{I} + 2\mu\boldsymbol{\varepsilon}'(\boldsymbol{u})) \cdot \boldsymbol{n} &= \boldsymbol{t}_n \ \text{on}\ \Gamma_N^{\boldsymbol{u}}\\
k\nabla T \cdot \boldsymbol{n} &= q_n \ \text{on}\ \Gamma_N^{T}
\end{aligned}$$

where $\boldsymbol{n}$ is the outer unit normal on the boundary and it is assumed that $\Gamma_D^f \cup \Gamma_N^f = \partial\Omega$, and $\Gamma_D^f \cap \Gamma_N^f = \emptyset$ for $f = T, \boldsymbol{u}$.

Determination of the thermodynamic pressure The time dependence of thermodynamic pressure $p^{\text{th}}(t)$ has to be determined independently of Eqs. (3.1)-(3.3). For open flows ($\Gamma_N^{\boldsymbol{u}} \neq \emptyset$) the thermodynamic pressure is given by the boundary conditions. For closed flows ($\Gamma_N^{\boldsymbol{u}} = \emptyset$) the thermodynamic pressure is determined through global conservation equations over domain Ω, taking advantage of the uniformity of p^{th}.

In a closed system without inflow-outflow, the total mass remains constant over time, and p^{th} may be obtained at each time subject to an integral form of the state equation

$$\int_\Omega \rho\left(T, p^{\mathrm{th}}\right) d\Omega = \int_\Omega \rho_0 \, d\Omega \tag{3.5}$$

where $\rho_0 = \rho\left(T_0, p_0^{\mathrm{th}}\right)$ is the initial density field.

In a closed system with inflow-outflow, the thermodynamic pressure may be determined by an equation obtained as a result of combining Eqs. (3.1), (3.3) and (3.4), given by

$$\frac{\alpha T}{\gamma - 1}\frac{dp^{\mathrm{th}}}{dt} + \frac{\gamma}{\gamma - 1}\frac{\alpha T}{K}\nabla \cdot \boldsymbol{u} - \nabla \cdot (k \nabla T) = Q \tag{3.6}$$

where γ, α and the compressibility coefficient $K = \frac{1}{\rho}\frac{\partial \rho}{\partial p}|_T$ are thermodynamic functions, depending on p^{th} and T. Integrating Eq. (3.6) over domain Ω yields an ordinary differential equation for p^{th} as

$$\frac{dp^{\mathrm{th}}}{dt}\int_\Omega \frac{\alpha T}{\gamma - 1} d\Omega + \int_\Omega \frac{\gamma}{\gamma - 1}\frac{\alpha T}{K}\nabla \cdot \boldsymbol{u} \, d\Omega = \int_\Omega Q d\Omega + \int_{\partial\Omega} \boldsymbol{n} \cdot k \nabla T d\Gamma \tag{3.7}$$

which is subject to the initial condition $p^{\mathrm{th}}(t = 0) = p_0^{\mathrm{th}}$.

Ideal gases For ideal gases, the state equation is $\rho = p^{\mathrm{th}}/RT$, with $R = \frac{\mathcal{R}}{M}$, where $\mathcal{R}$ is the universal gas constant and M the mean molecular mass. The thermal expansion and the compressibility coefficients for ideal gases are $\alpha = 1/T$ and $K = 1/p^{\mathrm{th}}$, respectively. Considering also uniform mean molecular mass (no combustion), Eqs. (3.5) and (3.7) take the form

$$p^{\mathrm{th}} = p_0^{\mathrm{th}} \frac{\int_\Omega \frac{1}{T_0} d\Omega}{\int_\Omega \frac{1}{T} d\Omega}$$

and

$$\frac{|\Omega|}{(\gamma - 1)}\frac{dp^{\mathrm{th}}}{dt} + \frac{\gamma}{\gamma - 1}p^{\mathrm{th}}\int_{\partial\Omega} \boldsymbol{n} \cdot \boldsymbol{u} \, d\Gamma = \int_\Omega Q d\Omega + \int_{\partial\Omega} \boldsymbol{n} \cdot k \nabla T d\Gamma \tag{3.8}$$

respectively, $|\Omega|$ being the measure of Ω.

3.2.2 Variational formulation

To obtain a variational formulation for the system (3.1)-(3.3), let us denote by $\boldsymbol{V}, Q, W$ the functional spaces where the solution is sought. When the Boussinesq approximation is considered they are given by $\boldsymbol{V} = \boldsymbol{L}^2\left(0, T; H^1(\Omega)^d\right)$, $Q = \mathcal{D}'\left(0, T; L^2(\Omega)\right)$, and $W = L^2\left(0, T; H^1(\Omega)\right)$ [25], where $\mathcal{D}'\left(0, T; L^2(\Omega)\right)$ is the set of $L^2(\Omega)$ functions in space which are distributions in time. For the low Mach number equations, the minimum regularity required is only known in very particular cases [64]. The corresponding space of (time independent) test functions will be denoted by $\boldsymbol{V}_0, Q_0, W_0$. Functions belonging to these spaces vanish on the part of the boundary where Dirichlet conditions are imposed. We also introduce the notation $(\cdot,\cdot) \equiv (\cdot,\cdot)_\Omega$ and $(\cdot,\cdot)_\Gamma$ for the L^2-inner product on Ω and Γ, respectively, or for the integral of the product of two functions if they are not square integrable but their product can be integrated (the product of two functions becomes the contraction when vectors or tensors are considered).

Using this notation the weak form of the problem consists of finding $(\boldsymbol{u}, p, T) \in \boldsymbol{V} \times Q \times W$ such that

$$\begin{aligned}
&\left(\frac{\partial \rho}{\partial t}, q\right) + \left(\nabla \cdot (\rho \boldsymbol{u}), q\right) = 0 && \forall q \in Q_0 && (3.9)\\
&\left(\rho \frac{\partial \boldsymbol{u}}{\partial t}, \boldsymbol{v}\right) + (\rho \boldsymbol{u} \cdot \nabla \boldsymbol{u}, \boldsymbol{v}) + \left(2\mu \boldsymbol{\varepsilon}'(\boldsymbol{u}), \nabla^s \boldsymbol{v}\right) \\
&\qquad - (p, \nabla \cdot \boldsymbol{v}) = (\rho \boldsymbol{g}, \boldsymbol{v}) + (\boldsymbol{t}_n, \boldsymbol{v})_{\Gamma_N^{\boldsymbol{u}}} && \forall \boldsymbol{v} \in \boldsymbol{V}_0 && (3.10)\\
&\left(\rho c_p \frac{\partial T}{\partial t}, w\right) + (\rho c_p \boldsymbol{u} \cdot \nabla T, w) + (k \nabla T, \nabla w) \\
&\qquad - \left(\alpha T \frac{d p^{\mathrm{th}}}{dt}, w\right) = (Q, w) + (q_n, w)_{\Gamma_N^T} && \forall w \in W_0 && (3.11)
\end{aligned}$$

3.3 Space discretization by scale splitting

Let us consider a finite element partition $\{K\}$ with n_e elements of the computational domain Ω, from which we can construct finite element spaces for the velocity, pressure and temperature in the usual manner. We will denote them by $\boldsymbol{V}_h \subset \boldsymbol{V}$, $Q_h \subset Q$ and $W_h \subset W$, respectively. We will assume that they are all built from continuous piecewise polynomials of the same degree k. In this section we assume zero Dirichlet boundary conditions to simplify the presentation.

Let us split the continuous space $\boldsymbol{Y} = \boldsymbol{V} \times Q \times W$ as $\boldsymbol{Y} = \boldsymbol{Y}_h \oplus \widetilde{\boldsymbol{Y}}$, where $\widetilde{\boldsymbol{Y}} = \widetilde{\boldsymbol{V}} \times \widetilde{Q} \times \widetilde{W}$ is the subgrid space, that can be in principle any space to complete $\boldsymbol{Y}_h = \boldsymbol{V}_h \times Q_h \times W_h$ in $\boldsymbol{Y}$. The continuous unknowns are split as

$$\begin{aligned}
\boldsymbol{u} &= \boldsymbol{u}_h + \widetilde{\boldsymbol{u}} && (3.12)\\
p &= p_h + \widetilde{p} && (3.13)\\
T &= T_h + \widetilde{T} && (3.14)
\end{aligned}$$

where the components with subscripts h belong to the corresponding finite element spaces, and the components with the $\widetilde{}$ correspond to the subgrid space. These additional components are what we will call subscales.

Each particular variational multiscale method will depend on the way the subscales are approximated. As presented in [49], there are many possibilities such as hierarchical order refinement, (residual free) bubbles or approximation to the element Green functions. In fact, two level schemes in which the subscales themselves are expanded in terms of bases functions have also been used to model turbulent flows [51, 52, 53]. However, it is also common to perform approximations to the differential operator in the subscale equations in order to obtain closed expressions for them, usually in terms of the residuals of the finite element equations, as will be explained in Section 3.3.1. This way permits to recover classical stabilized methods developed for linear equations (e.g. the Douglas-Wang, method originally developed for the

Stokes problem in [32]). *Our particular approach* is to keep time dependency of these subscales and keep the previous decompositions (3.12)-(3.14) in *all* the terms of the variational problem (3.9)-(3.11) even if the differential operator is approximated.

To arrive to the continuous variational formulation it was supposed that fluxes $2\mu\boldsymbol{\varepsilon}'(\boldsymbol{u})$ and $k\nabla T$ were continuous in Ω. The discrete approximation inherits this supposition in the sense that $2\mu\boldsymbol{\varepsilon}'(\boldsymbol{u}_h+\widetilde{\boldsymbol{u}})$ and $k\nabla\left(T_h+\widetilde{T}\right)$ need to be continuous through the interelement boundaries. The only approximation we will make for the moment is to assume that the subscales vanish on the interelement boundaries, ∂K. This happens for example if one assumes subscales as bubble functions, or that their Fourier modes correspond to high wave numbers, as it is explained in [19]. Ideas in the direction of relaxing this condition can be found in [26].

Substituting decompositions (3.12)-(3.14) in the variational problem (3.9) -(3.11), taking the tests functions in the corresponding finite element spaces, integrating some terms by parts and making use of the mass conservation statement, the problem consists in finding $(\boldsymbol{u}_h, T_h, p_h) \in \boldsymbol{V}_h \times Q_h \times W_h$ such that

$$\left(\frac{\partial\rho^h}{\partial t}, q_h\right) - \left(\rho^h\boldsymbol{u}_h, \nabla q_h\right) + \left(\rho^h\boldsymbol{n}\cdot\boldsymbol{u}_h, q_h\right)_{\partial\Omega} - \left(\rho^h\widetilde{\boldsymbol{u}}, \nabla q_h\right) = 0 \tag{3.15}$$

$$\begin{aligned}
&\left(\rho^h\frac{\partial\boldsymbol{u}_h}{\partial t}, \boldsymbol{v}_h\right) + \left(\rho^h\left(\boldsymbol{u}_h+\widetilde{\boldsymbol{u}}\right)\cdot\nabla\boldsymbol{u}_h, \boldsymbol{v}_h\right) + \left(2\mu\boldsymbol{\varepsilon}'(\boldsymbol{u}_h), \nabla^s\boldsymbol{v}_h\right) \\
&\quad - \left(p_h, \nabla\cdot\boldsymbol{v}_h\right) + \left(\rho^h\frac{\partial\widetilde{\boldsymbol{u}}}{\partial t}, \boldsymbol{v}_h\right) \\
&\quad - \left(\widetilde{\boldsymbol{u}}, -\frac{\partial\rho^h}{\partial t}\boldsymbol{v}_h + \rho^h\left(\boldsymbol{u}_h+\widetilde{\boldsymbol{u}}\right)\cdot\nabla\boldsymbol{v}_h + \nabla^h\cdot\left(2\mu\boldsymbol{\varepsilon}(\boldsymbol{v}_h)\right)\right) \\
&\quad - \left(\tilde{p}, \nabla\cdot\boldsymbol{v}_h\right) = \left(\rho^h\boldsymbol{g}, \boldsymbol{v}_h\right) + \left(\boldsymbol{t}_n, \boldsymbol{v}_h\right)_{\Gamma_N^{\boldsymbol{u}}}
\end{aligned} \tag{3.16}$$

$$\begin{aligned}
&\left(\rho^h c_p\frac{\partial T_h}{\partial t}, w_h\right) + \left(\rho^h c_p\left(\boldsymbol{u}_h+\widetilde{\boldsymbol{u}}\right)\cdot\nabla T_h, w_h\right) \\
&\quad + \left(k\nabla T_h, \nabla w_h\right) - \left(\alpha\left(T_h+\widetilde{T}\right)\frac{dp^{\text{th}}}{dt}, w_h\right) + \left(\rho^h c_p\frac{\partial\widetilde{T}}{\partial t}, w_h\right) \\
&\quad - \left(\widetilde{T}, -c_p\frac{\partial\rho^h}{\partial t}w_h + \rho^h c_p\left(\boldsymbol{u}_h+\widetilde{\boldsymbol{u}}\right)\cdot\nabla w_h + \nabla^h\cdot\left(k\nabla w_h\right)\right) \\
&\quad = \left(Q, w_h\right) + \left(q_n, w_h\right)_{\Gamma_N^T}
\end{aligned} \tag{3.17}$$

for any test functions $(\boldsymbol{v}_h, q_h, w_h) \in \boldsymbol{V}_{0,h} \times Q_{0,h} \times W_{0,h}$, where

$$\rho^h = \rho\left(T_h+\widetilde{T}, p^{\text{th}}\right) \tag{3.18}$$

is obtained applying the scale splitting to the state equation (3.4). Notation ρ^h indicates that the obtained density for the discrete problem is different from that in the continuous problem. The use of a superscript instead of a subscript is because density does not belong to any of the introduced finite element spaces but it is a nonlinear function evaluated using the finite element and subgrid temperatures (and it therefore depends, indirectly, on the mesh). The symbol ∇^h in equation (3.16) and (3.17) indicates that the integral is carried over the finite element interiors, for example

$$\left(\widetilde{T}, \nabla^h \cdot (k\nabla w_h)\right) = \sum_K \left(\widetilde{T}, \nabla \cdot (k\nabla w_h)\right)_K$$

where $(\cdot,\cdot)_K$ is the $L^2(K)$ inner product.

After a proper by parts integration of the discrete equations we made some manipulation to arrive to the discrete formulation of momentum and energy equations (3.16)-(3.17)) avoiding the presence of gradients of the subscale component. The continuous mass conservation equation (3.9) can be writen as

$$\left(\frac{\partial \rho^h}{\partial t}, q\right) = -\left(\nabla \cdot \left(\rho\left(\boldsymbol{u}_h + \widetilde{\boldsymbol{u}}\right)\right), q\right)$$

after an splitting of the unknowns. Note that this equation holds at the continous level. We replaced this continuous form of the mass equation into momentum and energy equations after performing some by parts integrations, to avoid terms involving gradients of the subscale component. Those replacements are crucial to account for the subscales in all the nonlinear terms. In particular we have replaced $\left(\widetilde{\boldsymbol{u}}, \nabla\left(\rho^h\left(\boldsymbol{u}_h + \widetilde{\boldsymbol{u}}\right)\right)\boldsymbol{v}_h\right)$ by $-\left(\widetilde{\boldsymbol{u}}, \frac{\partial \rho^h}{\partial t}\boldsymbol{v}_h\right)$ in the momentum equation, and $\left(\widetilde{T}, \nabla\left(\rho^h\left(\boldsymbol{u}_h + \widetilde{\boldsymbol{u}}\right)\right) w_h\right)$ by $-\left(\widetilde{T}, \frac{\partial \rho^h}{\partial t} w_h\right)$ in the energy equation.

In order to give a closure to system (3.15)-(4.16) we need to define how the subscales $\widetilde{\boldsymbol{u}}$, $\widetilde{p}$ and $\widetilde{T}$ are computed, which will be discussed in the rest of the section. As mentioned before, we will finally provide closed expressions for them in terms of the residuals of the finite element equations at each (integration point of each) element, and therefore this will provide an implicit definition of the spaces of subscales (in terms of the finite element spaces). However, we would like to point out that, once the velocity subscale is approximated in the momentum equation (3.16), it provides additional terms than those that appear in classical stabilized finite element methods. These are non standard terms in the sense that they are usually neglected and appear because we keep the scale splitting also in nonlinear terms. The terms involving the velocity subgrid scale arising from the convective term in the momentum equation $\left(\rho^h \widetilde{\boldsymbol{u}} \cdot \nabla \boldsymbol{u}_h, \boldsymbol{v}_h\right) - \left(\widetilde{\boldsymbol{u}}, \rho^h\left(\boldsymbol{u}_h + \widetilde{\boldsymbol{u}}\right) \cdot \nabla \boldsymbol{v}_h\right)$ can be understood as the contribution from the Reynolds- and cross- stress terms of a LES approach. Therefore, modeling $\widetilde{\boldsymbol{u}}$ implies modeling the subgrid scale tensor. The last row in (3.16) comes from the contribution of the pressure subscale, that reinforces mass balance, and the contribution from the external forces. Similar comments to those made for the momentum equation apply to the energy equation (3.17). Once the temperature subscale is approximated it provides additional terms that appear in classical stabilized methods. The terms involving the velocity and temperature subgrid scale arising from the convective term $\left(\rho^h c_p \widetilde{\boldsymbol{u}} \cdot \nabla T_h, w_h\right) - \left(\widetilde{T}, \rho^h c_p\left(\boldsymbol{u}_h + \widetilde{\boldsymbol{u}}\right) \cdot \nabla w_h\right)$ can be understood as the contribution from the Reynolds- and cross- stress terms of a LES approach, see [25]. In the mass conservation equation (3.15) the fourth term provides pressure stability once the velocity subscale is approximated.

To get the final numerical scheme we approximate the subscales in the element interiors. We do that below, but let us first write the subgrid equations before any approximation (apart from assuming that the subscales vanish on the interelement boundaries). In the same way the finite element equations can be understood as the projection of the original equations onto the finite element spaces, the equations for the subscales are obtained by projecting the original equations onto their corresponding spaces $\widetilde{\boldsymbol{Y}}$. If $\widetilde{P}$ denotes the L_2-projection onto any of these spaces, the subscale equations are written as

$$\begin{aligned}
\widetilde{P}\left(\rho^h \nabla \cdot \widetilde{\boldsymbol{u}} - \rho^h \alpha \left(\boldsymbol{u}_h + \widetilde{\boldsymbol{u}}\right) \cdot \nabla \widetilde{T}\right) &= \widetilde{P}\left(R_c\right) && (3.19)\\
\widetilde{P}\left(\frac{\partial\left(\rho^h \widetilde{\boldsymbol{u}}\right)}{\partial t} + \nabla \cdot \left(\rho^h \left(\boldsymbol{u_h} + \widetilde{\boldsymbol{u}}\right) \widetilde{\boldsymbol{u}}\right) - \nabla \cdot \left(2\mu \boldsymbol{\varepsilon}'\left(\widetilde{\boldsymbol{u}}\right)\right) + \nabla \widetilde{p}\right) &= \widetilde{P}\left(\boldsymbol{R}_m\right) && (3.20)\\
\widetilde{P}\left(c_p \frac{\partial\left(\rho^h \widetilde{T}\right)}{\partial t} + c_p \nabla \cdot \left(\rho^h \left(\boldsymbol{u}_h + \widetilde{\boldsymbol{u}}\right) \widetilde{T}\right) - \nabla \cdot \left(k \nabla \widetilde{T}\right)\right) &= \widetilde{P}\left(R_e\right) && (3.21)
\end{aligned}$$

where

$$\begin{aligned}
R_c &= -\frac{\partial \rho^h}{\partial t} - \rho^h \nabla \cdot \boldsymbol{u}_h + \rho^h \alpha \left(\boldsymbol{u}_h + \widetilde{\boldsymbol{u}}\right) \cdot \nabla T_h && (3.22)\\
\boldsymbol{R}_m &= \rho^h \boldsymbol{g} - \rho^h \frac{\partial \boldsymbol{u}_h}{\partial t} - \rho^h \left(\boldsymbol{u}_h + \widetilde{\boldsymbol{u}}\right) \cdot \nabla \boldsymbol{u}_h + \nabla \cdot \left(2\mu \boldsymbol{\varepsilon}'\left(\boldsymbol{u}_h\right)\right) - \nabla p_h && (3.23)\\
R_e &= Q + \alpha\left(T_h + \widetilde{T}\right) \frac{dp^{\text{th}}}{dt} - \rho^h c_p \frac{\partial T_h}{\partial t} - \rho^h c_p \left(\boldsymbol{u}_h + \widetilde{\boldsymbol{u}}\right) \cdot \nabla T_h + \nabla \cdot \left(k \nabla T_h\right) && (3.24)
\end{aligned}$$

are the residuals of the finite element unknowns in the momentum, continuity and heat equation, respectively. The temporal and convective terms of the momentum and energy subscale equations are written in conservative form. This form will be convenient for the development of the orthogonal subscale approximation, and also will permit to ease the implementation after grouping in the finite element equations the following terms

$$\begin{aligned}
\left(\rho^h \frac{\partial \widetilde{\boldsymbol{u}}}{\partial t}, \boldsymbol{v}_h\right) + \left(\widetilde{\boldsymbol{u}}, \frac{\partial \rho^h}{\partial t} \boldsymbol{v}_h\right) &= \left(\frac{\partial\left(\rho^h \widetilde{\boldsymbol{u}}\right)}{\partial t}, \boldsymbol{v}_h\right)\\
\left(\rho^h \frac{\partial \widetilde{T}}{\partial t}, w_h\right) + \left(\widetilde{T}, \frac{\partial \rho^h}{\partial t} w_h\right) &= \left(\frac{\partial\left(\rho^h \widetilde{T}\right)}{\partial t}, w_h\right)
\end{aligned}$$

Let us remark that writing some terms in the left or right-hand-side we are not assuming that they are known or unknown but just introducing a definition of the residuals (3.22)-(3.24). Eqs. (3.19)-(3.21) are actually coupled to the finite element equations (3.15)-(3.18) forming a coupled system whose linearization will be discussed in Section 3.6 after performing the approximations needed to obtain a numerical method. This definition of the residuals is motivated by the following observation: modeling the gradients of the subscales is much more involved than modeling the subscales themselves. Note that although all the unknowns are being split in Eqs. (3.15)-(3.18), those equations do not contain any subscale gradient nor any density gradient. This has been purposely achieved by a proper integration by parts of the continuous problem (3.9)-(3.11).

3.3.1 Approximation of the subscales

Up to this point the only approximation introduced is to assume that the subscales vanish on the element boundaries. This approximation is not sufficient to obtain a numerical method because the space of subscales is still infinite dimensional (the "broken" space $\cup_K H_0^1(K)$, for example) and therefore the subscale problem (3.19)-(3.21) is as difficult as the original continuous problem. To overcome this problem we adopt a simple approximation which consists in replacing the (spatial) differential operator by an algebraic operator which can be easily inverted. This old strategy, which can be understood as an approximation of the element Green's function by a Dirac distribution [49], has been already used, for example, in [19, 78] and references therein, and it is briefly described below.

The differential equations (3.19)-(3.21) over each element domain K can be written in vectorial form as

$$\widetilde{P}\left(\frac{\partial}{\partial t}(\boldsymbol{M}\widetilde{\boldsymbol{U}})+\mathcal{L}\widetilde{\boldsymbol{U}}\right)=\widetilde{P}(\boldsymbol{R}) \quad \text{in} \quad K$$

where $\widetilde{\boldsymbol{U}} \equiv \left[\widetilde{\boldsymbol{u}},\widetilde{p},\widetilde{T}\right]$, $\mathcal{L}$ is a spacial differential vector operator, $\boldsymbol{M}$ is the $(d+2)\times(d+2)$ diagonal matrix $\boldsymbol{M}$ =diag$\big(\rho^h\boldsymbol{I}_d, 0, \rho^h c_p\big)$, where $\boldsymbol{I}_d$ is the $d\times d$ identity matrix, and $\boldsymbol{R}\equiv[\boldsymbol{R}_m, R_c, R_e]$. In the present chapter we will consider the space of subscales as that of the residuals, that is, we will consider $\widetilde{P} = I$ (the identity) when applied to the finite element residuals. We will also consider $\widetilde{P}$ as the projection onto the space orthogonal to the finite element space, advocated in [19] for incompressible flows. This method presents some advantages for incompressible flows, like better accuracy, a clear identification of the energy transfer mechanisms between the finite element scales and the subscales [81], as well as improved stability and convergence estimates for transient Stokes and incompressible flows [4, 3]. The development of the Orthogonal Subscale Stabilization (OSS) method for low Mach number equations will be detailed in the next subsection, expecting to present some of the advantages achieved for incompressible flows.

We consider the algebraic approximation $\mathcal{L}\approx\boldsymbol{\tau}^{-1}$ in each K, where $\boldsymbol{\tau}$ is an $(d+2)\times(d+2)$ diagonal matrix. Taking $\boldsymbol{\tau}$ =diag$(\tau_m\boldsymbol{I}_d,\tau_c,\tau_e)$ the approximation to the subscales equations (3.19)-(3.21) within each element of the finite element partition reads

$$\frac{1}{\tau_c}\widetilde{p} = R_c + p_{\text{ort}} = R_c' \tag{3.25}$$

$$\frac{\partial(\rho^h\widetilde{\boldsymbol{u}})}{\partial t}+\frac{1}{\tau_m}\widetilde{\boldsymbol{u}} = \boldsymbol{R}_m + \boldsymbol{u}_{\text{ort}} = \boldsymbol{R}_m' \tag{3.26}$$

$$c_p\frac{\partial(\rho^h\widetilde{T})}{\partial t}+\frac{1}{\tau_e}\widetilde{T} = R_e + T_{\text{ort}} = R_e' \tag{3.27}$$

where p_{ort}, $\boldsymbol{u}_{\text{ort}}$ and T_{ort} are functions L_2-orthogonal to the subscale space. It is important to remark that, after the approximation $\mathcal{L}\approx\boldsymbol{\tau}^{-1}$, equations (3.25)-(3.27) become a set of ordinary differential equations at each integration point. Nevertheless, we keep the notation $\frac{\partial}{\partial t}$ for the temporal derivative to emphasize the fact that the subscales depend on the position.

The stabilization parameters can be motivated by an approximated Fourier analysis performed in [19], but they are usually obtained by scaling arguments. The same analysis can be performed for the present variable-density equation system to obtain

$$\tau_c = \frac{h^2}{c_1 \rho^h \tau_m} = \frac{\mu}{\rho^h} + \frac{c_2}{c_1}|\boldsymbol{u}_h + \widetilde{\boldsymbol{u}}|h \tag{3.28}$$

$$\tau_m = \left(c_1 \frac{\mu}{h^2} + c_2 \frac{\rho^h |\boldsymbol{u}_h + \widetilde{\boldsymbol{u}}|}{h} \right)^{-1} \tag{3.29}$$

$$\tau_e = \left(c_1 \frac{k}{h^2} + c_2 \frac{\rho^h c_p |\boldsymbol{u}_h + \widetilde{\boldsymbol{u}}|}{h} \right)^{-1} \tag{3.30}$$

where h is the element size and c_1 and c_2 are algorithmic constants whose values are $c_1 = 4$ and $c_2 = 2$ in the numerical experiments of Section 3.8 using linear elements.

It is important to remark that (3.26) and (3.27) are nonlinear equations as the velocity subscale contributes to the advection velocity in momentum and energy residuals and also in the stabilization parameters τ_c, τ_m, τ_e. The temperature subscale contributes through ρ^h to the residuals and to the coefficients of the stabilization parameters.

When the time derivative of the subscales is neglected, we will call them *quasi-static,* whereas otherwise we will call them *dynamic.* However, using quasi-static subscales in combination with the non-linear model presented here is an approach we do not favor for the following reason. Solutions of the nonlinear equations (3.26) and (3.27) display a dynamic behavior which may be radically different from the linear one. The values of $\widetilde{\boldsymbol{u}}$ and $\widetilde{T}$ for which these equations are satisfied when $\partial\widetilde{\boldsymbol{u}}/\partial t = 0$ and $\partial\widetilde{T}/\partial t = 0$ constitute the equilibria or fixed points of the dynamical system, which can be one or more, stable or unstable. Therefore, *quasi-static subscales can only be considered when solving linear subscale equations. To solve the nonlinear subscale equations (3.26) and (3.27) the subscales must be dynamic* in order to avoid possible lack of uniqueness in their calculations.

The space discretized formulation is now complete, but contrarily to what happens with linear quasi-static subscales it is not possible to obtain a closed-form expression for dynamic subscales and insert them into (4.13)-(3.17) to obtain a problem for the finite element unknowns only. Before discretizing in time we cannot go any further than saying that the problem consists in solving (3.15)-(3.17) together with (3.25)-(3.27). This final semidiscrete system of equations is highly nonlinear, even more when nonlinear subscales are considered. Some possibilities to linearize the (fully discrete) problem are described in Section 3.6.

Orthogonal subscale approximation

The starting point of our developments has been the decompositions $\boldsymbol{Y} = \boldsymbol{Y}_h \oplus \widetilde{\boldsymbol{Y}}$. There are many possibilities to choose $\widetilde{\boldsymbol{Y}}$. The easiest choice is to consider the space of subscales as that of the residuals, that is, to consider $\widetilde{P} = I$ (the identity) when applied to the finite element residuals. That amounts to take p_{ort}, $\boldsymbol{u}_{\text{ort}}$ and T_{ort} equal zero in Eqs. (3.25)-(3.27). Another possibility consists in taking precisely $\widetilde{\boldsymbol{Y}} = \boldsymbol{Y} \cap \boldsymbol{Y}_h^{\perp}$, respect to the inner product $(u, v)_\rho = \left(u\, , \rho^h v\right)$. Note that as the density ρ^h is time dependent, then the subscale space $\widetilde{\boldsymbol{Y}}$ will also depend on time. From the previous definition, any subscale function $\widetilde{\boldsymbol{u}}$ must satisfy the following relationship

$$\left(\rho^h \widetilde{\boldsymbol{u}}, \boldsymbol{u}_h\right) = 0 \, \forall \boldsymbol{u}_h \in \boldsymbol{V_h} \tag{3.31}$$

We need to find the appropriate p_{ort}, $\boldsymbol{u}_{\text{ort}}$ and T_{ort} in (3.25)-(3.27) to satisfy the orthogonal relationship (3.31). In what follows we will show the procedure of finding $\boldsymbol{u}_{\text{ort}}$ in the subcale momentum Eq. (3.26). The same procedure is applied to the energy and pressure subscale equations to determine p_{ort} and T_{ort}. Projecting expression (3.26) over the finite element space, and satisfying orthogonal condition (3.31) we get that

$$\left(\frac{\partial(\rho^h\widetilde{\boldsymbol{u}})}{\partial t}, \boldsymbol{v}_h\right) = 0 = \left(\boldsymbol{R}_m + \boldsymbol{u}_{\text{ort}} - \frac{\widetilde{\boldsymbol{u}}}{\tau_m}, \boldsymbol{v}_h\right) \quad \forall \boldsymbol{v}_h \in \boldsymbol{V}_h \tag{3.32}$$

from where it follows that $\boldsymbol{u}_{\text{ort}}$ is the following projection onto the finite element space with respect to L_2-inner product, denoted by P_h

$$\boldsymbol{u}_{\text{ort}} = P_h\left(-\boldsymbol{R}_m + \frac{\widetilde{\boldsymbol{u}}}{\tau_m}\right)$$

Replacing in (3.26) we find the momentum subscale equation

$$\frac{\partial(\rho^h\widetilde{\boldsymbol{u}})}{\partial t} = P_h^{\perp}\left(\boldsymbol{R}_m - \frac{\widetilde{\boldsymbol{u}}}{\tau_m}\right) \tag{3.33}$$

where $P_h^{\perp} = I - P_h$, and I is the identity in $\boldsymbol{V}_h$. This differential equation has been found to be unstable in the numerical experiments because the directional vectors $P_h^{\perp}\left(\tau_m^{-1}\widetilde{\boldsymbol{u}}\right)$ and $\widetilde{\boldsymbol{u}}$ do not have the same directions. In case they have opossite directions, then solution to Eq.(3.33) grows exponentially in time and the whole method becomes unstable. To overcome that problem we assume that $\rho^h\tau_m$ has a smooth variation from element to element, thus we can approximate $P_h\left(\frac{\widetilde{\boldsymbol{u}}}{\tau_m}\right) \approx \frac{1}{\rho^h\tau_m}P_h\left(\rho^h\widetilde{\boldsymbol{u}}\right) = 0$. After applying the same procedure to Eq. (3.27), and assuming $\widetilde{p} \in Q_h^{\perp}$ the orthogonal subscale equations will read

$$\begin{aligned}
\widetilde{p} &= \tau_c\left(R_c - \frac{1}{\tau_c\rho^h}P_h\left(\tau_c\rho^h R_c\right)\right) \approx \tau_c P_h^{\perp}\left(R_c\right) && (3.34)\\
\frac{\partial(\rho^h\widetilde{\boldsymbol{u}})}{\partial t} + \frac{1}{\tau_m}\widetilde{\boldsymbol{u}} &= P_h^{\perp}\left(\boldsymbol{R}_m\right) && (3.35)\\
c_p\frac{\partial(\rho^h\widetilde{T})}{\partial t} + \frac{1}{\tau_e}\widetilde{T} &= P_h^{\perp}\left(R_e\right) && (3.36)
\end{aligned}$$

The OSS method consists on solving the finite element equations (3.15)-(3.17) together with the subscale equations (3.34)-(3.36). The terms $\left(\partial_t\left(\rho^h\widetilde{\boldsymbol{u}}\right), \boldsymbol{v}_h\right)$ and $\left(\partial_t\left(\rho^h\widetilde{\boldsymbol{T}}\right), w_h\right)$ vanish in the finite element problem due to the orthogonality between $\widetilde{\boldsymbol{Y}}$ and $\boldsymbol{Y}_h$. The transient terms $\rho^h\frac{\partial \boldsymbol{u}_h}{\partial t}$ and $\rho^h\frac{\partial T_h}{\partial t}$ are neglected from the energy and momentum residuals $\boldsymbol{R}_m$ and R_e in subscale equations (3.35) and (3.36), because they are $L_2 - \rho^h-$orthogonal to the subscale space. That is $\widetilde{P}\left(\rho^h\partial_t\boldsymbol{u}_h\right) = 0$ and $\widetilde{P}\left(\rho^h\partial_t T_h\right) = 0$ in the original subscale equations (3.20)-(3.21).

3.3.2 Remark on pressure determination for closed flows

When the flow is closed ($\Gamma_N^{\boldsymbol{u}} = \emptyset$) the mechanical pressure p_h is determined up to a constant. That is, if p_h is solution to the numerical equations, then $p_h + C$ will also be solution to these numerical equations for any constant C. This is because the only term in the numerical equation depending on p_h (and not on ∇p_h) satisfies ,for closed flows, $(p_h, \nabla \cdot \boldsymbol{v}_h) = (p_h + C, \nabla \cdot \boldsymbol{v}_h)$, where $\boldsymbol{v}_h = \mathbf{0}$ on $\Gamma_D^{\boldsymbol{u}} = \partial\Omega$. For open flows p_h is determined from normal traction given by Neumann boundary conditions. This irresolute behavior is also present in the continuous problem, and the space of pressures needs to be the quotient space $Q/\mathbb{R}$.

An usual practice in incompressible flows is to impose the pressure over a fixed node a to get unique solution for pressure, implying to subtract a degree of freedom from Q_h, being the mass conservation equation solved over a smaller space Q_h. This restriction is needed to solve the problem and does not affect the velocity field, because when net flux $\int_{\partial\Omega} \boldsymbol{u}_h \cdot \boldsymbol{n}$ is zero, then Galerkin term $(\nabla \cdot \boldsymbol{u}_h, q_h) = 0 \quad \forall \boldsymbol{u}_h$ when q_h is uniform. Thus, Galerkin discrete mass conservation term forms a linearly dependent system of equations. When one equation is removed from this system due to a pressure restriction, the right solution is obtained. The stabilization terms depend on ∇q_h, being zero when q_h is uniform. Thus, to restrict one degree of freedom to Q_h in the stabilized formulation does not affect the mass conservation equation. In case net flux is different from zero (due to errors on Dirichlet boundary conditions) to impose the pressure at a node prejudices mass conservation equation over the restricted node, affecting the obtained solution around this node.

For compressible flows density is time dependent and the Galerkin terms $\left(\frac{\partial \rho^h}{\partial t} + \nabla \cdot \left(\rho^h \boldsymbol{u}_h\right), q_h\right)$ form a linear independent system of equations. As a result to impose the pressure at a fixed node a introduces an important error to mass conservation equation around this node for transient problems, prejudicing the obtained solution around this node. However, for stationary flows to impose pressure at a node is necessary and does not affect the velocity field, because as in the incompressible case the net mass flux $\int_{\partial\Omega} \rho^h \boldsymbol{u}_h \cdot \boldsymbol{n} = 0$, so Galerkin terms of mass equation form a linearly dependent system of equations.

To overcome mechanical pressure resolution p_h up to a constant for transient and variable density closed flows, an iterative penalization to the mass conservation equation (3.15) is applied, adding the term $\left(\varepsilon \left(p_h^{i+1} - p_h^i\right), q_h\right)$ at iteration $i + 1$. The factor ε needs to be defined in such a way that it does not detriment the algebraical solver convergence (when $\varepsilon \to 0$) and does not affect the convergence of the iterative nonlinear scheme (when ε is too large). This parameter was finally adjusted to $\varepsilon = 10^{-4}\rho^h/\mu$.

3.4 Global conservation properties

The aim of this section is to obtain global conservation statements similar to those holding for the continuous problem (3.1)-(3.3), but for the semidiscrete one. Global conservation properties for the incompressible formulation were discussed in Section 2.3, and are extended in this section to variable density flows formulation. The dissipative structure and energy transfer mechanisms of the present formulation will be discussed in Section 4.4. To do that it is necessary to consider the finite element spaces without Dirichlet boundary conditions and an augmented problem that also contains the tractions at the Dirichlet boundaries as unknowns [48]. This permits to take constant test functions (see below) and to arrive to conservation statements in terms of the tractions and flows at the boundaries. We shall see that the following conservation statements hold *when equal interpolation is used for all variables.*

3.4.1 Mass conservation

Taking the test function $q_h = 1$ in the mass equation (3.15) global mass conservation follows immediately:

$$\int_\Omega \frac{\partial \rho^h}{\partial t}\, d\Omega = -\int_{\partial\Omega} \boldsymbol{n} \cdot \rho^h \boldsymbol{u}_h \, d\Gamma \tag{3.37}$$

3.4.2 Momentum Conservation

Suppose that a canonical Cartesian coordinate system is used. Taking the tests function $\boldsymbol{v}_h = (1,0,0)$, $(0,1,0)$ and $(0,0,1)$ in (the augmented problem corresponding to) the finite element momentum equation (3.16), we get

$$\begin{aligned}\int_\Omega \rho^h \frac{\partial}{\partial t}\left(\boldsymbol{u}_h + \widetilde{\boldsymbol{u}}\right) d\Omega + \int_\Omega \rho^h \left(\boldsymbol{u}_h + \widetilde{\boldsymbol{u}}\right) \cdot \nabla \boldsymbol{u}_h \, d\Omega \\ + \int_\Omega \widetilde{\boldsymbol{u}} \frac{\partial \rho^h}{\partial t}\, d\Omega = \int_\Omega \rho^h \boldsymbol{g}\, d\Omega + \int_{\partial\Omega} \boldsymbol{t}_n \, d\Gamma\end{aligned} \tag{3.38}$$

When using equal interpolation spaces for the velocity components and pressure equations, we can take the test function equal to velocity components $q_h = u_{h,i}$, $i = 1, ..., d$, in the discrete mass equation (3.15). Therefore, we get the relation

$$\int_\Omega \rho^h \left(\boldsymbol{u}_h + \widetilde{\boldsymbol{u}}\right) \cdot \nabla \boldsymbol{u}_h \, d\Omega = \int_\Omega \left(\frac{\partial \rho^h}{\partial t}\right) \boldsymbol{u}_h \, d\Omega + \int_{\partial\Omega} \left(\boldsymbol{n} \cdot \boldsymbol{u}_h\right) \rho^h \boldsymbol{u}_h \, d\Gamma$$

Replacing in (3.38) we arrive to

$$\begin{aligned}\int_\Omega \rho^h \frac{\partial}{\partial t}\left(\boldsymbol{u}_h + \widetilde{\boldsymbol{u}}\right) d\Omega + \int_\Omega \left(\boldsymbol{u}_h + \widetilde{\boldsymbol{u}}\right) \frac{\partial \rho^h}{\partial t}\, d\Omega \\ = \int_\Omega \rho^h \boldsymbol{g}\, d\Omega + \int_{\partial\Omega} \left(\boldsymbol{t}_n - \left(\boldsymbol{n} \cdot \boldsymbol{u}_h\right) \rho^h \boldsymbol{u}_h\right) d\Gamma\end{aligned}$$

If momentum is defined as $\boldsymbol{p} = \rho^h \boldsymbol{u}_h + \rho^h \widetilde{\boldsymbol{u}}$, with the contributions due to the finite element and the subscale components, we arrive to the following conservation statement

$$\int_\Omega \frac{\partial \boldsymbol{p}}{\partial t}\, d\Omega = \int_\Omega \rho^h \boldsymbol{g}\, d\Omega + \int_{\partial\Omega} \left(\boldsymbol{t}_n - \left(\boldsymbol{n} \cdot \boldsymbol{u}_h\right) \rho^h \boldsymbol{u}_h\right) d\Gamma \tag{3.39}$$

This equality indicates that the change of the total momentum over the system is equal to the total force over the system plus the traction and momentum fluxes over the boundary $\partial\Omega$. Note that Eq. (3.39) holds independently of the subscale approximation. If, as we have formally assumed, it is zero on the element boundaries, $\rho^h \boldsymbol{u}_h|_{\partial\Omega} = \boldsymbol{p}|_{\partial\Omega}$. Otherwise, boundary subscale terms would need to be added.

3.4.3 Energy conservation

Taking the test function $w_h = 1$ in (the augmented problem corresponding to) the finite element energy equation (3.17) we get

$$\int_\Omega \left(\rho^h c_p \frac{\partial}{\partial t}\left(T_h + \widetilde{T}\right) + \rho^h c_p \left(\boldsymbol{u}_h + \widetilde{\boldsymbol{u}}\right) \cdot \nabla T_h + \widetilde{T} c_p \frac{\partial \rho^h}{\partial t} \right) d\Omega$$

$$= \int_\Omega \left(Q + \alpha \left(T_h + \widetilde{T}\right) \frac{dp^{\text{th}}}{dt} \right) d\Omega + \int_{\partial\Omega} q_n \, d\Gamma \qquad (3.40)$$

When using equal interpolation spaces for the temperature and pressure equations ($W_h = Q_h$), we can take $q_h = T_h$ in the discrete mass equation (3.15) to obtain

$$\int_\Omega \rho^h \left(\boldsymbol{u}_h + \widetilde{\boldsymbol{u}}\right) \cdot \nabla T_h \, d\Omega = \int_\Omega \left(\frac{\partial \rho^h}{\partial t} \right) T_h \, d\Omega + \int_{\partial\Omega} \rho^h \boldsymbol{n} \cdot \boldsymbol{u}_h T_h \, d\Gamma$$

Replacing this equality in (3.40) we get the relation

$$\int_\Omega c_p \frac{\partial}{\partial t}\left(\rho^h \left(T_h + \widetilde{T}\right)\right) d\Omega = \int_\Omega \left(Q + \alpha \left(T_h + \widetilde{T}\right) \frac{dp^{\text{th}}}{dt} \right) d\Omega$$

$$+ \int_{\partial\Omega} \left(q_n - \boldsymbol{n} \cdot \boldsymbol{u}_h \rho^h c_p T_h \right) d\Gamma \qquad (3.41)$$

which is the discrete counterpart of energy conservation equation (4.3) integrated over domain Ω. So, Eq. (3.41) implies energy conservation.

In the case of *ideal gases* (taking $p^{\text{th}} = \rho^h R (T_h + \widetilde{T})$ with $R = \frac{\gamma-1}{\gamma} c_p$ and $\alpha = 1/(T_h + \widetilde{T})$) equation (3.41) can be written as

$$\frac{|\Omega|}{\gamma - 1} \frac{dp^{\text{th}}}{dt} + \frac{\gamma p^{\text{th}}}{\gamma - 1} \int_{\partial\Omega} \boldsymbol{n} \cdot \boldsymbol{u}_h d\Gamma = \int_\Omega Q d\Omega + \int_{\partial\Omega} q_n d\Gamma \qquad (3.42)$$

which is the discrete version of equation (3.8), implying global energy conservation. For ideal gases the internal energy per unit mass is $e = c_v T = \frac{1}{\gamma-1} p^{\text{th}}/\rho$, where $c_v \equiv c_p/\gamma$. So, for the low Mach approximation internal energy per unit volume ρe is uniform and directly proportional to thermodynamic pressure p^{th}. According to that, we define at the discrete level, the discrete internal energy per unit volume as $\rho^h e^h = \frac{1}{\gamma-1} p^{\text{th}} = \rho^h c_v (T_h + \widetilde{T})$. Replacing this definition in Eq. (3.42), we arrive to the first law of thermodynamics for open systems in terms of the internal energy

$$\int_\Omega \frac{\partial \left(\rho^h e_h\right)}{\partial t} d\Omega = \int_\Omega Q \, d\Omega + \int_{\partial\Omega} \left(q_n - \boldsymbol{n} \cdot \boldsymbol{u}_h \left(\rho^h e^h + p^{\text{th}}\right)\right) d\Gamma \qquad (3.43)$$

that indicates that the change of internal energy of the system is equal to the heat power added to the system plus the work done over the system ($W = -\int_{\partial\Omega} \boldsymbol{n} \cdot \boldsymbol{u}_h p^{\text{th}} \, d\Gamma = -p^{\text{th}} \int_\Omega \nabla \cdot \boldsymbol{u}_h d\Omega$) plus the boundary fluxes of heat and internal energy q_n and $\boldsymbol{n} \cdot \boldsymbol{u}_h \rho^h e^h$. It has been proved in chapter 2 that for the Boussinesq approximation global conservation of energy is obtained when nonlinear and orthogonal subscales are used.

3.5 Time discretization

Any time integration scheme could now be applied to discretize in time the finite element equations (3.15)-(3.17), together with equations (3.25)-(3.27). As it is discussed in [27] the time integration for the subscales could be one order less accurate than for the finite element equations without affecting the accuracy of the scheme. To be specific we will consider backward differencing schemes, of second order for the finite element functions and of first order for subscale functions. The choice of a lower order accurate scheme for the subscales results in important memory savings.

Let δt be the time step size of a uniform partition of the time interval $[0, t_{\text{end}}]$, $0 = t^0 < t^1 < ... < t^N = t_{\text{end}}$. Functions approximated at time t^n will be identified with the superscript n. Temporal derivatives in equations (3.15)-(3.17) and (3.25)-(3.27) as well as in (3.22)-(3.24), will be approximated by

$$\begin{aligned} \left.\frac{\partial \phi}{\partial t}\right|_{t^{n+1}} &\approx \frac{3\phi^{n+1} - 4\phi^n + \phi^{n-1}}{2\delta t} := \delta_t \phi^{n+1} \\ \left.\frac{\partial \varphi}{\partial t}\right|_{t^{n+1}} &\approx \frac{\varphi^{n+1} - \varphi^n}{\delta t} := \widetilde{\delta}_t \varphi^{n+1} \end{aligned}$$

where operator $\delta_t \phi$ indicates discrete temporal derivatives over functions $\phi = \boldsymbol{u}_h$, $\phi = T_h$, $\phi = \rho^h$, $\phi = p^{\text{th}}$and the operator $\widetilde{\delta_t \varphi}$ indicates discrete temporal derivatives over the subscales $\varphi = \widetilde{\boldsymbol{u}}$ and $\varphi = \widetilde{T}$ whereas, as usual, all the rest of the terms in these equations are evaluated at t^{n+1} (eventually $\widetilde{\delta}_t = \delta_t$ if the same integration scheme is wished to be used for both the finite element and subscale component of an unknown). After doing this, the subscale equations (3.25)-(3.27) yield

$$\widetilde{p}^{n+1} = \tau_c^{n+1} R_c^{n+1} \tag{3.44}$$

$$\widetilde{\boldsymbol{u}}^{n+1} = \left(\frac{\rho^{h,n+1}}{\delta t} + \frac{1}{\tau_m^{n+1}} \right)^{-1} \left(\boldsymbol{R}_m^{n+1} + \frac{\rho^{h,n} \widetilde{\boldsymbol{u}}^n}{\delta t} \right) \tag{3.45}$$

$$\widetilde{T}^{n+1} = \left(\frac{\rho^{h,n+1} c_p}{\delta t} + \frac{1}{\tau_e^{n+1}} \right)^{-1} \left(R_e^{n+1} + \frac{\rho^{h,n} c_p \widetilde{T}^n}{\delta t} \right) \tag{3.46}$$

From these expressions, we see that the residual of the momentum and energy equations are multiplied respectively by

$$\tau_{tm} = \left(\frac{\rho^{h,n+1}}{\delta t} + \frac{1}{\tau_m^{n+1}} \right)^{-1} \tag{3.47}$$

$$\tau_{te} = \left(\frac{\rho^{h,n+1} c_p}{\delta t} + \frac{1}{\tau_e^{n+1}} \right)^{-1} \tag{3.48}$$

These can be considered the effective stabilization parameters for the transient Low Mach equations. Expressions with asymptotic behavior similar to coefficients τ_{tm}, τ_{te} in terms of $h, \mu, |\boldsymbol{u}_h + \widetilde{\boldsymbol{u}}|$, and δt can often be found in the literature (see e.g. [40]). It is important to note that if the stabilization parameter depends on δt and subscales are not considered time dependent, *the steady-state solution will depend on the time step size*. This does not happen if expressions (3.45) and (3.46) are used. It can be checked that, when steady state is reached the usual expressions employed for stationary problems are recovered, namely $\widetilde{\boldsymbol{u}} = \tau_m \boldsymbol{R}_m$, and $\widetilde{T} = \tau_e R_e$.

After introducing the temporal discretization described above one faces a coupled nonlinear problem for $\boldsymbol{u}_h^{n+1}$, p_h^{n+1}, T_h^{n+1}, $\widetilde{\boldsymbol{u}}^{n+1}$, $\widetilde{p}^{n+1}$ and $\widetilde{T}^{n+1}$ which consists of the time discrete version of (3.15)-(3.18), (4.30)-(3.46) together with the definition of the residuals (3.22)-(3.24). The linearization of this system is described in the following section.

3.6 Linearization strategy

In order to solve the strongly coupled nonlinear problem given by the time discrete version of (3.15)-(3.18), (3.44)-(3.46) together with the definition of the residuals (3.22)-(3.24), we perform an iterative loop of index i, at each time step n. In this loop, given $\boldsymbol{u}_h^{n+1,i}$, $T_h^{n+1,i}$, $\widetilde{\boldsymbol{u}}^{n+1,i}$ and $\widetilde{T}^{n+1,i}$, we first compute the finite element unknowns $\boldsymbol{u}_h^{n+1,i+1}$, $p_h^{n+1,i+1}$ and $T_h^{n+1,i+1}$ from the equations obtained when replacing the subscale expressions (3.44)-(3.46) into the time discretized finite element equations (3.15)-(3.17). Likewise, temporal derivatives of velocity and temperature subscales are written in terms of known iterates of subscales and residuals using (3.26) and (3.27) and replaced into the time discretized finite element equations (3.15)-(3.17). Finally, it is worth noting that the fourth term in (3.17) (the one involving the thermodynamic pressure) is treated differently: the temperature subscale is evaluated as $\widetilde{T}^{n+1,i}$ because in this way, when an ideal gas is considered, $\alpha^i \left(T_h^{n+1,i} + \widetilde{T}^{n+1,i}\right) = 1$, where

$$\alpha^i = -\frac{1}{\rho}\frac{\partial \rho}{\partial T}\bigg|_{T = T_h^{n+1,i} + \widetilde{T}^{n+1,i}}$$

The thermodynamic pressure itself is also evaluated at the end of each iteration, so this term can be considered as part of the right-hand-side.

In order to write the equations obtained in this way, we also introduce the notation

$$\begin{aligned} \boldsymbol{a}^i &= \boldsymbol{u}_h^{n+1,i} + \widetilde{\boldsymbol{u}}^{n+1,i} \\ \rho^i &= \rho\left(T_h^{n+1,i} + \widetilde{T}^{n+1,i}, p^{th,n+1,i}\right) \\ \rho^n &= \rho\left(T_h^n + \widetilde{T}^n, p^{th,n}\right) \end{aligned}$$

and we use these expressions to compute $\tau_c^{n+1,i}$, $\tau_m^{n+1,i}$, $\tau_e^{n+1,i}$ using (3.28)-(3.30) and $\tau_{tm}^{n+1,i}$,

$\tau_{te}^{n+1,i}$ using (3.47)-(3.48). Let us also define perturbations of test functions as

$$\begin{aligned} P_c^i(q_h) &= \tau_{tm}^{n+1,i}\rho^i\nabla q_h && (3.49)\\ \boldsymbol{P}_m^i(\boldsymbol{v}_h) &= \tau_{tm}^{n+1,i}\left[-\frac{\rho^i}{\delta t}\boldsymbol{v}_h+\rho^i\boldsymbol{a}^i\cdot\nabla\boldsymbol{v}_h+\nabla^h\cdot\left(2\mu\boldsymbol{\varepsilon}\left(\boldsymbol{v}_h\right)\right)\right] && (3.50)\\ \boldsymbol{P}_{tm}^i(\boldsymbol{v}_h) &= \tau_{tm}^{n+1,i}\left[\frac{1}{\tau_m^{n+1,i}}\boldsymbol{v}_h+\rho^i\boldsymbol{a}^i\cdot\nabla\boldsymbol{v}_h+\nabla^h\cdot\left(2\mu\boldsymbol{\varepsilon}\left(\boldsymbol{v}_h\right)\right)\right] && (3.51)\\ P_e^i(w_h) &= \tau_{te}^{n+1,i}\left[-\frac{\rho^i c_p}{\delta t}w_h+\rho^i c_p\boldsymbol{a}^i\cdot\nabla w_h+\nabla^h\cdot\left(k\nabla w_h\right)\right] && (3.52)\\ P_{te}^i(w_h) &= \tau_{te}^{n+1,i}\left[\frac{1}{\tau_e^{n+1,i}}w_h+\rho^i c_p\boldsymbol{a}^i\cdot\nabla w_h+\nabla^h\cdot\left(k\nabla w_h\right)\right] && (3.53)\end{aligned}$$

Using these definitions we can write mass conservation as

$$\begin{aligned} &-\left(\rho^i\boldsymbol{u}_h^{n+1,i+1},\nabla q_h\right)+\left(\rho^i\boldsymbol{n}\cdot\boldsymbol{u}_h^{n+1,i+1},q_h\right)_{\partial\Omega}\\ &+\left(\rho^i\delta_t\boldsymbol{u}_h^{n+1,i+1}+\rho^i\boldsymbol{a}^i\cdot\nabla\boldsymbol{u}_h^{n+1,i+1}+\nabla p_h^{n+1,i+1}-\nabla^h\cdot\left(2\mu\boldsymbol{\varepsilon}'\left(\boldsymbol{u}_h^{n+1,i+1}\right)\right),P_c^i(q_h)\right)\\ &\qquad=-\left(\delta_t\rho^i,q_h\right)+\left(\rho^i\boldsymbol{g}+\frac{\rho^n\widetilde{\boldsymbol{u}}^n}{\delta t},P_c^i(q_h)\right) \qquad (3.54)\end{aligned}$$

momentum conservation as

$$\begin{aligned} &\left(\rho^i\delta_t\boldsymbol{u}_h^{n+1,i+1}+\rho^i\boldsymbol{a}^i\cdot\nabla\boldsymbol{u}_h^{n+1,i+1},\boldsymbol{v}_h+\boldsymbol{P}_m^i(\boldsymbol{v}_h)\right)-\left(p_h^{n+1,i+1},\nabla\cdot\boldsymbol{v}_h\right)+\left(2\mu\boldsymbol{\varepsilon}'\left(\boldsymbol{u}_h^{n+1,i+1}\right),\nabla^s\boldsymbol{v}_h\right)\\ &+\left(\nabla p_h^{n+1,i+1}-\nabla^h\cdot\left(2\mu\boldsymbol{\varepsilon}'\left(\boldsymbol{u}_h^{n+1,i+1}\right)\right),\boldsymbol{P}_m^i(\boldsymbol{v}_h)\right)\\ &+\left(\rho^i\nabla\cdot\boldsymbol{u}_h^{n+1,i+1}-\rho^i\alpha^i\boldsymbol{a}^i\cdot\nabla T_h^{n+1,i},\tau_c^{n+1,i}\nabla\cdot\boldsymbol{v}_h\right)\\ &\qquad=\left(\boldsymbol{t}_n,\boldsymbol{v}_h\right)_{\Gamma_N^{\boldsymbol{u}}}-\left(\delta_t\rho^i,\tau_c^{n+1,i}\nabla\cdot\boldsymbol{v}_h\right)+\left(\rho^i\boldsymbol{g},\boldsymbol{v}_h+\boldsymbol{P}_m^i(\boldsymbol{v}_h)\right)+\left(\frac{\rho^n}{\delta t}\widetilde{\boldsymbol{u}}^n,\boldsymbol{P}_{tm}^i(\boldsymbol{v}_h)\right)\end{aligned}\tag{3.55}$$

and energy conservation as

$$\begin{aligned} &\left(\rho^i c_p\delta_t T_h^{n+1,i+1}+\rho^i c_p\boldsymbol{a}^i\cdot\nabla T_h^{n+1,i+1},w_h+P_e^i(w_h)\right)\\ &-\left(\nabla^h\cdot\left(k\nabla T_h^{n+1,i+1}\right),P_e^i(w_h)\right)+\left(k\nabla T_h^{n+1,i+1},\nabla w_h\right)=\left(q_n,w_h\right)_{\Gamma_N^T}\\ &\qquad+\left(Q+\alpha^i\left(T_h^{n+1,i}+\widetilde{T}^{n+1,i}\right)\delta_t p^{th,n+1,i},w_h+P_e^i(w_h)\right)+\left(\frac{\rho^n c_p}{\delta t}\widetilde{T}^n,P_{te}^i(w_h)\right)\end{aligned}\tag{3.56}$$

After solving these equations, the finite element unknowns $\boldsymbol{u}_h^{n+1,i+1}$, $p_h^{n+1,i+1}$ and $T_h^{n+1,i+1}$ are obtained.

Now we proceed to solve (3.44)-(3.46) together with the definition of the residuals (3.22)-(3.24) to obtain the subscales $\widetilde{\boldsymbol{u}}^{n+1,i+1}$ and $\widetilde{T}^{n+1,i+1}$. Note that equations (3.44)-(3.46) are nonlinear in $\widetilde{\boldsymbol{u}}^{n+1,i+1}$ (through the stabilization parameters) and in $\widetilde{T}^{n+1,i+1}$ (through the density). These dependencies are made explicit by rewriting (3.45) and (3.46) as

$$\begin{aligned} \widetilde{\delta}_t\left(\rho^h\left(\widetilde{T}\right)\widetilde{\boldsymbol{u}}\right)+\tau_m^{-1}\left(\widetilde{\boldsymbol{u}},\widetilde{T}\right)\widetilde{\boldsymbol{u}}+\rho^h\left(\widetilde{T}\right)\widetilde{\boldsymbol{u}}\cdot\nabla\boldsymbol{u}_h &= \boldsymbol{R}_{ml}\left(\widetilde{T}\right) && (3.57)\\ c_p\widetilde{\delta}_t\left(\rho^h\left(\widetilde{T}\right)\widetilde{T}\right)+\tau_e^{-1}\left(\widetilde{\boldsymbol{u}},\widetilde{T}\right)\widetilde{T}+\rho^h\left(\widetilde{T}\right)c_p\widetilde{\boldsymbol{u}}\cdot\nabla T_h &= R_{el}\left(\widetilde{T}\right) && (3.58)\end{aligned}$$

where all variables are evaluated at time step $n+1$ iteration $i+1$ and the residuals $\boldsymbol{R}_{ml}$ and R_{el} (not depending on $\widetilde{\boldsymbol{u}}$) are given by

$$
\begin{aligned}
\boldsymbol{R}_{ml}\left(\widetilde{T}\right) &= \rho^h \boldsymbol{g} - \rho^h \delta_t \boldsymbol{u}_h - \rho^h \boldsymbol{u}_h \cdot \nabla \boldsymbol{u}_h + \nabla \cdot \left(2\mu \boldsymbol{\varepsilon}'\left(\boldsymbol{u}_h\right)\right) - \nabla p_h - \left(I - \widetilde{P}\right) \boldsymbol{R}_m \\
R_{el}\left(\widetilde{T}\right) &= Q + \alpha \left(T_h + \widetilde{T}\right) \delta_t p^{\mathrm{th}} - \rho^h c_p \delta_t T_h - \rho^h c_p \boldsymbol{u}_h \cdot \nabla T_h + \nabla \cdot \left(k \nabla T_h\right) \left(I - \widetilde{P}\right) R_e
\end{aligned}
$$

The difference between $\boldsymbol{R}_{ml}$ and $\boldsymbol{R}_m$ (resp. R_e and R_{el}) is precisely the last term of the left-hand-side in (3.57) (resp. (3.58)), and the projection over the residual $\left(I - \widetilde{P}\right) R$ is only taken into account when orthogonal subscales method is used, being zero when $\widetilde{P} = \boldsymbol{I}$. To obtain $\widetilde{\boldsymbol{u}}^{n+1,i+1}$ and $\widetilde{T}^{n+1,i+1}$ at each integration point of each element we need to solve equations (3.57)-(3.58) iteratively. Their linearization will be discussed in the following, considering either fixed point (Picard) or Newton-Raphson's methods, and also either a monolithic or a segregated calculation of the velocity and temperature subscales. We will present the different methods and then their performance will be evaluated in a simple test case in Section 3.8.

The final time evolution and iterative scheme is presented in Algorithm 1.

Algorithm 1 Time evolution and iterative strategy

```
Set $\boldsymbol{u}_h^0$ and $\tilde{\boldsymbol{u}}^0$.
Set $n = 0$.
for $n < N$ do
    Set $\boldsymbol{u}_h^{n+1,0} = \boldsymbol{u}_h^n$ and $T_h^{n+1,0} = T_h^n$
    Set $\tilde{\boldsymbol{u}}^{n+1,0} = \tilde{\boldsymbol{u}}^n$ and $\widetilde{T}^{n+1,0} = \widetilde{T}^n$
    Set $i = 0$.
    while not converged do
        Solve (3.54)-(3.56) to obtain $\boldsymbol{u}_h^{n+1,i+1}$, $T_h^{n+1,i+1}$ and $p_h^{n+1,i+1}$
        for each integration point do
            Solve iteratively (3.57)-(3.58) to obtain $\tilde{\boldsymbol{u}}^{n+1,i+1}$ and $\widetilde{T}^{n+1,i+1}$
        end for
        Solve (3.5) or (3.7) to obtain $p^{th,n+1,i+1}$
        $i = i + 1$.
    end while
end for
```

3.6.1 Picard's linearization

Let us denote with a superscript k or $k+1$ the iteration counter for the subscales (remember that all unknowns need to be computed at time step $n+1$ and global iteration $i+1$). The finite element unknowns are assumed to be given as we need to solve problem (3.57) and (3.58). If the subscales are known at iteration k, the simplest way to approximate them at iteration $k+1$ is by solving

$$
\widetilde{\delta}_t \left(\rho^h \widetilde{\boldsymbol{u}}^{k+1}\right) + \tau_m^{-1} \left(\widetilde{\boldsymbol{u}}^k, \widetilde{T}^k\right) \widetilde{\boldsymbol{u}}^{k+1} + \rho^h \widetilde{\boldsymbol{u}}^{k+1} \cdot \nabla \boldsymbol{u}_h = \boldsymbol{R}_{ml}\left(\widetilde{T}^k\right) \tag{3.59}
$$

$$
c_p \widetilde{\delta}_t \left(\rho^h \widetilde{T}^{k+1}\right) + \tau_e^{-1} \left(\widetilde{\boldsymbol{u}}^k, \widetilde{T}^k\right) \widetilde{T}^{k+1} + \rho^h c_p \widetilde{\boldsymbol{u}}^{k+1} \cdot \nabla T_h = R_{el}\left(\widetilde{T}^k\right) \tag{3.60}
$$

where $\rho^h = \rho\left(p^{\text{th}}, T_h + \widetilde{T}^k\right)$ is computed from the unknowns at the last iteration. Note that solving (3.59) implies the solution of a $d \times d$ linear system at each integration point. This is due to the last term in the left-hand-side of (3.59) which was evaluated in iteration k in [27, 24, 47] (doing that permits to obtain a closed expression for $\widetilde{\boldsymbol{u}}^{k+1}$, but the iterative scheme may fail to converge).

3.6.2 Picard's linearization, Gauss-Seidel-type $\widetilde{\boldsymbol{u}}$-$\widetilde{T}$ calculation

It is observed that Eq. (3.59) does not depend on $\widetilde{T}^{k+1}$, and therefore this equation may be used to compute $\widetilde{\boldsymbol{u}}^{k+1}$. Once it is known, instead of using $\widetilde{\boldsymbol{u}}^k$ in Eq. (3.60) we could think of using this updated value, $\widetilde{\boldsymbol{u}}^{k+1}$, that is to say, using a Gauss-Seidel-type coupling of (3.59)-(3.60). The resulting problem is

$$
\begin{aligned}
\widetilde{\delta}_t\left(\rho^h \widetilde{\boldsymbol{u}}^{k+1}\right) + \tau_m^{-1}\left(\widetilde{\boldsymbol{u}}^k, \widetilde{T}^k\right)\widetilde{\boldsymbol{u}}^{k+1} + \rho^h \widetilde{\boldsymbol{u}}^{k+1} \cdot \nabla \boldsymbol{u}_h &= \boldsymbol{R}_{ml}\left(\widetilde{T}^k\right) \\
c_p \widetilde{\delta}_t\left(\rho^h \widetilde{T}^{k+1}\right) + \tau_e^{-1}\left(\widetilde{\boldsymbol{u}}^{k+1}, \widetilde{T}^k\right)\widetilde{T}^{k+1} + \rho^h c_p \widetilde{\boldsymbol{u}}^{k+1} \cdot \nabla T_h &= R_{el}\left(\widetilde{T}^k\right)
\end{aligned}
$$

This scheme has been proved to converge faster than (3.59)-(3.60). Note that the only difference between both methods is the way to evaluate τ_e.

3.6.3 Newton Raphson's linearization, monolithic $\widetilde{\boldsymbol{u}}$-$\widetilde{T}$ calculation

An alternative to fixed point schemes is to use the Newton-Raphson method. When applied to (3.57)-(3.58), the problem to be solved at each iteration is

$$
\widetilde{\delta}_t\left(\rho^h \widetilde{\boldsymbol{u}}^{k+1}\right) + \rho^h \widetilde{\boldsymbol{u}}^{k+1} \cdot \nabla \boldsymbol{u}_h + \tau_m^{-1}\left(\widetilde{\boldsymbol{u}}^k, \widetilde{T}^k\right)\widetilde{\boldsymbol{u}}^{k+1} + \frac{c_2 \rho^h}{h}\left[\frac{\left(\boldsymbol{u}_h + \widetilde{\boldsymbol{u}}^k\right)}{|\boldsymbol{u}_h + \widetilde{\boldsymbol{u}}^k|} \cdot \left(\widetilde{\boldsymbol{u}}^{k+1} - \widetilde{\boldsymbol{u}}^k\right)\right]\widetilde{\boldsymbol{u}}^k
$$

$$
-\left(\frac{c_2}{h}|\boldsymbol{u}_h + \widetilde{\boldsymbol{u}}^k|\widetilde{\boldsymbol{u}}^k + \left(\boldsymbol{u}_h + \widetilde{\boldsymbol{u}}^k\right) \cdot \nabla \boldsymbol{u}_h - \boldsymbol{g} + \delta_t \boldsymbol{u}_h + \frac{\widetilde{\boldsymbol{u}}^k}{\delta t}\right) \frac{\rho^h\left(\widetilde{T}^{k+1} - \widetilde{T}^k\right)}{T_h + \widetilde{T}^k} = \boldsymbol{R}_{ml}\left(\widetilde{T}^k\right)
$$

$$
c_p \widetilde{\delta}_t\left(\rho^h \widetilde{T}^{k+1}\right) + \tau_e^{-1}\left(\widetilde{\boldsymbol{u}}^k, \widetilde{T}^k\right)\widetilde{T}^{k+1} + \rho^h c_p \widetilde{\boldsymbol{u}}^{k+1} \cdot \nabla T_h + \frac{c_2 \rho^h c_p}{h}\left[\frac{\left(\boldsymbol{u}_h + \widetilde{\boldsymbol{u}}^k\right)}{|\boldsymbol{u}_h + \widetilde{\boldsymbol{u}}^k|} \cdot \left(\widetilde{\boldsymbol{u}}^{k+1} - \widetilde{\boldsymbol{u}}^k\right)\right]\widetilde{T}^k
$$

$$
-\left(\frac{c_2}{h}|\boldsymbol{u}_h + \widetilde{\boldsymbol{u}}^k|\widetilde{T}^k + \left(\boldsymbol{u}_h + \widetilde{\boldsymbol{u}}^{k+1}\right) \cdot \nabla T_h + \delta_t T_h + \frac{\widetilde{T}^k}{\delta t}\right) \frac{\rho^h c_p\left(\widetilde{T}^{k+1} - \widetilde{T}^k\right)}{T_h + \widetilde{T}^k} = R_{el}\left(\widetilde{T}^k\right)
$$

In our numerical tests we have observed that this scheme is the most robust, always achieving convergence but needing sometimes more iterations than the other schemes. Note that it implies to solve for $\widetilde{\boldsymbol{u}}^{k+1}$ and $\widetilde{T}^{k+1}$ in a monolithic (coupled) way.

3.6.4 Newton Raphson's linearization, segregated $\widetilde{\boldsymbol{u}}$-$\widetilde{T}$ calculation

An alternative to the monolithic scheme presented above would be to use $\widetilde{T}^k$ in the equation for $\widetilde{\boldsymbol{u}}^{k+1}$, so as to allow for a segregated calculation of $\widetilde{\boldsymbol{u}}^{k+1}$ and $\widetilde{T}^{k+1}$. The result is

$$\widetilde{\delta}_t\left(\rho^h\widetilde{\boldsymbol{u}}^{k+1}\right)+\rho^h\widetilde{\boldsymbol{u}}^{k+1}\cdot\nabla\boldsymbol{u}_h+\tau_m^{-1}\left(\widetilde{\boldsymbol{u}}^k,\widetilde{T}^k\right)\widetilde{\boldsymbol{u}}^{k+1}$$

$$+\frac{c_2\rho^h}{h}\left[\frac{\left(\boldsymbol{u}_h+\widetilde{\boldsymbol{u}}^k\right)}{|\boldsymbol{u}_h+\widetilde{\boldsymbol{u}}^k|}\cdot\left(\widetilde{\boldsymbol{u}}^{k+1}-\widetilde{\boldsymbol{u}}^k\right)\right]\widetilde{\boldsymbol{u}}^k=\boldsymbol{R}_{ml}\left(\widetilde{T}^k\right)$$

$$c_p\widetilde{\delta}_t\left(\rho^h\widetilde{T}^{k+1}\right)+\rho^hc_p\widetilde{\boldsymbol{u}}^{k+1}\cdot\nabla T_h+\tau_e^{-1}\left(\widetilde{\boldsymbol{u}}^{k+1},\widetilde{T}^k\right)\widetilde{T}^{k+1}$$

$$-\left(\frac{c_2}{h}|\boldsymbol{u}_h+\widetilde{\boldsymbol{u}}^{k+1}|\widetilde{T}^k+\left(\boldsymbol{u}_h+\widetilde{\boldsymbol{u}}^{k+1}\right)\cdot\nabla T_h+\delta_tT_h+\frac{\widetilde{T}^k}{\delta t}\right)\frac{\rho^hc_p\left(\widetilde{T}^{k+1}-\widetilde{T}^k\right)}{T_h+\widetilde{T}^k}=R_{el}\left(\widetilde{T}^k\right)$$

Note that $\widetilde{\boldsymbol{u}}^{k+1}$ is used in the evaluation of τ_e, using the same Gauss-Seidel-type update as for Picard's method.

3.7 Implementation of higher order elements

The development of higher-order methods for Navier-Stokes equations has been a hot research topic all over the world. The goal of these researches is to design cheaper and more efficient numerical methods able to handle very large and very complex problems.

It is known that significantly fewer degrees of freedom are required for higher-order methods than for classical second-order schemes to reach the same level of accuracy. Also higher order methods deal much better with complex geometries, representing better the curved boundaries and boundary conditions. However, the use of higher order methods increase the computer memory demanding, and better linear solvers are needed to solve the algebraical systems of equations.

The accuracy and efficiency of the formulation when using linear, quadratic and cubic elements will be shown in the section of numerical examples. Also, the competitiveness of the formulation will be tested. That is to say, if the associated increased computational complexity is worth affording compared to lower order methods, and compared to usual stabilization methods, such as SUPG method [11] .

3.7.1 About stability when using higher order elements

Although it is not possible to prove stability for the discrete Low Mach equations, it has been proved for the Oseen equations [20]. When using higher order elements the only change in the formulation is that now the diffusive terms in the residuals (3.22)-(3.24) are evaluated. A key ingredient of the stability analysis when using higher order elements is the anisotropic inverse estimate which can be derived from a scaling argument

$$||\nabla^2u_h||_K^2\leq\frac{C_{\text{inv}}^2p^4}{h_{\text{min}}^2}||\nabla u_h||_K^2\;\forall u_h\in V_h,\quad ||\nabla\cdot\boldsymbol{v}_h||_K^2\leq\frac{C_{\text{inv}}^2p^4}{h_{\text{min}}^2}||\boldsymbol{v}_h||_K^2\;\forall\boldsymbol{v}_h\in\left(V_h\right)^d \quad (3.61)$$

where p is the order of the polinomial being used. Estimate of inverse constant values C_{inv} are given in [42] and references therein. In the following, we will include p in the expression of C_{inv}. When requiring stability for the discrete Oseen and energy equations, the following conditions over the expression of stabilization parameter τ_m and τ_e in Eqs. (3.29) and (3.30) need to be satisfied in terms of the inverse constant C_{inv}, [78]

$$c_1 \frac{\mu}{h^2} + c_2 \frac{\rho^h |\boldsymbol{u}_h + \widetilde{\boldsymbol{u}}|}{h} > 4 \frac{\mu C_{\text{inv}}^2}{h_{\text{min}}^2} \tag{3.62}$$

$$c_1 \frac{k}{h^2} + c_2 \frac{\rho^h c_p |\boldsymbol{u}_h + \widetilde{\boldsymbol{u}}|}{h} > 4 \frac{k C_{\text{inv}}^2}{h_{\text{min}}^2} \tag{3.63}$$

It is seen here that high values of c_1 will satisfy easily this condition. We have set the algorithmic constants $c_1 = 12p^2$ and $c_2 = 2p$ in the numerical examples where higher order elements were implemented, where p is the interpolating order of the elements. It is common to set $c_1 = 4$ when using linear elements, as in [27, 2, 25, 78] because this parameter gives optimal solutions for 1D problems. However, when setting $c_1 = 4p^2$ we observed unstable solutions using the present nonlinear formulation. These instabilities disappeared setting $c_1 = 12p^2$, a behavior justified by conditions (3.62) and (3.63).

When diffusive terms in the perturbations of test functions (3.50)-(3.53) are omitted in the implementation, higher accuracy, faster assembly and better convergence is achieved. This modification in the implementation makes the formulation similar to the streamline upwind Petrov-Galerkin (SUPG) method [11], the most used in the literature to solve the compressible Navier Stokes equations with high order elements. In the numerical examples diffusive terms were omitted in perturbation of test functions (3.50)-(3.53).

Many works in the literature define c_1 proportional to p^2 and c_2 proportional to p, as in the present work. However, stability analysis developed in [66, 46] for the convection diffusion reaction equation shows that c_1 needs to be proportional to p^4 to get an stable formulation as p is increased. This is a consequence of estimates (3.61).

3.8 Numerical examples

In this section we present four examples. The first example, extensively studied in the literature, is a stationary flow in a differentially heated cavity and permits us to perform a detailed study of the behavior of the nonlinear subscale models and their iterative solution. A study of the convergence behavior using different element orders will be done. The second one is a transient bidimensional closed flow with increasing thermodynamic pressure and permits us to test the temporal accuracy and computational efficiency of the proposed scheme, it will be also solved using quadratic and cubic elements, comparing the computational efficiency of the method. The third one is a transient three dimensional fire compartment room in which, apart from testing the accuracy of the method we also present some preliminary conclusions on its computational efficiency. The fourth example consists on solving a dynamic and periodic flow over a hot cylinder, it will be tested the accuracy of the method using higher order elements. The effect of curved geometries should favor the use of higher order elements.

Whereas in the first example different subscale models are compared, in the second and third we compare the formulation presented in this chapter against the algebraic subgrid scale

(ASGS) method, as presented in [79], which is reduced to the stream upwind Petrov-Galerkin method (SUPG) [43] when linear elements are used. Bilinear (2D) and trilinear (3D) interpolated Q_1 elements are used the first three numerical examples for velocity, pressure and temperature. Convergence error of the solution using different stabilization methods are compared in the first, second and fourth examples using P_1, Q_2, P_2, Q_3, P_3 elements. In the first two examples the algebraic system corresponding to the finite element problem (line 8 in Algorithm 1) is solved using a direct method whereas in the last one it is solved using an iterative one (GMRES) whose convergence criteria is that any residual (for mass, momentum or energy equations) cannot be bigger than 10^{-6} of the initial one. The convergence criteria for the nonlinear iterations (loop starting at line 7 in Algorithm 1) was set as $\left|\phi_h^{n+1,i+1} - \phi_h^{n+1,i}\right| < \epsilon_1 \left|\phi_h^{n+1,i+1}\right|$ for any finite element unknown ϕ_h, where the tolerance ϵ_1 was set to 10^{-9} in the first example and to $5 \cdot 10^{-4}$ in the second and third ones. The subscales were computed at each integration point until $\left|\widetilde{\phi}^{n+1,i+1,k+1} - \widetilde{\phi}^{n+1,i+1,k}\right| < \epsilon_2 \left|\widetilde{\phi}^{n+1,i+1,k+1}\right|$, for any subscale $\widetilde{\phi}$. The tolerance was set to $\epsilon_2 = 10^{-3} \left|\phi_h^{n+1,i+1} - \phi_h^{n+1,i}\right| / \left|\phi_h^{n+1,i+1}\right|$ in all the examples.

In all examples we consider an ideal gas with constant values of $R = 287.0$ J kg^{-1} K^{-1} and $c_p = 1004.5$ J kg^{-1} K^{-1}.

3.8.1 Natural convection in a cavity

Problem description and numerical results

The present flow example has been proposed in [82] as a benchmark problem for natural convection flows with large temperature gradients. This example was also considered in, e.g. [43, 79, 40]. The problem domain is $\Omega = [0, L] \times [0, L]$ with $L = 1$ m. Adiabatic boundary conditions are prescribed for upper and lower walls $(q_n = k\boldsymbol{n} \cdot \nabla T_h = 0)$. The left wall is maintained at a fixed temperature T_H and the right wall at temperature T_C. The initial thermodynamic pressure and temperatures are $p_0^{\text{th}} = 101325$ Pa, $T_0 = 600$ K, yielding an initial uniform density of $\rho_0 = 0.58841$ kg/m^3. In contrast to the Boussinesq approximation, in the low Mach approximation the stationary solution depends on the initial thermodynamic pressure p_0^{th}. The dimensionless Prandtl and Rayleigh numbers are fixed to $\text{Pr} = \frac{c_p \mu}{k} = 0.71$, $\text{Ra} = 2\frac{|\boldsymbol{g}|\rho_0^2}{\mu^2}\varepsilon = 10^6$, where $\varepsilon = \frac{T_H - T_C}{T_H + T_C} = 0.6$. The viscosity is $\mu = 10^{-3}$ kg/(m s). Boundary left and right wall temperatures are $T_H = 960$ K and $T_C = 240$ K, satisfying the relation $(T_H + T_C)/2 = T_0$. Zero Dirichlet boundary conditions for the velocity are assumed on all boundaries.

Numerical results were obtained using meshes from 20×20 to 240×240 uniform elements. The reference solution was obtained using a grid of 720×720 uniform elements using both the ASGS and the DSS methods. The relative difference between these two solutions is 2.8×10^{-4} in the discrete $L^2(\Omega)$-norm of the velocities and 4.4×10^{-5} in the discrete $L^2(\Omega)$-norm of the temperatures. The discrete $L^2(\Omega)$ norm (denoted by $|\cdot|_h$) has been computed for any variable ϕ as

$$|\phi|_h^2 = \frac{1}{N_n} \sum_a \left[\phi(\boldsymbol{x}^a)\right]^2 \tag{3.64}$$

where the summation extends to all N_n mesh nodes a. As shown below, relative differences between results obtained with any other mesh and method with respect to the one obtained using the ASGS method in the 720×720 uniform mesh are, at least, one order of magnitude bigger. This proves that the comparisons against either the solution obtained in the 720×720 uniform mesh using the ASGS or the DSS method will give rise to the same conclusions. We choose the ASGS method as reference because it is a standard method extensively tested and compared against direct numerical simulations in the literature [5, 40].

The obtained velocities and temperatures are depicted in Fig. 3.1.

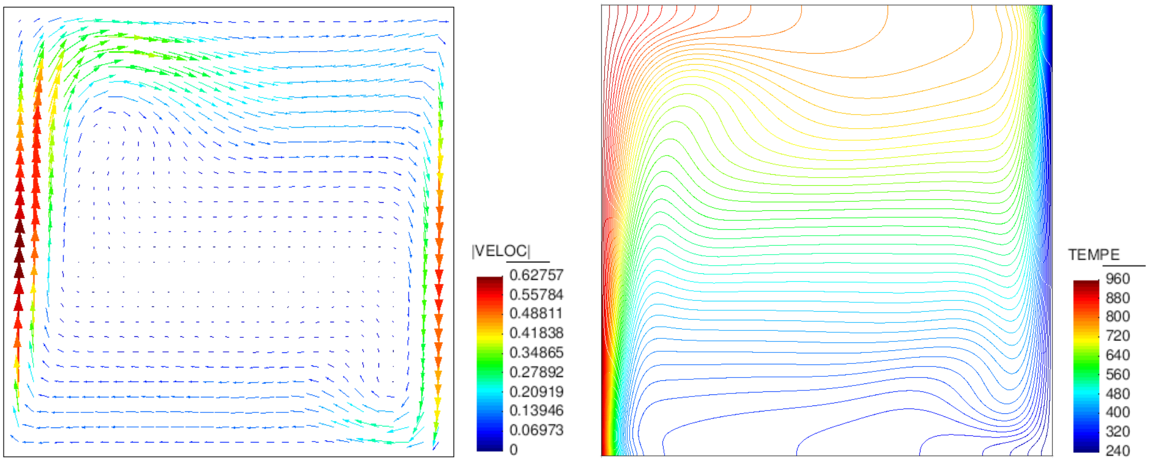

Figure 3.1: Velocity vectors and Temperature distribution inside the cavity

The compared stabilization methods are (note that the first three methods only differ in the subscale model):

- The method in the present chapter containing full nonlinear subscales, labeled as “DSS” in Fig. 3.2 and Fig. 3.3.

- The method in the present chapter containing full nonlinear subscales and using orthogonal subscales, labeled as “OSS” in Fig. 3.2.

- The method presented in this chapter, but neglecting the temperature subscale in the state equation, that is ρ^h is computed as $\rho^h = \frac{p^{\text{th}}}{RT_h}$, labeled as “SemiSGS” in Fig. 3.2 and Fig. 3.3.

- The method presented in this chapter, but using a linear approximation to the subscale equations (3.25)- (3.27), that is, taking τ_m, τ_c, τ_e and $\boldsymbol{R}_m, R_c, R_e$ independent of the velocity and temperature subscales $\widetilde{\boldsymbol{u}}$, $\widetilde{T}$. In all cases $|\boldsymbol{u}_h + \widetilde{\boldsymbol{u}}|$ is replaced by $|\boldsymbol{u}_h|$ as it is usually done, for example in [40] or [5]. As in the previous case the temperature subscale is neglected in the state equation. This method is labeled as “LinSGS” in Fig. 3.2 and Fig. 3.3.

- The ASGS method, a linear stabilization method as described in [79]. This method is equal to the classical SUPG method when using linear elements.

- The reference solution, labeled as “Ref” in Fig. 3.3.

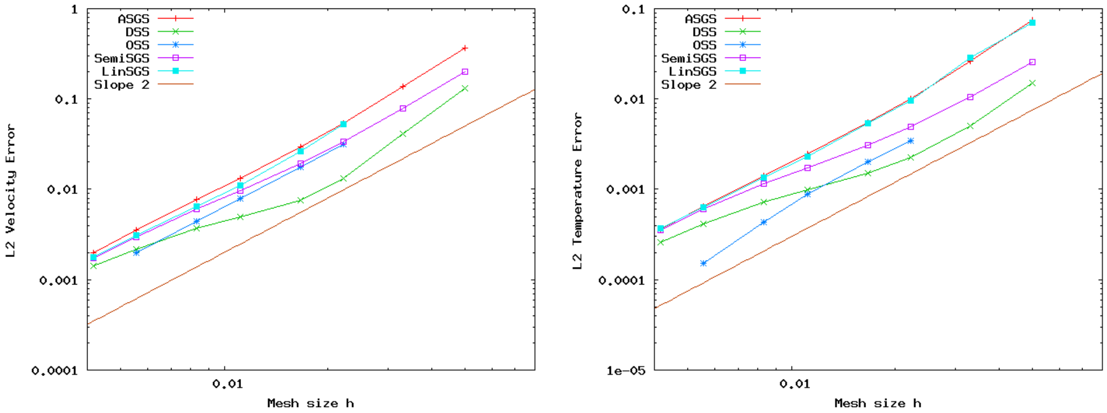

Figure 3.2: Discrete $L^2(\Omega)$ error of the solutions obtained using different methods against mesh size h.

The discrete $L^2\,(\Omega)$ norm of the error (with respect to the reference solution) as a function of the mesh size h is shown in Fig. 3.2 for the different stabilization methods. Second order convergence of the error for the smallest values of h is obtained for all the methods. However, the highest accuracy is obtained when subscales are kept in all the nonlinear terms, both in the finite element equations and in the subscale equations. As it can be seen in Fig. 3.2 the error obtained using the full nonlinear method is smaller than the one obtained using the ASGS method over all the mesh size range. Superconvergence is observed when solving with OSS method, specially for temperature. This behavior for OSS method has been observed for incompressible flows. When using the full nonlinear method a convergence rate of order greater than 2 is observed on the coarsest meshes. As it will be justified in the next Subsection 3.8.1 the full nonlinear method will converge to the ASGS method for h small enough and this implies the there must be a region in which this slope decreases below 2. When the temperature subscale is neglected in the state equation the solution is less accurate, the gain in accuracy respect to the ASGS method is lower, becoming negligible over the finer grids. Finally, when a linear approximation to the subscale equations (3.25)- (3.27) is considered, even less accurate solutions are obtained, the gain in accuracy respect to the ASGS method being negligible over all the mesh size range. A possible explanation for this phenomenon arises from the analysis of the subgrid velocity and temperature fields given in the following Subsection 3.8.1.

The higher accuracy of the fully nonlinear approximation for the subscales is further illustrated in Fig. 3.3 where the variation of the velocity and temperature solutions for different stabilization methods are depicted along three different lines cutting the domain.

Another quantity of interest is the heat transfer from the hot to the cold wall, represented by the Nusselt number, defined as

$$\mathrm{Nu}(\boldsymbol{x}) = \frac{L}{T_H - T_C}\boldsymbol{n}\cdot\nabla T(\boldsymbol{x}), \qquad \boldsymbol{x}\in\partial\Omega$$

The discrete $L^2(\partial\Omega)$-norm error of the Nusselt distribution against mesh size h is shown in Fig. 3.4 for the ASGS and DSS methods. When using finer grids both methods give similar errors. For the coarsest grids the DSS method gives slightly more accurate distributions, although the difference is not as significant as for the errors in the interior of the computational

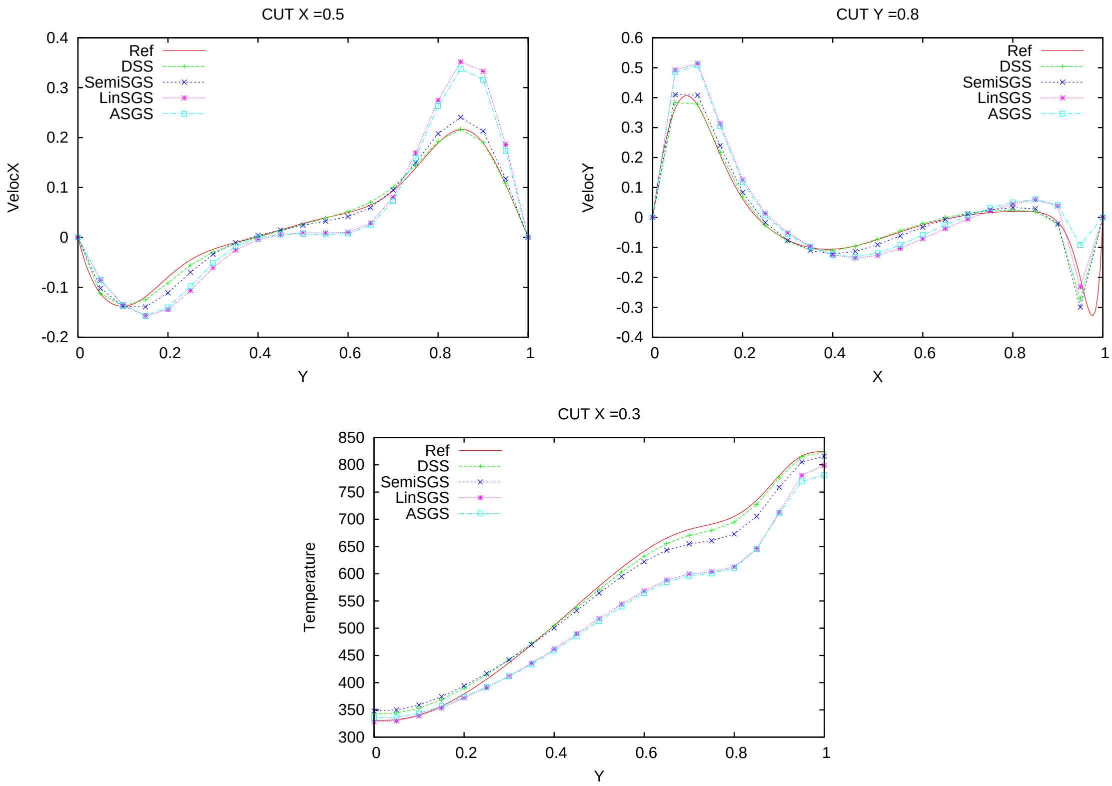

Figure 3.3: Solutions obtained on a 20×20 uniform grid using different stabilization methods against the reference solution

domain. In this case, the discrete $L^2(\partial\Omega)$-norm error is calculated as in (3.64), taking

$$\text{Error} = \frac{\sum_a \left(\text{Nu}_h(\boldsymbol{x}^a) - \text{Nu}(\boldsymbol{x}^a)\right)^2}{\sum_a \left(\text{Nu}(\boldsymbol{x}^a)\right)^2}$$

where now a refers to boundary nodes, $\text{Nu}_h(\boldsymbol{x}^a)$ is obtained variationally from T_h (as explained in [48]) and at node $\boldsymbol{x}^a$, and $\text{Nu}(\boldsymbol{x}^a)$ is the variational Nusselt number obtained from the reference solution at this node. Once again, this reference solution was obtained using the ASGS method over a grid of 720×720 elements. The convergence of the error against mesh size h is between linear and quadratic.

Even though the quality of the thermal fluxes is similar using the ASGS and the DSS methods, let us remark that due to the property of global conservation of energy (3.43) when using the DSS method, the average Nusselt number over all the boundary $\partial\Omega$ is identically zero. Instead it differs from zero when using ASGS method.

Reference solutions for the average Nusselt numbers over hot and cold walls can be found in [82]. Those differ in less than 0.02% from the Nusselt obtained in our reference solution. Let us mention that the ASGS yields better results on the hot wall, whereas the Nusselt number is better approximated using the DSS method on the cold wall. These observations are however inconclusive since, as we have seen, the global discrete $L^2(\partial\Omega)$ error is very similar in both methods.

In Fig. 3.4 the thermodynamic pressure convergence is depicted against the mesh size h

using the ASGS and the DSS methods. The reference value for p^{th} is taken from [82]. As for the Nusselt number, convergence is found to be between linear and quadratic for smaller h. When using coarser grids the DSS method yields more accurate values for p^{th} than the ASGS method. However, convergence is not monotone for coarser grids.

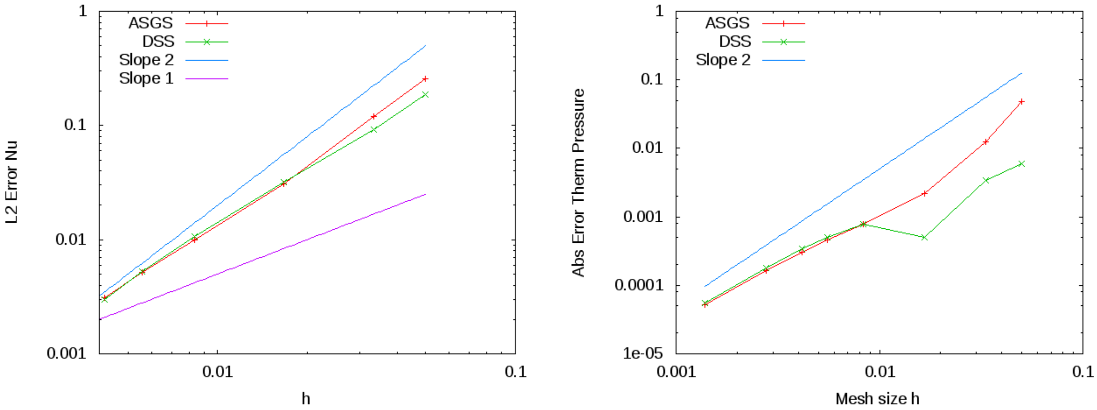

Figure 3.4: $L^2(\partial\Omega)$-norm error of the Nusselt numbers distributions (left) and absolute error for the thermodynamic pressure (right) against mesh size h.

Analysis of subscale models

Velocity and temperature subscales are depicted in Fig.3.5. As expected, higher values for the subscales are obtained on the boundary layer, where velocity and temperature gradients are larger. In fact, the temperature subscale can be significant when compared to the finite element temperature and the velocity subscale can be even higher than the finite element velocity, as can be seen comparing Fig.3.5 with Fig. 3.1. This is actually the case in boundary layers, as can be seen in Fig. 3.6, where the logarithmic ratio between subscale and finite element velocities is shown for two different meshes. This shows the importance of keeping the scale splitting everywhere in nonlinear terms. A common argument to develop linear subscale models [5, 40], is to assume that subscales are small compared to finite element components (i.e. $|\widetilde{\boldsymbol{u}}| \ll |\boldsymbol{u}_h|$) thus neglecting terms which are quadratic in the subscales (although nonlinear terms are kept in the finite element equations in [5, 40]). It is tempting to model subscales as linear and quasi-static because in this case there is no need to store them, and thus there would be no memory increase due to the subscale evaluation. However, more accurate solutions are obtained using the nonlinear model, as shown above.

Similar comments can be made regarding the temperature coupling. If we consider ρ^h not depending on $\widetilde{T}$ and τ_m, τ_e not depending on $\widetilde{\boldsymbol{u}}$ (i.e. replacing $|\boldsymbol{u}_h + \widetilde{\boldsymbol{u}}|$ by $|\boldsymbol{u}_h|$ in (4.28) and (3.30)) the subscales are modeled by a linear system of equations, although $\widetilde{\boldsymbol{u}}$ and $\widetilde{T}$ are still taken into account in the finite element residuals (3.22)-(3.24). This method does not require additional memory cost to store the subscales. However we did not find this method better than the method labeled “LinSGS” above and considered in [40, 5] in terms of accuracy, at least in the differentially heated cavity problem presented here. Further, the assumption that the density does not depend on $\widetilde{T}$ leads to a nonlinear system of equations where the velocity subscale $\widetilde{\boldsymbol{u}}$ is decoupled from the temperature subscale $\widetilde{T}$. This nonlinear system has one less

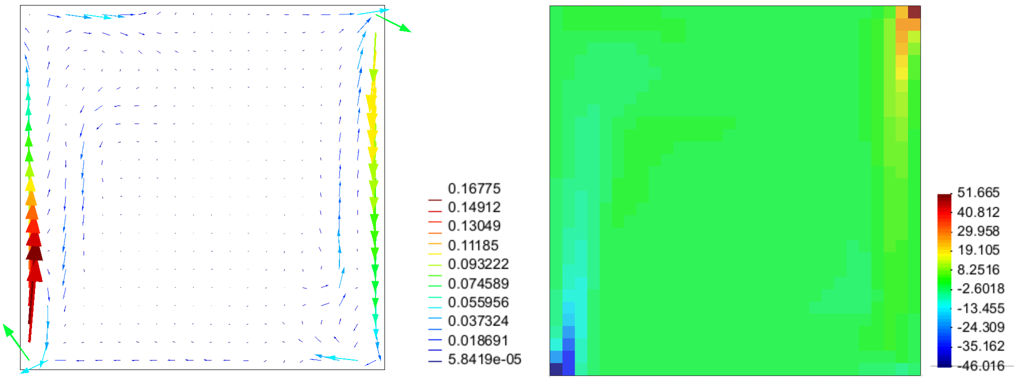

Figure 3.5: Velocity and Temperature subscales

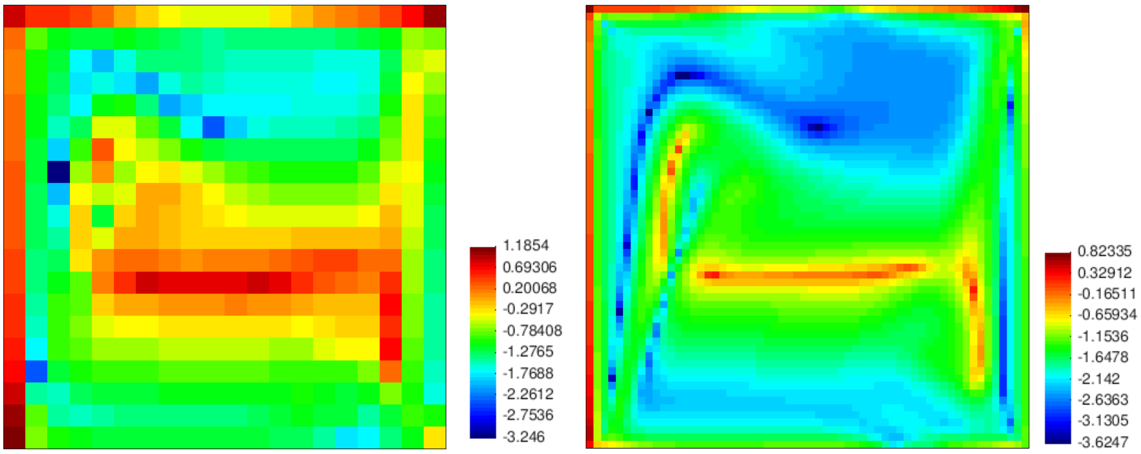

Figure 3.6: Logarithmic relation bewtween velocity subscale and finite element velocity norms, $\log_{10}(|\widetilde{\boldsymbol{u}}| \,/\, |\boldsymbol{u}_h|)$, over 20 × 20 (left) and 60 × 60 (right) meshes.

unknown, and the temperature subscale can be obtained later from the linear equation (3.60). However, it has been observed in the present example that the effect of considering the state equation depending on the temperature subscale improves the accuracy of the method as shown in Fig. 3.2.

We proceed now to present heuristic arguments showing why the nonlinear subscale model can be more accurate than a linear one. As shown in Fig. 3.6 one region in which the subscale velocity is bigger than the finite element velocity is the (left) boundary layer. As shown in Fig. 3.1 and Fig. 3.5, the finite element and subgrid velocities are parallel there and therefore (assuming that the finite element velocity only depends on the coordinate normal to the wall), from equation (3.59), we have $\widetilde{u}_1 = 0$ and $\widetilde{u}_2 = \tau_m R_{ml,2}$. Then, the ($y$ component of the) finite element velocity, the subscale velocity and the residual have the same sign, which we assume positive. Omitting subscript 2 and defining the linear parameter

$$\tau = \left(c_1 \frac{\mu}{h^2} + c_2 \frac{\rho^h u_h}{h} \right)^{-1}$$

this nonlinear equation can be written as

$$\tau^{-1}\widetilde{u} + \frac{c_2\rho\widetilde{u}^2}{h} - R_{ml} = 0$$

whose solution is

$$\widetilde{u} = \frac{h}{2c_2\rho\tau}\left[-1 + \left(1 + \frac{4c_2\rho\tau^2 R_{ml}}{h}\right)^{1/2}\right]$$

that behaves as

$$\widetilde{u} \approx \begin{cases} (c_2\rho)^{-1/2}\,(hR_{ml})^{1/2} & \text{when} \quad 4c_2\rho\tau^2 R_{ml}/h \gg 1 \\ \tau R_{ml} & \text{when} \quad 4c_2\rho\tau^2 R_{ml}/h \ll 1 \end{cases}$$

The parameter $\frac{4\rho\tau^2 R_{ml}}{h}$ tends to zero when the mesh is refined (expectedly as h^3 for linear elements) and that may explain why the LinSGS and the DSS methods give similar results when the mesh is fine enough. Whereas the LinSGS method approximates $\widetilde{u} = \tau R_{ml}$ regardless of the parameter $\frac{4\rho\tau^2 R_{ml}}{h}$, the fully nonlinear DSS method gives a different solution when $\frac{4\rho\tau^2 R_{ml}}{h} \gg 1$ (coarse meshes) and the ratio between these solutions is, precisely,

$$\frac{\widetilde{u}_{\text{LinSGS}}}{\widetilde{u}_{\text{DSS}}} = \frac{\tau R_{ml}}{(c_2\rho)^{-1/2}\,(hR_{ml})^{1/2}} = \frac{1}{2}\left(\frac{4c_2\rho\tau^2 R_{ml}}{h}\right)^{1/2} \tag{3.65}$$

We have verified that the maximum value of this parameter (it varies over the domain and the maximum occurs in the boundary layer) is around 16 for the 20×20 mesh and is around 0.02 for the 240×240 mesh. We therefore expect the subscale obtained using the LinSGS method to be around twice times the subscale obtained using the DSS method in the 20×20 mesh but nearly the same in the 240×240 mesh. The norm of the velocity subscales obtained using LinSGS and DSS methods for both meshes shown in Fig.3.7 confirms these expectations and helps to understand the results shown in Fig. 3.2 (smaller error using DSS for coarse meshes and the same result for finer meshes).

Testing the linearization methods

Let us describe the performance of the different methods presented in Section 3.6 to solve the subscale equations (line 10 in Algorithm 1) for this particular numerical example. In spite of the fact that the behavior of linearization methods is highly problem dependent, we have found the results to be presented representative of several test cases.

Consider thus the problem at $\mathrm{Ra} = 10^6$ with a 20×20 mesh. We took as initial condition the stationary solution using the ASGS method. We then solved the problem as transient setting a time step $\delta t = 14\delta t_c$, where δt_c is the critical time step that would be found using the forward Euler scheme for the viscous and convective terms, which behaves as the stabilization parameter (see [28]). We took as initial guess $\widetilde{\boldsymbol{u}} = \mathbf{0}$ and $\widetilde{T} = 0$. Convergence of the subgrid scale equations using the linearization schemes described in Section 3.6 are compared in Fig. 3.8 (left). In this figure, the method of Subsection 3.6.1 is labeled “Picard”, the method of Subsection 3.6.3 is labeled “Newton Raphson”, the method of Subsection 3.6.4 is labeled “NewRaph Segregated” and the method of Subsection 3.6.2 is labeled “Picard Gauss Seidel”.

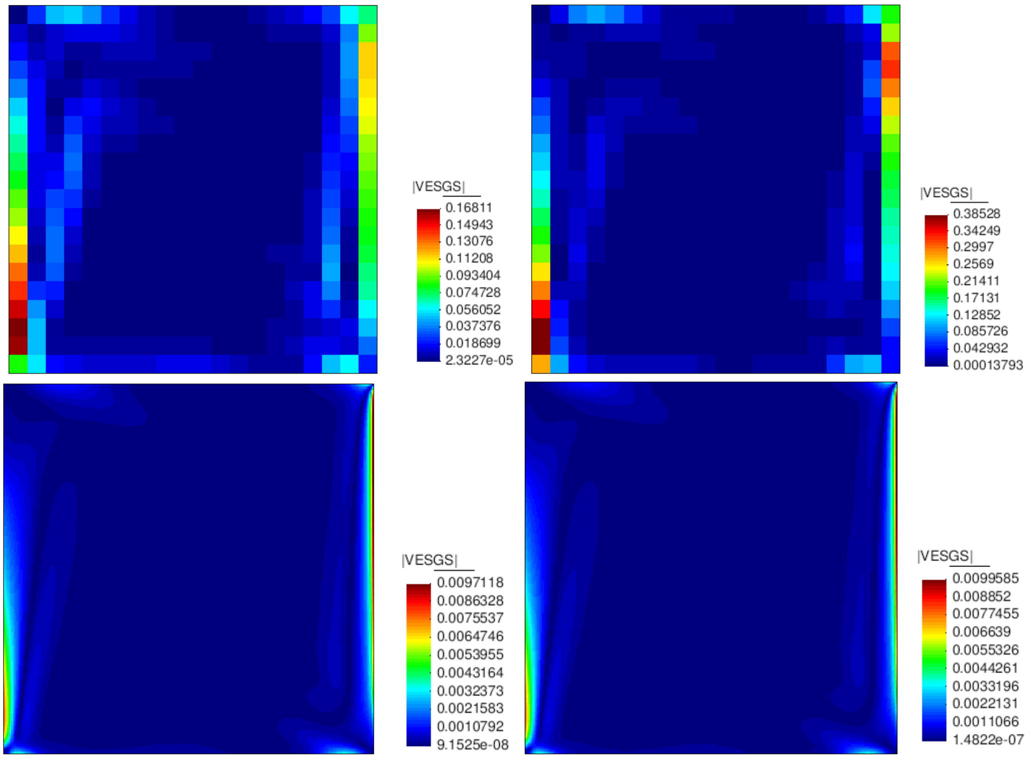

Figure 3.7: Velocity subscales norm obtained using the DSS (left) and the LinSGS (right) method in a 20×20 (top) and a 240×240 mesh (bottom)

We only show the velocity subscale convergence for simplicity, because the temperature subscale convergence has the same shape. It is observed that "Picard Gauss Seidel" converges faster than the original Picard method. The Newton-Raphson segregated method presents much faster convergence than Picard's methods. The Newton-Raphson monolithic method converges very slowly for some integration points in the first iterations and then converges much faster (quadratically) than all the other linearization methods, which only converge linearly, as expected.

The next test consists of taking the same initial conditions as in the first test, but duplicating the gravity force, (i.e. $\mathrm{Ra} = 2 \cdot 10^6$). The time step is set to $\delta t = 55\delta t_c$. In Fig. 3.8 (right) the convergence of the subgrid equations using the different linearization methods is compared. The most remarkable result is that only the full Newton-Raphson scheme achieves convergence at all integration points, in our case corresponding to a Gauss-Legendre quadrature. From a total of 1600 of such integration points (four per element) the Newton-Raphson segregated scheme does not achieve convergence at 4 of them, the Picard method with a Gauss-Seidel-type coupling at 16 and the original Picard method at 34. The conclusion is that the full Newton-Raphson scheme is the most robust, but sometimes needs more iterations to achieve convergence.

It was observed in practice that if the convergence of the subgrid scales is not achieved at only one integration point, then the finite element solution gets strongly affected. If the subscales are not well converged then the convergence of the finite element solutions gets strongly

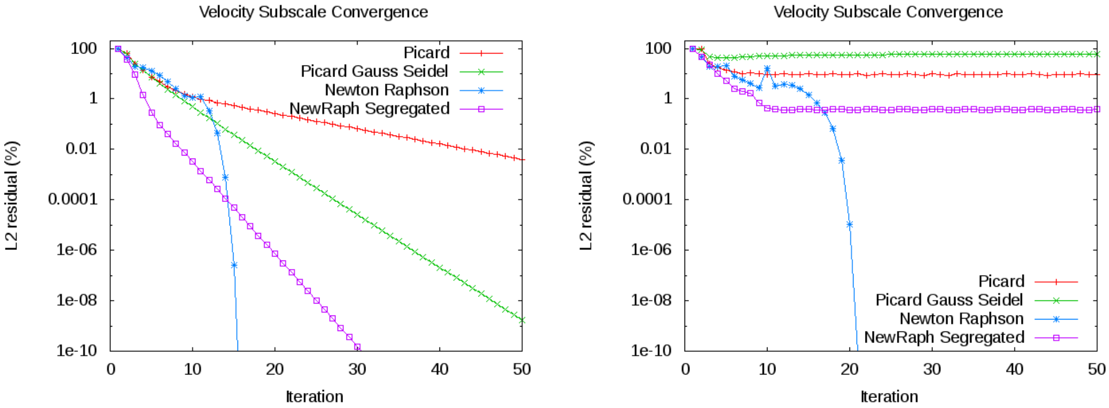

Figure 3.8: Subscale convergence history. Comparisons of Picard and Newton-Raphson strategies. $\mathrm{Ra} = 10^6$(left). $\mathrm{Ra} = 2 \cdot 10^6$ (right).

deteriorated, a fact already observed in [47]. When using the Newton-Raphson monolithic scheme we have always achieved convergence.

Convergence of the solution when using quadratic and cubic elements

We present in this subsection a study on the convergence of the solution as the mesh is refined for DSS, OSS and SUPG methods, when using elements of first, second and third order. The classical SUPG method [11] is idetical to ASGS method when using linear elements. We compare the accuracy of the different stabilization methods using structured and non structured meshes of quadratic and cubic elements P_2, Q_2, P_3 and Q_3. The L_2-norm error is computed comparing the numerical solution against a reference solution, obtained using a much finer mesh of Q_3 elements.

As shown in Fig 3.2 more accurate solutions are obtained when using nonlinear and dynamic subscales (DSS and OSS), than when solving with SUPG method. However, all methods present optimal convergence, unless OSS method that was shown to be superconverget for temperature. Convergence using OSS is superconvergent.

In Fig. 3.9 the $h-$convergence of L_2- error for velocity and temperature using quadratic and biquadratic elements P_2, Q_2 is shown. The same accuracy is observed when using different methods SUPG, DSS and OSS. Only a small gain in accuracy is observed for temperature for DSS and OSS methods.

In Fig. 3.10 the $h-$convergence of L_2-error for velocity and temperature using cubic and bicubic elements P_3 and Q_3 is shown. In this figure we observe optimal convergence with slope 4 for all stabilization methods. The gain in accuracy when using nonlinear DSS and OSS methods is neglible for the velocity, and very small for temperature.

It is concluded that the use of nonlinear stabilization methods lead to an important gain in accuracy of the numerical solution when using linear elements. However, this gain is neglible when using quadratic and cubic elements for the present stationary problem.

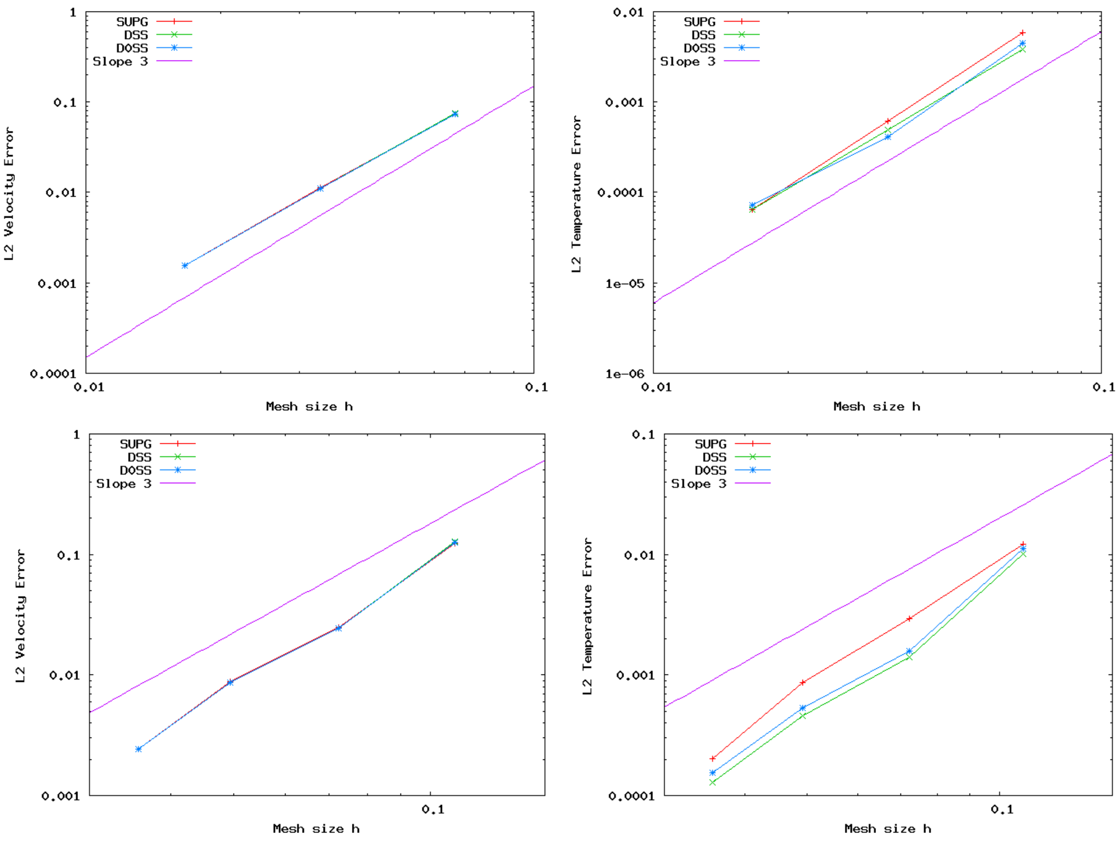

Figure 3.9: $L^2(\Omega)$ error of the solutions obtained using different methods against mesh size h over Q_2 (top) and P_2 elements (bottom) .

3.8.2 Transient injection flow at low Mach regime

This flow example was recently proposed in [6], and also considered in [40]. The problem domain is $\Omega = [-L/2, L/2] \times [0, H]$, where $L = 3$ m and $H = 7$ m. The initial values are $T_0 = 300$ K and $p_0^{\text{th}} = 10^5$ Pa resulting in an initial density of $1.161\ \frac{\text{kg}}{\text{m}^3}$. Furthermore $\mu = 0.005\ \frac{\text{kg}}{\text{m s}}$ and $\text{Pr} = 0.71$ are taken. Zero Dirichlet boundary conditions for the velocity are assumed on all boundaries, except for a small hole in the bottom wall at $[-l/2, l/2]$ where $l = 0.2$ m. Through this hole fluid is injected subject to a parabolic inflow profile $\boldsymbol{u}_d = (0, 2.5830\,(1.0 - 100x^2))$ m/s. The temperature of the injected fluid is $T_D = 600$ K. Aside from this, adiabatic boundary conditions are prescribed on all boundaries. We consider a gravity $\boldsymbol{g} = (0, -9.81)$ m/s^2.

The domain is discretized with 60×60 elements, and the time step size is chosen to be $\delta t = 0.06$ s. The computation is advanced until $t_{\text{end}} = 6.0$ s. The second order time integration scheme BDF2 was used.

The results obtained with our stabilization method using dynamic subscales (DSS) and orthogonal dynamic subscales (OSS) are compared to those obtained using the ASGS method and a reference solution obtained using a mesh of 180×180 uniform elements and the ASGS method. Temperature contours at $t = 5.1$ s and $t = t_{\text{end}} = 6.0$ s are shown in Fig. 3.11, showing that the jet has just impacted the top wall at the end of the simulation. Cuts of temperature

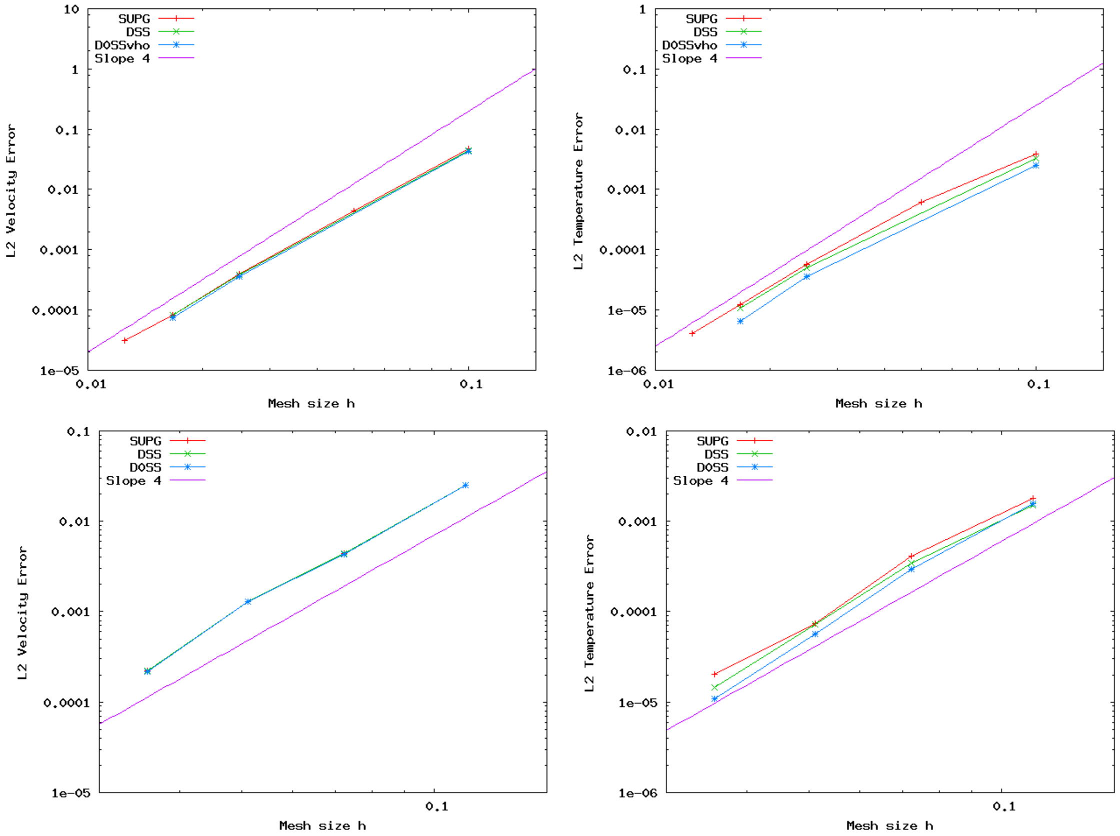

Figure 3.10: $L^2(\Omega)$ error of the solutions obtained using different methods against mesh size h over Q_3 (top) and P_3 elements (bottom) .

and x-velocity fields at $y = 5.6$ m and $x = 0.2$ m when $t = 6.0$ s are depicted in Fig. 3.12. As in the previous example, a gain in accuracy is observed when the method of dynamic and nonlinear subscales is used, specially when using orthogonal subscales. The obtained temperature distribution over $x = 0.2$ m is very different when $y \to 0$, close to the walls. This difference is due to the artificial conduction introduced by the method, which is greater for SUPG method, lower for DSS method, and much lower when using OSS method. This last method seems to be infra-diffusive close to the walls. Time evolutions of thermodynamic pressure, velocities and temperature at point $(0.4, 4.0)$ m are compared in Fig. 3.13. This figure shows a higher temporal accuracy of the scheme when transient nonlinear subscales are used, specially when they are orthogonal (OSS). It is observed in Fig. 3.13 that temperature and velocities evolution curves are *advanced in time* when using ASGS method, arriving earlier the information to a given point. This behaviour is due to an excessive artificial dissipation of ASGS method. From this reasoning it can be concluded that DSS method is less dissipative than ASGS, and OSS method introduces still less artificial diffusivity. Thermodynamic pressure evolution presents much higher accuracy when using DSS and OSS method. This is due to global energy conservation statement (3.42), where the conserved internal energy depends only on the thermodynamic pressure p^{th}. As the flow is closed the thermodynamic pressure evolution has been determined using global mass conservation equation (3.37).

Time evolution of the velocity and temperature subscales when using the DSS method are

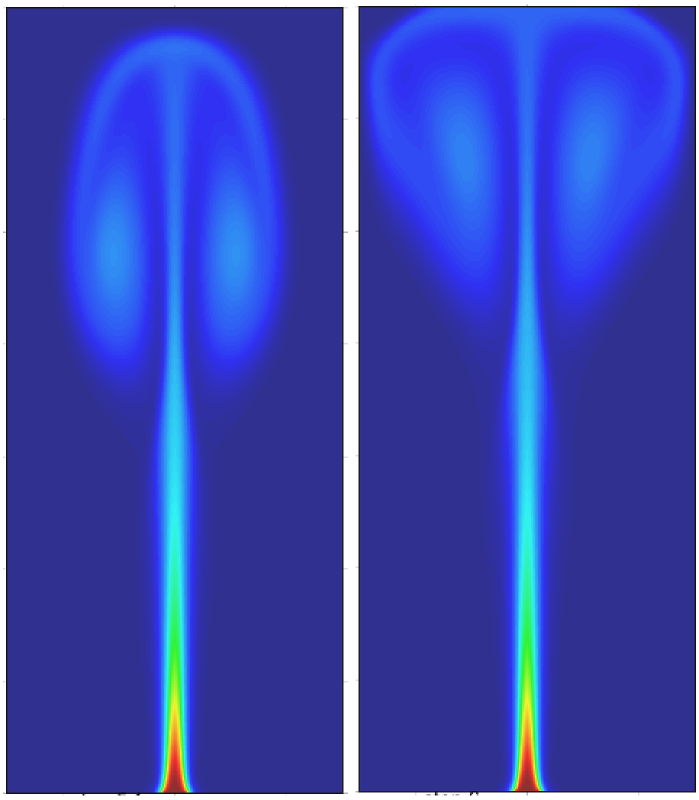

Figure 3.11: Snapshot of temperature contourn at $t = 5.1$ (left) and $t = t_{\text{end}} = 6.0s$ (right).

depicted in Fig. 3.14 at point $(0.4, 4.0)$ m . Although the relation between the subgrid scale and the finite element component is less than 0.5% for velocity and 0.1% for temperature, a significant improvement of the solution has been obtained, as observed in Figs. 3.12 and 3.13.

It is important to remark that the use of nonlinear subscales results in an increase in the cost of the solution of the nonlinear problem. The required number of nonlinear iterations increases a 25% with respect to the ASGS method. This is the price to be paid for the gain in accuracy.

The subscale equations were solved using the Newton-Raphson scheme. Convergence has been achieved at all integration points, needing at most four nonlinear iterations.

Compuational efficiency and convergence of the solution using linear, quadratic and cubic elements

In this subsection it will be compared the cpu-time against L_2-error when using elements of different order, and against SUPG stabilization method. As it will be seen, the solution for this transient problem is not regular enough to achieve optimal convergence, due to the Dirichlet-Newmann transition on temperature boundary condition at points $(\pm l/2, 0)$. Therefore no gain in convergence rate is expected when solving this problem with higher order elements, this convergence behavior puts higher order elements in disadvantage to be computational efficient compared to linear elements. Non regular solutions are very common in fully compressible flows at Mach number $M > 0.7$, where is usual the presence of shock discontinuities, for example in flows around airfoils. These shock discontinuities prevents higher order convergence when using higher order elements. Even in this unfavorable case the use of higher order ele-

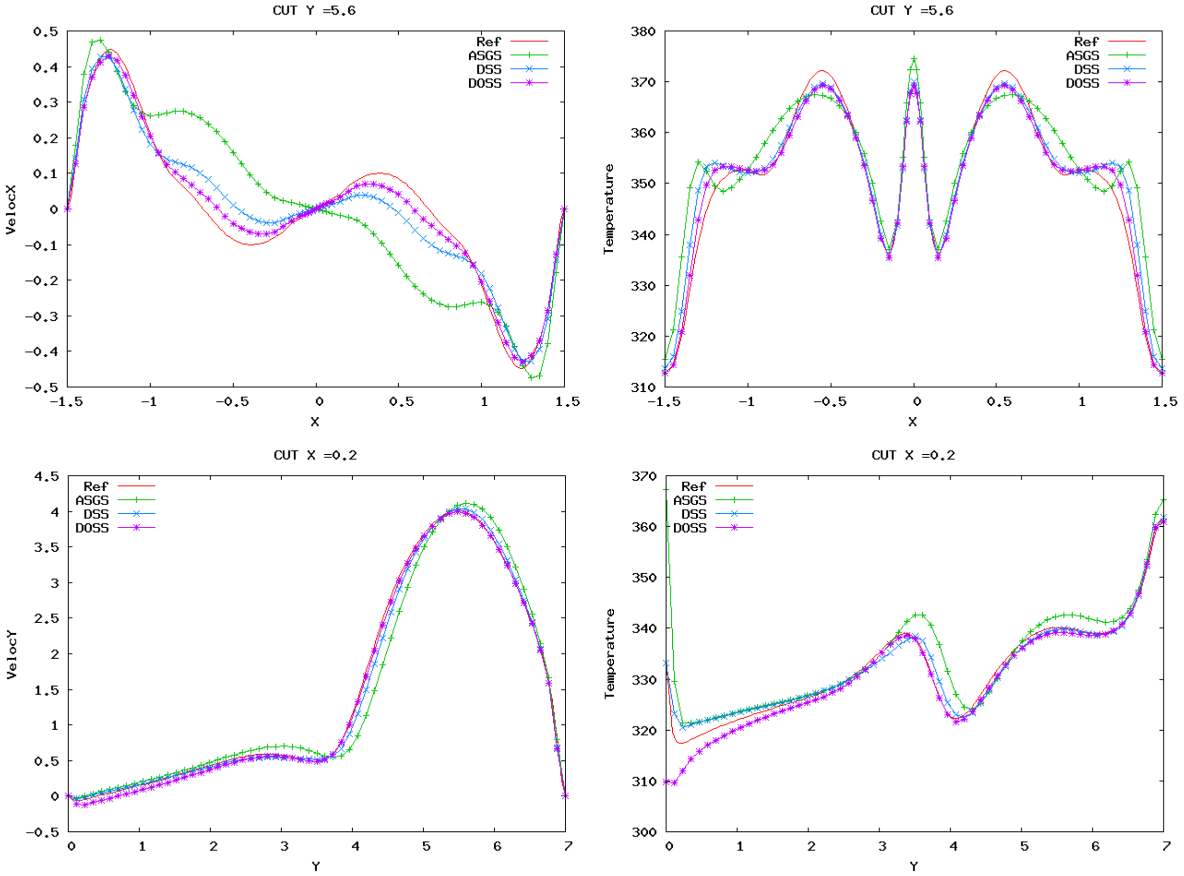

Figure 3.12: Cuts of the solution at $y = 5.6$ m and $x = 0.2$ m when $t = 6.0$ s for different stabilization methods against the reference solution.

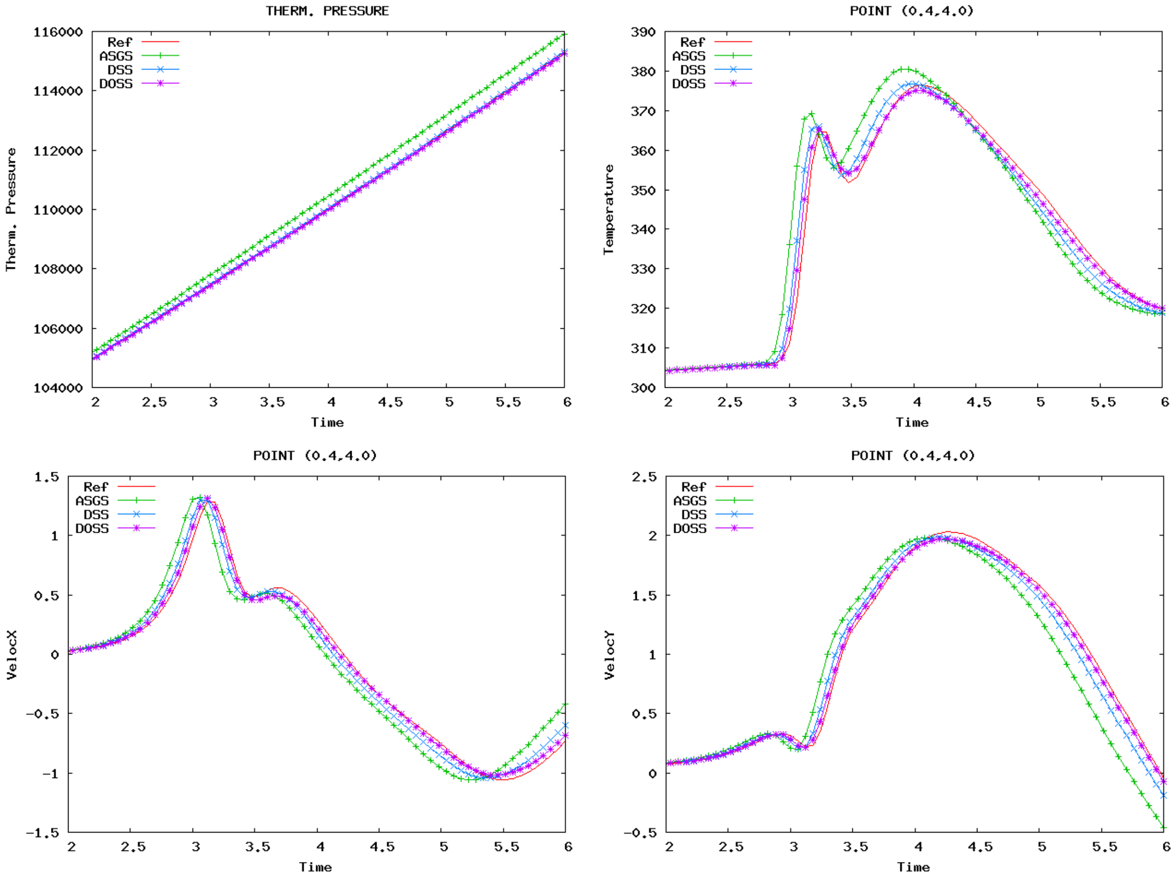

Figure 3.13: Point evolution of the unknowns when using the ASGS, the DSS and the OSS stabilization methods against the reference solution.

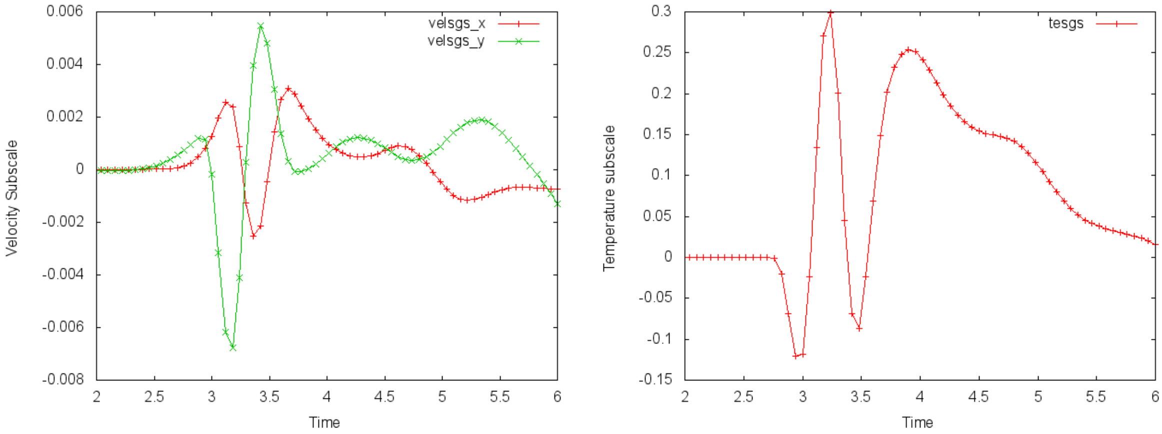

Figure 3.14: Point evolution of the subgrid scale velocity (left) and temperature (right) at point $(0.4, 4.0)$ m. when using the DSS method

ments can lead to efficient than the use of linear ones, due to the higher accuracy and better geometry representation.

The problem has been solved using bilinear, biquadratic and bicubic elements Q_1, Q_2, Q_3. Now, the reference solution was obtained using a much finer grid using bi-cubic elements Q_3. The time step Δt was choosen to be short enough to introduce an error 10 times smaller than the spatial error in all examples.

We have computed de $L_2(\Omega)$-norm of the error at time $t = t_{\text{end}}$ (with respect to the reference solution) as a function of the mesh size h. Supposing that the maximum error of the $L_2(\Omega)$-norm is produced at $t = t_{\text{end}}$, this norm approximates the $L^\infty(0, T; L_2(\Omega))$-norm of the error.

In Figs. 3.15, 3.16 and 3.17 the $L_2(\Omega)$-norm of the error (with respect to the reference solution) as a function of the mesh size h is shown.

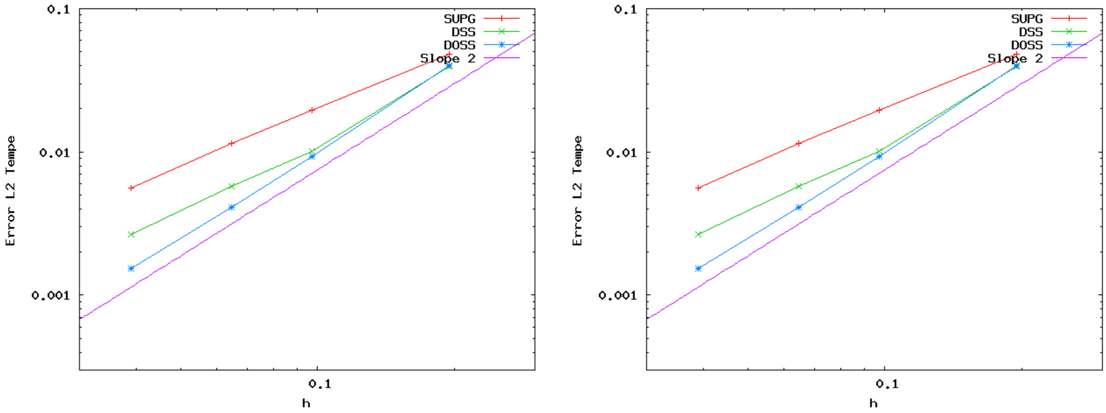

Figure 3.15: $L^2(\Omega)$ error of the solutions obtained using different methods against mesh size h over Q_1 elements .

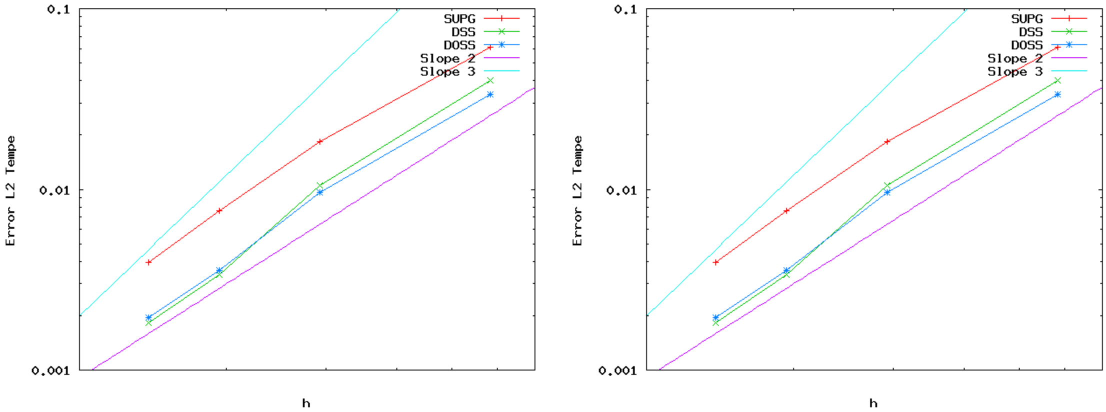

Figure 3.16: $L^2(\Omega)$ error of the solutions obtained using different methods against mesh size h over Q_2 elements .

It is observed that when solving with linear elements the convergence is suboptimal suboptimal for SUPG and DSS methods. However, second order optimal convergence is achieved when solving with the OSS method. When solving with higher order elements, suboptimal

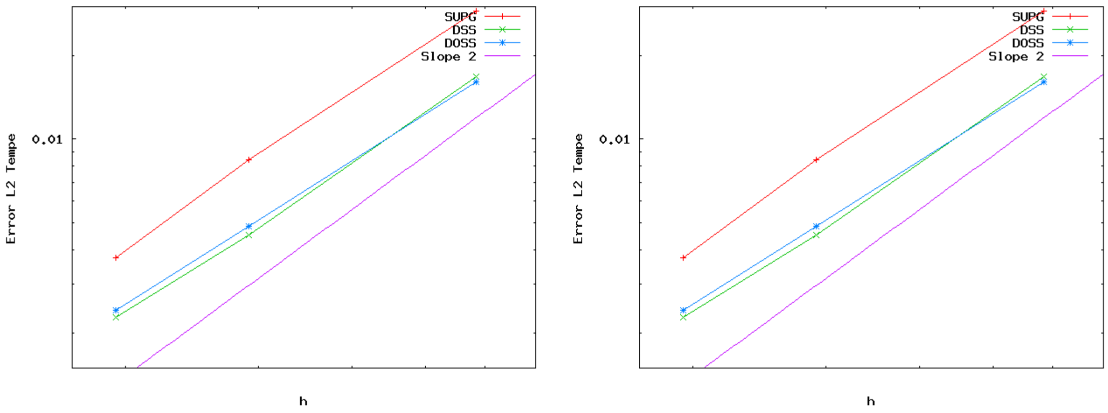

Figure 3.17: $L^2(\Omega)$ error of the solutions obtained using different methods against mesh size h over Q_3 elements .

second order h- convergence is achieved using all methods. Due to the optimal convergence of OSS method when using linear elements, we believe that the continuous solution $\boldsymbol{u}$ belongs to the space $\boldsymbol{u} \in \boldsymbol{H}^2(\Omega)$. As suboptimal convergence is obtained using quadratic elements we believe $\boldsymbol{u} \notin \boldsymbol{H}^3(\Omega)$, due to the Dirichlet- Neumann transition of temperature boundary condition at points $(\pm l/2, 0)$.

It is observed in Figs. 3.15, 3.16 and 3.17 that when using DSS and OSS stabilization methods lower L_2-errors are obtained than when using SUPG method, over the same mesh. Then, the use of nonlinear stabilization methods improve the accuracy of the numerical solution for this transient problem over the same mesh. In order to take into account the additional cpu-cost of computing the subscales, the L_2 error against the required cpu-time for the different stabilization methods is shown in Figs. 3.18, 3.19 and 3.20 when using Q_1, Q_2 and Q_3 elements respectively. It is observed in Fig. 3.18 that when using linear elements the most accurate solution is obtained using OSS method for a fixed cpu time, being the most computationally efficient stabilizing method. When using linear elements the less efficient method is SUPG . When solving using quadratic and cubic elements the most computationally efficient method is DSS. Although more accurate results are obtained with the orthogonal subscale method than using SUPG method over the same mesh, it is not more efficient than SUPG method when using higher order elements. When solving with OSS method, the projection P_h of the residual can be approximated by a lumped diagonal mass matrix when linear elements are used, leading to a save of computational time. Nevertheless, when using higher order elements the projection must be calculated using a consistent mass matrix, and a system of equations needs to be solved, making the projection more expensive, and the OSS method less efficient. Moreover, when using linear elements more accurate results are obtained when approximating the projection P_h with the lumped matrix, compared to the use of a consistent matrix.

It is known that fewer degrees of freedom are required for higher-order methods than for linear elements to reach the same level of accuracy. Due to the increase of computational complexity when using higher order methods, it is not known if it will be spent less cpu-time to achieve the same level of accuracy using higher order elements. In Fig. 3.21 the $L2$-error vs. cpu time using different stabilization methods over linear, quadratic and cubic elements is shown. It is observed that bi-quadratic elements Q_2 are the most efficient, needing less cpu time to reach a given level of accuracy. The use of second order elements is more efficient than linears although the same convergence rate is observed.

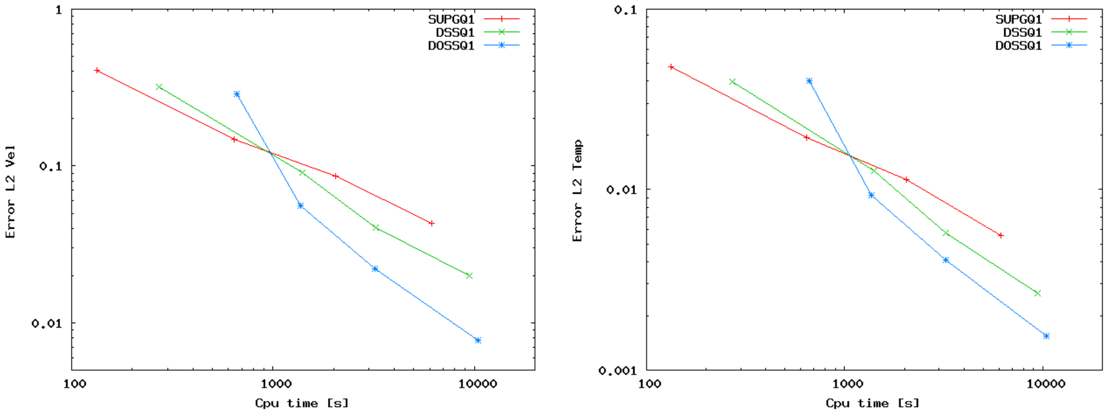

Figure 3.18: $L^2(\Omega)$ error of the solutions using different methods over Q_1 elements against required cpu time

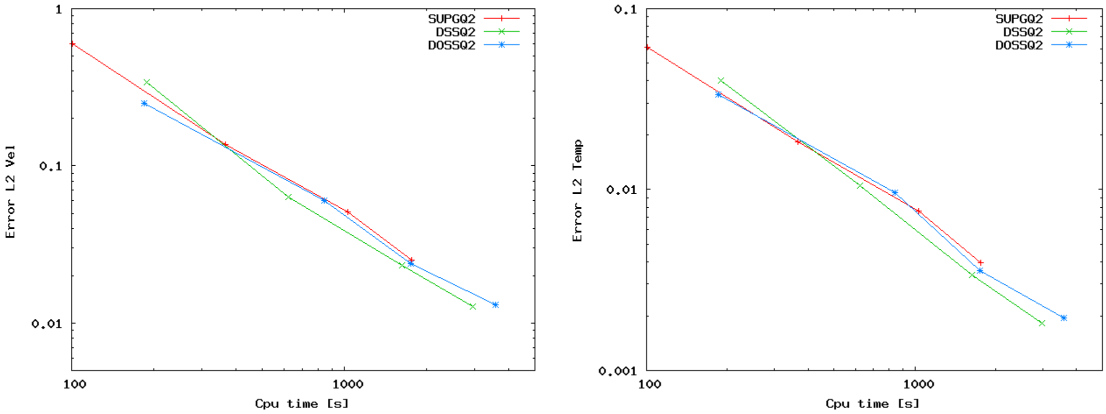

Figure 3.19: $L^2(\Omega)$ error of the solutions using different methods over Q_2 elements against required cpu time.

3.8.3 Fire in a 3D room with an open door

The third numerical test is a fire compartment similar to that considered in [65]. The problem domain is $\Omega = [0, L] \times [0, L] \times [0, H]$ where $L = 2.8$ m and $H = 2.18$ m. The compartment has an open door on the side wall of the room ($x = L$) whose dimension is 0.7×1.853 m^2. The fire is modeled by a uniform heat source of 5 kW, located at the center of the room just over the floor, with dimensions $0.84 \times 0.84 \times 0.218$ m^3. Adiabatic boundary conditions are imposed on all the walls. Non slip boundary conditions for velocity are imposed on all the boundaries except the door, where atmospheric boundary condition is imposed, that is, a traction $\boldsymbol{t}_n = (-\rho|\boldsymbol{g}|z, 0, 0)$. As the flow is open $((\Gamma_N^{\boldsymbol{u}} \neq \emptyset))$, the thermodynamic pressure is set constant in time to $p^{\text{th}} = 101325$ Pa. The initial temperature and velocity values are

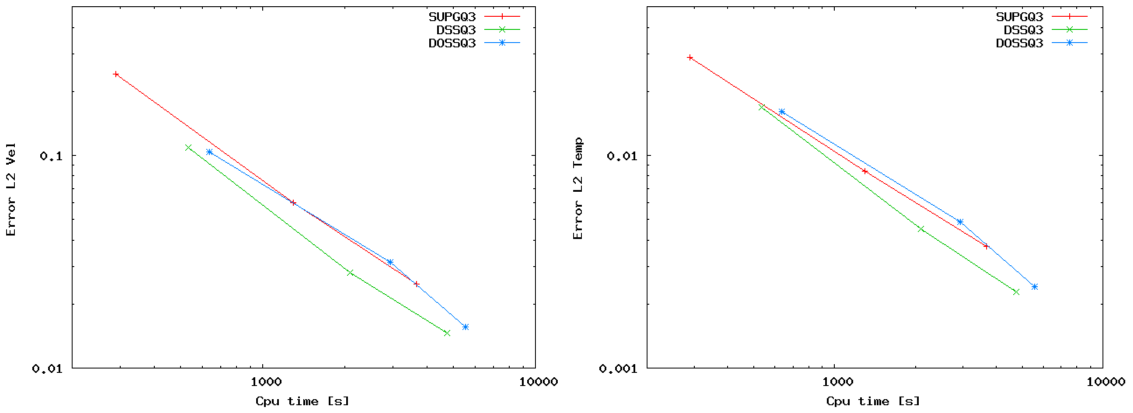

Figure 3.20: $L^2(\Omega)$ error of the solutions using different methods over Q_3 elements against required cpu time.

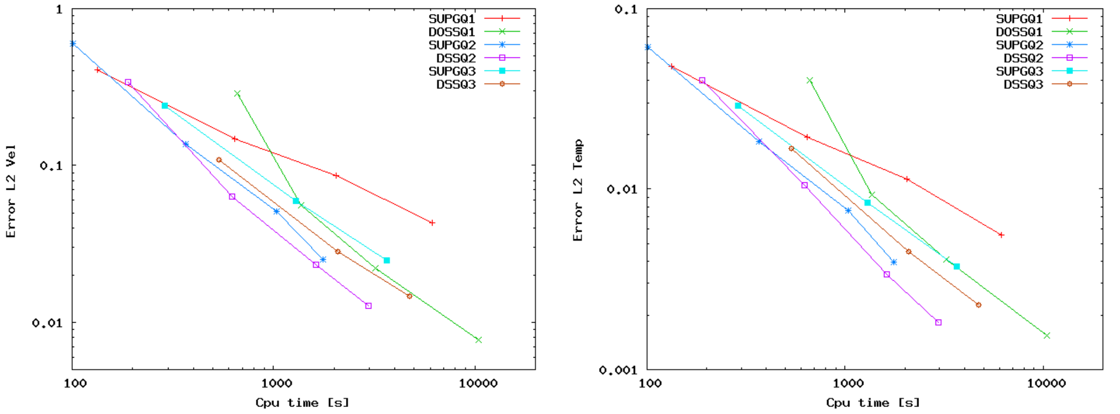

Figure 3.21: $L^2(\Omega)$ error of the solutions using different methods and different elements against required cpu time.

$T_0 = 300$ K and $\boldsymbol{u}_0 = \mathbf{0}$ over all the domain Ω. Furthermore, the viscosity is $\mu = 0.0094\ \frac{\text{kg}}{\text{m s}}$ and $\text{Pr} = 0.71$ m. The gravity is set to $\boldsymbol{g} = (0, 0, -9.8)$ m/s^2. A scheme of the room domain is depicted in Fig. 3.22. The compartment is meshed using grids of $20 \times 20 \times 20$ and $40 \times 40 \times 40$ uniform elements, stabilizing with the dynamic nonlinear subscale method (DSS) presented in this chapter and with the ASGS method. We compare the results against a reference solution obtained using the ASGS method over a fine mesh of $80 \times 80 \times 80$ uniform elements. We solved the problem using two different time steps of $\delta t = 0.25$ s and $\delta t = 1.0$ s. The major difference between the solutions using those different time steps is in the initial transient. After some time the solutions are very similar. The computation is advanced until $t_{\text{end}} = 100.0$ s using the second order time integration scheme BDF2. The tolerance for the nonlinear iterations was set to $5 \cdot 10^{-4}$ in the relative norm of the difference between two iterates.

In Fig. 3.23 the temperature and vertical velocity distributions along the z direction using the DSS and ASGS methods at $t = t_{\text{end}}$ are shown, whereas in Fig. 3.24 the temperature and vertical velocity distributions along the x direction at $t = t_{\text{end}}$ are shown. In all those figures it is clearly observed the greater similarity of the results respect to the reference solution when using the DSS method.

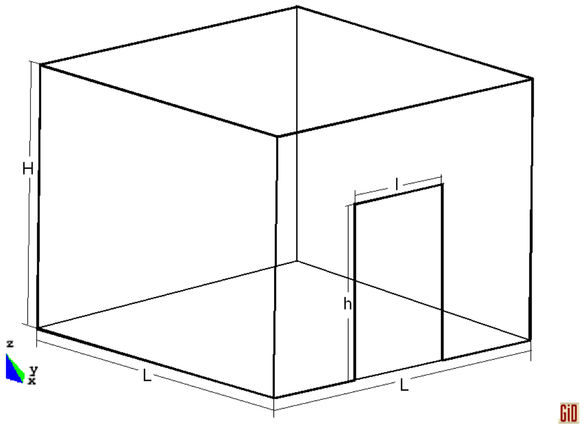

Figure 3.22: Three dimensional domain of the room with an open door

The time evolution of temperature and vertical velocity (along the z direction) at point $(1.55, 1.4, 0.55)$ m are compared in Fig. 3.25. It is observed that over the $20 \times 20 \times 20$ grid using the ASGS method the solution differs much more from the reference solution than when using the DSS method. The same can be said over the $40 \times 40 \times 40$ grid.

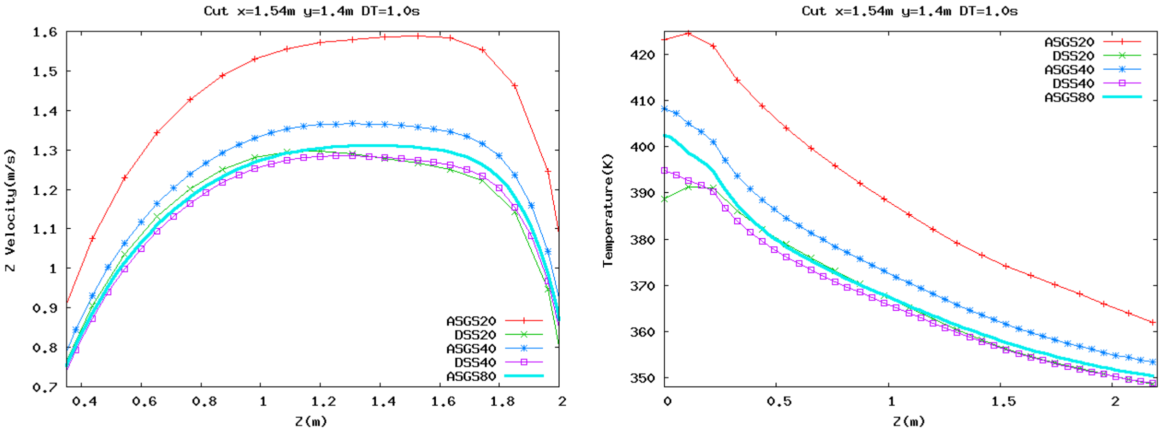

Figure 3.23: Temperature and vertical velocity distributions along z direction

The total number of nonlinear iterations needed to solve the problem (i.e. the sum of the nonlinear iterations performed in all time steps) and the total cpu time are indicated in Tables 3.1 and 3.2 for time steps $\delta t = 0.25$ s and $\delta t = 1.0$ s respectively. The cpu time spent for assembly (which includes numerical integration and solution of the subscale problem, i.e. operations involving a loop over integration points, indicated in line 10 of Algorithm 1) and cpu time spent in (linear) solver procedures are also indicated. The mean cpu times spent in nonlinear iterations are also indicated.

The total number of nonlinear iterations do not differ more than 5% between both methods. The extra cost to evaluate the subgrid scale computation is about 15% of the total element calculations (including all operations at numerical integration points and assembly). However, we did not try to make these calculations as efficient as possible.

The subscale equations were solved using the Newton-Raphson scheme, convergence was

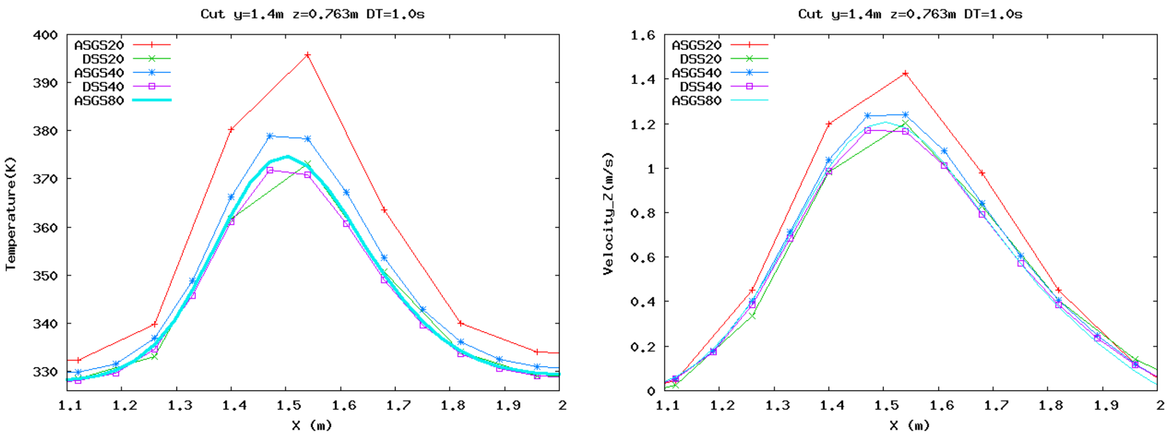

Figure 3.24: Temperature and vertical velocity distributions along x direction

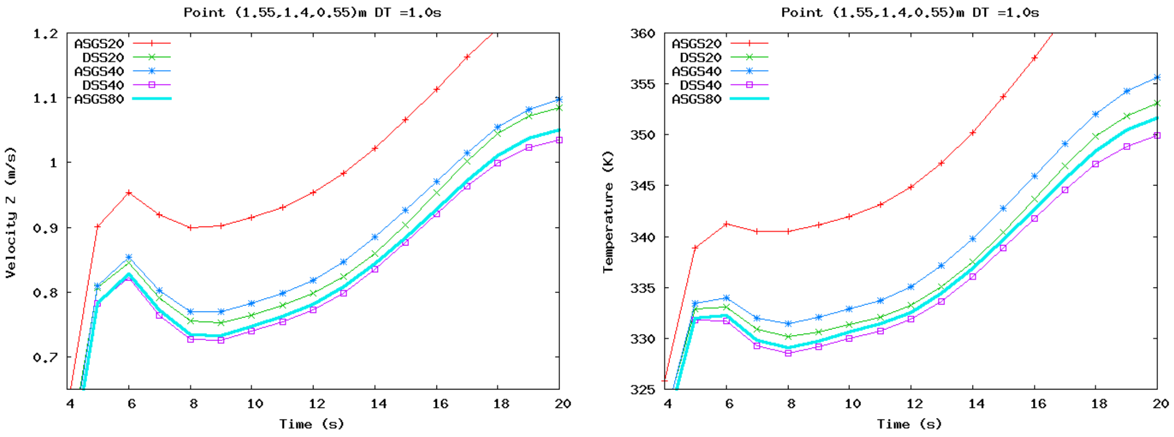

Figure 3.25: Time evolution of temperature and vertical velocity (i.e. u_z) in point $(1.55, 1.4, 0.55)$m

achieved at all integration points needing at most three nonlinear iterations.

3.8.4 Periodic flow over a heated cylinder

This example consists on solving a dynamic and periodic flow over a hot cylinder, with the effect of curved geometries that should favor the use of higher order elements. The cylinder walls are maintained at constant and uniform temperature T_w. The problem domain is $\Omega = [0, L] \times [-H/2, H/2]$ where $L = 7$ m and $H = 2.4$ m. The cylinder has a diameter $D = 0.2$ m centered at point $(0.8, 0)$ m. The flow is injected from the left wall with uniform velocity $\boldsymbol{u}_{in} = (1, 0)$ m/s and temperature $T_{in} = 300$ K. Over the adiabatic upper and lower walls symmetric boundary conditions are imposed, with vertical component of velocity and the x-component of the stress are imposed to zero $v_y = 0$, $t_{nx} = 0$. Over the cylinder surface no slip velocity is imposed and temperature is fixed to $T_w = 600$ K. Over the outflow wall $(x = L)$ zero stress $\boldsymbol{t}_n = 0$ and adiabatic boundary conditions are imposed. The Reynolds number of the problem is $Re = \frac{\rho_{in}|\boldsymbol{u}_{in}|D}{\mu} = 400$. The Prandtl number of the fluid is $Pr = \frac{c_p \mu}{k} = 0.71$.

A snapshot of the temperature distribution is shown in Fig. 3.26, where can be observed

$\delta t = 1.0$ s	# iterations	cpu time(s)	cpu assem(s)	cpu solv(s)	cpu assem/#iter	cpu solv/#iter
ASGS20	574	2559	857	1699	1.49	2.96
DSS20	573	2870	1019	1846	1.78	3.22
ASGS40	600	25670	6112	19530	10.19	32.55
DSS40	573	25976	6823	19116	11.91	33.36

Table 3.1: Comparison of the required cpu time for the different methods over different grids using $\delta t = 1.0$ s.

$\delta t = 0.25$ s	# iterations	cpu time(s)	cpu assem(s)	cpu solv(s)	cpu assem/#iter	cpu solv/#iter
ASGS20	1275	5216	1921	3285	1.51	2.57
DSS20	1307	6129	2296	3819	1.75	2.92
ASGS40	1298	43388	12561	30763	9.68	23.7
DSS40	1301	47608	14705	32817	11.3	25.2

Table 3.2: Comparison of the required cpu time for the different methods over different grids using $\delta t = 0.25$ s

the Von-Karman vortex shedding. For this problem the continuous solution is periodic in time. Time evolution of lift and drag coefficients and Nusselt number are shown in Fig. 3.27. These coefficients are defined in terms of net force and heat flux as follows

$$C_L = \frac{F_y}{0.5\rho_{in}|\boldsymbol{U}_{in}|} \tag{3.66}$$

$$C_D = -\frac{F_x}{0.5\rho_{in}|\boldsymbol{U}_{in}|} \tag{3.67}$$

$$Nu = \frac{\pi D Q}{k\,(T_w - T_{in})} = \frac{\pi D \int \boldsymbol{\nabla} T \cdot \boldsymbol{n} d\Gamma}{T_w - T_{in}} \tag{3.68}$$

where $\boldsymbol{F}$ and Q are respectively the net force and the net heat flux over the cylinder, defined as

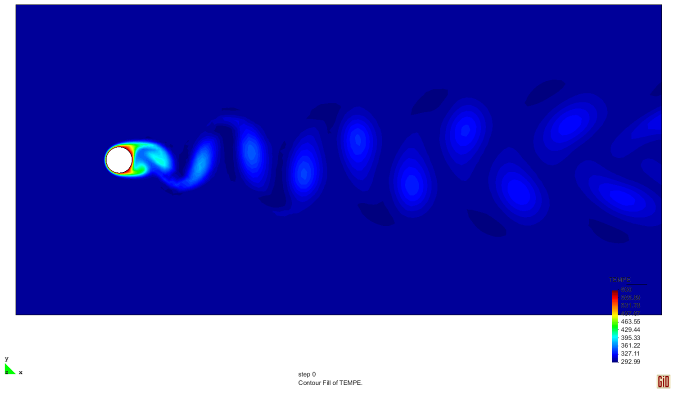

Figure 3.26: Temperature distribution around the hot cylinder.

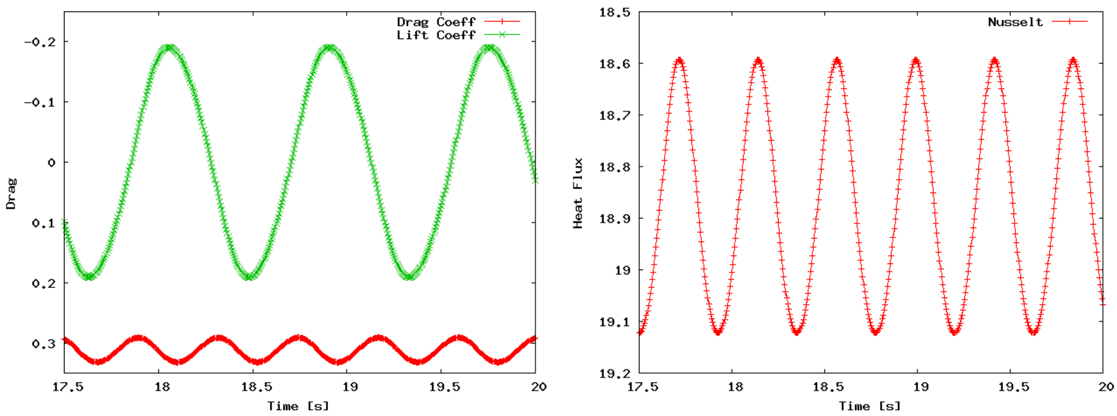

Figure 3.27: Peridic evolution of reference Drag and Lift coefficients (left) and Nusselt number (right).

$$\begin{aligned} \boldsymbol{F} &= \int_{\partial\Gamma_w} \left(-2\mu\boldsymbol{\varepsilon}'\left(\boldsymbol{u}\right) + p\boldsymbol{I}\right) \cdot \boldsymbol{n} d\Gamma \\ Q &= \int_{\partial\Gamma_w} k\boldsymbol{\nabla}T \cdot \boldsymbol{n} d\Gamma \end{aligned}$$

where $\partial\Gamma_w$ is the cylinder boundary. The net force and the heat flux over the cylinder are obtained variationally (as explained in Section 3.4 and [48]).

Numerical results obtained using unstructured meshes with linear, quadratic and cubic elements P_1, P_2 and P_3 will be compared. The time step is chosen to be small enough such temporal error is ten times lower than the spatial error. As a measure of the accuracy of the obtained solutions we will compare Drag, lift coefficients, and Nusselt number against reference values. This reference values are obtained using a symmetric and structured finer grid with cubic elements Q_3. The used time step to obtain the reference solution is also smaller.

The problem of comparing the net force over the cylinder is that the error is not a norm, and error compensation can occur. It is not possible to prove convergence laws for this kind of measures.

For a periodic function f of period T, the mean and fluctuating values of f are defined as

$$\bar{f} = \frac{1}{T}\int_t^{t+T} f\left(t\right) dt$$

$$f_\sigma = \left(\frac{1}{T}\int_t^{t+T} \left(f\left(t\right) - \bar{f}\right)^2 dt\right)^{1/2}$$

The relative errors for the obtained mean and fluctuationg values for drag, lift and Nusselt coefficients in terms of mesh size h are shown in Figs. 3.28 - 3.30 for different element types. The curved geometry of the cylinder is better represented using higher order elements. Moreover, when using linear elements the cylinder boundary is modeled as a polygon, introducing numerical entropy in the solution [87]. We expect to obtain better results with quadratic and cubic elements due to the better geometry representation in addition to better solution interpolation.

It is observed in Fig 3.28 that using linear elements the mean and fluctuation values of drag coefficient are better predicted using DSS method. Nevertheless, when using higher order

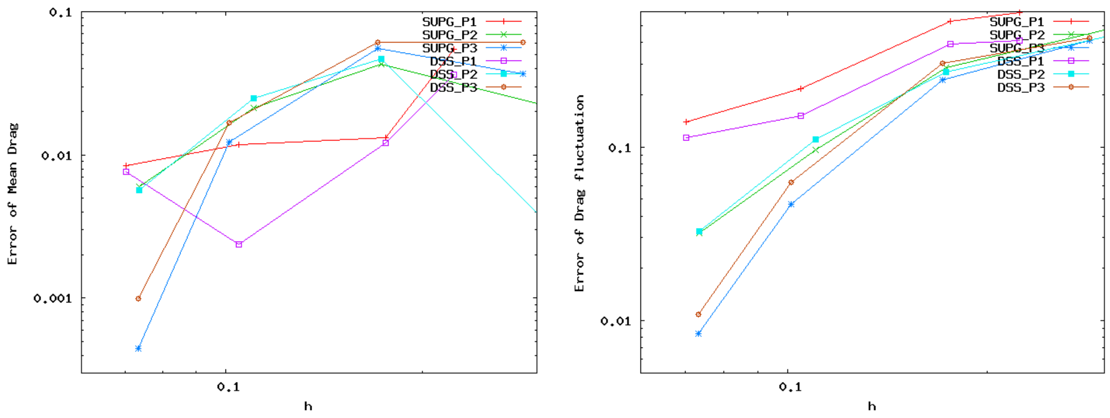

Figure 3.28: Relative error of mean (left) and fluctuating (right) values of Drag coefficient using DSS and SUPG stabilization methods, over P_1, P_2 and P_3 elements.

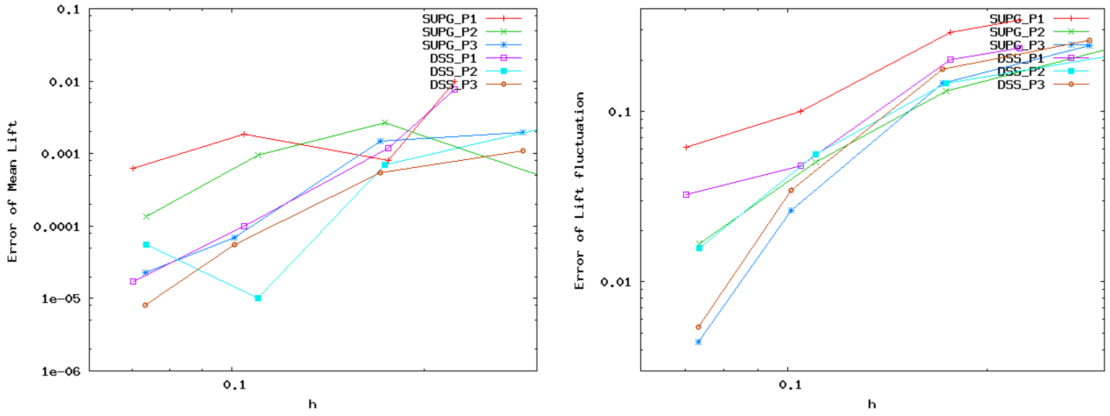

Figure 3.29: Relative error of mean (left) and fluctuating (right) values of Lift coefficient using DSS and SUPG stabilization methods, over P_1, P_2 and P_3 elements.

elements the obtained mean drag is more accurate using SUPG method. The mean drag and its fluctuation converge better as higher is the order of the element. The same behavior is observed for lift fluctuation and mean Nusselt number in Figs. 3.29 and 3.30. The better convergence behavior using higher order elements is not clearly observed for mean lift and Nusselt number fluctuation Figs. 3.29 and 3.30.

When using linear elements, deterioration of $h-$convergence is observed for finer meshes. We think this behavior is due to the error in geometry representation, that becomes dominant respect to the interpolation error for finer meshes.

Due to the symmetry of the problem in y direction, the real mean lift coefficient is zero. As the meshes are non symmetric the obtained mean lift coefficients are different from zero. It is observed in Fig. 3.29 that the obtained mean lift is always more accurate using DSS method, independently of the mesh size and the element order. Lift fluctuation is better predicted using DSS method only when linear elements are used. However, using quadratic elements SUPG and DSS method predict lift fluctuation with quite the same accuracy, and using cubic elements SUPG method gives better lift fluctuation values.

The mean Nusselt number is better predicted whith DSS method using different element

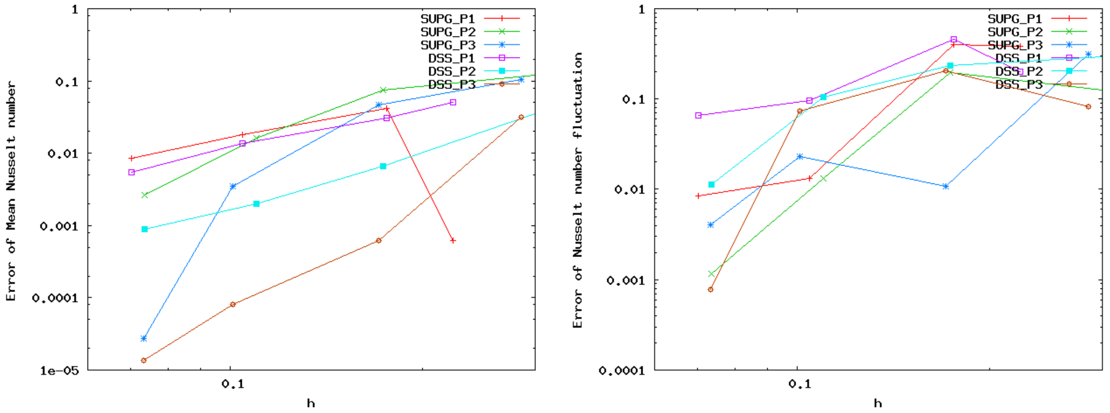

Figure 3.30: Relative error of mean (left) and fluctuating (right) values of Nusselt number using DSS and SUPG stabilization methods, over P_1, P_2 and P_3 elements.

orders. Nevertheless, Nusselt number fluctuation is better predicted using the SUPG method. Contrarily to conclusions of the other numerical examples, for this problem it cannot be concluded that the DSS method gives better results than the SUPG method over the same mesh.

To achieve a given convergence tolerance for the nonlinear iterations (loop starting at line 7 in Algorithm 1) more nonlinear iterations are needed using DSS than when using the SUPG method to achieve a given convergence tolerance. Then, over the same mesh DSS method is more cpu-time expensive, and then less computationally efficient.

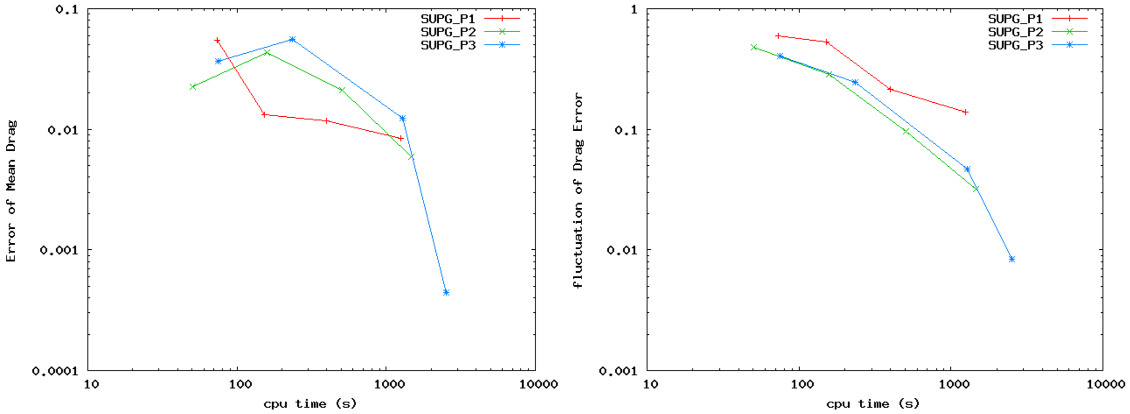

Figure 3.31: Relative error of mean (left) and fluctuating (right) values of Drag coefficient vs cpu time using SUPG, over P_1, P_2 and P_3 elements.

To evaluate the efficiency of the use of higher order methods, only solutions obtained with SUPG method will be considered. In Figs. 3.31, 3.32 and 3.33 are shown relative error of mean and fluctuating drag, lift and Nusselt coefficients against the cpu time. It is observed from these figures that second order method is the most efficient for almost all properties. The error of the mean lift coefficient is a measure of the $y-$symmetry in the discrete problems, being better predicted and more efficiently using cubic elements. This is due to better geometry representation using cubic elements. Depending on the required precision for the mean drag coefficient, less cpu time is needed using linear elements (stalled at error $= 1\%$). In case

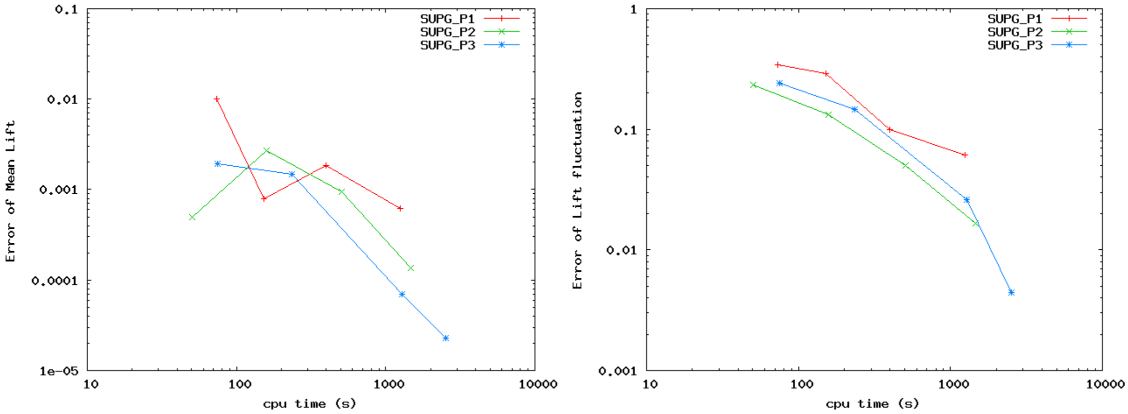

Figure 3.32: Relative error of mean (left) and fluctuating (right) values of Lift coefficient vs cpu time using SUPG, over P_1, P_2 and P_3 elements.

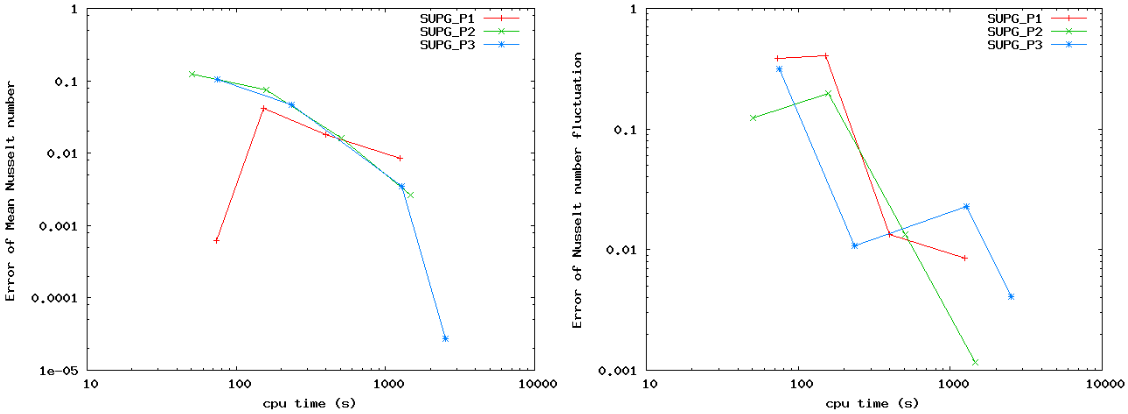

Figure 3.33: Relative error of mean (left) and fluctuating (right) values of Nusselt number vs cpu time using SUPG, over P_1, P_2 and P_3 elements.

drag needs to be determined with higher precisions, then higher order elements would be the most efficient choice for drag calculations. Heat amplitude presents a peculiar behaviour, and is difficult to reach any conclusion when using higher order elements.

3.9 Conclusions

In this chapter a finite element approximation of the low Mach number equations based on a splitting of the unknowns into finite element and unresolvable components has been developed. The main ingredients of the formulation are:

- To consider time dependent subscales.
- To keep the subscale components in all the nonlinear terms.

The effect of considering time dependent subscales is well known [27] and our experience with the low Mach number equations confirms the properties known for incompressible flows.

The effect of considering the splitting of the unknowns in all the terms (including the state equation) leads to a more accurate solution than classical stabilization methods and provides global mass, momentum and energy conservation when using equal interpolation spaces for the velocity, pressure and temperature equations. This improvement in the quality of the solution is quite remarkable in the interior of the computational domain, as we have shown in the numerical experiments, although it is not so important for boundary fluxes. This may be due to the poor approximation of the subscales close to boundaries, since boundary subgrid scales have been neglected.

We would like to stress, once again, that we keep the splitting of the unknowns in all terms *also in the subscale equations*, and we have numerically verified that this makes a substantial difference in the accuracy of the scheme. In other words, considering the scale splitting in the nonlinear terms in the finite element equation only results in a small improvement compared to that obtained with the full nonlinear scheme presented here. A detailed strategy for solving the nonlinear subscale problem has been also presented in Section 3.6. From numerical experiments it turns out that a fully coupled Newton Raphson is to be recommended.

This nonlinear and transient treatment of the subscales *also in the subscale equations* has a computational cost, in memory requirements and sometimes in the number of nonlinear iterations required to converge. Nevertheless, the extra amount of memory needed only grows linearly with the number of nodes (and will be usually dominated by the memory needed to solve the linear system).

The formulation intrinsically contains cross- and Reynolds- stress terms, and presents an open door to turbulence modeling. The present method remains unchanged irrespective of whether laminar, transitional and turbulent situations are present. Nevertheless, the adequacy of the present method for turbulent flows situations will be investigated in chapter 4.

It has been compared the computational efficiency of the different stabilization methods over elements of different order. In the first three numerical examples the method introduced in this chapter has been computationally more efficient than the classical SUPG method. Although some conclusions were carried out for bidimensional examples, we believe that for three dimensional problems the gain in efficiency of the method would be even better when comparing against SUPG.

Optimal convergence has been shown for both stabilization methods for all element orders.

Due to the better h-convergence of higher order methods, it is well known the convenience of using higher order elements as the required solution is more accurate. Even for cases where the solution is not regular enough to achieve optimal convergence, the use of second or higher order elements can be more efficients than the use of linear ones. It has also been observed for the case of solution not regular enough, that only the OSS method converges optimally, and linear element using SUPG converge very poorly when adding more degrees of freedom. Non regular solutions are obtained in presence of shock discontinuities in fully compressible flows, preventing higher order convergence when using higher order methods. Even in this unfavorable case the use of higher order elements can be more convenient than the use of linear elements.

The dynamic and nonlinear subscale stabilization method leads to a more accurate solution than classical stabilization method over quadratic and cubic elements when using structured and uniform grids. When curved boundaries and periodic solution the use of the nonlinear stabilization method did not seem to give better results than the classical SUPG method.

Elements of second and third order were used only in two dimensional problems, being in general quadratic elements the most computationally efficient choice. We are planing to test in the future the efficiency of higher order elements in three dimensional and transient problems using the proposed nonlinear stabilization method.

Chapter 4

Nonlinear subgrid scale modeling of turbulent variable density flows

This chapter is an elaboration of the material in

M. Avila, J. Principe and R. Codina. Large eddy simulation of low Mach number flows using a dynamical and nonlinear finite element subgrid scale model. Submitted.

In this chapter we present results of the numerical simulation of the turbulent channel flow with large temperature differences using a variational multiscale finite element approximation of the low Mach number equations. We study the numerical solution dealing with thermal turbulence from a strictly numerical point of view, without the use of any turbulent model, studying the behavior of our numerical method as a physical model.

In this work the low speed channel flow with strong heat transfer in the normal direction is solved. The Reynolds number is 180 based on the channel half height and the mean friction velocity. The physical model is described by the low Mach number equations, which are obtained as a limit of the compressible Navier-Stokes equations in the small Mach number regime.

We use a stabilized finite element approximation based on the variational multiscale method, in which a decomposition of the approximating space into a coarse scale resolvable part and a fine scale subgrid part is performed. Modeling the subscale and taking its effect on the coarse scale problem into account results in a stable formulation. The quality of the final approximation (accuracy, efficiency as turbulent numerical model) depends on the particular subscale model.

The finite element formulation used in this chapter was presented in chapter 3, and some information is repeated here for completeness.

The distinctive features of the implemented approach are to consider the subscales as transient and to keep the scale splitting in all the nonlinear terms, allowing us to approach the problem of dealing with thermal turbulence from a strictly numerical point of view. The obtained numerical solutions are as accurate as those obtained in the literature using a LES model over the same grid. A careful analysis of the dissipative structure of the method is presented, showing the physical interpretation of the subscales method.

4.1 Introduction

Turbulent flows with heat transfer arise in industrial applications, including flows in heat exchangers, combustion systems, etc. In those applications involving considerable variation in fluid properties, design methods based on the assumption of constant properties, as the Boussinesq approximation, generally prove to be inadequate. The present chapter is concerned with turbulence at very low Mach number flow of an ideal gas subjected to significant density variation, which are described by the compressible Navier–Stokes equations in the low-Mach number limit.

Despite the difference in the treatment of the incompressibility, the low Mach number equations present the same mathematical structure as the incompressible Navier–Stokes equations, in the sense that the mechanical pressure is determined from the mass conservation constraint. Consequently the same type of numerical instabilities can be found, namely the problem of compatibility conditions between the velocity and pressure finite element spaces, and the instabilities due to convection dominated flows. These instabilities are avoided by the use of stabilization techniques. In the present work we use a stabilized formulation developed in the context of the variational multiscale (VMS) concept introduced by Hughes [49]. The formulation is based on dynamic and nonlinear subscales, considering the transient nonlinear nature of the problem, see [2]. The idea is to consider the subgrid scale time dependent and to consider its effect on all the nonlinear terms, resulting in extra terms in the final discrete scheme. Important improvements in the discrete formulation of the Navier-Stokes problem have been observed. From a theoretical point of view, the use of transient subgrid scales explains how the stabilization parameter should depend on the time step size and makes space and time discretization commutative. The tracking of the subscales along the nonlinear process provides global mass, momentum and energy conservation, and also more accuracy of the solution. From a practical point of view, the use of time dependent nonlinear subscales results in a more robust and more accurate method (an unusual combination) as shown by numerical experiments [19, 27, 2]. These developments also opened the door to the use of numerical techniques to cope with the potential instabilities and to model turbulence at the same time, as pointed out in [19, 27]. This is a natural step as turbulence is originated by the presence of the nonlinear convective terms, as it is well known. The idea of modeling turbulence using only numerical ingredients actually goes back at least to [8], and the possibility to use the VMS framework for that purpose to [19]. It was fully developed for incompressible flows in [5] and for low Mach number flows recently in [39], where quantitative comparisons against direct numerical simulations are presented.

Large-eddy simulation (LES) of turbulent flows aims at resolving the larger flow structures and modeling the effect of the smaller ones. The variational multiscale approach to LES (VMLES) further separates the scales into resolved scales and unresolved scales or (subscales). The other distinguishing feature of VMLES compared to the traditional LES approach is the use of a variational projection instead of a filter for scale separation. A shortcoming of a LES approach is that it limits convergence rate, due to artificial viscosity effects ($O(h^{4/3})$ in the case of Smagorinsky-type models). This limitation is circumvented using the VMLES point of view.

A careful analysis of the dissipative structure of the variational multiscale method with nonlinear time dependent subscales was presented in [41, 81] for incompressible flows, giving physical interpretation to the method. In the present work the dissipative structure of the variational multiscale method applied to Low Mach Compressible flow equations is analyzed.

The chapter is organized as follows. In Section 4.2, the Low Mach number equations and their variational formulation are given. Afterwards, the VMS formulation through dynamic scale splitting is derived in Section 4.3. Numerical dissipation and kinetic energy conservation is analyzed in Section 4.4. A time averaged form of the numerical equations is presented in Section 4.5. The turbulent channel flow problem is introduced in Section 4.6, where the mean numerical equations are applied and analyzed. Numerical solutions for the turbulent channel flow are shown and discussed in Section 4.7.

4.2 Formulation of the Low Mach equations

4.2.1 Initial and boundary value problem

Let $\Omega \subset \mathbb{R}^d$,with $d = 2, 3$, be the computational domain in which the flow takes place during the time interval $[0, t_{\text{end}}]$, and let $\partial\Omega$ be its boundary. The initial and boundary value problem to be considered consists of finding a velocity field $\boldsymbol{u}$, a hydrodynamic pressure field p, a temperature field T, and the thermodynamic pressure $p^{\text{th}}(t)$ such that

$$\frac{\partial \rho}{\partial t} + \nabla \cdot (\rho \boldsymbol{u}) = 0 \ \text{ in } \Omega, \ t \in (0, t_{\text{end}}) \tag{4.1}$$

$$\rho \frac{\partial \boldsymbol{u}}{\partial t} + \rho \boldsymbol{u} \cdot \nabla \boldsymbol{u} - \nabla \cdot (2\mu \boldsymbol{\varepsilon}'(\boldsymbol{u})) + \nabla p = \boldsymbol{F} \ \text{ in } \Omega, \ t \in (0, t_{\text{end}}) \tag{4.2}$$

$$\rho c_p \frac{\partial T}{\partial t} + \rho c_p \boldsymbol{u} \cdot \nabla T - \nabla \cdot (k \nabla T) - \frac{dp^{\text{th}}}{dt} = Q \ \text{ in } \Omega, \ t \in (0, t_{\text{end}}) \tag{4.3}$$

where ρ denotes the density, μ the viscosity, $\boldsymbol{\varepsilon}'(\boldsymbol{u}) = \boldsymbol{\varepsilon}(\boldsymbol{u}) - \frac{1}{3}(\nabla \cdot \boldsymbol{u}) \boldsymbol{I}$ the deviatoric part of the rate of deformation tensor $\boldsymbol{\varepsilon}(\boldsymbol{u}) = \nabla^s \boldsymbol{u} = \frac{1}{2}\left(\nabla \boldsymbol{u} + \nabla \boldsymbol{u}^T\right)$, $\boldsymbol{I}$ the identity tensor, $\boldsymbol{F}$ the external force vector, c_p the specific heat coefficient at constant pressure, k the thermal conductivity and Q the heat source. Properties μ and k are assumed to vary with temperature T according to Sutherland's law

$$\mu = \left(\frac{T}{T_{\text{ref}}}\right)^{3/2} \left(\frac{T_{\text{ref}} + S}{T + S}\right) \mu_{\text{ref}}, \quad k = \frac{\mu}{\mu_{\text{ref}}} k_{\text{ref}} \tag{4.4}$$

using a reference temperature T_{ref}, a reference viscosity μ_{ref}, the Sutherland temperature S and the reference conductivity k_{ref}. Equations (4.1)-(4.3) represent the mass, momentum and energy conservation respectively. Additionally the system is closed by the state equation of ideal gases, relating density ρ, thermodynamic pressure p^{th} and temperature T as follows

$$\rho = p^{\text{th}} / RT \tag{4.5}$$

with $R = \frac{\mathcal{R}}{M}$, where $\mathcal{R}$ is the universal gas constant and M the mean molecular mass. These equations must be supplied with initial and boundary conditions. Initial conditions are

$$\begin{aligned} \boldsymbol{u} &= \boldsymbol{u}_0 \ \text{ in } \Omega, \ t = 0 \\ T &= T_0 \ \text{ in } \Omega, \ t = 0 \\ p^{\text{th}} &= p_0^{\text{th}} \ \text{ in } \Omega, \ t = 0 \end{aligned}$$

whereas Dirichlet and Neumann boundary conditions for Eqs. (4.2) and (4.3) are

$$\begin{aligned}
\boldsymbol{u} &= \widehat{\boldsymbol{u}} \text{ on } \Gamma_D^{\boldsymbol{u}} \\
T &= \widehat{T} \text{ on } \Gamma_D^T \\
(-p\boldsymbol{I} + 2\mu\boldsymbol{\varepsilon}'(\boldsymbol{u})) \cdot \boldsymbol{n} &= \boldsymbol{t}_n \text{ on } \Gamma_N^{\boldsymbol{u}} \\
k\nabla T \cdot \boldsymbol{n} &= q_n \text{ on } \Gamma_N^T
\end{aligned}$$

where $\boldsymbol{n}$ is the outer unit normal on the boundary and it is assumed that $\Gamma_D^f \cup \Gamma_N^f = \partial\Omega$, and $\Gamma_D^f \cap \Gamma_N^f = \emptyset$ for $f = T, \boldsymbol{u}$.

Determination of the thermodynamic pressure The time dependence of thermodynamic pressure $p^{\text{th}}(t)$ needs to be determined independently of Eqs. (4.1)-(4.3). For open flows ($\Gamma_N^{\boldsymbol{u}} \neq \emptyset$) the thermodynamic pressure must be given by the boundary conditions.

The turbulent channel flow is a closed system ($\Gamma_N^{\boldsymbol{u}} = \emptyset$) where the total mass remains constant over time, and p^{th} may be obtained at each time subject to an integral form of the state equation, implying global mass conservation on domain Ω. This leads to

$$p^{\text{th}} = p_0^{\text{th}} \frac{\int_\Omega \frac{1}{T_0}\, d\Omega}{\int_\Omega \frac{1}{T}\, d\Omega} \tag{4.6}$$

where p_0^{th} is the given initial thermodynamic pressure.

4.2.2 Variational formulation

To obtain a variational formulation for the system (4.1)-(4.3), let us denote by $\boldsymbol{V}, Q, W$ the functional spaces where the solution is sought. The corresponding space of (time independent) test functions will be denoted by $\boldsymbol{V}_0, Q_0, W_0$. Functions belonging to these spaces vanish on the part of the boundary where Dirichlet conditions are imposed. We also introduce the notation $(\cdot,\cdot) \equiv (\cdot,\cdot)_\Omega$ and $(\cdot,\cdot)_\Gamma$ for the L^2-inner product on Ω and Γ, respectively. In some instances we will abuse of the notation and use this symbol for the integral of the product of two functions, not necessarily square-integrable.

Using this notation the weak form of the problem consists of finding $(\boldsymbol{u}, p, T) \in \boldsymbol{V} \times Q \times W$ such that

$$\left(\frac{\partial \rho}{\partial t}, q\right) + (\nabla \cdot (\rho \boldsymbol{u}), q) = 0 \qquad \forall q \in Q_0 \tag{4.7}$$

$$\left(\rho \frac{\partial \boldsymbol{u}}{\partial t}, \boldsymbol{v}\right) + (\rho \boldsymbol{u} \cdot \nabla \boldsymbol{u}, \boldsymbol{v}) + (2\mu\boldsymbol{\varepsilon}'(\boldsymbol{u}), \nabla^s \boldsymbol{v}) - (p, \nabla \cdot \boldsymbol{v}) = (\boldsymbol{F}, \boldsymbol{v}) + (\boldsymbol{t}_n, \boldsymbol{v})_{\Gamma_N^{\boldsymbol{u}}} \qquad \forall \boldsymbol{v} \in \boldsymbol{V}_0 \tag{4.8}$$

$$\left(\rho c_p \frac{\partial T}{\partial t}, w\right) + (\rho c_p \boldsymbol{u} \cdot \nabla T, w) + (k\nabla T, \nabla w) = \left(Q + \frac{dp^{\text{th}}}{dt}, w\right) + (q_n, w)_{\Gamma_N^T} \qquad \forall w \in W_0 \tag{4.9}$$

4.3 Space discretization

Let us consider a finite element partition $\{K\}$ of the computational domain Ω, from which we can construct finite element spaces for the velocity, pressure and temperature in the usual manner. We will denote them by $\boldsymbol{V}_h \subset \boldsymbol{V}$, $Q_h \subset Q$ and $W_h \subset W$, respectively. We assume zero Dirichlet boundary conditions to simplify the presentation. Note that in the spaces introduced time has not yet been discretized.

4.3.1 Scale splitting

Let us split the continuous space $\boldsymbol{Y} = \boldsymbol{V} \times Q \times W$ as $\boldsymbol{Y} = \boldsymbol{Y}_h \oplus \widetilde{\boldsymbol{Y}}$**,** where $\widetilde{\boldsymbol{Y}} = \widetilde{\boldsymbol{V}} \times \widetilde{Q} \times \widetilde{W}$ is the subgrid space, that can be in principle any space to complete $\boldsymbol{Y}_h = \boldsymbol{V}_h \times Q_h \times W_h$ in $\boldsymbol{Y}$. The continuous unknowns are split as

$$\begin{aligned} \boldsymbol{u} &= \boldsymbol{u}_h + \widetilde{\boldsymbol{u}} && (4.10)\\ p &= p_h + \widetilde{p} && (4.11)\\ T &= T_h + \widetilde{T} && (4.12) \end{aligned}$$

where the components with subscripts h belong to the corresponding finite element spaces, and the components with the $\widetilde{\ }$ correspond to the subgrid space. These additional components are what we will call subscales.

Our particular approach is to keep time dependency of these subscales and keep the previous decompositions (4.10)-(4.12) in *all* the terms of the variational problem (4.7)-(4.9). The only approximation we will make for the moment is to assume that the subscales vanish on the interelement boundaries, ∂K. Substituting decompositions (4.10)-(4.12) in the variational problem (4.7) -(4.9), taking the tests functions in the corresponding finite element spaces and integrating some terms by parts in order to avoid derivatives of the subscales, the discrete problem consists of finding $(\boldsymbol{u}_h, T_h, p_h) \in \boldsymbol{V}_h \times Q_h \times W_h$ such that

$$\left(\frac{\partial \rho^h}{\partial t}, q_h\right) - \left(\rho^h \boldsymbol{u}_h, \nabla q_h\right) + \left(\rho^h \boldsymbol{n} \cdot \boldsymbol{u}_h, q_h\right)_{\partial\Omega} - \left(\rho^h \widetilde{\boldsymbol{u}}, \nabla q_h\right) = 0 \tag{4.13}$$

$$\begin{aligned} &\left(\rho^h \frac{\partial \boldsymbol{u}_h}{\partial t}, \boldsymbol{v}_h\right) + \left(\rho^h \left(\boldsymbol{u}_h + \widetilde{\boldsymbol{u}}\right) \cdot \nabla \boldsymbol{u}_h, \boldsymbol{v}_h\right) + \left(2\mu \boldsymbol{\varepsilon}'\left(\boldsymbol{u}_h\right), \nabla^s \boldsymbol{v}_h\right) - \left(p_h, \nabla \cdot \boldsymbol{v}_h\right) + \left(\frac{\partial \left(\rho^h \widetilde{\boldsymbol{u}}\right)}{\partial t}, \boldsymbol{v}_h\right)\\ &\quad - \left(\widetilde{\boldsymbol{u}}, \rho^h \left(\boldsymbol{u}_h + \widetilde{\boldsymbol{u}}\right) \cdot \nabla \boldsymbol{v}_h + \nabla^h \cdot \left(2\mu \boldsymbol{\varepsilon}\left(\boldsymbol{v}_h\right)\right)\right)_h - \left(\tilde{p}, \nabla \cdot \boldsymbol{v}_h\right) = \left(\boldsymbol{F}, \boldsymbol{v}_h\right) \end{aligned} \tag{4.14}$$

$$\begin{aligned} &\left(\rho^h c_p \frac{\partial T_h}{\partial t}, w_h\right) + \left(\rho^h c_p \left(\boldsymbol{u}_h + \widetilde{\boldsymbol{u}}\right) \cdot \nabla T_h, w_h\right) + \left(k \nabla T_h, \nabla w_h\right) + \left(c_p \frac{\partial \left(\rho^h \widetilde{T}\right)}{\partial t}, w_h\right)\\ &\quad - \left(\widetilde{T}, \rho^h c_p \left(\boldsymbol{u}_h + \widetilde{\boldsymbol{u}}\right) \cdot \nabla w_h + \nabla^h \cdot \left(k \nabla w_h\right)\right) = \left(Q, w_h + \frac{dp^{\mathrm{th}}}{dt}\right) \end{aligned} \tag{4.15}$$

for any test functions $(\boldsymbol{v}_h, q_h, w_h) \in \boldsymbol{V}_{0,h} \times Q_{0,h} \times W_{0,h}$, where

$$\rho^h = p^{\mathrm{th}} / R(T_h + \widetilde{T}) \tag{4.16}$$

is obtained applying the scale splitting to the state equation (4.5). The symbol ∇^h in equation (4.14) and (4.15) indicates that the integral is carried over the finite element interiors, and the subscript h in the corresponding inner product indicates that it is performed elementwise. After a proper by parts integration of the discrete equations we made some manipulation to arrive to the discrete formulation of momentum and energy equations (4.14)-(4.15)) avoiding the presence of gradients of the subscale component.

The continuous mass conservation equation (4.7) can be written as

$$\left(\frac{\partial\rho^h}{\partial t}, q\right) = -\left(\nabla\cdot\left(\rho^h\left(\boldsymbol{u}_h + \widetilde{\boldsymbol{u}}\right)\right), q\right)$$

after an splitting of the unknowns, note that this equation holds at the continous level. We replaced this continuous form of the mass conservation equation into the momentum and energy equations after performing some by parts integrations, to avoid terms involving gradients of the subscale component. Those replacements are crucial to account for the subscales in all the nonlinear terms. In particular we have replaced $\left(\widetilde{\boldsymbol{u}}, \nabla\left(\rho^h\left(\boldsymbol{u}_h + \widetilde{\boldsymbol{u}}\right)\right)\boldsymbol{v}_h\right)$ by $-\left(\widetilde{\boldsymbol{u}}, \frac{\partial\rho^h}{\partial t}\boldsymbol{v}_h\right)$ in the momentum equation, and $\left(\widetilde{T}, \nabla\left(\rho^h\left(\boldsymbol{u}_h + \widetilde{\boldsymbol{u}}\right)\right)w_h\right)$ by $-\left(\widetilde{T}, \frac{\partial\rho^h}{\partial t}w_h\right)$ in the energy equation.

In order to give a closure to system (4.13)-(4.16) we need to define how the subscales $\widetilde{\boldsymbol{u}}$, $\widetilde{p}$ and $\widetilde{T}$ are computed, which will be discussed in the rest of the section. However, we would like to point out that, once the velocity subscale is approximated in the momentum equation (4.14), it provides additional terms to those that appear in classical stabilized finite element methods. These are non standard terms in the sense that they are usually neglected and appear because we keep the scale splitting also in nonlinear terms. The terms involving the velocity subgrid scale arising from the convective term in the momentum equation, namely $\left(\rho^h\widetilde{\boldsymbol{u}}\cdot\nabla\boldsymbol{u}_h, \boldsymbol{v}_h\right) - \left(\widetilde{\boldsymbol{u}}, \rho^h\left(\boldsymbol{u}_h + \widetilde{\boldsymbol{u}}\right)\cdot\nabla\boldsymbol{v}_h\right)$ can be understood as the contribution from the Reynolds- and cross- stress terms of a LES approach. Therefore, modeling $\widetilde{\boldsymbol{u}}$ implies modeling the subgrid scale tensor. Similar comments apply to the energy equation (4.15), in which case the terms involving the velocity and temperature subgrid scales arising from the convective term are $\left(\rho^h c_p\widetilde{\boldsymbol{u}}\cdot\nabla T_h, w_h\right) - \left(\widetilde{T}, \rho^h c_p\left(\boldsymbol{u}_h + \widetilde{\boldsymbol{u}}\right)\cdot\nabla w_h\right)$. We believe that those terms will permit to model turbulent behavior without the need of any additional turbulence model.

To get the final numerical scheme we approximate the subscales in the element interiors. The equations for the subscales are obtained by projecting the original equations onto their corresponding spaces $\widetilde{\boldsymbol{Y}}$. If $\widetilde{P}$ denotes the L_2-projection onto any of these spaces, the subscale equations are written as

$$\widetilde{P}\left(\rho^h\nabla\cdot\widetilde{\boldsymbol{u}} - \frac{\rho^h\left(\boldsymbol{u}_h + \widetilde{\boldsymbol{u}}\right)}{T_h + \widetilde{T}}\cdot\nabla\widetilde{T}\right) = \widetilde{P}\left(R_c\right) \tag{4.17}$$

$$\widetilde{P}\left(\frac{\partial\left(\rho^h\widetilde{\boldsymbol{u}}\right)}{\partial t} + \boldsymbol{\nabla\cdot}\left(\rho^h(\boldsymbol{u_h} + \widetilde{\boldsymbol{u}})\,\widetilde{\boldsymbol{u}}\right) - \nabla\cdot\left(2\mu\varepsilon'\left(\widetilde{\boldsymbol{u}}\right)\right) + \nabla\widetilde{p}\right) = \widetilde{P}\left(\boldsymbol{R}_m\right) \tag{4.18}$$

$$\widetilde{P}\left(c_p\frac{\partial\left(\rho^h\widetilde{T}\right)}{\partial t} + c_p\nabla\cdot\left(\rho^h\left(\boldsymbol{u}_h + \widetilde{\boldsymbol{u}}\right)\widetilde{T}\right) - \nabla\cdot\left(k\nabla\widetilde{T}\right)\right) = \widetilde{P}\left(R_e\right) \tag{4.19}$$

where the residuals of mass, momentum and energy equations are respectively

$$\begin{aligned} R_c &= -\frac{\partial \rho^h}{\partial t} - \rho^h \nabla \cdot \boldsymbol{u}_h + \frac{\rho^h \left(\boldsymbol{u}_h + \widetilde{\boldsymbol{u}}\right)}{T_h + \widetilde{T}} \cdot \nabla T_h \qquad (4.20)\\ \boldsymbol{R}_m &= \boldsymbol{F} - \rho^h \frac{\partial \boldsymbol{u}_h}{\partial t} - \rho^h \left(\boldsymbol{u}_h + \widetilde{\boldsymbol{u}}\right) \cdot \nabla \boldsymbol{u}_h + \nabla \cdot \left(2\mu \boldsymbol{\varepsilon}'\left(\boldsymbol{u}_h\right)\right) - \nabla p_h \qquad (4.21)\\ R_e &= Q + \frac{dp^{\text{th}}}{dt} - \rho^h c_p \frac{\partial T_h}{\partial t} - \rho^h c_p \left(\boldsymbol{u}_h + \widetilde{\boldsymbol{u}}\right) \cdot \nabla T_h + \nabla \cdot \left(k \nabla T_h\right) \qquad (4.22) \end{aligned}$$

4.3.2 Approximation of the subscales

Up to this point the only approximation introduced is to assume that the subscales vanish on the element boundaries. We adopt a simple approximation which consists in replacing the (spatial) differential operator by an algebraic operator which can be easily inverted. The differential equations (4.17)-(4.19) over each element domain K can be written in vectorial form as

$$\widetilde{P}\left(\frac{\partial}{\partial t}(\boldsymbol{M}\widetilde{\boldsymbol{U}}) + \mathcal{L}\widetilde{\boldsymbol{U}}\right) = \widetilde{P}\left(\boldsymbol{R}\right) \quad \text{in} \quad K \qquad (4.23)$$

where $\widetilde{\boldsymbol{U}} \equiv \left(\widetilde{\boldsymbol{u}}, \widetilde{p}, \widetilde{T}\right)$, $\mathcal{L}$ is a nonlinear spatial differential vector operator, $\boldsymbol{M}$ is the $(d+2) \times (d+2)$ diagonal matrix $\boldsymbol{M}$ =diag$\left(\rho^h \boldsymbol{I}_d, 0, \rho^h c_p\right)$, where $\boldsymbol{I}_d$ is the $d \times d$ identity matrix, and $\boldsymbol{R} \equiv (\boldsymbol{R}_m, R_c, R_e)$. In the present chapter we will consider two options. First, we will take the space of subscales as that of the residuals, that is, we will consider $\widetilde{P} = I$ (the identity) when applied to the finite element residuals (DSS). We will also consider $\widetilde{P}$ as the projection onto the space orthogonal to the finite element space, known as orthogonal subgrid scale method (OSS), described in chapter 3.

We consider the algebraic approximation $\mathcal{L} \approx \boldsymbol{\tau}^{-1}$ in each K, where $\boldsymbol{\tau}$ is an $(d+2)\times(d+2)$ diagonal matrix. Taking $\boldsymbol{\tau}$ =diag$(\tau_m \boldsymbol{I}_d, \tau_c, \tau_e)$ the approximation to the subscales equations (4.17)-(4.19) within each element of the finite element partition reads

$$\begin{aligned} \frac{1}{\tau_c}\widetilde{p} &= R_c + p_{\text{ort}} = R_c' \qquad (4.24)\\ \frac{\partial(\rho^h \widetilde{\boldsymbol{u}})}{\partial t} + \frac{1}{\tau_m}\widetilde{\boldsymbol{u}} &= \boldsymbol{R}_m + \boldsymbol{u}_{\text{ort}} = \boldsymbol{R}_m' \qquad (4.25)\\ c_p \frac{\partial(\rho^h \widetilde{T})}{\partial t} + \frac{1}{\tau_e}\widetilde{T} &= R_e + T_{\text{ort}} = R_e' \qquad (4.26) \end{aligned}$$

where p_{ort}, $\boldsymbol{u}_{\text{ort}}$ and T_{ort} are functions L_2-orthogonal to the subscale space. After the approximation $\mathcal{L} \approx \boldsymbol{\tau}^{-1}$, equations (4.24)-(4.26) become a set of ordinary differential equations at each integration point. The stabilization parameters can be motivated by an approximated Fourier analysis performed in [19]. The same analysis can be repeated for the present variable-density equation system to obtain

$$\begin{aligned}
\tau_c &= \frac{h^2}{c_1 \rho^h \tau_m} = \frac{\mu}{\rho^h} + \frac{c_2}{c_1} |\boldsymbol{u}_h + \widetilde{\boldsymbol{u}}| h && (4.27)\\
\frac{1}{\tau_m} &= c_1 \frac{\mu}{h^2} + c_2 \frac{\rho^h |\boldsymbol{u}_h + \widetilde{\boldsymbol{u}}|}{h} && (4.28)\\
\frac{1}{\tau_e} &= c_1 \frac{k}{h^2} + c_2 \frac{\rho^h c_p |\boldsymbol{u}_h + \widetilde{\boldsymbol{u}}|}{h} && (4.29)
\end{aligned}$$

where h is the element size and c_1 and c_2 are algorithmic constants whose values are $c_1 = 12$ and $c_2 = 2$ in the numerical experiments to be presented. Those values are very important for the design of the stabilization parameters. An interpretation for coefficients c_1 and c_2 was found from a Fourier analysis in [19], implying the restriction $c_2^2 \leq c_1$. Note that larger c_1 values imply smaller τ_c, τ_m and τ_e, leading to a less dissipative scheme (as explained in section 4.4).

The Reynolds number based on the element length $\mathrm{Re}_h = \frac{\rho^h |\boldsymbol{u}_h + \widetilde{\boldsymbol{u}}| h}{\mu}$ gives the relation between the current mesh size h to Kolmogorov's length scale λ. The later is the needed mesh discretization to perform a DNS calculation, or to avoid numerical oscillations due to dominant convective terms when using Galerkin approximation. When solving turbulent flows using LES models or stabilized finite elements, generally $Re_h \gg 1$ away from the walls. When $\mathrm{Re}_h \gg 1$ it is very important to introduce numerical dissipation in order to obtain a stable numerical formulation. It is observed in Eqs. (4.27)-(4.29) that when $\mathrm{Re}_h \gg 1$ the values of τ_m and τ_e are barely sensitive to c_1 while τ_c is very sensitive to c_1. We have found in the numerical experiments that increasing c_1 decreases considerably the total numerical dissipation. This is due to the sensibility on τ_c of the total amount of numerical dissipation. When $\mathrm{Re}_h \lesssim 1$ (in viscous dominant regions close to boundary layers) $\tau_c \rightarrow \mu/\rho^h$, introducing a volumetric viscosity μ for incompressible flows. We have observed that to define τ_c such $\tau_c \rightarrow C\mu/\rho^h$ as $\mathrm{Re}_h \rightarrow 0$ with $C \geq 1$ deteriorates the boundary layer behavior if C differs from 1, giving very inaccurate results.

Equations (4.24) - (4.26) form a dynamic system of nonlinear equations at each integration point. Before discretizing in time, we cannot go any further than saying that the problem consists in solving (4.13)-(4.15) together with (4.24) - (4.26).

Time discretization of subscale equations

Any time integration scheme could now be applied to discretize in time the finite element equations (4.13)-(4.15), together with equations (4.24)-(4.26). A detailed explanation of time discretization of all those equations is found in [2]. As it is discussed in [27] the time integration for the subscales could be one order less accurate than for the finite element equations without affecting the accuracy of the numerical scheme. Considering the backward Euler differencing scheme, the subscale equations (4.24)-(4.26) yield

$$\widetilde{p}^{n+1} = \tau_c^{n+1} R_c'^{n+1} \tag{4.30}$$

$$\widetilde{\boldsymbol{u}}^{n+1} = \left(\frac{\rho^{h,n+1}}{\Delta t} + \frac{1}{\tau_m^{n+1}}\right)^{-1} \left(\boldsymbol{R}_m'^{n+1} + \frac{\rho^{h,n}\widetilde{\boldsymbol{u}}^n}{\Delta t}\right) \tag{4.31}$$

$$\widetilde{T}^{n+1} = \left(\frac{\rho^{h,n+1}c_p}{\Delta t} + \frac{1}{\tau_e^{n+1}}\right)^{-1} \left(R_e'^{n+1} + \frac{\rho^{h,n}c_p\widetilde{T}^n}{\Delta t}\right) \tag{4.32}$$

where the superscript n indicates that functions are approximated at time step n, and Δt is the time step size, assumed constant for simplicity. From these expressions, we see that the residual of the momentum and energy equations are multiplied respectively by

$$\tau_{tm} = \left(\frac{\rho^h}{\Delta t} + \frac{1}{\tau_m^{n+1}}\right)^{-1} \tag{4.33}$$

$$\tau_{te} = \left(\frac{\rho^h c_p}{\Delta t} + \frac{1}{\tau_e^{n+1}}\right)^{-1} \tag{4.34}$$

These can be considered the effective stabilization parameters for the transient Low Mach equations. Expressions with asymptotic behavior similar to coefficients τ_{tm}, τ_{te} in terms of $h, \mu, |\boldsymbol{u}_h + \widetilde{\boldsymbol{u}}|$, and Δt can often be found in the literature (see e.g. [40]). It is important to note that if the stabilization parameter depends on Δt and subscales are not considered time dependent, **the steady-state solution will depend on the time step size**. This does not happen if expressions (4.31) and (4.32) are used. It can be checked that, when steady state is reached the usual expressions employed for stationary problems are recovered, namely $\widetilde{\boldsymbol{u}} = \tau_m \boldsymbol{R}_m$, and $\widetilde{T} = \tau_e R_e$.

The equations for the subscales must be discretized in time as explained and linearized together with the finite element equations (4.13)-(4.15). Detailed linearization schemes for these equations are described in [2].

Remark Solutions to the nonlinear subscale Eqs. (4.25) and (4.26) display a dynamic behavior which may be radically different from the linear one. Due to the nonlinear modeling of the equations, the subscales must be dynamic, its time derivative cannot be neglected, in order to avoid possible lack of uniqueness in their calculations. □

4.4 Conservation of kinetic energy and dissipative structure

4.4.1 Continuous and discrete global balance of kinetic energy

Global conservation statements for mass, momentum and energy have been obtained for the present semi-discrete formulation in chapter 3 and [2]. In this section we discuss the conservation of kinetic energy, and the dissipative structure of the formulation. By kinetic energy we mean the norm of the velocity $\frac{1}{2}\left(\rho\boldsymbol{u}, \boldsymbol{u}\right)_\Omega$. For the continuous problem, kinetic energy conservation is obtained by taking the test function equal to the velocity in the momentum equation (4.8) , and using in a crucial manner the mass conservation equation to conclude that the convective terms in the corresponding equations only contribute through boundary terms. Doing this, the kinetic energy conservation for the continuous problem reads

$$\frac{\partial}{\partial t}\int_{\Omega} k + \int_{\partial\Omega} \boldsymbol{n}\cdot\boldsymbol{u}\cdot\left(\left(k+p\right)\boldsymbol{I} - 2\mu\boldsymbol{\varepsilon}'\left(\boldsymbol{u}\right)\right) + \int_{\Omega} 2\mu\boldsymbol{\varepsilon}' : \boldsymbol{\varepsilon}' = \int_{\Omega} \boldsymbol{F}\cdot\boldsymbol{u} + \int_{\Omega} p\nabla\cdot\boldsymbol{u} \tag{4.35}$$

where $k = \frac{1}{2}\rho\boldsymbol{u}\cdot\boldsymbol{u}$ is the kinetic energy per unit of volume. The first term on the left hand side is the total kinetic energy variation, the second term is the flux of energy through the boundary. The contribution of this energy flux are the kinetic energy k, the pressure p, and the viscous stress $2\mu\boldsymbol{\varepsilon}'$. The third term is the dissipation due to viscous effects. These terms are balanced on the right side by the mechanical work of external forces and pressure respectively.

The discrete kinetic energy conservation, obtained taking $\boldsymbol{v}_h = \boldsymbol{u}_h$ in the discrete equation (4.14), is

$$\frac{\partial}{\partial t}\int_{\Omega} k_h + \int_{\partial\Omega} \boldsymbol{n}\cdot\left(\left(\boldsymbol{u}_h + \widetilde{\boldsymbol{u}}\right)k_h + \boldsymbol{u}_h\cdot\boldsymbol{t}_n\right) \tag{4.36}$$

$$= -\int_{\Omega} 2\mu\boldsymbol{\varepsilon}'\left(\boldsymbol{u}_h\right) : \boldsymbol{\varepsilon}'\left(\boldsymbol{u}_h\right) + \int_{\Omega} p_h\nabla\cdot\boldsymbol{u}_h + \int_{\Omega}\boldsymbol{F}\cdot\boldsymbol{u}_h \tag{4.37}$$

$$+\sum_K \int_K \widetilde{\boldsymbol{u}}\cdot\left(\rho^h\boldsymbol{u}_h\cdot\boldsymbol{\nabla}\boldsymbol{u}_h\right) \tag{4.38}$$

$$+\sum_K \int_K \widetilde{\boldsymbol{u}}\cdot\left(\rho^h\widetilde{\boldsymbol{u}}\cdot\boldsymbol{\nabla}\boldsymbol{u}_h\right) \tag{4.39}$$

$$+\sum_K \int_K \widetilde{p}\nabla\cdot\boldsymbol{u}_h \tag{4.40}$$

$$+\frac{1}{2}\sum_K \int_K \left(\frac{\partial\rho^h}{\partial t} + \nabla\cdot\left(\rho^h\left(\boldsymbol{u}_h + \widetilde{\boldsymbol{u}}\right)\right)\right)\left|\boldsymbol{u}_h\right|^2 \tag{4.41}$$

$$-\sum_K \int_K \frac{\partial}{\partial t}\left(\rho^h\widetilde{\boldsymbol{u}}\right)\cdot\boldsymbol{u}_h \tag{4.42}$$

$$+\sum_K \int_K \widetilde{\boldsymbol{u}}\cdot\nabla\cdot\left(\mu\nabla\boldsymbol{\varepsilon}'(\boldsymbol{u}_h)\right) \tag{4.43}$$

where $k_h = \frac{1}{2}\rho^h\boldsymbol{u}_h\cdot\boldsymbol{u}_h$ is the discrete kinetic energy per unit of volume, and $\boldsymbol{t}_n = p_h\boldsymbol{I} - 2\mu\boldsymbol{\varepsilon}'\left(\boldsymbol{u}_h\right)$. The first two rows contain terms corresponding to the discrete counterpart of the continuous energy balance (4.35). All the other rows contain artificial energy balance terms due to numerical discretization. The total numerical dissipation ε_{num} is the sum of terms from (4.38) to (4.43). The terms (4.38) and (4.39) can be related to the Cross and Reynolds terms coming from a LES model, accounting for kinetic energy transfer to non resolved scales (until Kolmogorov scale length). Term (4.40) is the work done by the pressure subscale, penalizes local mass conservation error and its sign is not known a priori. For incompressible flows this work introduces always positive dissipation, penalizing incompressibility. Term (4.41) is the dissipation due to the convective and temporal term discretization, this term vanishes when the skew symmetric formulation is implemented, as it will be shown in section 4.4.2. The term in (4.42) is dissipation due to the subscale variation in time; note that this term vanishes when the OSS approximation is implemented, due to orthogonality between scale spaces. The last dissipative term (4.43) is only introduced when second or higher order finite elements are implemented.

We wish to understand if the numerical model behaves as a physical turbulence model. It is obvious from Equations (4.36)-(4.43) that there is no balance statement for the kinetic energy k_h, in the form of time variation plus dissipation equal to external input. However, for incompressible flow these balance statements are found when the contributions from the finite element components and the subscales are added up [25].

4.4.2 Skew symmetric formulation

The temporal and convective terms in the continuous problem (4.2) can be expressed equivalently in conservative or in non-conservative form. Through the mass conservation statement we get

$$\frac{\partial(\rho\boldsymbol{u})}{\partial t}+\nabla\cdot(\rho\boldsymbol{u}\boldsymbol{u})=\rho\frac{\partial\boldsymbol{u}}{\partial t}+\rho\boldsymbol{u}\cdot\nabla\boldsymbol{u}$$

The terms on the left and right hand side are known respectively as conservative and non-conservative temporal and convective terms. When these terms are tested against $\boldsymbol{u}$ they give the following kinetic energy conservation components

$$\int_\Omega\left(\frac{\partial(\rho\boldsymbol{u})}{\partial t}+\nabla\cdot(\rho\boldsymbol{u}\boldsymbol{u})\right)\cdot\boldsymbol{u}=\int_\Omega\left(\rho\frac{\partial\boldsymbol{u}}{\partial t}+\rho\boldsymbol{u}\cdot\nabla\boldsymbol{u}\right)\cdot\boldsymbol{u}=\frac{\partial}{\partial t}\int_\Omega k+\int_{\partial\Omega}\boldsymbol{n}\cdot\boldsymbol{u}\,k \quad (4.44)$$

accounting for kinetic energy transport only. The first term on the right hand side is the kinetic energy variation inside the domain Ω, whereas the second term is the net flux of kinetic energy through the domain boundary. We would like that the corresponding temporal and convective terms in the discrete problem account only for kinetic energy variation, and not for dissipation.

Given a vector field $\boldsymbol{a}$ we introduce the *non-conservative* and *conservative* convective forms as follows:

$$\begin{aligned}
c_{\mathrm{nc}}(\boldsymbol{a},\boldsymbol{u}_h,\boldsymbol{v}_h) &= \int_\Omega\left(\rho^h\frac{\partial\boldsymbol{u}_h}{\partial t}+\rho^h\boldsymbol{a}\cdot\nabla\boldsymbol{u}_h\right)\cdot\boldsymbol{v}_h && \text{Non conservative form}\\
c_{\mathrm{c}}(\boldsymbol{a},\boldsymbol{u}_h,\boldsymbol{v}_h) &= \int_\Omega\frac{\partial(\rho^h\boldsymbol{u}_h)}{\partial t}\cdot\boldsymbol{v}_h-\int_\Omega\rho^h\boldsymbol{a}\boldsymbol{u}_h:\nabla\boldsymbol{v}_h\\
&\quad+\int_{\partial\Omega}\rho^h(\boldsymbol{n}\cdot\boldsymbol{a})(\boldsymbol{u}_h\cdot\boldsymbol{v}_h) && \text{Conservative form}
\end{aligned}$$

For the discrete problem, the conservative formulation is obtained substituting the non-conservative term $c_{\mathrm{nc}}(\boldsymbol{a},\boldsymbol{u}_h,\boldsymbol{v}_h)$ used earlier by the conservative one $c_{\mathrm{c}}(\boldsymbol{a},\boldsymbol{u}_h,\boldsymbol{v}_h)$ in the discrete momentum Eq. (4.14), where $\boldsymbol{a}=\boldsymbol{u}_h+\widetilde{\boldsymbol{u}}$. After an adequate integration by parts it is found that

$$\begin{aligned}
c_{\mathrm{nc}}(\boldsymbol{a},\boldsymbol{u}_h,\boldsymbol{u}_h) &= \frac{\partial}{\partial t}\int_\Omega k_h+\int_{\partial\Omega}\boldsymbol{n}\cdot\boldsymbol{a}k_h-\frac{1}{2}\int_\Omega\left(\frac{\partial\rho^h}{\partial t}+\nabla\cdot(\rho\boldsymbol{a})\right)|\boldsymbol{u}_h|^2 && (4.45)\\
c_{\mathrm{c}}(\boldsymbol{a},\boldsymbol{u}_h,\boldsymbol{u}_h) &= \frac{\partial}{\partial t}\int_\Omega k_h+\int_{\partial\Omega}\boldsymbol{n}\cdot\boldsymbol{a}k_h+\frac{1}{2}\int_\Omega\left(\frac{\partial\rho^h}{\partial t}+\nabla\cdot(\rho\boldsymbol{a})\right)|\boldsymbol{u}_h|^2 && (4.46)
\end{aligned}$$

Comparing against the continuous equation (4.44) the first two terms on the right hand side represent the finite element kinetic energy variation inside the domain Ω plus the net flux of kinetic energy through the boundary. The third term is a nonphysical "dissipation" proportional to mass conservation error and to the square of velocity norm $|\boldsymbol{u}_h|^2$. This term is introduced with opposite sign in the non-conservative and conservative convective forms. To avoid this non-physical term, we define a skew symmetric convective form as follows:

$$\begin{aligned} c_{\mathrm{ss}}(\boldsymbol{a},\boldsymbol{u}_h,\boldsymbol{v}_h) &= \frac{1}{2}\left[c_{\mathrm{c}}(\boldsymbol{a},\boldsymbol{u}_h,\boldsymbol{v}_h)+c_{\mathrm{nc}}(\boldsymbol{a},\boldsymbol{u}_h,\boldsymbol{v}_h)\right] \\ &= \frac{1}{2}\int_\Omega\left(\rho^h\frac{\partial\boldsymbol{u}_h}{\partial t}+\frac{\partial(\rho^h\boldsymbol{u}_h)}{\partial t}+\rho^h\boldsymbol{a}\cdot\nabla\boldsymbol{u}_h\right)\cdot\boldsymbol{v}_h \\ &-\frac{1}{2}\int_\Omega\rho^h\boldsymbol{a}\boldsymbol{u}_h:\nabla\boldsymbol{v}_h+\frac{1}{2}\int_{\partial\Omega}\rho^h(\boldsymbol{v}_h\cdot\boldsymbol{a})(\boldsymbol{n}\cdot\boldsymbol{u}_h) \end{aligned}$$

The advantage of this formulation is that it does not introduce numerical dissipation, being

$$c_{\mathrm{ss}}(\boldsymbol{a},\boldsymbol{u}_h,\boldsymbol{u}_h)=\frac{\partial}{\partial t}\int_\Omega k_h+\int_{\partial\Omega}\boldsymbol{n}\cdot\boldsymbol{a}\,k_h$$

It is said in the CFD community that the skew-symmetric form is conservative *a priori* in the kinetic energy equation. The term "skew-symmetric" refers to the fact that: $c_{ss}(\boldsymbol{a},\boldsymbol{u}_h,\boldsymbol{u}_h)=0$ for steady flows and velocity vanishing over the boundaries. This formulation is widely used in incompressible turbulent flows [25] with the objective of diminishing artificial numerical dissipation.

In the present chapter the skew symmetric formulation is used, and therefore term (4.41) does not appear. We have observed in numerical simulations that the use of the skew symmetric formulation gives better results than the use of the non-conservative form, with the shortcoming that the algebraic iterative solver of equations needs more iterations to achieve the same convergence tolerance.

4.5 Time averaged numerical equations

Turbulent flows can only be described statistically. To be able to draw any conclusion from the chaotic flow field, mean values of variables need to be considered. The traditional approach for treating high Reynolds number (Re) turbulent flows has been to average in time the equations. A common type of time averaging for compressible flows is the Favre (density-weighted) approach, being an excellent tool to avoid density fluctuations in the Navier Stokes equations. The standard practice is to decompose the instantaneous equations into mean ad fluctuating parts and then to average them. The mean or Reynolds averaging of a variable u over a large enough time integration period T is given by

$$\bar{u}(\boldsymbol{x})=\frac{1}{T}\int_{t_i}^{t_i+T}u(\boldsymbol{x},t)\,dt$$

The Favre averaging of a variable u gives the Favre mean $\hat{u}$, defined as $\hat{u}=\frac{\overline{\rho u}}{\bar{\rho}}$. Now, any fluctuating in time variable u can be decomposed as

$$u=\bar{u}+u'(t)=\hat{u}+u''(t)$$

where, u' and u'' are the Reynolds and Favre fluctuations of u, being by definition $\overline{u'} = 0$ and $\widehat{u''} = 0$.

Applying the Reynolds averaging to the Favre decomposition one obtains the relation between Favre and Reynolds mean, namely, $\bar{u} = \hat{u} + \overline{u''}$. Decomposing this relationship, it is found that the Reynolds averaging of a Favre fluctuation is $\overline{u''} = \bar{u} - \overline{\rho u}/\bar{\rho} = -\frac{\overline{\rho' u'}}{\bar{\rho}}$. So $\overline{u''} = 0$ if and only if u is uncorrelated with the density, being $\bar{u} = \hat{u}$ in this case.

After Reynolds averaging of the instantaneous Navier Stokes equations (4.1)-(4.5) we get the mean Navier Stokes equations:

$$
\begin{aligned}
\frac{\partial \bar{\rho}}{\partial t} + \nabla \cdot (\bar{\rho} \hat{\boldsymbol{u}}) &= 0 && (4.47)\\
\frac{\partial (\bar{\rho} \hat{\boldsymbol{u}})}{\partial t} + \nabla \cdot (\bar{\rho} \widehat{\boldsymbol{u}\boldsymbol{u}}) - \nabla \cdot \left(2\overline{\mu (\boldsymbol{\varepsilon}' (\boldsymbol{u}))} \right) + \nabla \bar{p} &= \bar{\boldsymbol{F}} && (4.48)\\
c_p \frac{\partial \left(\bar{\rho} \hat{T} \right)}{\partial t} + c_p \nabla \cdot \left(\bar{\rho} \widehat{\boldsymbol{u} T} \right) - \nabla \cdot \left(\overline{k \nabla T} \right) &= \frac{d}{dt} \overline{p^{\mathrm{th}}} && (4.49)\\
\overline{p^{\mathrm{th}}} &= R \bar{\rho} \hat{T} && (4.50)
\end{aligned}
$$

The main reason for employing Favre averaging fluctuations (not for the density and the pressure) is that the resulting conservation equations do not include terms involving correlations of density fluctuations.

Assuming a statistically steady state, where mean variables do not depend on time, and developing the mean averaging of the product of two fluctuating variables as $\widehat{uv} = \hat{u}\hat{v} + \widehat{u''v''}$, the **statistically steady state** Navier Stokes equations read

$$
\begin{aligned}
\nabla \cdot (\bar{\rho} \hat{\boldsymbol{u}}) &= \boldsymbol{0} && (4.51)\\
\nabla \cdot (\bar{\rho} \hat{\boldsymbol{u}} \hat{\boldsymbol{u}}) - \nabla \cdot \left(2\overline{\mu (\boldsymbol{\varepsilon}' (\boldsymbol{u}))} \right) + \nabla \bar{p} &= \bar{\boldsymbol{F}} - \nabla \cdot \left(\bar{\rho} \widehat{\boldsymbol{u}'' \boldsymbol{u}''} \right) && (4.52)\\
c_p \nabla \cdot \left(\bar{\rho} \hat{\boldsymbol{u}} \hat{T} \right) - \nabla \cdot \left(\overline{k \nabla T} \right) &= -c_p \nabla \cdot \left(\bar{\rho} \widehat{\boldsymbol{u}'' T''} \right) && (4.53)\\
\overline{p^{\mathrm{th}}} &= R \bar{\rho} \hat{T} && (4.54)
\end{aligned}
$$

To get **the mean numerical equations for the discrete problem** we average the instantaneous discrete Eqs. (4.13)-(4.15), assuming that a statistically steady state has been reached numerically (time derivatives of all mean quantities are assumed null over a long enough time integration period). Introducing the notation $\boldsymbol{a} = \boldsymbol{u}_h + \widetilde{\boldsymbol{u}}$, the mean numerical equations for the statistically steady state read

$$
\begin{aligned}
\left(\overline{\rho^h}\hat{\boldsymbol{a}}, \nabla q_h\right) &= 0 && (4.55)\\
\left(\overline{\rho^h}\left(\hat{\boldsymbol{a}}\cdot\nabla\hat{\boldsymbol{u}}_h + \widehat{\boldsymbol{a}''\cdot\nabla\boldsymbol{u}_h''}\right), \boldsymbol{v}_h\right) + \left(\overline{2\mu\boldsymbol{\varepsilon}'\left(\boldsymbol{u}_h\right)}, \nabla^s\boldsymbol{v}_h\right) & && \\
-\left(\overline{\rho^h}\left(\hat{\boldsymbol{a}}\widehat{\widetilde{\boldsymbol{u}}} + \widehat{\boldsymbol{a}''\widetilde{\boldsymbol{u}}''}\right), \nabla\boldsymbol{v}_h\right) - \left(\overline{p_h} + \overline{\widetilde{p}}, \nabla\cdot\boldsymbol{v}_h\right) &= \left(\bar{\boldsymbol{F}}, \boldsymbol{v}_h\right) && (4.56)\\
\left(c_p\overline{\rho^h}\left(\hat{\boldsymbol{a}}\cdot\nabla\hat{T}_h + \widehat{\boldsymbol{a}''\widetilde{T}''}\right), w_h\right) & && \\
-\left(c_p\bar{\rho}\left(\hat{\boldsymbol{a}}\widehat{\widetilde{T}} + \widehat{\boldsymbol{a}''\cdot\nabla T_h''}\right), \nabla w_h\right) + \left(\overline{k\nabla T_h}, \nabla^s w_h\right) &= 0 && (4.57)\\
\overline{p^{\mathrm{th}}} &= \overline{\rho^h}R\left(\widehat{T_h} + \widehat{\widetilde{T}}\right) && (4.58)
\end{aligned}
$$

for all test functions $\boldsymbol{v}_h$, q_h and w_h.

4.6 The Turbulent Channel Flow

4.6.1 Statement of the problem

A simulation of a turbulent channel flow between two isothermal walls fixed at hot and cold temperatures T_h and T_c is considered. The friction Reynolds number $\mathrm{Re}_\tau = \frac{\rho u_\tau \delta}{\mu}$ is based on the friction velocity $u_\tau = \sqrt{\tau_w/\rho_w}$, where τ_w is the wall stress

$$
\tau_w = \mu\varepsilon'\left(\boldsymbol{u}_h\right)\cdot\boldsymbol{n} = \mu\partial_y\left(u_x - \frac{2}{3}u_y\right)_{\text{wall}}
$$

δ is the channel half-width and ρ_w the density over the wall. Since ρ, μ and u_τ are variable and different in the hot and cold walls, reference values need to be defined. With the definition of these values described later, the friction Reynolds number we have taken in $\mathrm{Re}_\tau = 180$.

The molecular Prandtl number is $\mathrm{Pr} = \frac{c_p\mu}{k} = 0.71$. Two cases with temperature ratios $T_h/T_c = 1.01$ and $T_h/T_c = 2.00$ are investigated. DNS data for this Reynolds number and these temperature ratios T_h/T_c are provided in [74, 73], LES results were reported in [61, 96, 39]. In the case of lower temperature ratio the temperature is almost uniform, offering the opportunity to compare the results to the well-established incompressible DNS data in [71].

As usual in DNS and LES studies of this case, scaled initial temperatures and density fields $T_0 = T_c = 1$ K, $\rho_0 = 1$ Kg/m^3 are prescribed. In this way the gas constant and specific heat capacity are assumed to be $R = 287.0\,\mathrm{J\,kg^{-1}\,K^{-1}}$ and $c_p = 1004.5\,\mathrm{J\,kg^{-1}\,K^{-1}}$ giving a specific heat ratio $\gamma = \frac{c_p}{c_p - R} = 1.4$. A scaled Sutherland law (4.4) as used in [74, 73, 39] is employed, where $T_{\text{ref}} = 1.0$ K and $S = 0.368$ K.

Let the coordinate directions x, y and z denote the streamwise, wall-normal and spanwise directions, respectively. The dimensions of the domain are $4\pi\delta \times 2\delta \times \frac{4}{3}\pi\delta$, as in [74]. The walls of the channels are held at zero velocity and constant temperature, the hot wall is at $y = \delta$ and the cold wall at $y = -\delta$. On the other hand, the boundaries of the domain normal to the x and z directions are periodic. Therefore, the total mass of the system is conserved, i.e., this is an example of flow in a closed domain and thermodynamic pressure will be determined at each time step from Eq.(4.6). The total mass of the system is initially fixed as $m_0 = \int_\Omega \rho_o d\Omega$. To impose periodic conditions for the pressure a body force $\boldsymbol{F}$ needs to be imposed in form of a driving pressure gradient in the streamwise x-direction, as driving mechanism for the flow.

Three different meshes of 32^3, 48^3 and 64^3 Q_1 finite elements are employed. The distribution of the nodes is uniform in streamwise and spanwise directions x, z . In wall normal direction y the distribution of nodes obeys an hyperbolic tangent function refining towards the wall, as in [74, 39]. For the case of lower temperature ratio a symmetric node distribution between lower and upper walls is used. The location y^i of each grid node i, $i = 0, \ldots, n_y$, where n_{el} is the number of elements in the wall normal direction, is given by

$$y^i = \frac{\tanh\left(2.1\left(\frac{2i}{n_{el}} - 1\right)\right)}{\tanh(2.1)}$$

For the higher temperature ratio the Reynolds number near the hot wall is expected to be smaller than near the cold wall and the following non-symmetric distribution is used:

$$y^i = 2\frac{\hat{y}^i + 1}{\hat{y}^{n_{el}} + 1} - 1$$

with

$$\hat{y}^i = \frac{\tanh\left(2.1\left(\frac{2\alpha i}{n_{el}} - 1\right)\right)}{\tanh(2.1)}$$

and $\alpha = 0.9$.

The equations are integrated in time using a second order scheme BDF2 and a constant time step $\Delta t = 0.004\text{s}$ which expressed in wall units is $\Delta t^+ = \frac{\Delta t}{\Delta t^*} = \frac{\Delta t \rho u_\tau^2}{\mu} = 0.72$. At least 5000 time steps are performed to allow the flow to develop and reach statistically steady state. The statistics are collected during $T = 5000$ time steps, a time period of order $T \approx 15\delta/\overline{u_\tau}$, where $\overline{u_\tau} = (u_{\tau h} + u_{\tau c})/2$ is the mean friction velocity, $u_{\tau h}$ and $u_{\tau c}$ being the friction velocities of the hot and cold walls, respectively.

Due to the difference in densities and viscosities the hot and cold walls have different friction Reynolds numbers. A friction Reynolds number needs to be defined in order to characterize the channel flow problem as a whole. Let us define this friction Reynolds number as $\mathrm{Re}_\tau = \frac{\rho_0 u_\tau \delta}{\mu_{\mathrm{ref}}}$, where $u_\tau = \sqrt{\frac{\tau_{wh} + \tau_{wc}}{2\rho_0}}$ is the reference friction velocity based on the averaging of hot and cold wall stresses and μ_{ref} is the reference viscosity corresponding to temperature T_{ref}. Applying global momentum balance over the entire channel, assuming statistically steady state, we get the following relationship between the driven force in the streamwise direction F_x and the wall stresses:

$$2F_x\delta = \tau_{wh} + \tau_{wc} = 2\rho_0 u_\tau^2$$

Making use of this relationship, the friction Reynolds number is expressed in terms of the driving force as

$$\mathrm{Re}_\tau = \frac{\sqrt{F_x \rho_0 \delta^3}}{\mu_{\mathrm{ref}}}$$

Fixing the driving force to $F_x = 1\mathrm{N/m}$, and the reference viscosity to $\mu_{\mathrm{ref}} = \frac{1}{180}\ \mathrm{Kg\ m^{-1}s^{-1}}$ it is imposed $\mathrm{Re}_\tau = 180$.

4.6.2 Solution of the mean numerical equations applied to the turbulent channel flow

In this section we specialize the mean numerical equations (4.55)-(4.57) to the turbulent channel problem. The flow is assumed to be fully developed, so that a statistically steady state has been reached. Due to periodic boundary conditions, the average of the unknowns of the problem are assumed to be uniform in x and z directions, that is, $\frac{\partial}{\partial x}\bar{f} = \frac{\partial}{\partial z}\bar{f} = 0$ for $f = \boldsymbol{u}_h, p_h, T_h, \rho^h, \widetilde{\boldsymbol{u}}, \widetilde{p}, \widetilde{T}$. The time averaged unknowns are assumed to depend only on the y direction, so the corresponding equations must be one-dimensional. To understand the behavior of the one-dimensional time averaged unknowns, the assumptions described are applied to Eqs. (4.55)-(4.57) for the mean variables. Introducing again the notation $\boldsymbol{a} = \boldsymbol{u}_h + \widetilde{\boldsymbol{u}}$, after an integration by parts we get

$$\left(\overline{\rho^h}\widehat{a_y}, \partial_y q_h\right) = 0 \tag{4.59}$$

$$\left(\overline{\rho^h}\hat{a}_y^2 + \bar{\rho}^h\widehat{a_y''^2} - \frac{4}{3}\overline{\mu\partial_y u_{hy}} + \bar{p}_h + \bar{\widetilde{p}}, \partial_y v_{hy}\right) = \left(\overline{\nabla\cdot\left(\rho^h\boldsymbol{a}\right)u_{hy}}, v_{hy}\right) \tag{4.60}$$

$$\begin{aligned}\left(\partial_y\left(\overline{\rho^h}\hat{a}_y\hat{a}_x + \overline{\rho^h}\widehat{a_y''a_x''} - \overline{\mu\partial_y u_{hx}}\right), v_{hx}\right) &= \left(F_x, v_{hx}\right)\\ &+ \left(\overline{\nabla\cdot\left(\rho^h\boldsymbol{a}\right)u_{hx}}, v_{hx}\right)\end{aligned} \tag{4.61}$$

$$\left(\overline{k\partial_y T_h} - c_p\overline{\rho^h}\left(\hat{a}_y\hat{T}_h + \widehat{a_y''T_h''} + \hat{a}_y\widehat{\widetilde{T}} + \widehat{a_y''\widetilde{T}''}\right), \partial_y w_h\right) = \left(\overline{\nabla\cdot\left(\rho^h\boldsymbol{a}\right)T_h}, w_h\right) \tag{4.62}$$

Remark When the conservative form is used, all terms of the form $\left(\overline{\nabla\cdot\left(\rho^h\boldsymbol{a}\right)f_{hy}}, g_{hy}\right)$ in (4.60)- (4.62) disappear. When the skew formulation is used, those terms appear multiplied by a factor 0.5. □

From Eq. (4.59) it is seen that the solution to Eqs. (4.59)-(4.62) has wall-normal velocity components such $\left(\widehat{u_{hy}} + \widehat{\widetilde{u}_y}\right)$ projected onto the space where $\overline{\rho^h}\ \partial_y q_h$ belongs is zero. This is a good approximation to the continuous solution, which satisfies $\overline{\rho u_y} = 0$ (see Eq. (4.47), now reading $\partial_y\left(\overline{\rho}\widehat{u}_y\right)$). Note that the Reynolds average of the wall normal component of velocity is equal to zero (i.e., $\overline{u_y} = 0$) only for incompressible flows.

Results of Favre mean vertical velocity across the channel, that should be close to zero, are depicted in Fig. 4.5, in Section 4.7. These values are much lower than the Reynolds mean of vertical velocity shown in Fig. 4.6, specially for the case of higher temperature ratio.

The **wall-normal numerical** mean momentum equation (4.60) is obtained testing against $\boldsymbol{v}_h = (0, v_{hy}, 0)$ in (4.56). We need to make some approximations to this equation in order to obtain a solution, and be able to characterize the behavior of the mean unknowns. Making use of the mean mass conservation statement (4.59) we will consider the terms $\left(\bar{\rho}^h\hat{a}_y^2, \partial_y v_{hy}\right)$ and $\left(\overline{\nabla\cdot\left(\rho^h\boldsymbol{a}\right)u_{hy}}, v_{hy}\right)$ to be negligible compared to all other terms. The viscous term $\frac{4}{3}\left(\overline{\mu\partial_y u_{hy}}, \partial_y v_{hy}\right)$ can be shown to be very small with respect to all other terms by dimensional analysis, and it will be omitted. After these hypotheses the mean wall-normal balance of momentum reads

$$\left(\bar{\rho}^h\widehat{a_y''a_y''} + \bar{p}_h + \bar{\widetilde{p}}, \partial_y v_{hy}\right) \approx 0 \tag{4.63}$$

and a uniform distribution of the sum $\bar{\rho}^h\widehat{a''_y a''_y} + \bar{p}_h + \bar{\widetilde{p}}$ satisfies Eq. (4.63). As the fluctuation $\bar{\rho}^h\widehat{a''_y a''_y}$ vanishes at the walls, $\bar{p}_h + \bar{\widetilde{p}}$ should be greater at the walls and decrease towards the center of the channel. This result is shown in Fig. 4.8 in Section 4.7.

The **streamwise-mean numerical** momentum equation (4.61) is obtained testing Eq. (4.56) against $\boldsymbol{v}_h = (v_{hx}, 0, 0)$. Making use of mean mass conservation equation (4.59), the terms $\left(\bar{\rho}^h\hat{a}_y, \hat{a}_x\partial_y v_{hx}\right)$ and $\left(\overline{\nabla\cdot(\rho^h\boldsymbol{a})\,u_{hx}}, v_{hx}\right)$ are considered to be negligible. After these hypothesis the mean streamwise momentum balance reads

$$(\partial_y\tau_h, v_{hx}) = \left(\partial_y\left(\bar{\rho}^h\widehat{a''_y a''_x} - \overline{\mu\partial_y u_{hx}}\right), v_{hx}\right) \approx (F_x, v_{hx}) \tag{4.64}$$

Here we have defined the **discrete mean shear stress** τ_h such that it compensates the driving force F_x. A linear distribution of τ_h satisfies (4.64). The **discrete shear stress** is decomposed as $\tau_h = \bar{\rho}^h\widehat{u''_{hy}u''_{hx}} - \overline{\mu\partial_y u_{hx}} + \bar{\rho}^h\left(\widehat{u''_{hy}\widetilde{u}''_x} + \widehat{\widetilde{u}''_y u''_{hx}} + \widehat{\widetilde{u}''_y\widetilde{u}''_x}\right)$, and these three terms are identified respectively as the resolvable Reynolds shear stress (like in a LES model), the viscous shear stress and the modeled SGS shear stress. The modeled SGS shear stress depends on the subscales, and can be identified with the modeled SGS shear stress $\overline{\mu_{\text{tur}}\partial_y u_x}$ when using LES models, μ_{tur} being the turbulent viscosity (see for example [96]). At the walls only the viscous shear stress contributes to τ_h, so it is equal to τ_{wc} and τ_{wh} at cold and hot walls, respectively, having a linear variation along the channel section. It is an usual practice when solving the turbulent channel flow using LES models to show the obtained distribution of τ_h. This distribution is shown in Fig. 4.13. When the obtained distribution is linear it can be said that statistically steady state has been reached and average forces are in equilibrium.

In the **mean energy numerical** equation (4.62), the terms $\left(\overline{\rho^h}\hat{a}_y(\hat{T}_h + \widetilde{T}), \partial_y w_h\right)$ and $\left(\overline{\nabla\cdot(\rho^h\boldsymbol{a})\,T_h}, w_h\right)$ are neglected due to the mean mass conservation equation (4.55). After these hypothesis the mean energy numerical equation reads

$$(Q_h, \partial_y w_h) = \left(-\overline{k\partial_y T_h} + c_p\overline{\rho^h}\left(\widehat{u''_{hy}T''_h} + \widehat{u''_{hy}\widetilde{T}''} + \widehat{\widetilde{u}''_y T''_h} + \widehat{\widetilde{u}''_y\widetilde{T}''}\right), \partial_y w_h\right) \approx 0 \tag{4.65}$$

where

$$Q_h = c_p\overline{\rho^h}\widehat{u''_{hy}T''_h} - \overline{k\partial_y T_h} + c_p\overline{\rho^h}\left(\widehat{u''_{hy}\widetilde{T}''} + \widehat{\widetilde{u}''_y T''_h} + \widehat{\widetilde{u}''_y\widetilde{T}''}\right)$$

is the total mean heat flux. The three terms composing Q_h represent respectively the resolvable turbulent heat flux, the heat conduction, and the modeled SGS heat flux. Note that a uniform Q_h in y satisfies the above equation. If the obtained distribution of the turbulent heat flux Q_h is uniform in the numerical results, then statistically steady state has been reached for temperature. At the walls only the heat conduction contributes to Q_h, being over the walls $Q_h = \pm\overline{k\partial_y T_h}|_{y=\pm\delta}$. The obtained distributions of Q_h are shown in Fig. 4.14, showing a uniform distribution.

4.6.3 Dissipative equations for the turbulent channel flow

In turbulent flows we are interested in kinetic energy conservation, dissipation, transfer mechanisms, etc. Kinetic energy conservation in the steady state turbulent channel flow follows from applying Reynolds' averaging to the conservation equation (4.35), giving for the continuous problem

$$\int_\Omega \overline{F_x u_x} = \int_\Omega 2\overline{\mu\boldsymbol{\varepsilon}' \colon \boldsymbol{\varepsilon}'} - \int_\Omega \overline{p\nabla\cdot\boldsymbol{u}}$$

meaning that the power done by the force $\boldsymbol{F}$ is balanced by viscous dissipation and pressure work. For the discrete problem, after applying Reynolds' averaging to the kinetic conservation equation (4.36)-(4.43) and neglecting Eq. (4.43) because linear interpolation is assumed, we get

$$\int_\Omega \overline{F_x u_{hx}} = \int_\Omega F_x \overline{u_{hx}} = \int_\Omega 2\overline{\mu\boldsymbol{\varepsilon}' : \boldsymbol{\varepsilon}'} - \int_\Omega \overline{p_h \nabla\cdot\boldsymbol{u}_{hK}} \tag{4.66}$$

$$-\sum_K \int_K \overline{\widetilde{\boldsymbol{u}}\cdot(\rho^h \boldsymbol{u}_h \cdot \nabla\boldsymbol{u}_h)} \tag{4.67}$$

$$-\sum_K \int_K \overline{\widetilde{\boldsymbol{u}}\cdot(\rho^h \widetilde{\boldsymbol{u}} \boldsymbol{\cdot} \boldsymbol{\nabla}\boldsymbol{u}_h)} \tag{4.68}$$

$$-\sum_K \int_K \overline{\widetilde{p}\nabla\cdot\boldsymbol{u}_h} \tag{4.69}$$

$$+\sum_K \int_K \overline{\frac{\partial}{\partial t}(\rho^h\widetilde{\boldsymbol{u}})\cdot\boldsymbol{u}_h} \tag{4.70}$$

The power done by the force $\boldsymbol{F}$ is balanced by viscous dissipation and pressure work in the first row. The remaining terms should model the viscous dissipation of the unresolved scales of the flow. The last term (4.70) is not null due to correlations between $\widetilde{\boldsymbol{u}}$ and $\boldsymbol{u}_h$. However, this term is zero when orthogonal subgrid scales are considered. The total numerical dissipation is thus

$$\bar{\varepsilon}_{\text{num}} = -\sum_K \int_K \overline{\widetilde{\boldsymbol{u}}\cdot(\rho^h \boldsymbol{u}_h \cdot \nabla\boldsymbol{u}_h)} - \sum_K \int_K \overline{\widetilde{\boldsymbol{u}}\cdot(\rho^h \widetilde{\boldsymbol{u}} \boldsymbol{\cdot} \boldsymbol{\nabla}\boldsymbol{u}_h)} - \sum_K \int_K \overline{\widetilde{p}\nabla\cdot\boldsymbol{u}_h} + \sum_K \int_K \overline{\frac{\partial}{\partial t}(\rho^h\widetilde{\boldsymbol{u}})\cdot\boldsymbol{u}_h} \tag{4.71}$$

The numerical dissipation is proportional to the value of the subgrid components $\widetilde{\boldsymbol{u}}$ and $\widetilde{p}$.

4.7 Numerical results

In this section results for the turbulent channel flow are presented. As usual results are averaged in time within the statistical period and in space over the two homogeneous spatial directions. A snapshot of the velocities and temperature distribution inside the channel when $T_2/T_1 = 2$ is shown in Fig. 4.1, with the only purpose of having a general view of the flow.

It is known that the use of stabilization techniques as SUPG using trilinear elements to solve turbulent problems introduce too much numerical dissipation. On the other hand, as showed in chapter 3, the present DSS and OSS methods are less dissipative and more accurate than the SUPG method, at least for laminar flows. [2]. Nevertheless, excellent results have been obtained recently in Trofimova et al [92], for the turbulent channel flow using only SUPG stabilization without any turbulence model, tunning the stabilization parameter in order to add the

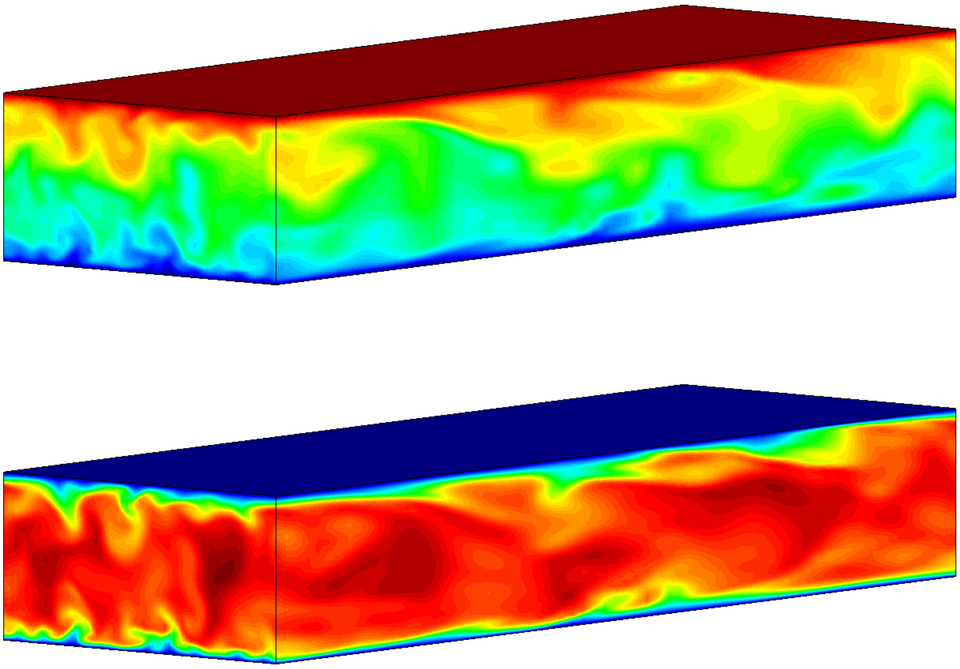

Figure 4.1: Snapshot of temperature (top) and velocity (bottom) distribution inside the turbulent channel for the case $T_2/T_1 = 2$.

smallest possible amount of numerical dissipation. The obtained results were also better than those obtained using advanced LES model over the same mesh. Tejada and Jansen [89] solved the turbulent channel flow using SUPG stabilization together with the dynamic Smagorinsky model, showing that better results are obtained when the introduced numerical dissipation is diminished, thus concluding that numerical dissipation does not behave like physical dissipation. It is our aim to show that numerical dissipation introduced by DSS and OSS methods behaves as physical, in the sense that our numerical results display the characteristic features of turbulent flows

We have observed in our numerical model that the results improve when less numerical dissipation is introduced (comparing to DNS given by Moser et al [71]). We have also observed that the numerical dissipation comes mainly from cross dissipation and from the work of the pressure subscale terms (4.67) and (4.69) in the kinetic energy conservation balance. As depicted in Fig 4.15 those terms are dominant respect to all other dissipative terms in Eq. (4.71). Numerical dissipation depends on the value of the subgrid components $\widetilde{\boldsymbol{u}}$ and $\widetilde{p}$. Due to the highly anisotropic shape of the elements, we have found crucial to define h in (4.27)-(4.29) as the element length in $y-$direction, being the minimum element length in almost all domain. In this way lower values for τ_m and τ_c are obtained, and therefore the introduced amount of numerical dissipation is lower. As the mesh is non uniform, the obtained $y-$distribution of the stabilization parameters τ_c, τ_m and τ_e are discontinuous and highly oscillatory element by element. We have observed that to smooth the stabilization parameters improves the obtained results. The results that we show in this section have been obtained using the minimum ele-

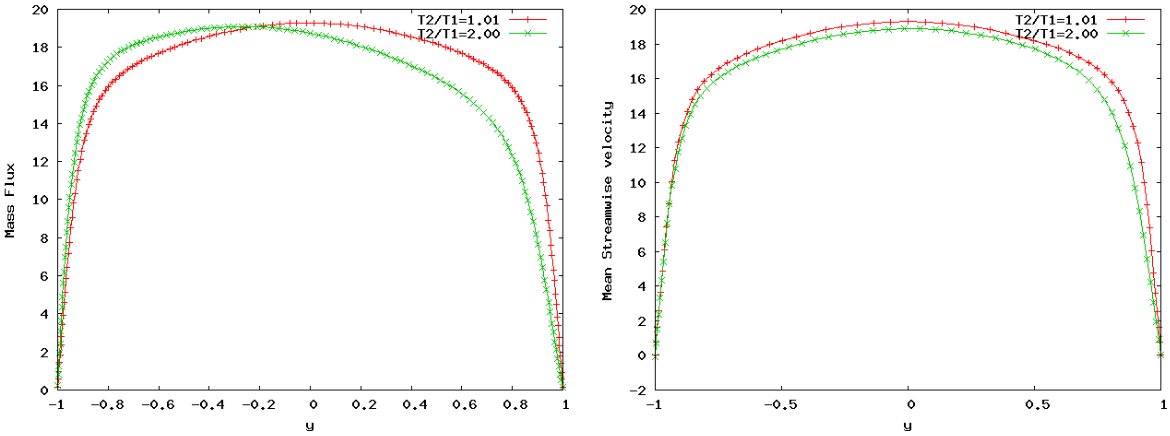

Figure 4.2: Mean profile of velocity (right) and mass flux ρu_x across the channel (left) for cases $T_2/T_1 = 1.01$ and $T_2/T_1 = 2$. Mesh of 64^3 elements and DSS method

ment length h and smoothing the obtained stabilization parameters. This smoothing is done by projecting the mesh size h over the finite element space, obtaining a continuous distribution of h and then smoothed stabilization parameters.

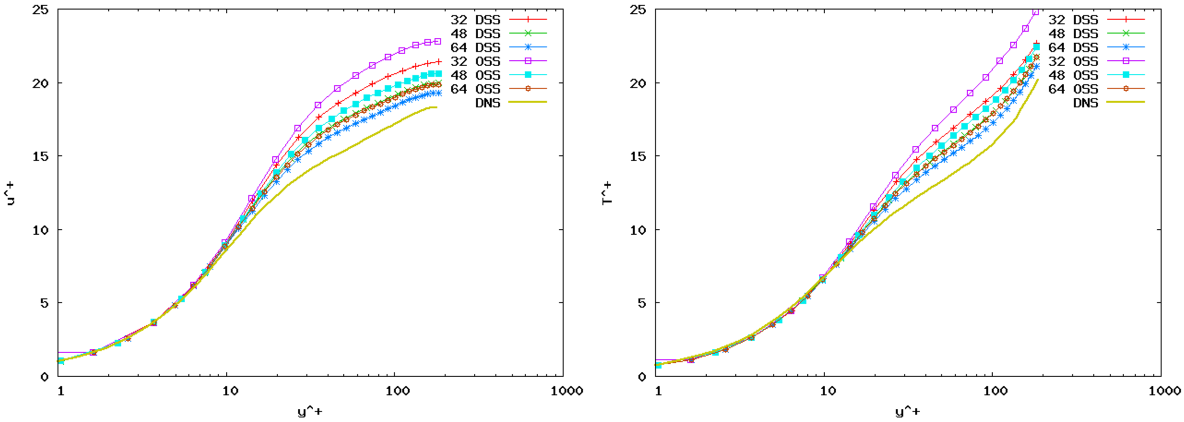

Figure 4.3: Mean profile of velocity (left) and temperature (right) for the case $T_2/T_1 = 1.01$ using the DSS and OSS methods.The number of elements per direction is indicated in the legends.

We have tried to solve the present problem using SUPG stabilization only, finding that stabilization parameters τ_m, τ_e need to depend on time step size Δt to obtain a stable solution. Otherwise the nonlinear system of equations is unable to converge. To consider τ_m and τ_e depending on Δt and to consider the subscales not time dependent is inconsistent, because the steady-state solution (in case of being reached) would depend on the time step size [27].

For the high temperature ratio problem $T_2/T_1 = 2$, Nicoud [74] found Reynolds values of $\mathrm{Re}_{\tau c} = 200$ and $\mathrm{Re}_{\tau h} = 82$ over cold and hot walls using Sutherland's law for viscosity and conductivity, as in Eq. (4.4). The friction Reynolds number over the hot wall is too low to maintain full turbulence, therefore the solution could reflect low-Reynolds number effects. For greater temperature ratios T_2/T_1 the Reynolds number over the hot wall is expected to be smaller. To overcome this low Reynolds problem some authors assume that viscosity and

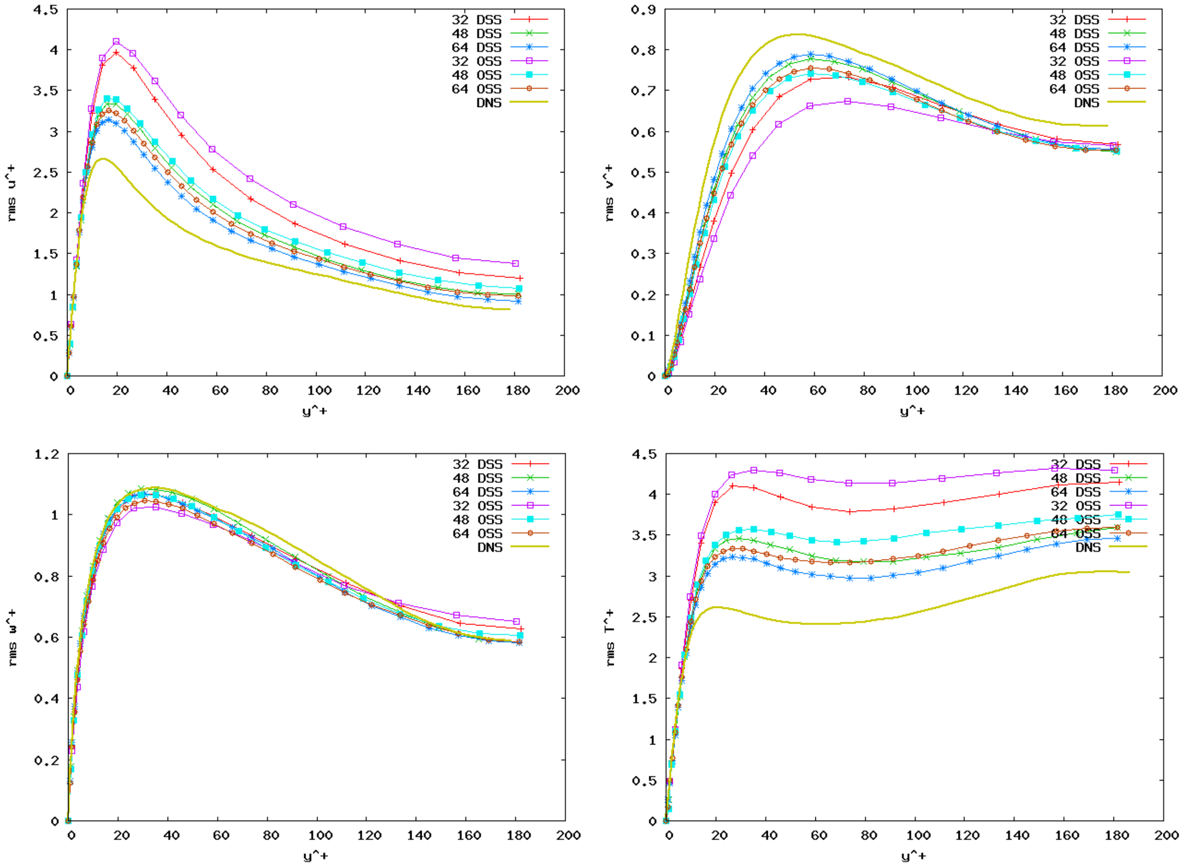

Figure 4.4: Velocity and temperature fluctuations for the case $T_2/T_1 = 1.01$ using DSS and OSS methods. The number of elements per direction is indicated in the legends.

thermal conductivity decrease with temperature as $\mu, k \propto 1/\sqrt{T}$, being this kind of behavior relevant to a liquid. The advantage of assuming this temperature dependence is that the friction Reynolds number over the hot wall is not too small in comparison with the value over the cold wall, obtaining a more symmetric solution, and therefore being able to use a symmetric mesh.

Fig. 4.2 on the left depicts mass flow rate per unit area across the channel. It is seen that for the lower heat transfer case the mass flow is nearly symmetric since the density is nearly constant, whereas for the case $T_2/T_1 = 2$ the mass flow on the cold wall side is considerably larger than that on the hot wall side due to density variation across the channel. The right of Fig. 4.2 depicts mean velocity across the channel for cases $T_2/T_1 = 1.01$ and $T_2/T_1 = 2$. For the high ratio case $T_2/T_1 = 2$ velocity profile does not deviate much from the low cooling/heating case $T_2/T_1 = 1.01$. But as will be shown shortly, the deviations are nevertheless quite significant when plotted in wall coordinates y^+. Upon a closer examination, it is found that the slope of the velocity profile is steeper on the cold side ($y \to -1$) than on the hot side ($y \to +1$).

Considering that a uniform heat flux Q_h satisfies the energy conservation Eq. (4.65), the wall heat flux must be the same through the hot and cold walls, i.e., $\overline{k\partial_y T_h} \mid_h = \overline{k\partial_y T_h} \mid_c$. Therefore, temperature profiles will be steeper close to the cold wall due to Sutherland's law.

The flow and heat transfer parameters of interest for both heat transfer cases are listed

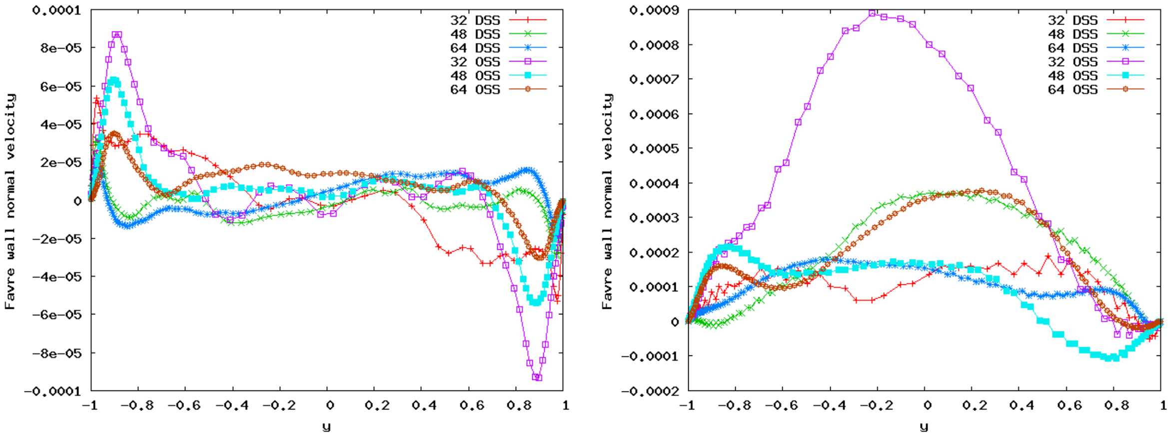

Figure 4.5: Favre average profile of wall normal velocity for cases $T_2/T_1 = 1.01$ (left) and $T_2/T_1 = 2.00$ (right) using the DSS and OSS methods. The number of elements per direction is indicated in the legends.

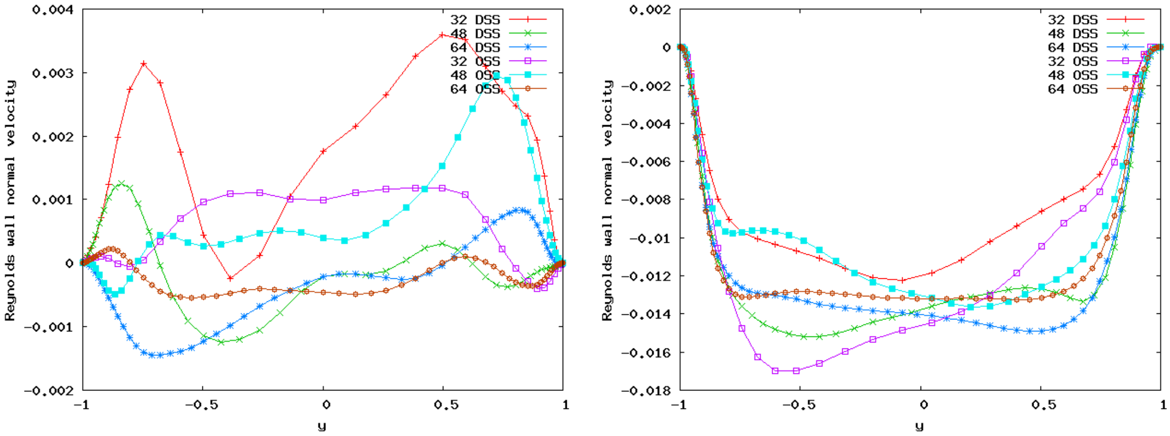

Figure 4.6: Reynolds average profile of wall normal velocity for cases $T_2/T_1 = 1.01$ (left) and $T_2/T_1 = 2.00$ (right) using the DSS and OSS methods. The number of elements per direction is indicated in the legends.

in Table 4.1 and Table 4.2 against DNS data. The friction Reynolds number at the cold and hot walls are denoted as $\mathrm{Re}_{\tau c}$ and $\mathrm{Re}_{\tau h}$, respectively, and are compared against the values obtained by Nicoud in [75] for the nearly incompressible case, and against the values obtained by Nicoud in [73] for the most compressible case. The friction Reynolds numbers obtained for the high compressible case by Nicoud differ a little from those obtained in the present work. This is due because the Prandtl number that was set to $\mathrm{Pr} = 0.76$ by Nicoud, and to $\mathrm{Pr} = 0.71$ in the present work. The friction values are very sensitive to the conductivity values over the wall.

The bulk Reynolds number in Table 1 and Table 2 is defined as

$$\mathrm{Re}_b = \frac{\rho_m U_m \delta}{\mu_m} \tag{4.72}$$

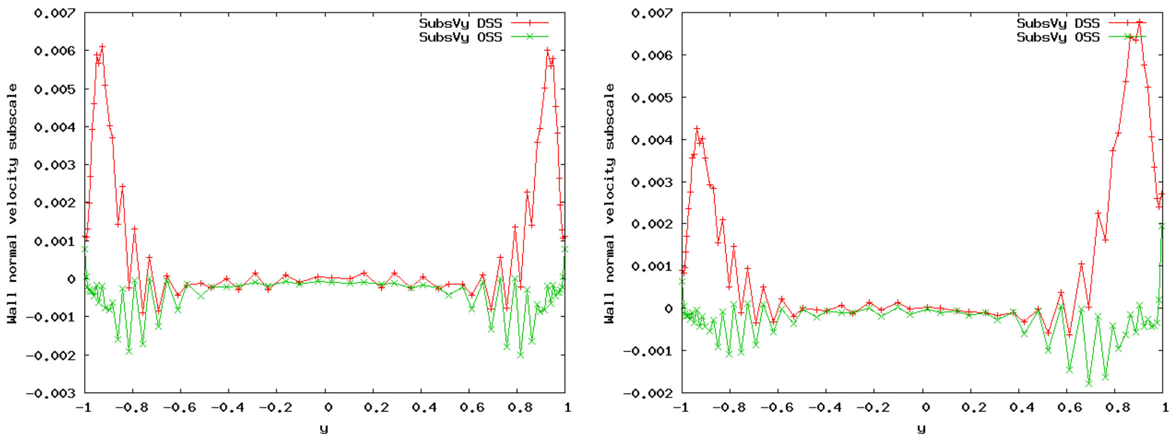

Figure 4.7: Mean profile of wall normal subgrid scale velocity for cases $T_2/T_1 = 1.01$ (left) and $T_2/T_1 = 2$ (right) using the DSS and OSS methods over the coarsest grid of 32^3 elements.

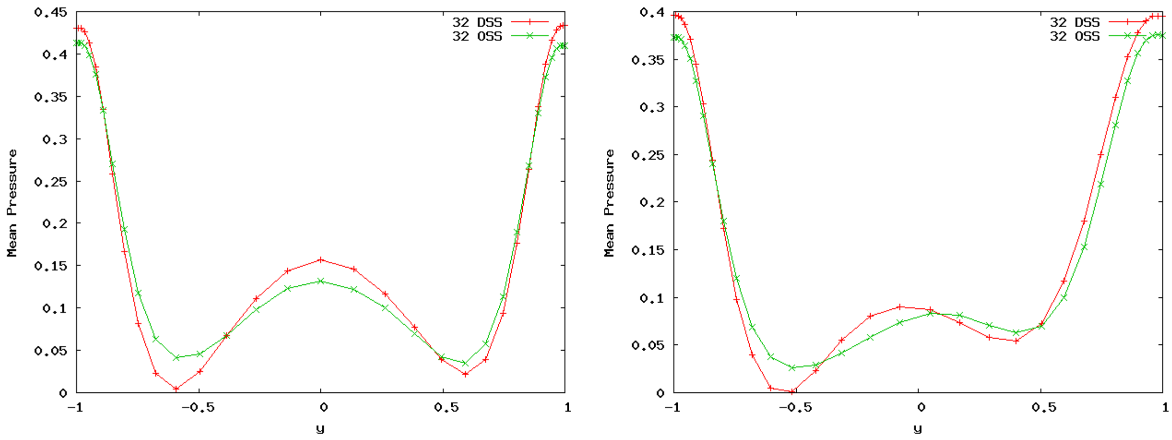

Figure 4.8: Mean profile of pressure for cases $T_2/T_1 = 1.01$ (left) and $T_2/T_1 = 2.00$ (right) with coarser mesh 32^3 using the DSS and OSS methods.

where

$$\rho_m = \frac{1}{2\delta}\int_{-\delta}^{+\delta} \bar{\rho}\, dy, \quad U_m = \frac{1}{2\delta\rho_m}\int_{-\delta}^{+\delta} \bar{\rho}\hat{u}_x\, dy$$

The bulk viscosity μ_m is evaluated at the bulk temperature T_m, defined as

$$T_m = \frac{1}{2\delta\rho_m U_m}\int_{-\delta}^{+\delta} \bar{\rho}\widehat{u_x T}\, dy$$

The Nusselt number is

$$\mathrm{Nu} = \frac{4}{T_m^+}\frac{\partial T^+}{\partial y}\bigg|_{\mathrm{wall}}$$

where

$$T_m^+ = \frac{\mid T_w - T_m \mid}{T_\tau}$$

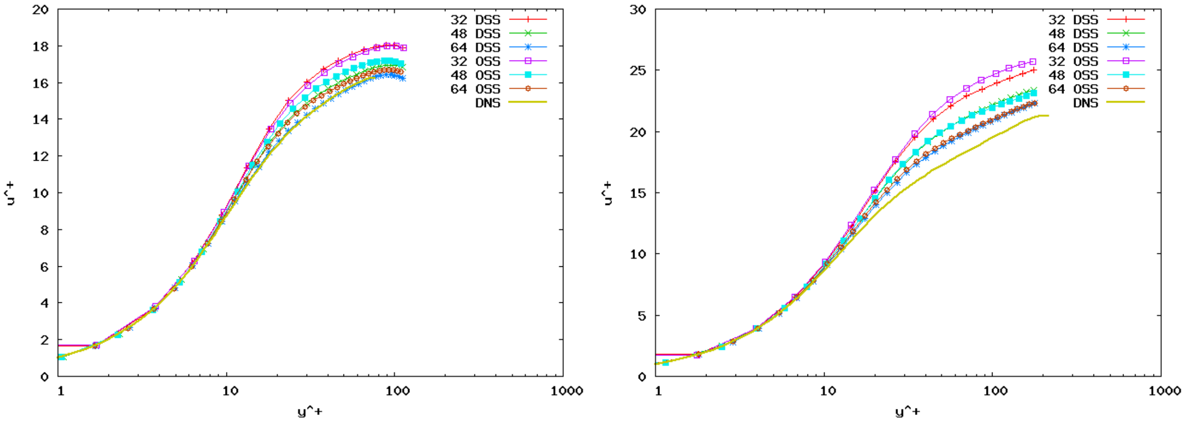

Figure 4.9: Mean profile of velocity for the case $T_2/T_1 = 2$ using the DSS and OSS methods against DNS (left: Cold wall, right: Hot wall).

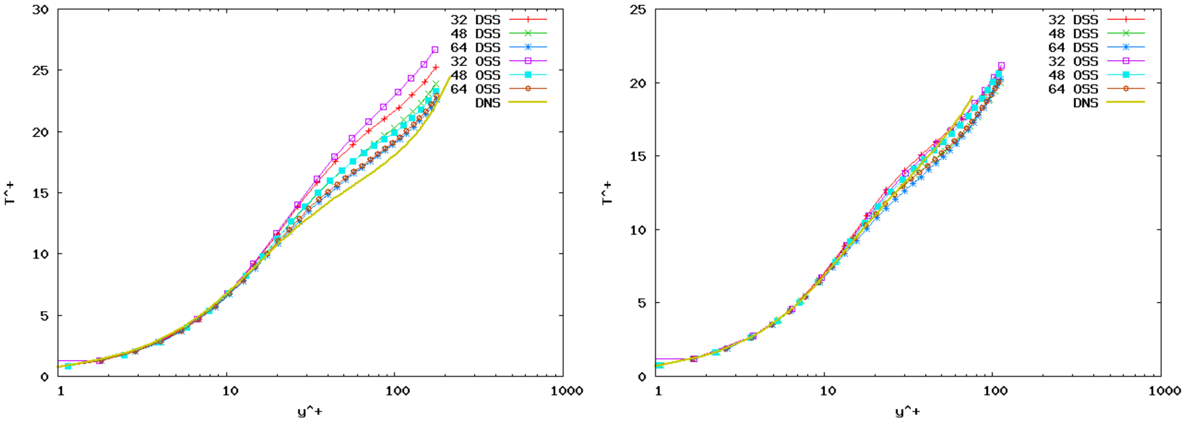

Figure 4.10: Mean profile of temperature for the case $T_2/T_1 = 2$ using the DSS and OSS methods (left: Cold wall, right: Hot wall).

and the subscript w indicates that the property is evaluated over the wall. The friction temperature T_τ and the wall heat flux q_w are

$$T_\tau = q_w/(\rho_w c_p u_\tau), \quad q_w = -k_w \frac{\partial T_w}{\partial n}$$

and $T^+ = \frac{|T - T_w|}{T_\tau}$ is a dimensionless temperature scaled by the friction temperature. Finally, the heat flux wall parameter B_q is

$$B_q = \frac{q_w}{\rho_w c_p u_{\tau w} T_w}$$

The friction factor at the wall C_f is based on the mean density on the channel ρ_m and the maximum velocity $U_{\max}$. It is defined as

$$C_f = \frac{2\tau_w}{\rho_m U_{\max}^2}$$

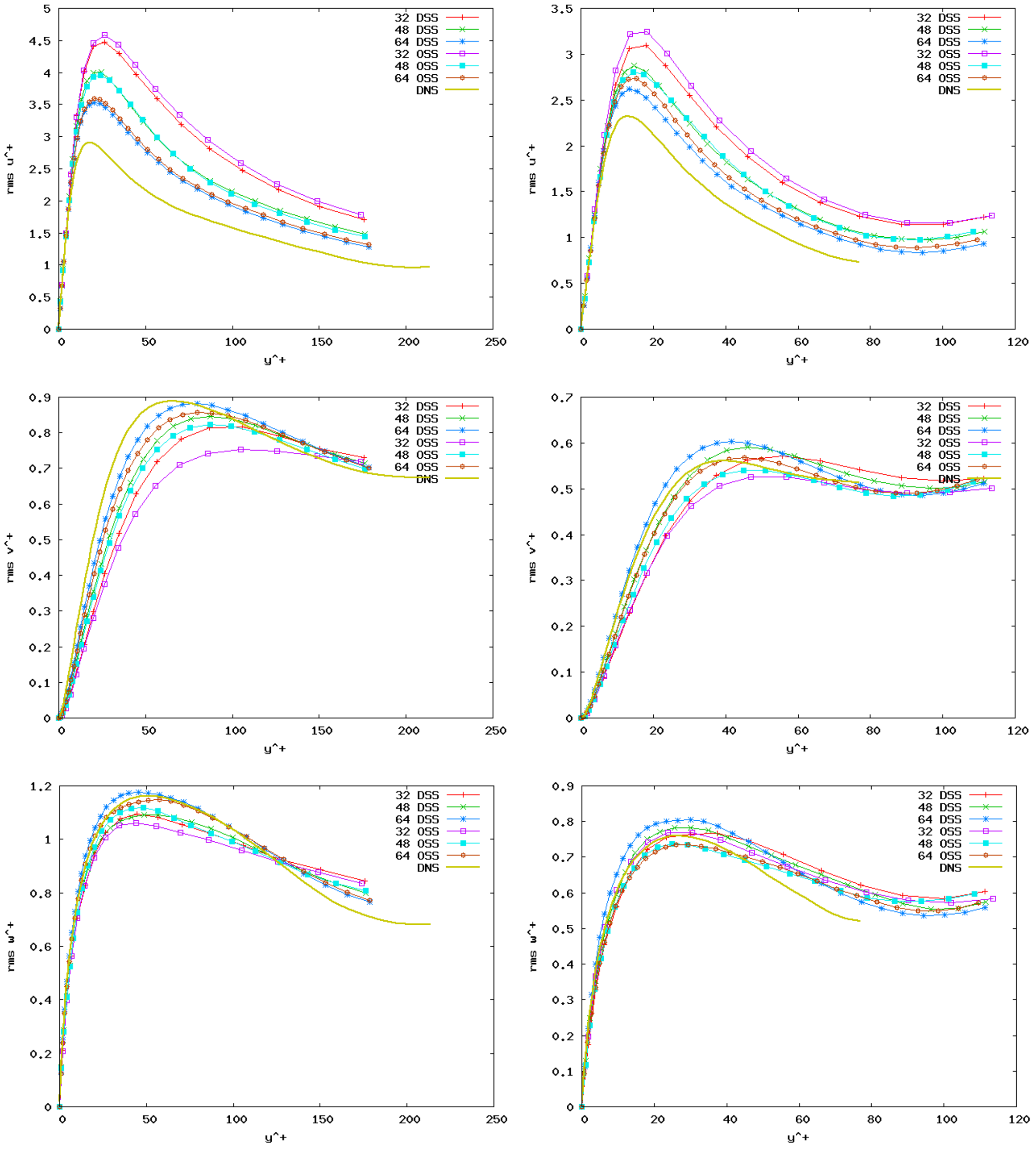

Figure 4.11: Velocity fluctuations for the case $T_2/T_1 = 2$ using the DSS and OSS methods(left: Cold wall, right :Hot wall).

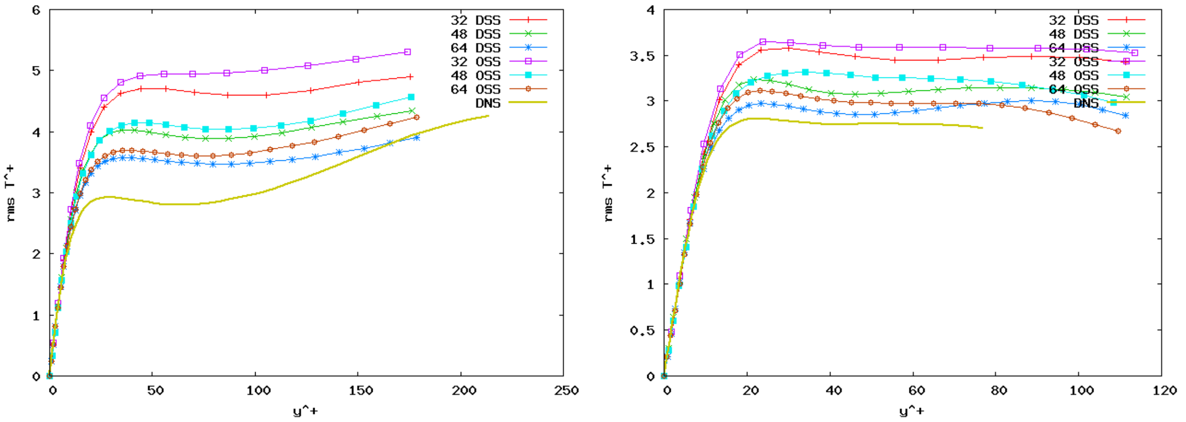

Figure 4.12: Root mean square of temperature and Correlation of velocity and temperature fluctuations for the case $T_2/T_1 = 2$ using the DSS and OSS methods (left: Cold wall, right :Hot wall).

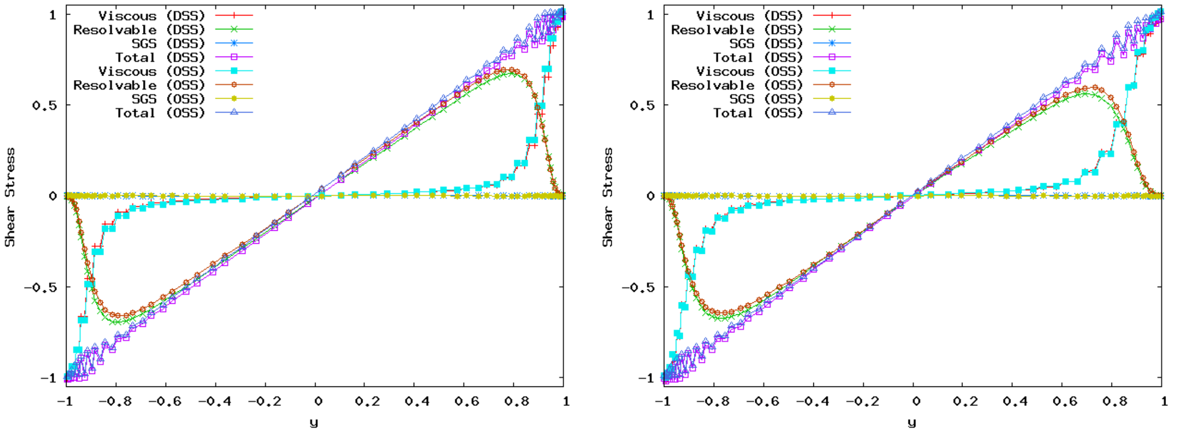

Figure 4.13: Shear stress distribution across the channel (scaled by the mean pressure gradient F_x) for cases $T_2/T_1 = 1.01$ (left) and $T_2/T_1 = 2$ (right) using the DSS and OSS methods over the coarsest grid of 32^3 elements.

For the incompressible case the tabulated values are over the cold wall, and are compared against the DNS data from [75]. The obtained Nusselt numbers are compared to DNS values referred in [96]. For the highly compressible case $T_2/T_1 = 2$ the tabulated values are compared to the DNS data from [75].

For both cases the bulk Reynolds numbers are larger than DNS data. All results converge to DNS values as mesh is refined. Slightly better values are obtained using the DSS method than when using the OSS method.

Fig. 4.3 depicts mean streamwise velocity profiles for the case $T_2/T_1 = 1.01$, scaled by the wall shear stress velocity, $u^+ = \frac{u}{u_\tau}$ for the three meshes using the DSS and OSS methods. Results are compared against DNS data for incompressible flow, given in [71]. For all discretizations it can be observed that the results obtained with the DSS method are closer to DNS data than those obtained with the OSS method. This happens because, as it will be shown later, the DSS method is less dissipative. Note that this is an effect due to the evolution in time of the subscales and the time correlations that contribute to the numerical dissipation (4.71),

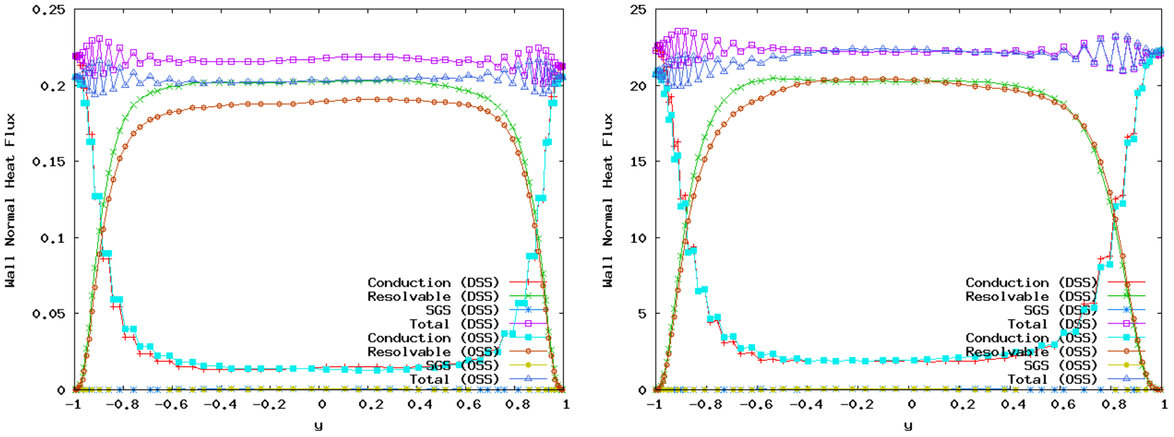

Figure 4.14: Thermal energy balance across the channel for cases $T_2/T_1 = 1.01$ (left) and $T_2/T_1 = 2$ (right) using the DSS and OSS methods over the coarsest grid of 32^3 elements.

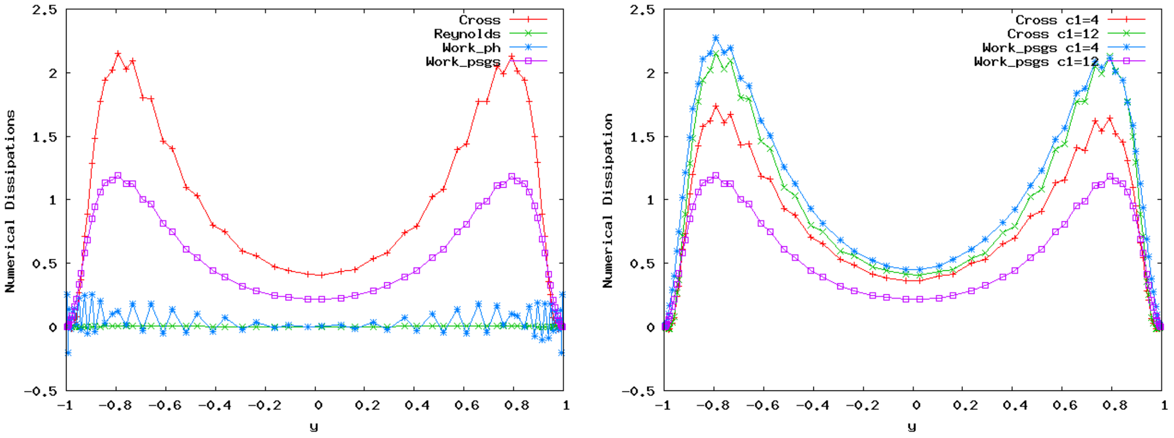

Figure 4.15: Numerical dissipation components along the channel (left), and comparison of cross dissipation and work of subscale pressure using $c_1 = 4$ and $c_1 = 12$ (right) for the case $T_2/T_1 = 1.01$ using the DSS method over the coarsest grid of 32^3 elements.

because by its structure the OSS method is always less dissipative in space.

We have also observed that setting $c_1 = 12$ in (4.27)-(4.29) instead of setting $c_1 = 4$ as in chapter 3 improves significantly the obtained mean values and fluctuations of the unknowns (being closer to DNS data). As explained in Section 4.3, this is due because fixing $c_1 = 12$ lowers the value of τ_c, reducing the numerical dissipation introduced by the pressure subscale (4.40). It is worth noting that setting $c_1 = 12$ gives the exact asymptotic value for the advection diffusion equation using one-dimensional uniform mesh.

On the right of Fig. 4.3 the mean temperature profiles scaled by wall temperature, $T^+ = \frac{|T-T_w|}{T_\tau}$, where $T_\tau = q_w/(\rho_w c_p u_\tau)$ and $q_w = -k_w \frac{\partial T_w}{\partial n}$, for the case $T_2/T_1 = 1.01$ over the three meshes are shown. As for the velocity profile, it is seen that better temperature profiles are predicted using the DSS method than using the OSS method. The reason of this misbehavior of the OSS method is again because it is more dissipative.

Root-mean-square values of streamwise, spanwise and wall normal velocities are shown in Fig. 4.4 for the case $T_2/T_1 = 1.01$ compared against DNS data by Moser et al [71]. The

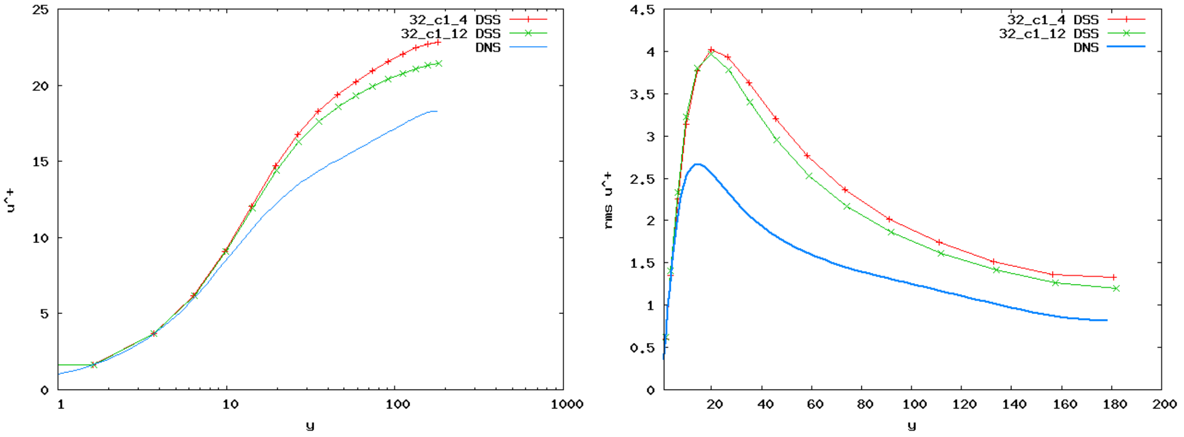

Figure 4.16: Mean velocity profile (right) and its root mean square value using $c_1 = 4$ and $c_1 = 12$ for the case $T_2/T_1 = 1.01$ using the DSS method over the coarsest grid of 32^3 elements.

Mesh-method	$\mathrm{Re}_{\tau c}$	$\mathrm{Re}_{\tau h}$	Re_b	$10^3 C_f$	Nu
32DSS	182	178	3378	4.4	22.6
48DSS	181	178	3143	5.0	23.6
64DSS	182	179	3034	5.4	24.4
32OSS	180	180	3558	3.9	20.8
48OSS	182	178	3255	4.7	23.0
64OSS	182	178	3126	5.1	23.7
DNS	185	182	2855	6.1	21.0

Table 4.1: Mean flow and heat transfer parameters for the channel flow when $T_2/T_1 = 1.01$. The number of elements per direction is indicated in the mesh-method definition.

obtained results overpredict velocity fluctuation in streamwise direction, but underpredict fluctuation in wall-normal and spanwise directions.

Root-mean-square values of temperature are shown in Fig. 4.4 for the case $T_2/T_1 = 1.01$, comparing them to DNS data. Temperature fluctuation and its correlation with velocity are overpredicted when comparing against DNS data.

As the case is nearly incompressible, all results have been shown only for the cold wall. Results for the hot wall are in agreement with the ones for the cold wall with differences lower than 1%.

Fig. 4.5 depicts the Favre average of wall normal velocity profiles for all discretizations using the DSS and OSS methods for cases $T_2/T_1 = 1.01$ and $T_2/T_1 = 2$. These values should be close to zero according to the discrete continuity Eq. (4.59). For both heat transfer cases the obtained Favre values are of the same order of magnitude. As it is shown in Fig. 4.6, Reynolds average values of wall normal velocity are much higher than the Favre average values, especially for the case of large density variation $T_2/T_1 = 2$. However, both values are of the same order of magnitude for the lower temperature ratio case $T_2/T_1 = 1.01$ due to the small density variation ratio. Close to walls the results obtained using the DSS method have opposite sign to those obtained with the OSS method. This can be explained from the solution to mass con-

Mesh-method	$\mathrm{Re}_{\tau c}$	$\mathrm{Re}_{\tau h}$	Re_b	$10^3 C_f(c)$	$10^3 C_f(h)$	$10^2 B_q(c)$	$10^2 B_q(h)$	$\mathrm{Nu}(c)$	$\mathrm{Nu}(h)$
32DSS	219	93	2406	4.7	4.5	1.82	1.29	23.4	13.3
48DSS	220	93	2247	5.3	5.1	1.91	1.36	24.6	13.9
64DSS	222	93	2169	5.8	5.5	1.99	1.36	26.0	13.9
32OSS	217	95	2431	4.4	4.6	1.70	1.29	21.8	13.3
48OSS	219	91	2290	5.4	4.9	1.83	1.39	24.8	13.3
64OSS	223	91	2239	5.7	5.2	1.83	1.45	25.4	13.8
DNS	200	82	1786	6.5	5.6	1.8	1.4	N A	N A

Table 4.2: Mean flow and heat transfer parameters for the channel flow $T_2/T_1 = 2$. (h): hot wall, (c): cold wall. The number of elements per direction is indicated in the mesh-method definition.

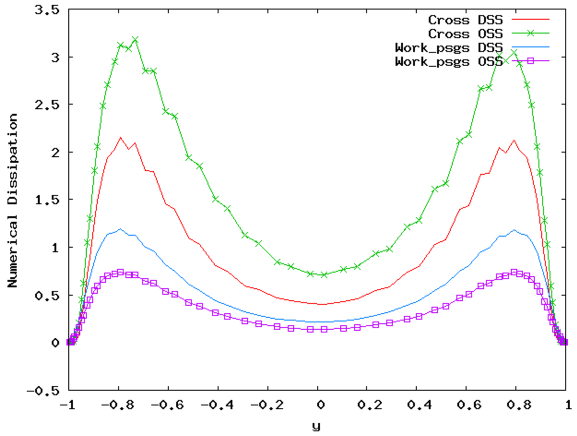

Figure 4.17: Comparison of the obtained main numerical dissipation when using the DSS and OSS methods for the case $T_2/T_1 = 1.01$ over the grid of 32^3 elements.

servation equation (4.59) and observing in Fig. 4.7 that the mean average of velocity subgrid scales have opposite sign for the DSS and OSS methods.

Fig. 4.8 depicts mean pressure profiles for the lower and higher temperature ratio cases, using the DSS and OSS methods in the coarser mesh of 32^3 elements. It is seen that the mean pressure is lower away from the walls, as predicted by the wall normal momentum Eq. (4.63). Similar results are obtained using the finer discretizations. For the almost incompressible case the pressure profile is nearly symmetric, but not for the higher compressible case.

Figs. 4.9 and 4.10 illustrate the mean streamwise velocity and mean temperature results for the higher temperature ratio $T_2/T_1 = 2$, comparing them to DNS data. It is observed that the results predicted by the DSS and OSS methods have the same accuracy for almost all cases. When using the coarse mesh of 32^3 elements the results predicted by DSS method are in some cases closer to DNS data than the ones predicted by the OSS method. The temperature difference is strong enough to induce a significant asymmetry in the mean quantities.

Root-mean-square values of streamwise, spanwise and wall normal velocities are shown in Fig. 4.11. Root-mean-square values of temperature are shown in Fig. 4.12. The predictions of the DSS and OSS methods are very similar when using fine grids. However DSS results are closer to the reference DNS data when using coarse meshes.

The shear stress distribution across the channel is illustrated in Fig. 4.13 using the coarsest mesh of 32^3 elements and both heat transfer cases. The shear stress balance was derived in Eq. (4.64) from the streamwise momentum equation. It is seen that in both heat transfer cases the contribution of the modeled shear stress is very small. This finding is in qualitative agreement with [96] at a similar Reynolds number. The total shear stress distribution is linear, implying that forces are in equilibrium, statistically steady state has been reached and the flow is fully developed. Using finer grids similar distributions were obtained for the shear stress, with the advantage that less time steps were needed to obtain a linear distribution of the total shear stress. High oscillatory distributions of the total shear stress are observed close to the walls; this is due because it is not possible to obtain a non oscillatory linear distribution adding the element by element uniform discontinuous function $\overline{\mu \partial_y u_{hx}}$ and the continuous function $\bar{\rho}^h \widehat{u''_{hy} u''_{hx}}$, both with the strong variation showed in the figure. Lower oscillations were found when finer grids were used.

Fig. 4.14 presents the normal heat flux distribution across the channel for both temperature ratio cases using the coarser mesh of 32^3 elements. The heat flux balance was derived in Eq. (4.62) from the energy equation. As for the shear stress distribution, it is observed that the modeled SGS heat flux is very small. Whereas results for the lower heat transfer case are nearly symmetric with respect to channel centerline, a shift of both heat conduction and resolvable turbulent heat flux distributions towards the cold wall is observed for the high case, due to its higher Reynolds number and the steeper boundary layer. Note that the total heat flux is constant along the channel as a consequence of the flow being fully developed. Similar distributions were obtained when using finer grids. We have observed that less time steps were needed when using finer grids to obtain a uniform distribution of the total heat flux. We have also observed that more time steps were needed to reach the statistically steady case for the high heat transfer case $T_2/T_1 = 2$.

Fig. 4.15 depicts numerical dissipation distribution along the channel for the case $T_1/T_2 = 1.01$ using the coarse mesh of 32^3 elements. There, the distributions of cross and Reynolds numerical stresses, the work of mechanical pressure and the work of pressure subscale are shown. The cross stress and the work of pressure subscales are dominant over all the other terms. The Reynolds stress term is very low because it depends on the square of the velocity subscale. This velocity subscale is much lower than the finite element component over all the domain, except very close to the walls where all dissipations are very low. The work done by the pressure subscale is higher than the work done by the mechanical pressure, because the pressure subscale $\widetilde{p}$ is highly correlated with the velocity divergence, whose mean value tends to zero in the nearly incompressible case $T_2/T_1 = 1.01$.

On the right of Fig. 4.15 the distributions of cross and pressure subscale dissipations when setting the numerical parameters $c_1 = 4$ and $c_1 = 12$ are compared. As explained in section 4.3, the obtained cross dissipation is barely sensitive to the c_1 value, obtaining very similar distributions. However, the pressure subscale dissipation is much lower when setting $c_1 = 12$, as discussed in Section 4.3, and a less dissipative scheme is obtained. In Fig. 4.16 the obtained dimensionless mean streamwise velocities and its root-mean-square values when setting $c_1 = 4$ and $c_1 = 12$ are compared against DNS values. It is observed than the obtained solutions using $c_1 = 12$ are closer to DNS value than those obtained when setting $c_1 = 4$. In Fig. 4.17 the numerical dissipations introduced by the DSS and OSS methods are compared. The cross dissipation introduced by the OSS method is considerably higher than the one introduced using the DSS method. The pressure subscale dissipation is only a little lower for the OSS method, but the combination of both makes the OSS method a more dissipative scheme. This makes the DSS method more accurate when looking at time-averaged quantities.

Due to the orthogonal projection the mean subscale values are lower using the OSS method. As it was shown in chapter 3, for laminar problems the OSS method introduces less numerical diffusion than the DSS method. Surprisingly, this is not the observed behavior in turbulent flows due to correlation in time between variables in the dissipative terms. From Eq. (4.71), the total numerical dissipation $\bar{\varepsilon}_{\text{num}}$ can be approximated by

$$\begin{aligned}
\bar{\varepsilon}_{\text{num}} &\approx -\sum_K \int_K \overline{\widetilde{\boldsymbol{u}} \cdot (\rho^h \boldsymbol{u}_h \cdot \nabla \boldsymbol{u}_h)} - \sum_K \int_K \overline{\widetilde{p} \nabla \cdot \boldsymbol{u}_h} \\
&= -\sum_K \int_K \overline{\widetilde{\boldsymbol{u}}} \cdot \overline{\rho^h \boldsymbol{u}_h \cdot \nabla \boldsymbol{u}_h} - \sum_K \int_K \overline{\widetilde{p}} \nabla \cdot \overline{\boldsymbol{u}_h} \qquad (4.73) \\
&\quad -\sum_K \int_K \overline{\widetilde{\boldsymbol{u}}' \cdot (\rho^h \boldsymbol{u}_h \cdot \nabla \boldsymbol{u}_h)'} - \sum_K \int_K \overline{\widetilde{p}' \nabla \cdot \boldsymbol{u}_h'} \qquad (4.74)
\end{aligned}$$

where it is seen that numerical dissipation depends directly on subscale values of $\widetilde{\boldsymbol{u}}$ and $\widetilde{p}$, but also on their correlation with convective and divergence terms $\rho^h \boldsymbol{u}_h \cdot \nabla \boldsymbol{u}_h$ and $\nabla \cdot \boldsymbol{u}_h$ respectively. For incompressible flows, the second term in (4.73) is almost zero, and the contribution of fluctuating terms in (4.74) is much more important. The velocity subscales obtained with the DSS and the OSS method have quite opposite direction, as shown in Fig. 4.7. The cross dissipation is larger when using the OSS method than when using the DSS method (as showed in Fig. 4.17). This happens because the correlation between the velocity subscale and convective term in (4.74) are greater using the OSS method,

From numerical experiments we have found that results are quite sensitive to the parameter τ_c in Eq. (4.27). In order to obtain more accurate results we have tried to reduce the total amount of numerical dissipation, modifying expression for tau_c in Eq. (4.27). It was shown in[18] that the linearized incompressible Navier Stokes equations are stable and convergent only if τ_c is defined such $\rho^h \tau_c \tau_m < C_1 h^2$. Parameter τ_c helps to improve control on the divergence of the velocity and it was found to be effective in practice for laminar problems. If τ_c in expression (4.27) is multiplied by a constant factor C condition $\rho^h \tau_c \tau_m < C_1 h^2$ is still satisfied. When $|\boldsymbol{u}_h + \widetilde{\boldsymbol{u}}| \rightarrow 0$ the viscous term in the Navier Stokes equations is dominant, and the pressure subscale term plays a very important role, being $\tau_c \rightarrow C \frac{\mu}{\rho^h}$, which is a physically meaningful bulk viscosity for $C \approx 1$. We have observed numerically that when this factor is greater than one, the obtained solution deteriorates close to the walls, affecting the solution over all domain. We found experimentally that if $c_1 \rho^h \tau_c \tau_m \leq 0.2\, h^2$ the calculation went unstable. Later, the parameter was re defined as $\tau_c = \mu + C \frac{c_2}{c_1} |\boldsymbol{u}_h + \widetilde{\boldsymbol{u}}|$ in order to lower its value in the mean flow when $Re_h \gg 1$, and maintaining the correct value $\tau_c \rightarrow \frac{\mu}{\rho^h}$ close to the walls. When using $C < 1$ we obtained improved solutions, but when using $C < 0.2$ the calculation went unstable. This can be explained because condition $\rho^h \tau_c \tau_m < C_1 h^2$ is no longer satisfied when $C < 1$. Finally, we increased the value of c_1 parameter in Eq. (4.27) , obtaining better results, and satisfying always condition $\rho^h \tau_c \tau_m < C_1 h^2$.

4.8 Conclusions

In this chapter we have applied the numerical formulation introduced in chapter 3 to turbulent low Mach number flow problems without introducing any additional turbulence model. In particular, the turbulent channel flow has been solved using *only* numerical techniques. The nonlinear numerical model for the subscales can be understood as a LES modeling of the Reynolds stress tensor, and it has been shown to be adequate for the simulation of turbulent flows without the use of a physical model. The obtained solutions are stable and convergent to DNS values. The convergent behavior and the accuracy is good compared to the results obtained when using modern LES methods, as in [74, 96, 61].

The dissipative structure of the formulation proposed has been analyzed, identifying its main dissipative mechanisms. The influence of the numerical parameters on the total dissipation has been discussed. An skew symmetric formulation avoiding non physical dissipation mechanisms has also been proposed.

The possibility of using dynamic subscales permits to obtain stable solutions when using small time steps, defining the stabilization parameters as consistent in time. Because the steady-state solution (in case of being reached) would not depend on the time step size.

The space of the subscales can be chosen to be orthogonal to the finite element space (OSS) or in the space of the residuals (DSS). When considering the OSS method the numerical scheme is less diffusive than DSS method for laminar flows. However, surprisingly the OSS method is more dissipative than the DSS method for turbulent flows. An explanation to this behavior is that correlations in time between the subscales and the convective terms is greater using OSS method. When using coarser meshes the OSS method gives worst results than the DSS method. However, as the mesh is refined the OSS and DSS methods give a similar level of accuracy.

We have found that the numerical solutions are very sensitive to the numerical parameter c_1, which appears in the definition of the stabilization parameters τ_c, τ_m and τ_e. For linear elements (trilinear, in our examples), best results are obtained when c_1 is fixed to $c_1 = 12$, instead of $c_1 = 4$ as in [2] for laminar flows.

Even though the behavior of the method has been presented for a turbulent wall flow problem, analyzed in full detail, we believe that the material presented here is a clear indication of the potential of the method to model all kinds of turbulent thermally coupled flows.

Chapter 5

Approximations for the radiation transfer equation

This chapter is an elaboration of the material in

M. Avila, J. Principe and R. Codina. Spatial approximation of the radiation transport equation using a subgrid-scale finite element method. Computer Methods in Applied Mechanics and Engineering, 2011, vol. 200: 425-438.

In this chapter we study the radiative transfer equation in order to consider its coupling to the Navier-Stokes equation in chapter 6. The general problem of radiative transfer entails determining the radiative intensity from an integro differential equation in six independent variables - three spatial coordinates, two directional coordinates and the frequency, a prohibitive task. There exist several models to obtain an approximate solution of arbitrary high order of the radiation transport equation. In the present chapter two simplificative models for the radiative transfer equation will be presented in detail, these are the discrete ordinates method (DOM) and the spherical harmonics approximation (PN). These models can be understood as angular discretization of the radiation transpor equation. The development, finite element formulation and implementation of both models will be discussed in detail. In this chapter we present stabilized finite element methods to discretize in space the monochromatic radiation transport equation, independently of the angular discretization, or the simplificative model. These numerical methods are based on the decomposition of the unknowns into resolvable and subgrid scales, with an approximation for the latter that yields a problem to be solved for the former. This approach allows us to design the algorithmic parameters on which the method depends, which we do here when the discrete ordinates method is used for the directional approximation. We concentrate on two stabilized methods, namely, the classical SUPG technique and the orthogonal subscale stabilization. A numerical analysis of the *spatial* approximation for both formulations is performed, they are both stable and optimally convergent in the same mesh-dependent norm. A comparison with the behavior of the Galerkin method, for which a non-standard numerical analysis is done, is also presented. Numerical examples are presented to confirm the theoretical results.

5.1 Introduction

Radiation is energy propagation due to movement of subatomic particles or photons. Thermal radiation in particular refers to radiation caused by electromagnetic waves or photons. From the mathematical point of view, the problem consists in finding the radiative intensity field u, which depends on the position ($\boldsymbol{x}$), on the propagating direction ($\boldsymbol{s}$) and on the wave length (λ), that is $u = u(\lambda, \boldsymbol{x}, \boldsymbol{s})$. In many cases of interest it is possible to assume that different frequencies do not interact and therefore the radiative intensity is computed for each frequency separately. The problem is still very hard to approximate numerically, as it involves in one way or another the discretization of the spatial and directional domains to obtain approximations to the solution of the integro-differential radiative transport equation (RTE). An exception is the Monte Carlo method, in which these discretizations are not explicitly built but the movement of individual photons is followed invoking statistical concepts to solve the problem. It is widely recognized as a simple and efficient method, but also very time consuming, especially in three dimensions.

During the last decades there were numerous efforts to develop suitable numerical schemes for the radiative transfer equation (RTE) [70]. Several options for the directional discretization have been considered in the literature, including the discrete ordinates method (DOM) and the method of spherical harmonics (also called PN approximation). In both cases the directional discretization transforms the integro-differential RTE into a set of coupled differential equations. In the case of the DOM the unknown of each equation is the radiative intensity in a given direction and integration over the solid angle is replaced by a quadrature sum, which is a set of discrete ordinate directions and the corresponding weights. The DOM was first proposed by Chandrasekhar [12] in his work on stellar and atmospheric radiation, analyzing radiation problems within a plane parallel medium. The PN approximation was first proposed by Jeans [57] in his work on radiative transfer in stars.

Besides the selection of the directional discretization, a proper spatial discretization is needed. When the problem also involves convective heat transfer, the numerical scheme for the RTE should be compatible with those for the mass, momentum and energy conservation equations governing the flow field. Implementation of inhomogeneity and anisotropic radiative scattering is required for practical applications in a multidimensional complex geometry, using different grids. In these situations natural candidates are finite volume methods (FVM) and finite element methods (FEM). These methods have the advantage that can deal with complex geometric shape and boundary conditions conveniently without increasing the computational complexity.

A finite element approximation of radiative heat transfer in one-dimensional problems was proposed by Viskanta [95] in 1965. Razzaque et al. [83] studied the finite element solution of radiative heat transfer in a two dimensional rectangular enclosure. Fiveland [38] developed a finite element formulation based on the DOM to solve absorbing, emitting and isotropic scattering in multidimensional problems. That formulation, however, cannot deal with the problem of anisotropic scattering. Richling et al. [85] formulated the radiative transfer equation in three dimensions for discrete ordinates using finite elements for anisotropically scattering media.

It is well known that a careful numerical formulation of the problem is needed to avoid numerical instabilities due to the first order hyperbolic nature of the problem. The Galerkin formulation is known to be unstable and therefore a stabilized formulation is necessary. For example, Kanschat [58] applied and analyzed the streamline upwind Petrov Galerkin (SUPG) formulation [11] for the problem continuous in the propagating direction. A discontinuous Galerkin approximation in space combined with the DOM for the directional discretization was proposed in [1].

In this work we propose a stabilized finite element formulation based on an arbitrary angular discretization for solving the radiative transfer equation in multidimensional geometries for absorbing, emitting and anisotropic scattering media. We analyze the SUPG method and the orthogonal subscales stabilization (OSS) method [17] introduced in previous chapters for the Navier Stokes equations, which can be described in the variational multiscale framework introduced in [49]. A comparison with the behavior of the Galerkin method, for which a non-standard numerical analysis is performed, is also presented.

The chapter is organized as follows. After an introduction to the physical model in Section 5.2, we present a term by term development of the radiative transfer equation and its mathematical description in Section 5.3. In Sections 5.4 and 5.5 are presented in detail the simplificative Discrete Ordinates Method, and the PN model for the radiative transfer equation. The variational form of the monochromatic radiation equation is described in Section 5.6. The numerical approximation, consisting in a spatial and directional discretization is presented in Section 5.7. The semidiscrete spatial discretization is based on the variational multiscale formulation and the algebraic approximation to the subscales. A general directional discretization and its particular form for the DOM is presented, and the choice of the stabilization parameters is discussed. A complete numerical analysis of the formulation is done in Section 5.8, where stability and optimal convergence of the SUPG and OSS methods are proved, together with a non-standard stability and convergence analysis of the Galerkin method. The accuracy and efficiency of the scheme are discussed in Section 5.9, where some numerical experiments are presented. Concluding remarks close the chapter in Section 5.10.

5.2 Physical Problem

In this section we introduce radiation from a physical point of view, see [70] for background.

Radiation is energy propagation due to movement of subatomic particles or photons. Subatomic particles can be electrons (beta radiation), neutrons, protons, atom nucleus (like in alfa radiation), etc.

Radiation can be classified as ionizing or not ionizing. Ionizing radiation produces ionization of the medium detaching electrons from atoms or molecules. Ionizing radiation is caused by charged particles as protons, electrons or atom nucleus. High energy photons as X and gamma radiation are able to produce ionization too. Non ionizing radiation is due to the transpor of low energy photons and not charged particles as neutrons. A photon is the elementary particle responsible for electromagnetic phenomena. It is the carrier of electromagnetic radiation of all wavelengths (gamma rays, X-rays, ultraviolet light, visible light, infrared light, microwaves, and radio waves). Radiation of nuclear particles is of interest in the use of accelerators, nuclear reactors, astrophysics, etc, but the terms *radiative heat transfer* and *thermal radiation* are commonly used to describe the science of heat transfer caused by electromagnetic waves or photons.

5.2.1 Nature of thermal radiation

Thermal radiative energy may be viewed as consisting of electromagnetic waves or photons. Neither point of view is able to describe completely all radiative phenomena that have been observed. It is therefore customary to use both concepts interchangeably. Photons are massless and propagate for any medium at the speed of light c. Speed of light depends of the medium through which it travels, and may be related to the speed of light in vacuum $c_0 = 299792458$ m/s, by the formula

$$c = \frac{c_0}{n}$$

where n is known as the refractive index of the medium. For most gases the refractive index is very close to unity, for example for air it is $n = 1.0029$ over the visible spectrum.

A photon is identified by its

- frequency, ν [Hz].
- wavelength, λ [μm].

Frequency ν and wavelength λ are always related by velocity c as $\nu\lambda = c$.

The momentum $\boldsymbol{p}$ and the energy E carried by a single photon are

$$\begin{aligned} \boldsymbol{p} &= \frac{h}{\lambda}\boldsymbol{s} \\ E &= \frac{hc}{\lambda}, \qquad h = 6.626 \times 10^{-34}\text{Js}, \end{aligned}$$

where h is the Plank constant and $\boldsymbol{s}$ a unit vector with propagation direction. Note that momentum and energy increase with frequency. When photons collide with a surface they transfer energy and momentum, the later causes radiation pressure that can never compete with the pressure exerted by a molecular gas. Photon momentum is always neglected in engineering applications. As we shall see, for heat transfer applications wavelengths between 10^{-7}m and 10^{-3}m (ultraviolet, visible and infrared) are of greatest importance and are therefore the only ones considered here.

5.2.2 Radiative intensity

When we want to know the radiation field in a medium, we need to know its directional and spectral dependence. Therefore we define

Definition 1 *Spectral intensity:* $u_\lambda(\boldsymbol{x}, \boldsymbol{s})$ $[\frac{\text{J}}{\text{s}\cdot\text{m}^2\cdot\text{sr}\cdot\mu\text{m}}] \equiv$ *radiative energy flow due to radiation of wavelength* λ *propagating in* $\boldsymbol{s}$ *direction per unit solid angle, unit wavelength and unit area normal to the rays.*

Definition 2 *Total intensity:* $u(\boldsymbol{x}, \boldsymbol{s})$ $[\frac{\text{J}}{\text{s}\cdot\text{m}^2\cdot\text{sr}\cdot}] \equiv$ *radiative energy flow due to radiation propagating in* $\boldsymbol{s}$ *direction per unit solid angle and unit area normal to the rays.*

In the above definitions, $\boldsymbol{x}$ is a position vector fixing the location of a point in space, and $\boldsymbol{s}$ is a unit direction vector. The total intensity is related with the spectral intensity as

$$u(\boldsymbol{x}, \boldsymbol{s}) = \int_0^\infty u_\lambda(\boldsymbol{x}, \boldsymbol{s}) d\lambda \tag{5.1}$$

that is, the total intensity is the sum of all spectral intensity contributions.

The **radiative heat flux $\boldsymbol{q}$** can be obtained from the spectral intensity as

$$\boldsymbol{q}(\boldsymbol{x}) = \int_0^\infty \boldsymbol{q}_\lambda(\boldsymbol{x}) d\lambda = \int_0^\infty d\lambda \int_{4\pi} u_\lambda(\boldsymbol{x}, \boldsymbol{s}) \boldsymbol{s} ds \tag{5.2}$$

where $\boldsymbol{q}_\lambda(\boldsymbol{x})$ is the **spectral heat flux** due to radiation at wavelength λ. The **incident radiation function** G is the total intensity impinging on a point from all sides, defined as

$$G = \int_{4\pi} \int_0^\infty u_\lambda d\lambda ds = \int_{4\pi} u ds \tag{5.3}$$

In all the expressions above and in what follows, integrals over 4π denote integration along all directions, that is to say, along the complete solid angle of 4π.

5.2.3 Interaction of radiation with media

A medium that does not interact with radiation or interacts negligibly is called a “non participating medium”. An electromagnetic beam in a non participating medium does not change its direction neither its intensity. Participating media continuously emit electromagnetic radiation randomly into all directions at a rate depending on the temperature and the properties of the material. When a photon travels by a participating medium it can be absorbed or suffer collisions with any atom, molecule or particle. This interactions produce changes in the intensity of electromagnetic waves when they pass through a medium. In order to be able to know the radiation field in any medium we need to know and model the way that the medium interacts with radiation.

Radiation characteristics of opaque surfaces

When an electromagnetic wave strikes a *surface*, the wave may be reflected, absorbed and/or transmitted. If no radiation is transmitted, the surface is known as *opaque*. If the wave passes through the surface without any attenuation, it is known as *transparent*, if partial attenuation occurs it is known as *semitransparent*. An *opaque* surface that does not reflect any radiation is called *a perfect absorber* or *a black surface*. A black body also emits more spectral radiation for all wavelengths than any other surface at the same temperature.

Let us introduce some concepts related to emission:

Blackbody emissive spectrum A *black surface* is a perfect absorber and emitter at every wavelength and for any direction of incoming or outgoing electromagnetic waves. At a given temperature a *black surface* emits radiation isotropically (diffuse emitter) with spectral emissive power distribution $E_{b\lambda}$, known as *Plank's law* distribution.

$$E_{b\lambda}\left(T\right) = \frac{2hc_o^2}{\lambda^5 n^2\left(e^{\frac{hc}{n\lambda KT}} - 1\right)} \tag{5.4}$$

where $K = 1.3807 \times 10^{-23}$ is known as the Boltzmann constant and n as the refraction index of the transparent medium bounding the surface. The emissive power of a black surface is

$$E_b = \int_0^\infty E_{b\lambda} d\lambda = \sigma_B T^4 \tag{5.5}$$

where $\sigma_B = 5.6704 \times 10^{-8}$ is the Stefan-Boltzmann constant.

It is often necessary to calculate the emissive power contained within a finite wavelength band, say between wavelengths λ_1 and λ_2. It is customary to express it in terms of the fraction of blackbody emissive power $F\left(0 \to \lambda\right)$ contained between 0 and λ and calculated as

$$F\left(0 \to \lambda\right) \equiv \frac{\int_0^\lambda E_{b\lambda} d\lambda}{\int_0^\infty E_{b\lambda} d\lambda} = \frac{\int_0^\lambda E_{b\lambda} d\lambda}{\sigma_B T^4} = f\left(\lambda T\right)$$

which depends only on the product of a single variable λT and it is therefore easily tabulated. From these values we find the heat flux emitted by a black surface at temperature T between wavelengths λ_1 and λ_2 from the expression

$$\int_{\lambda_1}^{\lambda_2} E_{b\lambda} d\lambda = \left(F\left(0 \to \lambda_2\right) - F\left(0 \to \lambda_1\right)\right)\sigma_B T^4$$

As the blackbody emission is diffuse, the total and spectral intensities I_b and $I_{b\lambda}$ emitted by a black surface are

$$\begin{aligned}
E_{b\lambda} &= \int_{2\pi+} I_{b\lambda} \boldsymbol{n} \cdot \boldsymbol{s} ds = \pi I_{b\lambda} \\
I_b &= \frac{E_b}{\pi} = \frac{\sigma_B T^4}{\pi} \\
u_{\lambda 1 \to \lambda 2} &= \left(F\left(0 \to \lambda_2\right) - F\left(0 \to \lambda_1\right)\right)\frac{\sigma_B T^4}{\pi}
\end{aligned}$$

Real surfaces emission The notion of blackbody serves to describes ideal surface behavior from the fact that no real surface can emit more radiation than a blackbody at the same temperature. It is therefore convenient to choose the blackbody as a reference in describing emission from a real surface. It is important to note that, in general, the spectral radiation emitted by a real surface differs from the *Plank distribution* (5.4). Moreover the directional distribution may be other than diffuse.

Definition 3 *The* spectral directional emissivity $\epsilon_{\lambda\mu}(\boldsymbol{s}, T)$ *of a surface at temperature* T *is the ratio of the spectral intensity emitted at wavelength* λ *in direction* $\boldsymbol{s}$ *to the intensity emitted by a blackbody at the sames values of* T *and* λ. *That is,*

$$\epsilon_{\lambda\mu}(\boldsymbol{s}, T) = \frac{u_\lambda(\boldsymbol{s})}{I_{b\lambda}} \tag{5.6}$$

where μ represents the cosine of the angle between $\boldsymbol{s}$ and $\boldsymbol{n}$. For most engineering calculations surfaces are modeled working with directional averages.

Definition 4 *The* Spectral emissivity $\epsilon_\lambda(T)$ *of a surface at temperature T is the ratio of the spectral emissive power at wavelength λ to the spectral emissive power of a blackbody at the same temperature. That is*

$$\epsilon_\lambda(T) = \frac{\int_{2\pi^+} u_\lambda(\boldsymbol{s})\boldsymbol{s}\cdot\boldsymbol{n}ds}{E_{b\lambda}} = \frac{\int_{2\pi^+} \epsilon_{\lambda\mu}(\boldsymbol{s},T)\boldsymbol{s}\cdot\boldsymbol{n}ds}{\pi} \tag{5.7}$$

When we average over all wavelengths we use

Definition 5 *The* total emissivity or emittance $\epsilon(T)$ *of a surface at temperature T is the ratio of the emissive power of the surface to the emissive power of a blackbody at the same temperature. That is*

$$\epsilon(T) = \frac{\int_0^\infty \int_{2\pi^+} u_\lambda(\boldsymbol{s})\boldsymbol{s}\cdot\boldsymbol{n}dsd\lambda}{E_{b\lambda}} = \frac{\int_0^\infty \epsilon_\lambda(T) I_{b\lambda}d\lambda}{I_b} \tag{5.8}$$

Radiation characteristics of gases

In thermal radiation applications we generally deal with a participating gas medium bounded by surfaces. Like a solid medium, gases can absorb and continuously emit radiative energy. Emission is due to transition from atoms or molecules to lower internal energy states. When absorption of a photon occurs a molecule rises its internal energy level.

The internal molecular energy consists of a number of contributions, primarily of the electronic energy state, but also of vibration and rotation energy states. Quantum mechanics postulates that for any atom or molecule only a finite number of discrete energy levels are possible, i.e., electrons have discrete energy states. Vibration can occur with a number of distinct amplitudes, and discrete rotational velocities are allowed. Therefore, a molecular gas emits and absorbs photons at discrete energy levels.

A change of an electronic level causes absorption-emission in the ultraviolet and visible parts of the spectrum ($\lambda \gtrapprox 1\ \mu$m). A change in the vibrational energy level of a molecule (a monatomic gas does not rotate) causes absorption-emission in the intermediate infrared part of the spectrum ($1\mu\text{m} \leq \lambda \leq 15\mu\text{m}$). Rotational energy changes take place in the intermediate to far infrared ($\lambda \geq 10\mu$m). Vibrational energy changes are usually accompanied by changes in rotational energy level, producing continuous spectra for absorption and emission. Emission of photons in a gas occurs spontaneously in random directions, due to transition from atoms or molecules from higher to lower energy states. The rate of transitions is proportional to the number of atoms or molecules in the higher energy levels, a function of temperature and material properties. Complete descriptions of the microscopic phenomena may be found on books on statistical mechanics.

Radiation characteristics of particulate media

In most radiative heat transfer applications is usual to threat with particulate media, as for example in the case of smoke produced by fire. When an electromagnetic wave or a photon interacts with a medium containing small particles, the radiative intensity may be changed by absorption and/or scattering. A common example is light passing through a cloud of smoke.

Scattering consists of photon collision with particles. Scattering can be elastic, maintaining photon's wavelength, or inelastic, changing photon's wavelength, as, for example, in Compton's effect. In radiative heat transfer coming from thermal effects scattering is considered as elastic. Inelastic scattering as in Compton's effect occurs with high energy photons (X-ray and gamma). For our purposes scattering only affects the direction in which the photon travels. Scattering can occur by diffraction, reflection from the particle and refraction when penetrating the particle. How much and into which direction a particle scatters an electromagnetic wave passing through its vicinity depends on

1. the shape of the particle
2. the material of the particle
3. its relative size compared with radiation wavelength

In radiative analysis the shape of particles is usually assumed to be spherical. This simplifying assumption gives generally excellent results. Depending on the size compared with radiation wavelength we may distinguish between three different regimes:

1. Rayleigh scattering, when particles are much smaller than the radiation wavelength. This happens for example in atmospheric air whose molecules are treated as very fine particles.
2. Mie scattering, when the size of particles and the radiation wavelength are of the same order. It is widely used in radiative heat transfer applications.
3. Geometric optics, when the size of particles is much bigger than the radiation wavelength.

5.3 The Radiative Heat Transfer Equation

In this section we present the Radiative Transfer Equation, which governs the behavior of radiation intensity in the presence of an absorbing, emitting, and scattering medium. The equation to be obtained here is the one that needs to be approximated numerically.

5.3.1 Attenuation by absorption and scattering

When the medium in which radiation travels is *participating*, any incident beam will be attenuated by absorption and scattering while it travels through the medium. Let us elaborate these concepts:

Absorption The absolute amount of absorption for a monochromatic beam is directly proportional to its intensity u_λ. When more photons cross per surface unit more probability of absorption. For a differential ray path dr we may write

$$du_\lambda \mid_{\text{abs}} = -\kappa_\lambda u_\lambda dr$$

where κ_λ is the *spectral absorption coefficient*, with units $[\mathrm{m}^{-1}]$. This coefficient is obtained experimentally and it is directly proportional to the number of particles per unit volume.

Scattering Attenuation by scattering, or “out-scattering” away from the direction under consideration, is very similar to absorption. It is given by

$$du_\lambda \mid_{\text{sca}} = -\sigma_{s\lambda} u_\lambda dr$$

Total attenuation The total attenuation of intensity in a pencil of rays by both absorption and scattering is known as *extinction*. Thus, an *extinction coefficient* is defined as

$$\beta_\lambda = \kappa_\lambda + \sigma_{s\lambda} \tag{5.9}$$

The *optical distance* based on extinction coefficient is defined as

$$\tau_\lambda = \int_0^r \beta_\lambda dr \tag{5.10}$$

5.3.2 Augmentation by emission and scattering

Emission The emitted intensity along any path (which is the rate of emitted energy per unit area) must be proportional to the volume, and so to the length of the path. The emitted energy for a path of length dr must be proportional to the local energy content in the volume $d\Omega = 1dr$. Since from Kirchhoff law, at thermodynamic equilibrium the intensity everywhere must be equal to the blackbody intensity, the emitted intensity is

$$du_\lambda \mid_{\text{em}} = \kappa_\lambda I_{b\lambda} dr$$

The proportionally constant for emission is the same as for absorption.

Scattering Augmentation due to scattering or “in-scattering” has contribution from all directions and, therefore must be calculated from integration over all solid angles. Augmentation due to elastic scattering is given by

$$du_\lambda(\boldsymbol{s}) \mid_{\text{sca}} = dr \frac{\sigma_{s\lambda}}{4\pi} \int_{4\pi} u_\lambda\left(\boldsymbol{s}'\right) \phi_\lambda\left(\boldsymbol{s}', \boldsymbol{s}\right) ds'$$

where ds' is a differential of solid angle around direction $\boldsymbol{s}'$. As it has been mentioned, the quantity 4π below the integral operator means integration over all solid angles.

The function $\phi_\lambda\left(\boldsymbol{s}', \boldsymbol{s}\right)$ is the *scattering phase function* and describes the probability that a ray coming from direction $\boldsymbol{s}'$ will be scattered into a certain other direction $\boldsymbol{s}$. This function is always normalized such that

$$\frac{1}{4\pi}\int_{4\pi}\phi_\lambda\left(\boldsymbol{s}', \boldsymbol{s}\right)ds' \equiv 1$$

When $\phi_\lambda = 1$, equal amounts of energy are scattered into all directions and we have *isotropic scattering*. If $\phi_\lambda \neq 1$ we have *anisotropic scattering*.

In almost all physical models the *scattering phase function* $\phi_\lambda\left(\boldsymbol{s}', \boldsymbol{s}\right)$ depends only of the angle between the vector directions $\boldsymbol{s}'$ and $\boldsymbol{s}$. Therefore, the *scattering phase function* has the following properties

$$\phi_\lambda\left(\boldsymbol{s}', \boldsymbol{s}\right) = \phi_\lambda\left(\boldsymbol{s}, \boldsymbol{s}'\right) = \phi_\lambda\left(-\boldsymbol{s}', -\boldsymbol{s}\right) = f(\cos\left(\boldsymbol{s}, \boldsymbol{s}'\right))$$

Inelastic scattering Augmentation due to inelastic scattering has contribution from all directions and all wavelengths, normally from lower wavelengths (higher energies). It is given by

$$du_\lambda(\boldsymbol{s})\mid_{\text{sca}} = \int_0^\infty d\lambda' \frac{\sigma_{s\lambda'}}{4\pi}\int_{4\pi} u\left(\boldsymbol{x}, \boldsymbol{s}', \lambda'\right)\phi\left(\boldsymbol{s}', \lambda' \to \boldsymbol{s}, \lambda\right)ds'$$

where the function $\phi\left(\boldsymbol{s}', \lambda' \to \boldsymbol{s}, \lambda\right)$ is the *inelastic scattering phase function* and describes the probability that a ray with wavelength λ' coming from direction $\boldsymbol{s}'$ will be scattered into a certain other direction $\boldsymbol{s}$ with wavelength λ. The normalization of ϕ is such that

$$\int_0^\infty d\lambda' \int_{4\pi}\phi\left(\boldsymbol{s}', \lambda' \to \boldsymbol{s}, \lambda\right)ds' \equiv 1$$

Generally, it holds that

$$\int_0^\infty d\lambda\prime \int_{4\pi}\phi\left(\boldsymbol{s}', \lambda' \to \boldsymbol{s}, \lambda\right)ds' = \int_0^\lambda d\lambda\prime \int_{4\pi}\phi\left(\boldsymbol{s}', \lambda' \to \boldsymbol{s}, \lambda\right)ds'$$

5.3.3 The radiative transfer equation

Making an energy balance on the radiative energy traveling in direction $\boldsymbol{s}$ we get the radiative transport equation for general problems, which is expressed as

$$\begin{aligned}
&\frac{1}{c}\frac{\partial u_\lambda\left(\boldsymbol{x}, \boldsymbol{s}, t\right)}{\partial t} + \boldsymbol{s}\cdot\nabla u_\lambda\left(\boldsymbol{x}, \boldsymbol{s}, t\right) + \left(\kappa_\lambda\left(\boldsymbol{x}\right) + \sigma_{s\lambda}\left(\boldsymbol{x}\right)\right)u_\lambda\left(\boldsymbol{x}, \boldsymbol{s}, t\right)\\
&\quad - \int_0^\infty d\lambda' \frac{\sigma_{s\lambda}\left(\boldsymbol{x}\right)}{4\pi}\int_{4\pi} u\left(\boldsymbol{x}, \boldsymbol{s}', \lambda', t\right)\phi\left(\boldsymbol{s}', \lambda' \to \boldsymbol{s}, \lambda\right)ds'\\
&\quad = \kappa_\lambda\left(\boldsymbol{x}\right)I_{b\lambda}\left(T\left(x\right)\right)
\end{aligned} \tag{5.11}$$

Equation (5.11) is valid anywhere inside an arbitrary enclosure. For the vast majority of engineering applications, the speed of light is so large compared to local time and length scales that the first term in equation (5.11) may be neglected. In thermal radiation, scattering is always considered as elastic, so we will replace $\phi\left(\boldsymbol{s}', \lambda' \to \boldsymbol{s}, \lambda\right)$ by $\phi(\boldsymbol{s}', \boldsymbol{s})$. Making those suppositions we arrive to the ***monochromatic radiative transfer equation*** (RTE) decoupled for each wavelength λ, which is given by

$$\boxed{\boldsymbol{s}\cdot\nabla u_\lambda\left(\boldsymbol{x},\boldsymbol{s}\right)+\left(\kappa_\lambda+\sigma_{s\lambda}\right)u_\lambda\left(\boldsymbol{x},\boldsymbol{s}\right)-\frac{\sigma_{s\lambda}}{4\pi}\int_{4\pi}u_\lambda\left(\boldsymbol{x},\boldsymbol{s}'\right)\phi\left(\boldsymbol{s}',\boldsymbol{s}\right)d\boldsymbol{s}'=\kappa_\lambda I_{b\lambda}} \tag{5.12}$$

Equation (5.12) is the main equation in the present work. In the following we will discuss properties, solutions and numerical methods for solving (5.12) in an aim to find the radiative energy field.

5.3.4 Boundary value problem of the monochromatic equation

Let $\Omega\subset\mathbb{R}^3$ and let $\mathcal{S}^2$ be the unit sphere in $\mathbb{R}^3$. For conciseness, we consider the three dimensional problem, but all what follows can be applied to the two-dimensional case as well. We remark that also in two dimensional problems the directional dependence of the radiation intensity belongs to the unit sphere $\mathcal{S}^2$. Since the monochromatic equation is decoupled for each wavelength, the subindex λ will be omitted.

The monochromatic radiative transfer problem consists in finding $u:\Omega\times\mathcal{S}^2\longrightarrow\mathbb{R}$ such that

$$Lu=f\quad\text{in }\Omega\times\mathcal{S}^2, \tag{5.13}$$

where the source of intensity $f(\boldsymbol{x},\boldsymbol{s})$ is a given function (depending on the temperature in thermal radiation problems) and the operator L is defined as

$$Lu(\boldsymbol{x},\boldsymbol{s})=\boldsymbol{s}\cdot\nabla u(\boldsymbol{x},\boldsymbol{s})+\kappa(\boldsymbol{x})u(\boldsymbol{x},\boldsymbol{s})+S_\sigma u(\boldsymbol{x},\boldsymbol{s}),\quad(\boldsymbol{x},\boldsymbol{s})\in\Omega\times\mathcal{S}^2, \tag{5.14}$$

where

$$S_\sigma u(\boldsymbol{x},\boldsymbol{s}):=\sigma_s(\boldsymbol{x})S_1u(\boldsymbol{x},\boldsymbol{s}), \tag{5.15}$$

$$S_1u(\boldsymbol{x},\boldsymbol{s}):=u(\boldsymbol{x},\boldsymbol{s})-\frac{1}{4\pi}\int_{\mathcal{S}^2}\phi(\boldsymbol{s},\boldsymbol{s}')u(\boldsymbol{x},\boldsymbol{s}')\mathrm{d}\boldsymbol{s}'. \tag{5.16}$$

For clarity, the arguments on which the functions depend have been explicitly displayed. Functions $\kappa(\boldsymbol{x})\geq 0$ and $\sigma_s(\boldsymbol{x})\geq 0$ in (5.14) and (5.15) are the absorption and extinction coefficients, respectively. They only need to be bounded for the following developments, although we will consider them constant in the numerical analysis section for simplicity.

The operator S_σ defined in (5.15) is the so called scattering operator. It depends on the phase function $\phi\in\mathcal{C}^\infty(\mathcal{S}^2\times\mathcal{S}^2;\mathbb{R}^+)$, which is normalized in such a way that

$$\int_{\mathcal{S}^2}\phi(\boldsymbol{s},\boldsymbol{s}')\mathrm{d}\boldsymbol{s}'=4\pi\quad\forall\boldsymbol{s}\in\mathcal{S}^2.$$

According to the physical model, the phase function $\phi(\boldsymbol{s},\boldsymbol{s}')$ usually depends only on the cosine of the angle between $\boldsymbol{s}$ and $\boldsymbol{s}'$. For heterogeneous media, it could also depend on the position $\boldsymbol{x}$.

The monochromatic radiative transfer problem (5.13) is an integrodifferential equation of first order. Note that if $\sigma_s = 0$ we have a first order hyperbolic convection-reaction equation for each direction $\boldsymbol{s}$.

The boundary $\Gamma = \partial\Omega \times \mathcal{S}^2$ of $\Omega \times \mathcal{S}^2$ is divided into the inflow Γ^- and outflow Γ^+ boundaries, defined as

$$\Gamma^- = \{(\boldsymbol{x}, \boldsymbol{s}) \in \Gamma \mid \boldsymbol{s} \cdot \boldsymbol{n} < 0\}, \quad \Gamma^+ = \{(\boldsymbol{x}, \boldsymbol{s}) \in \Gamma \mid \boldsymbol{s} \cdot \boldsymbol{n} \geq 0\}, \tag{5.17}$$

where $\boldsymbol{n}$ is the unit normal vector pointing outwards $\partial\Omega$ at $\boldsymbol{x}$. We shall also make use of the hemispheres

$$\mathcal{S}^-_{\partial_x} := \{\boldsymbol{s} \in \mathcal{S}^2 \mid \boldsymbol{s} \cdot \boldsymbol{n} < 0\}, \quad \mathcal{S}^+_{\partial_x} := \{\boldsymbol{s} \in \mathcal{S}^2 \mid \boldsymbol{s} \cdot \boldsymbol{n} \geq 0\}, \tag{5.18}$$

which are defined for each $\boldsymbol{x} \in \partial\Omega$.

The monochromatic radiative transfer equation (5.13) is subject to boundary conditions of the type

$$u(\boldsymbol{x}, \boldsymbol{s})|_{\mathcal{S}^-_{\partial_x}} = \epsilon I_b(T) + \frac{\rho}{\pi} \int_{2\pi^+} u(\boldsymbol{x}, \boldsymbol{s}) \boldsymbol{n} \cdot \boldsymbol{s} \mathrm{d}s \tag{5.19}$$

where ρ is the diffuse reflection wall coefficient, ϵ is the emissive wall coefficient, and T the wall temperature at $\boldsymbol{x}$. To compute the reflected intensity we need to integrate over all the outgoing directions $2\pi^+$ at boundary point $\boldsymbol{x}$.

5.3.5 Formal solution to the radiation transport equation

The monochromatic equation (5.12) can be adimensionalized defining the scattering albedo coefficient,

$$\omega = \frac{\sigma_s}{\beta}$$

and the nondimensional optical coordinate

$$\tau = \int_0^r \beta dr'$$

integrated from a point $r' = 0$ at the boundary up to a point $r' = r$ inside the medium along a ray direction. Equation (5.12) is then written in the form

$$\frac{du}{d\tau} + u = S(\tau, \boldsymbol{s}) = \frac{\omega}{4\pi} \int_{4\pi} u(\boldsymbol{s}') \phi(\boldsymbol{s}', \boldsymbol{s}) d\boldsymbol{s} + (1 - \omega) I_b \tag{5.20}$$

The last two terms are often combined and are then known as the source function $S(\tau, \boldsymbol{s})$ for radiative intensity. Multiplying equation (5.20) by $\mathrm{e}^{-\tau}$ and integrating from a point $r' = 0$ at the boundary up to a point $r' = r$ along $\boldsymbol{s}$ direction we get

$$u(\tau, \boldsymbol{s}) = u(0, \boldsymbol{s},) e^{-\tau_n} + \int_0^r S(\tau, s) e^{-(\tau - \tau')} d\tau' \tag{5.21}$$

Equation (5.21) is exact, and expressed in exponential semi-analytical form. It can be solved numerically with finite element methods. Physically, the first term on right hand side of equation (5.21) is the contribution to the local intensity by the intensity entering the enclosure at $r = 0$ which decays exponentially due to extinction over the optical distance τ. The integrand of the second term is the contribution from the local emission at τ', attenuates exponentially by self-extinction between the distance $\tau - \tau'$.

5.3.6 Radiative heat exchange at the surface

We define the *surface irradiation* $H(\boldsymbol{x})$ as the radiative heat rate impinging into the surface at point $\boldsymbol{x}$. That is

$$H(\boldsymbol{x}) = \int_{2\pi^+} u\left(\boldsymbol{x}, \boldsymbol{s}\right) \boldsymbol{s} \cdot \boldsymbol{n} ds \tag{5.22}$$

The *surface radiosity* $J(\boldsymbol{x})$ is the component of heat flux leaving the surface at location $\boldsymbol{x}$ entering into domain Ω.

$$J(\boldsymbol{x}) = \int_{2\pi^-} u\left(\boldsymbol{x}, \boldsymbol{s}\right) |\boldsymbol{s} \cdot \boldsymbol{n}| \mathrm{d}s \tag{5.23}$$

Radiosity and irradiation are very useful magnitudes in heat radiation calculations. Boundary condition for an emissive and reflective boundary (5.19) imposes radiosity J in terms of irradiation H over all the boundary $\partial\Omega$, as

$$J(\boldsymbol{x}) = \epsilon\pi I_b + \rho H(\boldsymbol{x}) \tag{5.24}$$

The net radiative heat flux exiting the domain Ω at any point of the boundary can be expressed in terms of radiosity J or irradiation H by means of equation (5.24)

$$\begin{aligned} \boldsymbol{q} \cdot \boldsymbol{n} &= \int_{4\pi} u\left(\boldsymbol{x}, \boldsymbol{s}\right) \boldsymbol{s} \cdot \boldsymbol{n} ds = H - J && (5.25) \\ &= \frac{\left(1-\rho\right) J - \epsilon\pi I_b}{\rho} = \left(1-\rho\right) H + \epsilon\pi I_b && (5.26) \end{aligned}$$

In presence of an opaque surface, where $\rho = 1 - \epsilon$, the net heat flux over the boundary is expressed as

$$\boldsymbol{q} \cdot \boldsymbol{n} = \frac{\epsilon}{1-\epsilon}\left(J - \pi I_b\right) = \epsilon\left(H - \pi I_b\right) \tag{5.27}$$

These equations are comonly used to calculate wall temperatures and net radiative heat fluxes between walls interachanging radiative heat transfer without participating media.

5.3.7 Frequency discretization

In heat transfer calculations it is only the total radiative heat flux or, more precisely, its divergence what is of interest. This is what affects the energy balance equation from which the temperature needs to be computed. Equation (5.12) solves the flux for a single wavelength. For a molecular gas the absorption coefficient κ_λ varies very rapidly across the spectrum, and with it the radiative intensity. It is therefore in principle possible to replace the actual absorption coefficient (and intensity) by smoothened values appropriately averaged over a narrow spectral range called spectral band or group.

If we integrate the monochromatic equation (5.12) between a spectral band from λ_i to λ_{i+1} we get the relation

$$\begin{aligned} &\boldsymbol{s} \cdot \nabla \left(\int_{\lambda_i}^{\lambda_{i+1}} d\lambda u_\lambda \left(\boldsymbol{x}, \boldsymbol{s}\right) \right) + \int_{\lambda_i}^{\lambda_{i+1}} d\lambda \left(\kappa_\lambda + \sigma_{s\lambda}\right) u_\lambda \left(\boldsymbol{x}, \boldsymbol{s}\right) \\ &- \int_{\lambda_i}^{\lambda_{i+1}} d\lambda \frac{\sigma_{s\lambda}}{4\pi} \int_{4\pi} u_\lambda \left(\boldsymbol{x}, \boldsymbol{s}'\right) \phi\left(\boldsymbol{s}', \boldsymbol{s}\right) d\boldsymbol{s}' = \int_{\lambda_i}^{\lambda_{i+1}} d\lambda \kappa_\lambda I_{b\lambda} \end{aligned}$$

Defining the i-th spectral band intensity u_i as

$$u_i = \int_{\lambda_i}^{\lambda_{i+1}} d\lambda u_\lambda$$

we would like to solve an equation of the form

$$\begin{aligned} & s \cdot \nabla u_i \left(\boldsymbol{x}, \boldsymbol{s}\right) + \left(\kappa_{ai} + \sigma_{si}\right) u_i \left(\boldsymbol{x}, \boldsymbol{s}\right) - \frac{\sigma_{s\lambda}}{4\pi} \int_{4\pi} u_i \left(\boldsymbol{x}, \boldsymbol{s}'\right) \phi \left(\boldsymbol{s}', \boldsymbol{s}\right) d\boldsymbol{s}' \\ & = \kappa_{ei} I_{b\lambda_i,\lambda_{i+1}} \\ & = \kappa_{ei} \left(F\left(0 \to \lambda_{i+1}\right) - F\left(0 \to \lambda_i\right)\right) \frac{\sigma_B T^4}{\pi} \end{aligned}$$

where the spectral band parameters κ_{ei}, κ_{ai} and σ_{si} are known respectively as spectral band emission, absorption and scattering coefficients, and should be given by

$$\int_{\lambda_i}^{\lambda_{i+1}} d\lambda \kappa_\lambda u_\lambda = \kappa_{ai} \int_{\lambda_i}^{\lambda_{i+1}} d\lambda u_\lambda \tag{5.28}$$

$$\int_{\lambda_i}^{\lambda_{i+1}} d\lambda \sigma_{s\lambda} u_\lambda = \sigma_i \int_{\lambda_i}^{\lambda_{i+1}} d\lambda u_\lambda \tag{5.29}$$

$$\int_{\lambda_i}^{\lambda_{i+1}} d\lambda \kappa_\lambda I_{b\lambda_i} = \kappa_{ei} \int_{\lambda_i}^{\lambda_{i+1}} d\lambda I_{b\lambda} \tag{5.30}$$

that is, spectral band parameters depend on the spectral intensity distribution that we do not know a priori. Emission and absorption coefficients κ_{ei} and κ_{ai} have different values because the spectral blackbody emission $I_{b\lambda}$ and radiation intensity u_λ have different spectral distribution. Some models give consider the same values of emission and absorption coefficients $\kappa_{ei} = \kappa_{ai}$.

There has been a lot of research in models and many spectral band properties for different gases and mixtures, giving good results in engineering applications, they can be found tabulated. For fire applications 6 spectral bands are usually used. For more accurate solutions, of the order of 100 bands are used. For nuclear reactor design applications usual software uses about 70 bands, with the additional problem that band unknowns are coupled because neutrons loss energy during scattering moving to less energetic bands. Fortunately, in heat transfer applications spectral bands are not coupled, so they can be solved independently. This implies much less memory demand in the numerical approximation of the problem.

Gray medium A medium is said to be gray when parameters κ_λ, σ_λ, and ϕ_λ are independent of the wavelength. In this case the monochromatic RTE (5.12) reads

$$\boldsymbol{s} \cdot \nabla u + (\kappa + \sigma) u - \frac{\sigma}{4\pi} \int_{4\pi} u(\boldsymbol{s}') \phi(\boldsymbol{s}', \boldsymbol{s}) d\boldsymbol{s} = \kappa \frac{\sigma_B T^4}{\pi} \tag{5.31}$$

There exist some smoothing models that treat the medium as gray (1 group) considering and absorption coefficient κ_a different of the emission coefficient κ_e. These models assume an spectral distributions of the obtained solution. Those smoothed nongray models read as

$$\boldsymbol{s} \cdot \nabla u + (\kappa_a + \sigma) u - \frac{\sigma}{4\pi} \int_{4\pi} u(\boldsymbol{s}') \phi(\boldsymbol{s}', \boldsymbol{s}) d\boldsymbol{s} = \kappa_e \frac{\sigma_B T^4}{\pi} \tag{5.32}$$

5.3.8 Radiative equilibrium

The right-hand-side term of the RTE (5.12) depends on the temperature of the medium. In the case that we need to solve the temperature field in Ω we need to make an energy balance imposing radiative equilibrium condition. When we have only radiation heat transfer, we need to impose divergence of radiative heat flux to be null.

Applying the divergence to heat flux from (5.2) we get the **heat flux divergence** in terms of spectral intensity

$$\nabla \cdot \boldsymbol{q} = \int_{4\pi} \int_0^{\infty} \boldsymbol{s} \cdot \nabla u_\lambda d\lambda \mathrm{d}s = \int_{4\pi} \boldsymbol{s} \cdot \nabla u \mathrm{d}s \tag{5.33}$$

replacing the monochromatic equation (5.12) into (5.33), and imposing null divergence to heat flux $\boldsymbol{q}$, we obtain the radiative equilibrium condition

$$\nabla \cdot \boldsymbol{q} = \int_0^{\infty} \kappa_\lambda \left(4\pi I_{b\lambda}(T) - \int_{4\pi} u_\lambda(\boldsymbol{s}) \, \mathrm{d}s \right) \mathrm{d}\lambda = 0 \tag{5.34}$$

So, to impose radiative equilibrium is to add an extra equation for solving temperature field. As $I_{b\lambda}$ is nonlinear on T we have a system of nonlinear equations in T. We will need to face nonlinear methods to solve the radiation field (when the medium can not be assumed as gray).

Gray medium For a gray medium, where κ does not depend on λ, radiative equilibrium condition can be written in terms of incident radiation G, replacing equation (5.3) into equation (5.34), which reads

$$\nabla \cdot \boldsymbol{q} = 4\pi\kappa I_b - \kappa G = 0 \tag{5.35}$$

The radiative equilibrium condition for a gray medium reads

$$G = 4\pi \int_0^{\infty} I_{b\lambda} d\lambda = 4\pi I_b = 4\sigma_B T^4 \tag{5.36}$$

In the case of gray medium with thermal equilibrium, replacing equation (5.36) into the transfer equation (5.31), the radiative intensity is obtained from the linear equation

$$\boldsymbol{s} \cdot \nabla u + (\kappa + \sigma_s) u - \frac{\sigma_s}{4\pi} \int_{4\pi} u(\boldsymbol{s}') \phi(\boldsymbol{s}', \boldsymbol{s}) d\boldsymbol{s}' - \frac{\kappa}{4\pi} \int_{4\pi} u(\boldsymbol{s}') ds' = 0 \tag{5.37}$$

5.3.9 Isotropic and linearly anisotropic scattering

An usual approximation of anisotropic scattering is the so called linearly anisotropic scattering, which consists in having a scattering phase function of the form

$$\phi(\boldsymbol{x}, \boldsymbol{s}, \boldsymbol{s\prime}) = 1 + A_1(\boldsymbol{x}) \, \boldsymbol{s} \cdot \boldsymbol{s}' \tag{5.38}$$

$A_1(\boldsymbol{x})$ is the linear anisotropic parameter $A_1 = 3\mu_0$, where μ_0 is the mean cosine of the scattering angle in a collision. That is, having a nonlinear phase function $\tilde{\phi}(\boldsymbol{s}, \boldsymbol{s}')$, A_1 is usually calculated as

$$A_1 = \frac{3}{4\pi} \int_{4\pi} \tilde{\phi}(\boldsymbol{s}, \boldsymbol{s}') \cos(\boldsymbol{s}, \boldsymbol{s}') d\boldsymbol{s} \tag{5.39}$$

With the linear anisotropic scattering assumption, replacing (5.38) into the monochromatic radiation equation we get

$$\boldsymbol{s} \cdot \nabla u_\lambda + (\kappa_\lambda + \sigma_{s\lambda})\, u_\lambda - \frac{\sigma_{s\lambda}}{4\pi}\,(G_\lambda + A_1 \boldsymbol{q}_\lambda \cdot \boldsymbol{s}) = \kappa_\lambda I_{b\lambda} \tag{5.40}$$

where G is the incident radiation and $\boldsymbol{q}$ the heat flux.

For the special case of gray medium, isotropic scattering and thermal equilibrium condition, combining equation (5.40) with (5.36) we get that radiative intensity satisfies the linear equation

$$\boldsymbol{s} \cdot \nabla u + (\kappa + \sigma_s)\, u = (\kappa + \sigma_s) I_{b\lambda} \tag{5.41}$$

and therefore radiative intensity only depends on the extinction coefficient $\beta = \kappa + \sigma$ (Equation(5.9)). That means that for a gray medium at radiative equilibrium there is no difference between absorption and isotropic scattering: any energy absorbed at $\boldsymbol{x}$ must be reemitted isotropically at the same location, although at different wavelengths; any isotropically scattered energy is simply redirected isotropically (at the same wavelengths). Since a gray medium is "colorblind" it cannot distinguish between emission and isotropic scattering.

5.4 The Discrete Ordinates Method

This section describes the Discrete Ordinates Method (DOM), a numerical approximation of the equation we have to solve to account for heat radiation, that is to say, equation (5.12). In particular, for background in the method described here, see [70, 93, 94] and references therein.

5.4.1 Discrete ordinates model

The discrete ordinates method (DOM) is a tool to transform the monochromatic equation, which is of integro-differential type, into a set of simultaneous partial differential equations. The method was first proposed by Chandrasekhar in his work on stellar and atmospheric radiation. The DOM method was firstly applied to problems in neutron transport theory, notably by Lee and Lathrop. However, only during the past twenty years has the DOM been applied to, and optimized for, general radiative heat transfer problems, primarily through the pioneering work of Fiveland and Truelove, [36, 37, 93].

The DOM is based on a discrete representation of the directional variation of the radiative intensity. A solution to the transport problem is found by solving the monochromatic equation of transfer(5.12) for a set of discrete directions $\boldsymbol{s}_i$ spanning the total solid angle range 4π. As such, the DOM is simply a discretization of the directional dependence of the equation of transfer. Integrals over the solid angle are approximated by numerical quadrature. For simplicity and without loss of generality we will treat the medium as gray.

Discrete ordinates equations

In the DOM, equation (5.31) is solved for a set of N different directions $\boldsymbol{s}_\beta$, $\beta = 1, 2, \ldots, N$, and the integral over direction are replaced by numerical quadratures of the form

$$\int_{4\pi} f(\boldsymbol{s})ds \simeq \sum_{\beta=1}^{N} w_\beta f(\boldsymbol{s}_\beta)$$

where w_β are the weights of each direction.

Let us introduce the variable $u_\beta(\boldsymbol{x})$ as the radiation heat in direction $\boldsymbol{s}_\beta$, that is to say, the approximation to $u(\boldsymbol{x}, \boldsymbol{s}_\beta)$. We have to solve the monochromatic equation over a domain $\Omega \subset \mathbb{R}^d$, which we may write as

$$\boldsymbol{s} \cdot \nabla u(\boldsymbol{x}, \boldsymbol{s}_\beta) + (\kappa + \sigma_s)u(\boldsymbol{x}, \boldsymbol{s}_\beta) - \frac{\sigma_s}{4\pi}\int_{4\pi} u(\boldsymbol{x}, \boldsymbol{s}')\phi(\boldsymbol{s}', \boldsymbol{s}_\beta)ds' = \kappa I_b \quad \beta = 1, 2, \ldots, N \tag{5.42}$$

Discretizing over all directions we get

$$\boldsymbol{s}_\beta \cdot \nabla u_\beta(\boldsymbol{x}) + (\kappa + \sigma_s)u_\beta(\boldsymbol{x}) - \frac{\sigma_s}{4\pi}\sum_{\alpha=1}^{N} w_\alpha u_\alpha(\boldsymbol{x})\phi(\boldsymbol{s}_\alpha, \boldsymbol{s}_\beta) = \kappa I_b \quad \beta = 1, 2, \ldots, N \tag{5.43}$$

This system of partial differential equations needs to be solved subject to the boundary conditions

$$u(\boldsymbol{x}, \boldsymbol{s})|_{\Gamma_{\text{in}}} = \epsilon I_b + \frac{\rho}{\pi}\int_{2\pi^+} u(\boldsymbol{x}, \boldsymbol{s})|\boldsymbol{n} \cdot \boldsymbol{s}|ds \tag{5.44}$$

which need also to be discretized. Discretizing as above over all directions, we have to impose boundary conditions to u_α with direction $\boldsymbol{s}_\alpha$ entering the domain Ω. These conditions are

$$u_\alpha(\boldsymbol{x}) = \frac{\epsilon\sigma_B T^4}{\pi} + \frac{\rho}{\pi}\sum_{\beta\in\Gamma_{\text{out}}} w_\beta u_\beta(\boldsymbol{x})|\boldsymbol{n} \cdot \boldsymbol{s}_\beta| \quad \forall\alpha \in \Gamma_{\text{in}} \tag{5.45}$$

We have a system of N first order partial differential equations coupled when we have a scattering medium or reflective boundary condition, that is to say, when $\sigma_s \neq 0$ or $\rho \neq 0$. Once this system is solved, the radiative heat flux may be found from its definition, equation (5.2), properly discretized:

$$\boldsymbol{q}(\boldsymbol{x}) = \sum_{\beta=1}^{N} w_\beta u_\beta(\boldsymbol{x})\, \boldsymbol{s}_\beta \tag{5.46}$$

Selection of discrete ordinates directions

It is customary to choose sets of directions and weights that are completely symmetric (i.e. sets that are invariant after any rotation of 90°), and exact for the zeroth, first and second moments, that is, the associated quadrature satisfies

$$\begin{aligned}
\int_{4\pi} ds = &\quad 4\pi &= \sum_{\beta=1}^{N} w_\beta \\
\int_{4\pi} \boldsymbol{s} ds = &\quad \boldsymbol{0} &= \sum_{\beta=1}^{N} w_\beta \boldsymbol{s}_\beta \\
\int_{4\pi} s_i s_j ds = &\quad \tfrac{4\pi}{3}\delta_{ij} &= \sum_{\beta=1}^{N} w_\beta^N s_{\beta i} s_{\beta j}
\end{aligned}$$

Not all sets of directions currently used satisfy the second moment equation. Heat fluxes at a wall are evaluated through a first moment of intensity over a half range of 2π. An important conclusion is that the set of ordinates and weights should also satisfy the first moment over a half range, that is,

$$\int_{\boldsymbol{n}\cdot\boldsymbol{s}<0} |\boldsymbol{n}\cdot\boldsymbol{s}| = \int_{\boldsymbol{n}\cdot\boldsymbol{s}>0} \boldsymbol{n}\cdot\boldsymbol{s} = \pi = \sum_{\boldsymbol{n}\cdot\boldsymbol{s}_\beta>0} w_\beta \boldsymbol{n}\cdot\boldsymbol{s}_\beta \tag{5.47}$$

It is impossible to satisfy equation (5.47) for arbitrary orientations of the surface normal $\boldsymbol{n}$, but it can be satisfied if $\boldsymbol{n} = \boldsymbol{i}, \boldsymbol{j}, \boldsymbol{k}$ (the unit vectors along the Cartesian directions). The sets of ordinates and weights S_N given by Lathrop and Carlson satisfy *(i)* the symmetry requirement, *(ii)* the moment equations and *(iii)* the half moment equation (5.47) for the three principal directions, and are widely used. Each S_N set has $N(N+2)$ directions. Another important and widely used quadrature and direction set is the T_N set given by Thurgood. Several other quadratures schemes can be found in the literature.

Thermal radiative equilibrium When the temperature field is an unknown of the problem and needs to be computed, we need to impose thermal equilibrium. In these problems we will consider the medium as gray, for the sake of simplicity. From equation (5.36) we have to satisfy the relation

$$\sum_{\beta=1}^{N} u_\beta = 4\sigma_B T^4 \tag{5.48}$$

For a gray medium, we get the radiation field u_β discretizing the homogeneous linear system (5.37) as

$$\boldsymbol{s}_\beta\cdot\nabla u_\beta + (\kappa+\sigma)u_\beta - \frac{1}{4\pi}\sum_{\alpha=1}^{N} w_\alpha u_\alpha \left(\kappa + \sigma_s\phi(\boldsymbol{s}_\alpha, \boldsymbol{s}_\beta)\right) = 0 \quad \beta = 1, 2, \ldots, N \tag{5.49}$$

Once we know the radiation intensity we find the temperature directly from equation (5.48).

As the system is homogeneous, if we put zero temperature boundary condition, which also means no emissivity from the walls, temperature and radiation intensity will be 0 over all the domain Ω.

5.5 The Method of Spherical harmonics, P_N Approximation

The DOM has a clear motivation and interpretation. However, it turns out to be excessively expensive in the applications. In this section we describe an alternative which is computationally cheaper.

The Method of *Spherical Harmonics* provides a vehicle to obtain an approximate solution of arbitrarily high order (i.e. accuracy), by transforming the equation of transfer into a set of simultaneous partial differential equations. The approach was fist proposed by Jeans [57] in his work on radiative transfer in stars. Further description of the method may be found in the books by Kourganoof [59], Davison [30] and Murray [72] (the latter two dealing with the closely related neutron transport theory).

The general principle of this method for solving the monochromatic equation (5.12) is that the angular dependency of the intensity $u(\boldsymbol{s})$ is expanded in a complete set of elementary functions. These functions are the Spherical Harmonics.

5.5.1 Theoretical background of the P_N model

Spherical Harmonics and Legendre functions

In this section we present the Legendre and Spherical Harmonics functions, and some of their properties, needed for developing the P_1 approximation.

The normalized spherical harmonics, Y_l^m are defined by

$$Y_{lm}\left(\theta,\varphi\right)=\sqrt{\frac{2l+1}{4\pi}\frac{(l-m)!}{(l+m)!}}P_l^m\left(\cos\theta\right)\exp\left(im\varphi\right) \tag{5.50}$$

that satisfy Laplace equation over a sphere in spherical coordinates. In (5.50) P_l^m is the associated Legendre Function, defined for integral values of $m=0,1,\cdots,l$ by the formula

$$P_l^m=(-1)^m\left(1-x^2\right)^{m/2}\frac{d^mP_l\left(x\right)}{dx^m} \tag{5.51}$$

where P_l are the Legendre Polynomials defined by the relations

$$\begin{aligned} P_0\left(x\right) &= 1 \\ P_n\left(x\right) &= \frac{1}{2^n n!}\frac{d^n}{dx^n}\left(x^2-1\right)^n \quad n=1,2,\ldots \end{aligned}$$

From (5.51)it is seen that $P_l^0(\boldsymbol{x})=P_l(\boldsymbol{x})$.

The spherical harmonics are orthonormal, in the sense that

$$\int_{4\pi}Y_{lm}Y_{l'm'}^*ds=\int_0^{2\pi}\int_{-1}^1Y_{lm}\left(\theta,\varphi\right)Y_{l'm'}^*\left(\theta,\varphi\right)d\cos\theta d\varphi=\delta_{ll'}\delta_{mm'} \tag{5.52}$$

They are also complete, in the sense that a function $f(\theta,\varphi)$ can be expanded in the series

$$f\left(\theta,\varphi\right)=\lim_{L\to\infty}\sum_{l=0}^{L}\sum_{m=-l}^{+l}f_{lm}Y_{lm}\left(\theta,\varphi\right)$$

with

$$f_{lm} = \int_{4\pi} f(\boldsymbol{s})\, Y_{lm}^{*}(\boldsymbol{s})\, d\boldsymbol{s}$$

The limit will be approached for any suitable function $f(\theta, \varphi)$, in particular if $f(\theta, \varphi)$ is continuous. If f is piecewise continuous, then at a discontinuity the mean value will be approached.

The spherical harmonics satisfy the important ***addition theorem***. Let two points on the unit sphere P and P' have coordinates (θ, φ) and (θ, φ'). Let γ be the angle between the vectors to P and P'. We have

$$\begin{aligned} P_l(\cos\gamma) &= \frac{4\pi}{2l+1}\sum_{m=-l}^{l} Y_{lm}^{*}(\theta', \varphi')\, Y_{lm}(\theta, \varphi) \\ &= P_l(\cos\theta)\, P_l(\cos\theta') + 2\sum_{m=1}^{l}\frac{(l-m)!}{(l+m)!}P_l^m(\cos\theta)\, P_l^m(\cos\theta')\cos(m(\varphi - \varphi')) \end{aligned}$$

When we want to expand an axisymmetric function $f(\theta)$, that does not to depend on φ, in terms of spherical harmonics, what we get is an expansion into a series of **Legendre Polynomials**. That comes from the fact that if we want (Y_{lm}) not depend on φ, m must be 0, and $(Y_{l0}) = \sqrt{(2l+1)/4\pi P_l}$, that is,

$$f(\theta) = \sum_{l=0}^{\infty}\frac{2l+1}{4\pi} f_l P_l(\cos\theta)$$

where the coefficients f_l are

$$f_l = 2\pi\int_{-1}^{1} f(\theta)\, d\cos\theta$$

Legendre Polynomials form a complete and orthogonal set, that is

$$\lim_{L\to\infty}\sum_{l=0}^{L}\frac{2l+1}{4\pi} f_l P_l(\cos\theta) = f(\theta)$$

and

$$2\pi\int_{-1}^{1} P_n(\theta)\, P_m(\theta)\, d\cos\theta = \frac{4\pi}{2n+1}\delta_{nm}$$

Legendre Polynomials satisfy the **recurrence relation**

$$(2m+1)\,\mu P_m(\mu) = (m+1)\, P_{m+1}(\mu) + m P_{m-1}(\mu) \tag{5.53}$$

Development of the general P_N approximation

Expanding the radiation intensity $u(\boldsymbol{x}, \boldsymbol{s})$ using spherical harmonic functions, we get

$$u(\boldsymbol{x}, \boldsymbol{s}) = \sum_{l=0}^{\infty}\sum_{m=-l}^{+l} u_{lm}(\boldsymbol{x})\, Y_{lm}(\boldsymbol{s}) \tag{5.54}$$

where $u_{lm}(\boldsymbol{x})$ are position dependent coefficients.

We may substitute eq. (5.54) into the monochromatic equation (5.12) and expand the scattering phase function $\phi(\boldsymbol{s}, \boldsymbol{s}')$ into a series of Legendre Polynomials as

$$\phi(\boldsymbol{s}, \boldsymbol{s}') = \phi(\mu_0) = \sum_{l=0}^{\infty} \frac{2l+1}{4\pi} A_l P_l(\mu_0) \qquad \mu_0 = \boldsymbol{s}' \cdot \boldsymbol{s} \tag{5.55}$$

Specifying $\boldsymbol{s}$ with coordinates μ, φ, where $\mu = \cos\theta$, according to the addition theorem of Legendre Polynomials we have

$$P_l(\mu_0) = P_l(\mu) P_l(\mu') + 2 \sum_{m=1}^{l} \frac{(l-m)!}{(l+m)!} P_l^m(\mu) P_l^m(\mu') \cos(m(\varphi - \varphi')) \tag{5.56}$$

The source term I_b is isotropic, so $I_b = I_b P_0(\cos\theta)$. Inserting all this into the monochromatic eq. (5.12) we get

$$\begin{aligned}
&\boldsymbol{s} \cdot \sum_{l=0}^{\infty} \sum_{m=-l}^{+l} \nabla u_{lm}(\boldsymbol{x}) Y_{lm}(\mu', \varphi') + (\kappa + \sigma_s) \sum_{l=0}^{\infty} \sum_{m=-l}^{+l} u_{lm}(\boldsymbol{x}) Y_{lm}(\mu', \varphi') \\
&- \frac{\sigma_s}{4\pi} \int_{4\pi} \sum_{n=0}^{\infty} \left(\frac{2n+1}{4\pi} A_n \left(P_n(\mu) P_n(\mu') \right.\right. \\
&\left.\left. + 2 \sum_{m=1}^{n} \frac{(n-m)!}{(n+m)!} P_n^m(\mu) P_n^m(\mu') \cos(m(\varphi - \varphi')) \right)\right) \\
&\times \sum_{l,m} u_{lm}(\boldsymbol{x}) Y_{lm}(\mu', \varphi') \, d\mu' d\varphi' = \kappa I_b \delta_{l0}
\end{aligned}$$

The next step is to multiply by $\boldsymbol{Y}_{kn}$ followed by integration over all directions. Exploiting the orthogonality properties of Spherical harmonics leads to infinitely many coupled partial differential equations in the unknown position-dependent functions u_{lm}. Up to this point the above representation is an exact method for the determination of the intensity field. To simplify the problem an approximation is now made by truncating the series in equation (5.54) after N terms. By doing so, we have replaced the single unknown $u(\boldsymbol{x}, \boldsymbol{s})$ by $(N+1)^2$ $u_{lm}(\boldsymbol{x})$ unknowns that are functions of space only. The number of terms in the series, N, gives the method its order and its name. A detailed derivation of the general three-dimensional case in Cartesian coordinates has been given by Cheng [13, 14].

Development of the P_N method for the one dimensional plane parallel medium

In this subsection we will develop the general P_N method in some detail for the one-dimensional problem of a plane parallel medium, in order to shed further light on the general method. In one dimensional problems, the intensity only depends of one spacial coordinate $\boldsymbol{x}$ and one directional coordinate θ, the polar angle from the coordinate axis . So $u = u(x, \mu)$, where $\mu = \cos\theta$, is independent of the azimuthal angle φ. The monochromatic equation for the one dimensional problem is

$$\mu \frac{\partial u}{\partial x} + (\kappa + \sigma_s) u - \frac{\sigma_s}{4\pi} \int_{4\pi} \phi(\boldsymbol{s}, \boldsymbol{s}') u(\boldsymbol{s}') ds = \kappa I_b \tag{5.57}$$

The radiation intensity is expanded in Legendre polynomials as

$$u\left(\boldsymbol{x},\mu\right)=\sum_{l=0}^{\infty}\frac{2l+1}{4\pi}u_l(\boldsymbol{x})P_l\left(\mu\right)$$

The scattering phase function ϕ is expanded in Legendre Polynomials as in (5.56) and (5.55). Upon insertion of all Legendre developments into the equation of transfer (5.57), the terms containing $\cos\left(m\left(\varphi-\varphi'\right)\right)$ vanish upon integration over φ'. Then the integral operator of scattering becomes:

$$\frac{\sigma_s}{4\pi}\int_{4\pi}\phi\left(\boldsymbol{s},\boldsymbol{s}'\right)u\left(\boldsymbol{s}'\right)ds=\frac{\sigma_s}{2}\sum_{l=0}^{\infty}\frac{2l+1}{4\pi}A_lP_l\left(\mu\right)\int_{-1}^{1}P_l\left(\mu'\right)\frac{2l+1}{4\pi}u_l\left(x\right)P_l\left(\mu'\right)d\mu$$

Using the orthogonality properties of Legendre functions, the radiation equation in 1D is recasted as

$$\sum_{m=0}^{\infty}\frac{2m+1}{4\pi}\left(\mu\frac{du_m}{dx}+\left(\kappa+\sigma_s\right)u_m\right)P_m\left(\mu\right)-\frac{\sigma_s}{4\pi}\sum_{m=0}^{\infty}\frac{2m+1}{4\pi}A_mu_mP_m\left(\mu\right)=\kappa I_b$$

The recurrence relation of Legendre polynomials (5.53) is used to eliminate μ multiplying the derivative term. Then the resulting expression is multiplied by $P_n(\mu)$ and integrated over μ from -1 to 1. After using the orthogonality of Legendre polynomials it is found that

$$\left(n+1\right)\frac{du_{n+1}}{dx}+n\frac{du_n}{dx}+(2n+1)\left(\kappa+\sigma_s-\sigma_s\frac{A_n}{4\pi}\right)u_n=4\pi I_b\delta_{0m}\quad n=0,1,2,\ldots \tag{5.58}$$

with the requirement that u_{-1} is zero. The P_N approximation is defined by considering the first $N+1$ of these equations and setting $u_N=0$ or, alternatively, $du_{N+1}/dx=0$. We have a set of $(N+1)$ simultaneous first order ordinary differential equations for the unknown functions $u_n(x)$. As such it requires a set of $(N+1)$ boundary conditions for its solution.

5.5.2 The P_1 method, approximation to a general geometry

In this section we present the P_1 model equations and some of its derivation. For a detailed derivation see [70].

If the series in equation (5.54) is truncated beyond $l=1$, we get the lowest order, or P_1 approximation. Carrying out the expansion in spherical harmonics, the $P1$ approximation to intensity $u(\boldsymbol{s})$ is.

$$u(\boldsymbol{x},\boldsymbol{s})=\frac{1}{4\pi}\left(G(\boldsymbol{x})+3\boldsymbol{q}(\boldsymbol{x})\cdot\boldsymbol{s}\right) \tag{5.59}$$

where G is the incident radiation, and $\boldsymbol{q}$ the heat flux.

Assuming linear anisotropic scattering (it can be shown from equation (5.57) that the P_1 approximation remains unchanged for nonlinear anisotropic scattering)

$$\phi(\boldsymbol{x},\boldsymbol{s},\boldsymbol{s}\prime)=1+A_1\left(\boldsymbol{x}\right)\boldsymbol{s}\cdot\boldsymbol{s}' \tag{5.60}$$

Replacing eqs. (5.59) and (5.60) in the transport equation (5.12) leads to

$$\frac{1}{4\pi}\left(\nabla G+\nabla\cdot\left(\left(3\boldsymbol{q}\cdot\boldsymbol{s}\right)\boldsymbol{s}\right)\right)+\frac{1}{4\pi}\left(\kappa+\sigma_s\right)\left(G+3\boldsymbol{q}\cdot\boldsymbol{s}\right)-\frac{\sigma_s}{4\pi}\left(G+A_1\boldsymbol{q}\cdot\boldsymbol{s}\right)=\kappa I_b \tag{5.61}$$

Integrating eq. (5.61) over all solid angles we get the zeroth moment equation

$$\nabla\cdot\boldsymbol{q}=\kappa\left(4\pi I_b-G\right) \tag{5.62}$$

This equation is identical to eq. (5.35) since it does not depend on the functional form for intensity.

To obtain additional equations we may multiply eq. (5.61) by Y_{1m}, $m=-1,0,1$, and then integrate over all directions leading to the vector equation

$$\boldsymbol{\nabla}G=-\left(3\left(\kappa+\sigma_s\right)-A_1\sigma_s\right)\boldsymbol{q} \tag{5.63}$$

Equations (5.62) and (5.63) form a complete set of one scalar and one vector equation in the unknowns G and $\boldsymbol{q}$, and are the governing equations of the P_1 approximation. The heat flux may be eliminated from these equations. Defining the diffusion coefficient D as

$$D=\frac{1}{\left(3\left(\kappa+\sigma_s\right)-A_1\sigma_s\right)} \tag{5.64}$$

We get the diffusion equation

$$\boxed{-\nabla\cdot\left(D\nabla G\right)+\kappa G=4\pi\kappa I_b} \tag{5.65}$$

Once G is solved from equation (5.65), the radiative heat flux is obtained from the next diffusion Fick's law equation

$$\boxed{\boldsymbol{q}=-D\nabla G} \tag{5.66}$$

Finally, the radiation intensity $u(\boldsymbol{x},\boldsymbol{s})$ is obtained from (5.59).

Boundary conditions

Equation (5.65) requires a single boundary condition. We want to satisfy entering radiation boundary conditions in an integral sense. For a surface which emits and reflects radiation diffusely, we want equation (5.26) to hold, that can be written as

$$J=\frac{\rho\boldsymbol{q}\cdot\boldsymbol{n}+\epsilon\pi I_b}{1-\rho}=\frac{1-\epsilon}{\epsilon}\boldsymbol{q}\cdot\boldsymbol{n}+\pi I_b \tag{5.67}$$

where J is the surface radiosity, defined in section (5.3.6) as the total heat flux emitted and reflected from the surface into the medium. The second equality holds for a diffuse and opaque surface ($\rho=1-\epsilon$). Replacing the P_1 approximation for the intensity, equation (5.59), with the radiosity definition, equation (5.23), we need to satisfy the equality

$$J=\int_{n\cdot\boldsymbol{s}<0}u\left(\boldsymbol{s}\right)\boldsymbol{s}\cdot\boldsymbol{n}ds=\frac{1}{4\pi}\int_{2\pi^-}\left(G+3\boldsymbol{q}\cdot\boldsymbol{s}\right)\boldsymbol{s}\cdot\boldsymbol{n}ds=\frac{1}{4}\left(G-2\boldsymbol{q}\cdot\boldsymbol{n}\right) \tag{5.68}$$

Satisfying simultaneously equations (5.67) and (5.68) we get the relation that we want to prescribe over all the boundary

$$\boldsymbol{q} \cdot \boldsymbol{n} = \frac{(1-\rho)\,G - \epsilon 4\pi I_b}{2+2\rho} = \frac{\epsilon}{4-2\epsilon}\,(G - 4\pi I_b) \tag{5.69}$$

The second relation only holds for opaque surfaces. Modest [69] has shown that equation (5.69) also holds if the surface reflectance consists of purely diffuse and purely specular components, i.e, if $\epsilon = 1 - \rho^d - \rho^s$. Thus, within the accuracy of the P_1 approximation the results for enclosures with diffusely and/or specularly reflecting surfaces are identical. Substituting $\boldsymbol{q}$ from equation (5.66) into boundary relation (5.69), we get the correct boundary condition for G

$$\boxed{-D\frac{\partial G}{\partial n} = \frac{(1-\rho)\,G - \epsilon 4\pi I_b}{2+2\rho} = \frac{\epsilon}{4-2\epsilon}\,(G - 4\pi I_b)} \tag{5.70}$$

where the second equality only holds for an opaque surface. This is a boundary condition of Robyn type, and must hold over all the boundary. When a boundary condition is satisfied in integral sense, it is a Marshak's type of boundary condition. In the case of vacuum boundary conditions, meaning no wall and no entering radiation to the domain, we must set $\rho = 0$ and $\epsilon = 1$ getting the relation $D\frac{\partial G}{\partial n} + \frac{1}{2}G = 0$, frequently used in neutron transport theory.

The P_1 approximation is a very popular method since it reduces the spectral or gray equation of transfer from a very complicated integral equation to a relatively simple partial differential equation.The method is powerful allowing nonblack surfaces, nonconstant properties, anisotropic scattering, etc. It is important to remember that the P_1-approximation may be substantially in error in optically thin media with strongly anisotropic intensity distributions, in particular in multidimensional geometries with large aspect ratios (i.e., long an narrow configurations) and/or when surface emission dominates over medium emission.

Radiative equilibrium

When radiative equilibrium prevails, we need to solve temperature of the medium by an extra equation, imposing that all absorbed energy must be emitted, that is $\nabla \cdot \boldsymbol{q} = 0$. The P_1 equation for this condition reads

$$\boxed{-\nabla \cdot (D\nabla G) = 0} \tag{5.71}$$

This equation needs boundary condition (5.70) to be imposed.

Once incident radiation G is solved temperature field $T(\boldsymbol{x})$ can be found from the thermal equilibrium condition applied to Eq. (5.65)

$$4\pi \int_0^\infty \kappa_\lambda I_b d\lambda = \int_0^\infty \kappa_\lambda G_\lambda d\lambda \tag{5.72}$$

5.6 Problem statement for the radiation transport equation

In this section is analyzed the boundary value problem of the monochromatic equation stated in subsection 5.3.4

5.6.1 Variational form

For simplicity, in the description and analysis of the formulation we shall supply (5.13) with the simplest boundary condition $u = 0$ on Γ^-, although in the numerical examples we shall deal also with emissive and reflective boundary conditions. Changes required to extend the numerical approximation and its analysis to this situation are explained in subsection 5.6.2.

In order to write the weak form of the problem let us introduce the spaces

$$\begin{aligned}\mathcal{V} &= \{u : \Omega \times \mathcal{S}^2 \to \mathbb{R} \mid u, \boldsymbol{s}\cdot\nabla u \in L^2(\Omega)\; \forall \boldsymbol{s} \in \mathcal{S}^2\},\\ \mathcal{W} &= \{u : \Omega \times \mathcal{S}^2 \to \mathbb{R} \mid \|u\|_\Omega,\ \|\boldsymbol{s}\cdot\nabla u\|_\Omega \in L^2(\mathcal{S}^2)\} = L^2(\mathcal{S}^2;\mathcal{V}),\end{aligned}$$

where $\|u\|_\Omega$ is the usual $L^2(\Omega)$-norm. We also define the inner product for functions in $\mathcal{W}$ (not the one associated to its topology) as

$$(u,v) = \int_{\mathcal{S}^2}\int_\Omega u(\boldsymbol{x},\boldsymbol{s})\, v(\boldsymbol{x},\boldsymbol{s})\, \mathrm{d}\boldsymbol{x}\mathrm{d}\boldsymbol{s} = \int_{\mathcal{S}^2} (u,v)_\Omega\, \mathrm{d}\boldsymbol{s}, \tag{5.73}$$

where $(u,v)_\Omega$ is the usual $L^2(\Omega)$-inner product. The norm associated to $(\cdot,\cdot)$ is written as $\|u\| = (u,u)^{1/2}$. If $\gamma \subset \partial\Omega \times \mathcal{S}^2$, we define

$$(u,v)_\gamma = \int_\gamma u(\boldsymbol{x},\boldsymbol{s}) v(\boldsymbol{x},\boldsymbol{s})\, |\boldsymbol{n}\cdot\boldsymbol{s}|\, \mathrm{d}\boldsymbol{x}\mathrm{d}\boldsymbol{s},$$

and the associated norm $\|u\|_\gamma = (u,u)_\gamma^{1/2}$. In particular, we will use this definition for $\gamma = \Gamma^+$, case in which $|\boldsymbol{n}\cdot\boldsymbol{s}| = \boldsymbol{n}\cdot\boldsymbol{s}$.

The weak form of problem ((5.13)) consists in finding $u \in \mathcal{W}$ such that

$$\mathcal{B}(u,v) := (Lu,v) = (\boldsymbol{s}\cdot\nabla u, v) + (\kappa u, v) + (S_\sigma u, v) = (f,v) =: \mathcal{L}(v)\; \forall v \in L^2(\mathcal{S}^2; L^2(\Omega)). \tag{5.74}$$

By assumption, ϕ is a bounded and symmetric function on $\mathcal{S}^2\times\mathcal{S}^2$, and therefore S_1 defined in (5.16) is a self-adjoint operator from $L^2(\mathcal{S}^2)$ onto itself. It is a compact perturbation of the identity operator and has a real and countable spectrum confined to the interval $[0,1]$. The set of eigenfunctions corresponding to the eigenvalue $\lambda_0 = 0$ contains at least the constants on $\mathcal{S}^2$ and, furthermore, zero is an isolated eigenvalue, see [58, 98] for details.

By the Hilbert-Schmidt theorem there is an orthonormal set $\{u_n(\boldsymbol{s})\}$ of eigenfunctions corresponding to non-zero eigenvalues $\{\lambda_n\}$ of S_1 such that every function $u(\boldsymbol{x},\cdot) \in L^2(\mathcal{S}^2)$ has an unique decomposition of the form [98]

$$u(\boldsymbol{x},\boldsymbol{s}) = \sum_{n=1}^{\infty} \alpha_n(\boldsymbol{x}) u_n(\boldsymbol{s}) + u_0(\boldsymbol{x},\boldsymbol{s}), \tag{5.75}$$

where $\alpha_n(\boldsymbol{x}) \in \mathbb{R}$, $u_0(\boldsymbol{x},\boldsymbol{s}) \in \ker S_1$ and

$$S_1 u(\boldsymbol{x},\boldsymbol{s}) = \sum_{n=1}^{\infty} \lambda_n \alpha_n(\boldsymbol{x}) u_n(\boldsymbol{s}). \tag{5.76}$$

For $\boldsymbol{x} \in \Omega$ fixed, $L^2(\mathcal{S}^2)$ can be decomposed as $L^2(\mathcal{S}^2) = \ker S_1 \oplus (\ker S_1)^{\perp}$. If we denote by $\Pi^{\perp}$ the orthogonal projection onto $(\ker S_1)^{\perp}$, from (5.75) and (5.76) it is easily seen that the scattering operator satisfies the following properties when applied to functions $u, v \in L^2(\Omega \times \mathcal{S}^2)$:

$$\begin{aligned} (S_1 u, v) &= \left(\Pi^{\perp} S_1 u, \Pi^{\perp} v\right) = \left(\Pi^{\perp} S_1 v, \Pi^{\perp} u\right), \\ \lambda_1 \|\sigma_s \Pi^{\perp} u\| &\leq \|S_{\sigma} u\| \leq \|\sigma_s \Pi^{\perp} u\|, \\ \|S_1 u\|^2 &\leq (S_1 u, u). \end{aligned} \tag{5.77}$$

5.6.2 Emissive and reflective boundary conditions

A generalization of the homogeneous boundary conditions that we will use for the presentation of the method is a boundary condition of the form

$$\begin{aligned} u(\boldsymbol{x}, \boldsymbol{s})|_{\mathcal{S}^-_{\partial x}} &= \epsilon \bar{u}(\boldsymbol{x}, \boldsymbol{s})|_{\mathcal{S}^-_{\partial x}} + \frac{1-\epsilon}{\pi} A^+ u(\boldsymbol{x}), \\ A^{\pm} u(\boldsymbol{x}) &:= \int_{\mathcal{S}^{\pm}_{\partial x}} u(\boldsymbol{x}, \boldsymbol{s}') |\boldsymbol{n} \cdot \boldsymbol{s}'| \mathrm{d}\boldsymbol{s}', \end{aligned} \tag{5.78}$$

where $\bar{u}$ is a given function and $0 \leq \epsilon \leq 1$. Note that the last term in (5.78) does not depend on $\boldsymbol{s}$. Such type of boundary condition corresponds to the so called emissive and reflective boundaries. In this case, $\rho := 1 - \epsilon$ and ϵ are the diffuse reflection and emissive wall coefficients, respectively, and $\bar{u}(\boldsymbol{x}, \boldsymbol{s}) = I_b(\boldsymbol{x})$ is the blackbody radiation, given by $I_b = \sigma_B T^4/\pi$, where T is the wall temperature and $\sigma_B = 5.6704 \cdot 10^{-8}$ W/m^{2}K is the Stefan-Boltzmann constant. Note that in this case the whole right-hand-side in (5.78) is independent of $\boldsymbol{s}$.

Condition (5.78) can be imposed weakly, leading to the following variational form of the problem: find $u \in \mathcal{W}$ such that

$$\mathcal{B}(u, v) + \eta (u, v)_{\Gamma^-} - \eta \frac{1-\epsilon}{\pi} (A^+ u, v)_{\Gamma^-} = \mathcal{L}(v) + \eta \epsilon (\bar{u}, v)_{\Gamma^-} \quad \forall v \in \mathcal{W}, \tag{5.79}$$

where η is a dimensionless parameter that has to satisfy the conditions indicated later. Observe that the space of test functions is now $\mathcal{W}$, since traces of this test functions are required on Γ^-.

The introduction of the new terms in (5.79) with respect to (5.74) does not offer any problem for the numerical approximation. In fact, it can be understood that the boundary condition (5.78) is imposed with Nitsche's method [76].

The stability properties of both the continuous problem (5.79) and of its discrete finite element approximation are similar to those of (5.74). This is so because the positivity of the bilinear form in the left-hand-side of (5.79) can be guaranteed as explained in the following. Let us start noting that

$$A^{\pm} u(\boldsymbol{x}) \leq \left(\int_{\mathcal{S}^{\pm}_{\partial x}} |\boldsymbol{n} \cdot \boldsymbol{s}| \mathrm{d}\boldsymbol{s} \right)^{1/2} \left(\int_{\mathcal{S}^{\pm}_{\partial x}} u^2(\boldsymbol{x}, \boldsymbol{s}) |\boldsymbol{n} \cdot \boldsymbol{s}| \mathrm{d}\boldsymbol{s} \right)^{1/2} = \left(\pi \int_{\mathcal{S}^{\pm}_{\partial x}} u^2(\boldsymbol{x}, \boldsymbol{s}) |\boldsymbol{n} \cdot \boldsymbol{s}| \mathrm{d}\boldsymbol{s} \right)^{1/2},$$

and therefore

$$A^+ u(\boldsymbol{x}) A^-(\boldsymbol{x}) \leq \frac{\pi}{2} \left(\frac{1}{\alpha} \int_{\mathcal{S}^-_{\partial x}} u^2(\boldsymbol{x}, \boldsymbol{s}) |\boldsymbol{n} \cdot \boldsymbol{s}| \mathrm{d}\boldsymbol{s} + \alpha \int_{\mathcal{S}^+_{\partial x}} u^2(\boldsymbol{x}, \boldsymbol{s}) |\boldsymbol{n} \cdot \boldsymbol{s}| \mathrm{d}\boldsymbol{s} \right),$$

for all $\alpha > 0$. Using the positive definiteness of S_1, the fact that $\kappa \geq 0$ and this last inequality it follows that

$$\begin{aligned}
&\mathcal{B}\,(u,u) + \eta(u,u)_{\Gamma^-} - \eta\frac{1-\epsilon}{\pi}(A^+u,u)_{\Gamma^-} \\
&\quad\geq \frac{1}{2}(u,u)_{\Gamma^+} - \frac{1}{2}(u,u)_{\Gamma^-} + \eta(u,u)_{\Gamma^-} - \eta\frac{1-\epsilon}{\pi}\int_{\partial\Omega} A^+u(\boldsymbol{x})A^-u(\boldsymbol{x})\mathrm{d}\boldsymbol{x} \\
&\quad\geq \|u\|^2_{\Gamma^+}\left(\frac{1}{2} - \eta\frac{1-\epsilon}{2}\alpha\right) + \|u\|^2_{\Gamma^-}\left(-\frac{1}{2} + \eta - \eta\frac{1-\epsilon}{2\alpha}\right).
\end{aligned} \tag{5.80}$$

Positivity of (5.80) follows from conditions

$$\eta \leq \frac{1}{\alpha(1-\epsilon)}, \quad \eta\left(1 - \frac{1-\epsilon}{2\alpha}\right) \geq \frac{1}{2}. \tag{5.81}$$

For $\epsilon = 1$ the only requirement is $\eta \geq \frac{1}{2}$, whereas for $\epsilon < 1$ it is easily checked that the above conditions are feasible. For example, for $\alpha = 1 - \epsilon$ they read $1 \leq \eta \leq (1-\epsilon)^{-2}$. If fact, a little analysis shows that the upper bound for η is maximized if $\alpha = \frac{1}{\rho} - \sqrt{\frac{1}{\rho^2} - 1}$ (where $\rho = 1 - \epsilon$), which satisfies $\alpha \geq \frac{\rho}{2}$ and is obtained by choosing α as the smallest value satisfying $(\rho\alpha)^{-1} \geq \left[2\left(1 - \frac{\rho}{2\alpha}\right)\right]^{-1}$. Note that when the $=$ sign holds in the first inequality of (5.81), control on $\|u\|_{\Gamma^+}$ is lost. If this norm is to be included in the stability norm (see (5.108) below), the $\leq$ symbol has to be replaced by $<$. In the case $\epsilon = 0$ one must choose $\alpha = 1$ and thus $\eta = 1$. Therefore, $\epsilon > 0$ is needed if (5.81) has to hold with strict inequalities.

The positivity of (5.80) is enough to extend the formulation and analysis of the methods that follow to (5.78) with minor modifications.

5.7 Numerical approximation of the monochromatic equation

In this section we consider the numerical approximation of problem (5.74). Spatial and directional discretizations will be considered independently. Our main concern is the former, and we will therefore consider a generic finite dimensional space of functions defined on $\mathcal{S}^2$. However, we will also particularize our formulation to the DOM directional discretization, which will be used in the numerical experiments of Section 5.9.

5.7.1 Semidiscrete spatial discretization

Let us consider a finite element partition $\mathcal{P}_h = \{K\}$ of the domain Ω of diameter h. From this finite element partition we build up conforming finite element spaces $\mathcal{V}_h \subset \mathcal{V}$ in the usual manner. Let also $\mathcal{W}_h = L^2\left(\mathcal{S}^2; \mathcal{V}_h\right)$. Discrete test functions will also be taken in this space.

Galerkin finite element approximation

The spatial Galerkin finite element approximation of problem (5.74) consists in finding $u_h \in \mathcal{W}_h$ such that

$$\mathcal{B}(u_h, v_h) = \mathcal{L}(v_h) \quad \forall v_h \in \mathcal{W}_h. \tag{5.82}$$

The question that arises once the discrete problem is set is whether it is stable or not. The bilinear form $\mathcal{B}(u_h, v_h)$ is not coercive with respect to the graph norm (in particular, with respect to the derivatives involved), as we shall see later. In the particular case of null scattering ($\sigma_s = 0$ on Ω), the problem decouples into a system of convection-reaction equations on Ω. This system is hyperbolic, and the Galerkin finite element method is known to produce spurious oscillations in this case.

Stabilized finite element approximation using subscales

In this section we describe the finite element approximation proposed, which can be cast in the variational multiscale framework proposed in [49]. For completeness, we briefly describe it in the following, also adapted to our particular proposal.

As in [49], let us split the continuous space $\mathcal{V}$ as $\mathcal{V} = \mathcal{V}_h \oplus \tilde{\mathcal{V}}$, where $\tilde{\mathcal{V}}$ is any space to complete $\mathcal{V}_h$ in $\mathcal{V}$, obviously infinite-dimensional. From $\mathcal{V}_h$ and $\tilde{\mathcal{V}}$ we may define $\mathcal{W}_h = L^2(\mathcal{S}^2; \mathcal{V}_h)$ and $\tilde{\mathcal{W}} = L^2(\mathcal{S}^2; \tilde{\mathcal{V}})$, which satisfy $\mathcal{W} = \mathcal{W}_h \oplus \tilde{\mathcal{W}}$. Since $\tilde{u} \in \tilde{\mathcal{W}}$ represents the component of u whose spatial dependence cannot be represented in the finite element space, we call $\tilde{\mathcal{W}}$ the space of *subscales* or *subgrid scales*. We may also decompose the space of test functions as $L^2(\mathcal{S}^2; L^2(\Omega)) = \mathcal{W}_h + \tilde{\mathcal{W}}_T$.

The weak form of the continuous problem (5.74) is exactly equivalent to find $u_h \in \mathcal{W}_h$ and $\tilde{u} \in \tilde{\mathcal{W}}$ such that

$$\mathcal{B}(u_h, v_h) + \mathcal{B}(\tilde{u}, v_h) = \mathcal{L}(v_h) \quad \forall v_h \in \mathcal{W}_h, \tag{5.83}$$

$$\mathcal{B}(u_h, \tilde{v}) + \mathcal{B}(\tilde{u}, \tilde{v}) = \mathcal{L}(\tilde{v}) \quad \forall \tilde{v} \in \tilde{\mathcal{W}}_T. \tag{5.84}$$

Integrating the convective term by parts in the second term in the left-hand-side of (5.83) and in (5.84) it is found that problem (5.83)-(5.84) can be written as

$$\mathcal{B}(u_h, v_h) + (L^* v_h, \tilde{u}) + (v_h, \tilde{u})_{\Gamma +} = (v_h, f), \tag{5.85}$$

$$(\tilde{v}, L\tilde{u}) = (\tilde{v}, f - Lu_h), \tag{5.86}$$

where L^* denotes the adjoint operator, which is defined as

$$L^* u(\boldsymbol{x}, \boldsymbol{s}) = -\boldsymbol{s} \cdot \nabla u(\boldsymbol{x}, \boldsymbol{s}) + \kappa u(\boldsymbol{x}, \boldsymbol{s}) + S_\sigma u(\boldsymbol{x}, \boldsymbol{s}).$$

Equation (5.86) is equivalent to

$$L\tilde{u} = f - Lu_h + v_{h,\text{ort}} \quad \text{in } \Omega, \quad v_{h,\text{ort}} \in \tilde{\mathcal{W}}_T^{\perp}, \tag{5.87}$$

where $v_{h,\text{ort}}$ is responsible to enforce that the previous equation holds in the space of the subscales. The goal of all subscale methods is to approximate $\tilde{u}$ to end up with a modified problem for u_h with enhanced stability properties.

There are several possibilities to deal with problem (5.87). We consider the algebraic approximation $L\tilde{u} \approx \tau^{-1}\tilde{u}$, which has to be understood in the L^2-norm (see [19]). Another possibility is to approximate $\tilde{u}$ by bubble functions, which leads to a similar method for a proper identification of this bubble functions (see [35], for example). When replaced into equation (5.87) this approximation gives

$$\tilde{u} = \tau (f - Lu_h + v_{h,\text{ort}}), \tag{5.88}$$

where τ is an algorithmic parameter depending on the geometry of each element domain K and the coefficients of operator L. This approximation for $\tilde{u}$ is intended to mimic the effect of the exact subscales in the volume integral of (5.85), whereas the integral over the boundary Γ^+ will be neglected. It remains to define the stabilization parameter τ in terms of the equation coefficients and the mesh size and to define $v_{h,\mathrm{ort}}$, thus selecting the space of subscales. The approximation performed to obtain τ is based on an (approximate) Fourier analysis of the problem as in [19] and will be discussed in Subsection 5.7.3 after the directional discretization is introduced. The choice of the space of subscales is discussed in the rest of this section, where two different possibilities are considered.

Algebraic subscales and the SUPG method

The simplest choice for the space of subscales is to take $v_{h,\mathrm{ort}} = 0$, which implies that the subscales belong to the space of the residuals. This results in what we will call algebraic subgrid scale method (ASGS). Inserting (5.88) in (5.85), the discrete problem in this case reads: find $u_h \in \mathcal{W}_h$ such that

$$\mathcal{B}_{\mathrm{asgs}}\left(u_h, v_h\right) = \mathcal{L}_{\mathrm{asgs}}(v_h) \quad \forall v_h \in \mathcal{W}_h,$$

where

$$\begin{aligned} \mathcal{B}_{\mathrm{asgs}}\left(u_h, v_h\right) &:= \mathcal{B}\left(u_h, v_h\right) + (-L^* v_h, \tau L u_h), \\ \mathcal{L}_{\mathrm{asgs}}\left(v_h\right) &:= \mathcal{L}\left(v_h\right) + (-L^* v_h, \tau f). \end{aligned}$$

This method is a generalization of the well known SUPG method in which only the advective term is considered to weight the subscales instead of the whole adjoint operator L^*. In this method the discrete problem reads: find $u_h \in \mathcal{W}_h$ such that

$$\mathcal{B}_{\mathrm{supg}}\left(u_h, v_h\right) = \mathcal{L}_{\mathrm{supg}}(v_h) \quad \forall v_h \in \mathcal{W}_h, \tag{5.89}$$

where

$$\begin{aligned} \mathcal{B}_{\mathrm{supg}}\left(u_h, v_h\right) &:= \mathcal{B}\left(u_h, v_h\right) + (\boldsymbol{s} \cdot \nabla v_h, \tau L u_h), \\ \mathcal{L}_{\mathrm{supg}}\left(v_h\right) &:= \mathcal{L}\left(v_h\right) + (\boldsymbol{s} \cdot \nabla v_h, \tau f). \end{aligned} \tag{5.90}$$

Orthogonal subscales

The starting point has been the decomposition $\mathcal{V} = \mathcal{V}_h \oplus \tilde{\mathcal{V}}$. Among the possibilities to choose $\tilde{\mathcal{V}}$, a particular choice is to take the space for the subscales orthogonal to the finite element space, that is to say,

$$\tilde{\mathcal{V}} = \mathcal{V}_h^{\perp} \cap \mathcal{V} \approx \mathcal{V}_h^{\perp}, \tag{5.91}$$

where the symbol $\approx$ has to be understood in the sense that conformity is violated. Using the same reasoning as in [19], this approximation together with some additional simplifications lead to the expression for the subscales

$$\tilde{u} = -\tau P_h^{\perp}\left(\boldsymbol{s} \cdot \nabla u_h\right),$$

with $P_h^\perp = I - P_h$, I being the identity and P_h the L^2-projection onto the finite element space. Replacing this expression into equation (5.85) and taking into account that subscale functions vanish on $\partial\Omega$ we get the final discrete problem: find $u_h \in \mathcal{W}_h$ such that

$$\mathcal{B}_{\text{oss}}\left(u_h, v_h\right) = \mathcal{L}(v_h) \quad \forall v_h \in \mathcal{W}_h, \tag{5.92}$$

where, for constant physical coefficients and uniform meshes,

$$\mathcal{B}_{\text{oss}}\left(u_h, v_h\right) := \mathcal{B}\left(u_h, v_h\right) + (\boldsymbol{s} \cdot \nabla v_h, \tau P_h^\perp(\boldsymbol{s} \cdot \nabla u_h)). \tag{5.93}$$

The simplifying assumptions yield a method that is easy to implement and with good stability properties, as we shall see in Section 5.8. Comparing expressions (5.89) and (5.93) it is observed that the latter *has less terms to evaluate*, since it is not necessary to weight the whole residual by $\boldsymbol{s} \cdot \nabla v_h$. However, the term $P_h^\perp(\boldsymbol{s} \cdot \nabla u_h)$ leads to a wider connectivity between the mesh nodes. Nevertheless, iterative schemes may be devised to deal with this coupling, which may be very effective when the RTE is coupled with nonlinear flow problems.

5.7.2 Semidiscrete directional discretization

Approximation of the directional component

As mentioned in Section 5.1, there exist several possible choices for the directional discretization. Introducing a generic basis $\{\psi^\alpha(\boldsymbol{s}), \alpha = 1, ..., N\}$ to approximate $L^2(\mathcal{S}^2)$ with a space of dimension N, we can approximate $\mathcal{W} = L^2(\mathcal{S}^2; \mathcal{V})$ by

$$\mathcal{W}_N := \left\{ v \in L^2(\mathcal{S}^2; \mathcal{V}) \mid v(\boldsymbol{x}, \boldsymbol{s}) = \sum_{\alpha=1}^{N} \psi^\alpha(\boldsymbol{s}) v^\alpha(\boldsymbol{x}),\ v^\alpha(\boldsymbol{x}) \in \mathcal{V}\, \forall \alpha \right\}.$$

The space of test functions $L^2(\mathcal{S}^2; L^2(\Omega))$ can be approximated similarly, replacing the condition $v^\alpha(\boldsymbol{x}) \in \mathcal{V}$ by $v^\alpha(\boldsymbol{x}) \in L^2(\Omega)$. The resulting space is denoted by $\mathcal{W}_{T,N}$.

The Galerkin method applied to the directional discretization of problem (5.74) consists in finding $u_N \in \mathcal{W}_N$ such that

$$\mathcal{B}(u_N, v_N) = \mathcal{L}(v_N) \quad \forall v_N \in \mathcal{W}_{T,N}. \tag{5.94}$$

If u^α and v^α are the components of the unknown and test function in $\mathcal{W}_N$, we may write

$$\mathcal{B}(u_N, v_N) = \sum_{\alpha,\beta=1}^{N} \left[(v^\alpha, A_i^{\alpha\beta} \partial_i u^\beta)_\Omega + (v^\alpha, S^{\alpha\beta} u^\beta)_\Omega \right], \quad \mathcal{L}(v_N) = \sum_{\alpha=1}^{N} (v^\alpha, f^\alpha)_\Omega, \tag{5.95}$$

where

$$A_i^{\alpha\beta} = \int_{\mathcal{S}^2} s_i \psi^\alpha(\boldsymbol{s}) \psi^\beta(\boldsymbol{s}) \mathrm{d}\boldsymbol{s}, \tag{5.96}$$

$$S^{\alpha\beta}(\boldsymbol{x}) = (\kappa(\boldsymbol{x}) + \sigma_s(\boldsymbol{x})) \int_{\mathcal{S}^2} \psi^\alpha(\boldsymbol{s}) \psi^\beta(\boldsymbol{s}) \mathrm{d}\boldsymbol{s} - \frac{\sigma_s(\boldsymbol{x})}{4\pi} \int_{\mathcal{S}^2} \int_{\mathcal{S}^2} \psi^\alpha(\boldsymbol{s}) \phi(\boldsymbol{s}, \boldsymbol{s}') \psi^\beta(\boldsymbol{s}') \mathrm{d}\boldsymbol{s} \mathrm{d}\boldsymbol{s}', \tag{5.97}$$

$$f^\alpha(\boldsymbol{x}) = \int_{\mathcal{S}^2} \psi^\alpha(\boldsymbol{s}) f(\boldsymbol{x}, \boldsymbol{s}) \mathrm{d}\boldsymbol{s}. \tag{5.98}$$

Repeated indexes i in (5.95) and below that run over the space dimensions (from 1 to 3) imply summation.

Defining the vector fields $\boldsymbol{u} \in \mathcal{V}^N$ and $\boldsymbol{f} : \Omega \to \mathbb{R}^N$ by their components u^α, f^α, $\alpha = 1, ..., N$, and introducing the vector operator $\boldsymbol{L}$ defined by

$$\boldsymbol{Lu}|^\alpha = \sum_{\beta=1}^{N} \big(A_i^{\alpha\beta} \partial_i u^\beta + S^{\alpha\beta} u^\beta \big), \tag{5.99}$$

we may write the discrete problem (5.94) (see (5.95)) as: find $\boldsymbol{u} \in \mathcal{V}^N$ such that

$$(\boldsymbol{v}, \boldsymbol{Lu})_\Omega = (\boldsymbol{v}, \boldsymbol{f})_\Omega \quad \forall \boldsymbol{v} \in L^2(\Omega)^N. \tag{5.100}$$

The discrete ordinates method

The simplest way to discretize the directional domain $\mathcal{S}^2$ is using the so called *discrete ordinates method* (DOM). Let us consider a partition of the unit sphere of the form $\mathcal{S}^2 = \bigcup_{\alpha=1}^{N} \mathcal{S}^{2,\alpha}$, and let $w_\alpha := \operatorname{meas}(\mathcal{S}^{2,\alpha})$. The DOM is defined by setting $\psi^\alpha(\boldsymbol{s}) = \chi^\alpha(\boldsymbol{s})$, the characteristic function of $\mathcal{S}^{2,\alpha}$ (equal to 1 if $\boldsymbol{s} \in \mathcal{S}^{2,\alpha}$, 0 otherwise).

If $\boldsymbol{s}^\alpha$ is the barycenter of $\mathcal{S}^{2,\alpha}$, expressions (5.96), (5.97) and (5.98) may be approximated by

$$A_i^{\alpha\beta} = s_i^\alpha w_\alpha \delta_{\alpha\beta}, \tag{5.101}$$

$$S^{\alpha\beta}(\boldsymbol{x}) = (\kappa(\boldsymbol{x}) + \sigma_s(\boldsymbol{x}))\, w_\alpha \delta_{\alpha\beta} - \frac{\sigma_s(\boldsymbol{x})}{4\pi} w_\alpha w_\beta \phi(\boldsymbol{s}^\beta, \boldsymbol{s}^\alpha), \tag{5.102}$$

$$f^\alpha(\boldsymbol{x}) = w_\alpha f(\boldsymbol{x}, \boldsymbol{s}^\alpha). \tag{5.103}$$

In this case the unknown $u^\alpha(\boldsymbol{x})$ represents the radiation intensity in the direction $\boldsymbol{s}^\alpha$, that is to say, $u^\alpha(\boldsymbol{x}) = u\,(\boldsymbol{x}, \boldsymbol{s}^\alpha)$.

5.7.3 Fully discrete problem using the discrete ordinates method

Spatial and directional discretization

We may now proceed to the spatial discretization of directional-semidiscrete problem (5.100). Let

$$\mathcal{W}_{h,N} := \Big\{ v \in L^2(\mathcal{S}^2; \mathcal{V}) \mid v(\boldsymbol{x}, \boldsymbol{s}) = \sum_{\alpha=1}^{N} \psi^\alpha(\boldsymbol{s}) v_h^\alpha(\boldsymbol{x}),\ v_h^\alpha(\boldsymbol{x}) \in \mathcal{V}_h\ \forall \alpha \Big\}$$

be the finite element space to approximate $\mathcal{W}_N$. This same space can be used to approximate the space of test functions $\mathcal{W}_{T,N}$. The Galerkin fully discrete problem, corresponding to the directional discretization of (5.82), consists in finding $u_{h,N} \in \mathcal{W}_{h,N}$ such that

$$\mathcal{B}(u_{h,N}, v_{h,N}) = \mathcal{L}(v_{h,N}) \quad \forall v_{h,N} \in \mathcal{W}_{h,N}. \tag{5.104}$$

As explained earlier, this formulation lacks numerical stability. To design stabilized finite element methods we may proceed as in the previous subsection, simply replacing scalar-valued unknowns and test functions by their vector-valued counterparts, as well as the scalar operator L defined in (5.14) by the vector operator $\boldsymbol{L}$ introduced in (5.99). In particular, the equation for the subscales $\tilde{\boldsymbol{u}} \in \tilde{\mathcal{V}}^N$ will be

$$\tilde{P}(\boldsymbol{L}\tilde{\boldsymbol{u}}) = \tilde{P}(\boldsymbol{f} - \boldsymbol{L}\boldsymbol{u}_h), \tag{5.105}$$

where $\tilde{P} = I$ for the ASGS formulation and $\tilde{P} = P_h^{\perp}$ in the OSS method. It is understood that $\tilde{P}$ acts componentwise. The approximation of $\boldsymbol{L}\tilde{\boldsymbol{u}}$ we use is described next.

The general approach to design the stabilization parameters

The unresolved subscales are modeled with the algebraic approximation in (5.88). The behavior of the stabilization parameter τ can be analyzed using an approximate Fourier analysis of the problem, in the same way as it is done in [22] and [19].

Let us consider problem (5.105) posed in each element domain K. Our purpose is to approximate $\boldsymbol{L}\tilde{\boldsymbol{u}} \approx \boldsymbol{\tau}^{-1}\tilde{\boldsymbol{u}}$ in a certain sense, with $\boldsymbol{\tau}^{-1}$ a *diagonal* matrix that has to be determined and that we will call matrix of stabilization parameters. We propose to do this imposing that the induced L^2-norm of $\boldsymbol{\tau}^{-1}$ is an upper bound for the induced L^2-norm of $\boldsymbol{L}$, that is to say $\|\boldsymbol{L}\|_{L^2(K)} \leq \|\boldsymbol{\tau}^{-1}\|_{L^2(K)}$. The symbol $\leq$ has to be understood up to constants and holding independently of the equation coefficients. From an approximate Fourier analysis (see [22, 19]) it may be concluded that $\|\boldsymbol{L}\|_{L^2(K)} \leq |\widehat{\boldsymbol{L}}(\boldsymbol{k}^0)|$ for a certain wave number, denoted $\boldsymbol{k}^0$, where the $\widehat{\boldsymbol{L}}$ is the algebraic operator resulting from the Fourier transform of $\boldsymbol{L}\boldsymbol{u}$. In view of this fact, our proposal is to choose $\boldsymbol{\tau}^{-1}$ such that $|\widehat{\boldsymbol{L}}(\boldsymbol{k}^0)| = |\boldsymbol{\tau}^{-1}|$. Obviously $\boldsymbol{k}^0$ is unknown and has to be understood in this context as a vector of algorithmic coefficients.

The norm $|\widehat{\boldsymbol{L}}(\boldsymbol{k}^0)|$ can be computed as the square root of the maximum eigenvalue (in module) of the generalized eigenvalue problem

$$\widehat{\boldsymbol{L}}(\boldsymbol{k}^0)^*\widehat{\boldsymbol{L}}(\boldsymbol{k}^0)\boldsymbol{u} = \lambda\boldsymbol{u}. \tag{5.106}$$

This leads to an effective way to determine the expression of matrix of stabilization parameters $\boldsymbol{\tau}$. Taking it as diagonal, it can be computed as $\boldsymbol{\tau} = \lambda_{\max}^{-1/2}\boldsymbol{I}$.

The general idea exposed allows us to obtain the correct matrix of stabilization parameters for several problems (see [21, 22] for an obtention of this matrix in the context of the hyperbolic wave equation and the three field formulation of the Stokes problem, for example). In particular, we will apply it now to the design of the $\boldsymbol{\tau}$ matrix for the DOM presented above. Let us also note that in some vector cases it is necessary to introduce a scaling matrix in the definition of $\boldsymbol{\tau}$, which in the problem considered is not required.

Tau matrix for the discrete ordinates method

For the sake of simplicity we will assume isotropic scattering, that is $\phi = 1$, and constant physical properties. Let us introduce the abbreviations $\bar{\kappa} = \kappa + \sigma_s$, $\bar{w}_\alpha = w_\alpha \frac{\sigma_s}{4\pi}$. We wish to apply the previous ideas to problem (5.105). If we call $\boldsymbol{r}$ the right-hand-side term, the Fourier transformed equation for the DOM reads

$$\sum_{\beta=1}^{N} w_\alpha \left[\mathrm{i}h^{-1}(\boldsymbol{k}\cdot\boldsymbol{s}^\alpha)\delta_{\alpha\beta} + \bar{\kappa}\delta_{\alpha\beta} - \bar{w}_\beta\right]\hat{u}^\beta = w_\alpha\hat{r}^\alpha,$$

where $\mathrm{i} = \sqrt{-1}$, $\hat{r}^\alpha$ is the Fourier transform of $\boldsymbol{r}(\boldsymbol{x}, \boldsymbol{s})$ evaluated at $\boldsymbol{s}^\alpha$ and use has been made of (5.101), (5.102) and (5.103). From this expression we see that we need to estimate the maximum eigenvalue of (5.106), the matrices involved having components

$$\begin{aligned}
\widehat{L}_{\alpha\beta}(\boldsymbol{k}^0) &= \mathrm{i}h^{-1}(\boldsymbol{k}^0 \cdot \boldsymbol{s}^\alpha)\delta_{\alpha\beta} + \bar{\kappa}\delta_{\alpha\beta} - \bar{w}_\beta, \\
\widehat{L}^*_{\alpha\beta}(\boldsymbol{k}^0) &= -\mathrm{i}h^{-1}(\boldsymbol{k}^0 \cdot \boldsymbol{s}^\beta)\delta_{\alpha\beta} + \bar{\kappa}\delta_{\alpha\beta} - \bar{w}_\alpha.
\end{aligned}$$

After some algebraic manipulations that are omitted, it can be shown that

$$\lambda_{\max} \leq 2c\frac{\sigma_s}{N} + c^2 + \bar{\kappa}^2,$$

where c is a constant, independent of the equation coefficients and the number of modes in the DOM expansion N. In view of this, for our problem we will take a diagonal matrix of stabilization parameters $\boldsymbol{\tau}$ given by

$$\boldsymbol{\tau} = \left[\left(\frac{c_1}{h}\right)^2 + (\kappa + \sigma_s)^2 + 2c_1\frac{\sigma_s}{hN}\right]^{-1/2} \boldsymbol{I}, \tag{5.107}$$

where c_1 is an algorithmic constant. We take it as $c_1 = 2$ in the numerical examples of Section 5.9 using linear elements. In the analysis presented in the following section this constant is required to be large enough, but the value indicated is what we have found effective in practice.

The matrix of stabilization parameters is an algebraic approximation to the radiative transport operator in (5.13). The first term in (5.107) approximates the convective operator, the second term approximates the non integral reactive term and the last term approximates the integral operator. Observe that in the last term the directional and spatial discretization parameters N and h appear, and that it vanishes as $N \to \infty$. In any case, for practical values of N this last term is negligible, even if h decreases as N grows. A simple analysis of the magnitude of the different terms in (5.107) when both $N \to \infty$ and $h \to 0$ shows that the last term can never dominate. Thus, (5.107) has the behavior of the stabilization parameters usually found in the literature and that will be used in the numerical analysis presented next.

Implementation aspects

The linear system of equations resulting from the discretization is large and strongly coupled due to the integral scattering operator. For a problem with scattering the memory demand increases with the square of ordinates directions N^2. Running a problem with N ordinates directions needs N^2 more memory than a scalar problem with the same mesh, demanding much more time. That makes that a problem with 40 ordinates, that gives an acceptable resolution is 1600 times more expensive than a scalar problem in the same mesh. Using a single cpu and 40 ordinates, it is very difficult to solve a problem with more than 3000 nodes, and that makes it impossible to solve real application problems.

In order to save memory and be able to run real problems we have solved the radiation field for each direction separately, using a Gauss-Seidel iterative scheme to couple different directions. This scheme is always convergent, converging faster the larger the relation κ/σ_s is.

5.8 Numerical analysis of the spatial semidiscrete problem

5.8.1 Preliminaries

In the present section we present a stability and convergence analysis of the SUPG and OSS methods, as well as a non-standard analysis of the Galerkin method, when they are used for the spatial discretization of the RTE, for simplicity with essential homogeneous boundary conditions on Γ^-.

For simplicity, we will consider quasi-uniform refinements, and thus all the element diameters can be bounded above and below by constants multiplying h. The extension of the following analysis to non quasi-uniform refinements and non uniform properties can be done using the strategy followed in [20]. We also consider uniform properties κ and σ_s. With these assumptions, the stabilization parameters can be considered constant in the whole computational domain.

For the SUPG and the OSS methods the norm in which the results will be presented is

$$|||v_h|||^2 := \tau\|\boldsymbol{s}\cdot\nabla v_h\|^2 + \|v_h\|^2_{\Gamma^+} + \kappa\|v_h\|^2 + \lambda_1\sigma_s\|\Pi^\perp v_h\|^2, \quad v_h(\cdot,\boldsymbol{s})\in\mathcal{V}_h,\ \boldsymbol{s}\in\mathcal{S}^2. \tag{5.108}$$

It is understood that the directional variable $\boldsymbol{s}$ remains continuous, that is to say, the semidiscrete problem is analyzed, although minor modifications permit the extension of our analysis to the fully discrete DOM, for example. When the directional dependence is accounted for, $v_h \in \mathcal{W}_h = L^2(\mathcal{S}^2;\mathcal{V}_h)$. If ω is a spatial domain, we will use the abbreviation $\|v_h\|_\omega := \|v_h\|_{L^2(\mathcal{S}^2;L^2(\omega))}$. Likewise, if $|\cdot|_{H^i(\Omega)}$ is the seminorm of $H^i(\Omega)$, we will write $\|\,|v|_{H^i(\Omega)}\,\|_{L^2(\mathcal{S}^2)} = |v|_{L^2(\mathcal{S}^2;H^i(\Omega))}$.

Let $u\in\mathcal{W}$ be the solution of the continuous problem and $\hat{u}_h\in\mathcal{W}_h$ a finite element interpolant of degree p. If $\|u-\hat{u}_h\|_{L^2(\mathcal{S}^2;H^i(\Omega))} \le Ch^{p+1-i}|u|_{L^2(\mathcal{S}^2;H^{p+1}(\Omega))} =: \varepsilon_i(u)$, $i=0,1$, we will show that the error function of the SUPG and OSS methods in the norm (5.108) is given by

$$E(h) := \tau^{-1/2}\varepsilon_0(u) + \tau^{1/2}\varepsilon_1(u). \tag{5.109}$$

Obviously, we could express $E(h)$ in terms of $\varepsilon_0(u)$ or $\varepsilon_1(u)$, but we prefer to keep the explicit dependence on both to stress the behavior of $E(h)$ in terms of the physical coefficients of the problem.

We will use the notation $A_h \gtrsim B_h$ and $A_h \lesssim B_h$ to indicate that $A_h \ge CB_h$ and $A_h \le CB_h$, respectively, where A_h and B_h are expressions that may depend on h and C is a generic constant, independent of h and of the physical parameters.

The expression of τ we will use corresponds to the limit for $N\to\infty$ of the diagonal in (5.107), that is to say,

$$\tau^{-2} = (\kappa+\sigma_s)^2 + c_1^2h^{-2}. \tag{5.110}$$

Since the finite element partitions are assumed quasi-uniform, there is a positive constant C_{inv} independent of the mesh size h (the maximum of all element diameters), such that

$$\|\nabla v_h\|_K \le C_{\text{inv}}h^{-1}\|v_h\|_K\,, \tag{5.111}$$

for all finite element functions v_h defined on an element $K \in \mathcal{P}_h$. Remember that the subscript K denotes that the spatial integral involved in $\| \cdot \|$ is carried over element K. Similarly, the trace inequality

$$\|v\|_{\partial K}^2 \leq C_{\text{trace}} \left(h^{-1} \|v\|_K^2 + h \|\nabla v\|_K^2 \right) \tag{5.112}$$

is assumed to hold for functions $v \in L^2(\mathcal{S}^2; H^1(K))$, $K \in \mathcal{P}_h$. Now, subscript ∂K denotes the $L^2(\partial K)$-norm. The last term can be dropped if v is a polynomial on the element domain K. Thus, if v_h is a piecewise continuous polynomial, it follows that

$$\|v_h\|_{\partial K}^2 \leq C_{\text{trace}} h^{-1} \|v_h\|_K^2. \tag{5.113}$$

Lemma 1 *For sufficiently smooth solutions u of the continuous problem there holds*

$$|||u - \hat{u}_h||| \lesssim E(h).$$

Proof. The results follows easily from the definition of $|||\cdot|||$ and the behavior (5.110) assumed for τ, together with the trace inequality (5.112), which implies

$$\|u - \hat{u}_h\|_{\Gamma^+} \lesssim h^{-1/2} \varepsilon_0(u) + h^{1/2} \varepsilon_1(u). \tag{5.114}$$

This inequality will be used later on. ■

Remark 1 The previous result makes sense for smooth enough functions u, in particular for u at least in $L^2(\mathcal{S}^2; H^1(\Omega))$. Thus, the traces of u on Γ^+ are well defined for almost every direction, as well as the traces of functions in the finite element spaces we have constructed. However, if instead of seeking the order of convergence we only want to prove convergence towards a solution with the minimum regularity requirements, that is to say, $u \in \mathcal{W}$, the trace of u on Γ^+ is not necessarily defined. As it is shown in [34] (Lemma 3.1) this trace makes sense if Γ^+ and Γ^- defined in (5.17) are well separated. □

5.8.2 SUPG method

In this subsection we will prove that the solution of the discrete problem (5.89) is stable and convergent to the solution of the continuous problem (5.13).

Lemma 2 *(Coercivity of the SUPG method) The bilinear form $\mathcal{B}_{\text{supg}}$ defined in (5.90) satisfies*

$$\mathcal{B}_{\text{supg}}(v_h, v_h) \gtrsim |||v_h|||^2 \quad \forall v_h \in \mathcal{W}_h.$$

Proof. From the definition of $\mathcal{B}_{\text{supg}}$ it follows that

$$\begin{aligned}
\mathcal{B}_{\text{supg}}(v_h, v_h) &= (\boldsymbol{s} \cdot \nabla v_h, v_h) + \kappa (v_h, v_h) + (S_\sigma v_h, v_h) \\
&\quad + \tau (\boldsymbol{s} \cdot \nabla v_h, \boldsymbol{s} \cdot \nabla v_h) + \kappa \tau (v_h, \boldsymbol{s} \cdot \nabla v_h) + \tau (S_\sigma v_h, \boldsymbol{s} \cdot \nabla v_h) \\
&\geq \frac{1}{2} \|v_h\|_{\Gamma^+}^2 + \kappa \|v_h\|^2 + \sigma_s (S_1 v_h, v_h) \\
&\quad + \tau \|\boldsymbol{s} \cdot \nabla v_h\|^2 - \kappa \tau \|v_h\| \|\boldsymbol{s} \cdot \nabla v_h\| - \sigma_s \tau \|S_1 v_h\| \|\boldsymbol{s} \cdot \nabla v_h\|.
\end{aligned} \tag{5.115}$$

The last two terms can be bounded using Young's inequality and expression (5.110), for example in the form

$$\begin{aligned}
&- \kappa\tau\|v_h\|\|\boldsymbol{s}\cdot\nabla v_h\| - \sigma_s\tau\|S_1 v_h\|\|\boldsymbol{s}\cdot\nabla v_h\| \\
&\quad \geq -\kappa^{1/2}\tau^{1/2}\|v_h\|\|\boldsymbol{s}\cdot\nabla v_h\| - \sigma_s^{1/2}\tau^{1/2}\|S_1 v_h\|\|\boldsymbol{s}\cdot\nabla v_h\| \\
&\quad \geq -\frac{2}{3}\kappa\|v_h\|^2 - \frac{3}{8}\tau\|\boldsymbol{s}\cdot\nabla v_h\|^2 - \frac{2}{3}\sigma_s\|S_1 v_h\|^2 - \frac{3}{8}\tau\|\boldsymbol{s}\cdot\nabla v_h\|^2.
\end{aligned}$$

The Lemma follows using the fact that $-\|S_1 v_h\|^2 \geq -(S_1 v_h, v_h)$, using the last inequality in (5.115) and that $(S_1 v_h, v_h) \geq \lambda_1\|\Pi^{\perp} v_h\|^2$. ■

Lemma 3 *(Interpolation error of the SUPG method) There holds*

$$\mathcal{B}_{\text{supg}}\left(u - \hat{u}_h, v_h\right) \lesssim E(h)|||v_h||| \quad \forall v_h \in \mathcal{W}_h.$$

Proof. Integrating by parts the first term in $\mathcal{B}_{\text{supg}}\left(u - \hat{u}_h, v_h\right)$ and using Schwartz inequality and the behavior (5.110) assumed for τ it is found that

$$\begin{aligned}
\mathcal{B}_{\text{supg}}\left(u - \hat{u}_h, v_h\right) \leq{}& \tau^{-1/2}\|u - \hat{u}_h\|\tau^{1/2}\|\boldsymbol{s}\cdot\nabla v_h\| + \|u - \hat{u}_h\|_{\Gamma^+}\|v_h\|_{\Gamma^+} \\
&+ \kappa^{1/2}\|u - \hat{u}_h\|\kappa^{1/2}\|v_h\| + \sigma_s^{1/2}\|u - \hat{u}_h\|\sigma_s^{1/2}\|\Pi^{\perp} v_h\| \\
&+ \tau^{1/2}\|\nabla(u - \hat{u}_h)\|\tau^{1/2}\|\boldsymbol{s}\cdot\nabla v_h\| + \kappa^{1/2}\|u - \hat{u}_h\|\tau^{1/2}\|\boldsymbol{s}\cdot\nabla v_h\| \\
&+ \sigma_s^{1/2}\|u - \hat{u}_h\|\tau^{1/2}\|\boldsymbol{s}\cdot\nabla v_h\|.
\end{aligned}$$

Estimate (5.114) and the definitions of $E(h)$ and $|||\cdot|||$ yield the result. ■

Theorem 6 *(Convergence of the SUPG method) The solution u_h of problem (5.89) satisfies*

$$|||u - u_h||| \lesssim E(h).$$

Proof. The proof is completely standard. From the coercivity given by Lemma 2, the obvious consistency of the SUPG method and the interpolation error estimate in Lemma 3 it follows that

$$\begin{aligned}
|||u_h - \hat{u}_h|||^2 &\lesssim \mathcal{B}_{\text{supg}}\left(u_h - \hat{u}_h, u_h - \hat{u}_h\right) \\
&= \mathcal{B}_{\text{supg}}\left(u - \hat{u}_h, u_h - \hat{u}_h\right) \\
&\lesssim E(h)|||u_h - \hat{u}_h|||.
\end{aligned}$$

The result is a consequence of this, Lemma 1 and the triangle inequality. ■

5.8.3 OSS method

In this subsection we prove that method (5.92) is stable and the solution converges to the continuous one as for the SUPG method. We start proving stability in the form of an inf-sup condition for the bilinear form in (5.93):

Lemma 4 *(Stability of the OSS method) Suppose that c_1 in (5.110) is large enough. Then, there is a constant $C > 0$ such that*

$$\inf_{u_h \in \mathcal{W}_h \setminus \{0\}} \sup_{v_h \in \mathcal{W}_h \setminus \{0\}} \frac{\mathcal{B}_{\mathrm{oss}}\left(u_h, v_h\right)}{\left\|\!\left| u_h \right|\!\right\| \left\|\!\left| v_h \right|\!\right\|} \geq C. \tag{5.116}$$

Proof. Let us start noting that, for any function $u_h \in \mathcal{W}_h$, we have

$$\mathcal{B}_{\mathrm{oss}}\left(u_h, u_h\right) = \frac{1}{2}\|u_h\|_{\Gamma^+}^2 + \kappa\|u_h\|^2 + \left(S_\sigma u_h, u_h\right) + \tau\|P_h^\perp\left(\boldsymbol{s}\cdot\nabla u_h\right)\|^2. \tag{5.117}$$

Clearly, $\mathcal{B}_{\mathrm{oss}}$ is not coercive in the norm (5.108). The basic idea is to obtain control on the components on the finite element space for the terms whose orthogonal components appear in this expression. The key point is that this control comes from the Galerkin terms in the bilinear form $\mathcal{B}_{\mathrm{oss}}$. Let us consider $v_{h,0} := \tau P_h\left(\boldsymbol{s}\cdot\nabla u_h\right)$. We have that

$$\begin{aligned}
\mathcal{B}_{\mathrm{oss}}\left(u_h, v_{h,0}\right) &= \left(\boldsymbol{s}\cdot\nabla u_h + \kappa u_h + S_\sigma u_h, \tau P_h\left(\boldsymbol{s}\cdot\nabla u_h\right)\right) \\
&\quad + \left(P_h^\perp\left(\boldsymbol{s}\cdot\nabla u_h\right), \tau\boldsymbol{s}\cdot\nabla\left(\tau P_h\left(\boldsymbol{s}\cdot\nabla u_h\right)\right)\right) \\
&\geq \tau\|P_h\left(\boldsymbol{s}\cdot\nabla u_h\right)\|^2 + \kappa\tau\left(u_h, P_h\left(\boldsymbol{s}\cdot\nabla u_h\right)\right) + \tau\left(S_\sigma u_h, P_h\left(\boldsymbol{s}\cdot\nabla u_h\right)\right) \\
&\quad - \tau^2\|P_h^\perp\left(\boldsymbol{s}\cdot\nabla u_h\right)\|\|\nabla\left(P_h\left(\boldsymbol{s}\cdot\nabla u_h\right)\right)\|.
\end{aligned}$$

Using the inverse estimate (5.111), the fact that $\tau c_1 \leq h$, Young's inequality and (5.77), we get

$$\begin{aligned}
\mathcal{B}_{\mathrm{oss}}\left(u_h, v_{h,0}\right) &\geq \tau\|P_h\left(\boldsymbol{s}\cdot\nabla u_h\right)\|^2 - \frac{3}{4}\tau\kappa^2\|u_h\|^2 - \frac{3}{4}\tau\sigma_s^2\|S_1 u_h\|^2 \\
&\quad - \frac{2}{3}\tau\|P_h\left(\boldsymbol{s}\cdot\nabla u_h\right)\|^2 - \tau^2\frac{C_{\mathrm{inv}}}{h}\|P^\perp\left(\boldsymbol{s}\cdot\nabla u_h\right)\|\|P_h\left(\boldsymbol{s}\cdot\nabla u_h\right)\| \\
&\geq \frac{1}{3}\tau\|P_h\left(\boldsymbol{s}\cdot\nabla u_h\right)\|^2 - \frac{3}{4}\tau\kappa^2\|u_h\|^2 \\
&\quad - \frac{3}{4}\tau\sigma_s^2(S_1 u_h, u_h) - \frac{C_{\mathrm{inv}}}{c_1}\tau\|\boldsymbol{s}\cdot\nabla u_h\|^2.
\end{aligned} \tag{5.118}$$

Let $v_h = u_h + \alpha v_{h,0}$. Adding up inequality (5.118) multiplied by α to (5.117) it follows that

$$\begin{aligned}
\mathcal{B}_{\mathrm{oss}}\left(u_h, v_h\right) &\geq \frac{1}{2}\|u_h\|_{\Gamma^+}^2 + \kappa\|u_h\|^2 + \left(S_\sigma u_h, u_h\right) + \tau\|P_h^\perp\left(\boldsymbol{s}\cdot\nabla u_h\right)\|^2 \\
&\quad + \alpha\left(\frac{\tau}{3}\|P_h\left(\boldsymbol{s}\cdot\nabla u_h\right)\|^2 - \frac{3}{4}\tau\kappa^2\|u_h\|^2 - \frac{3}{4}\tau\sigma_s^2(S_1 u_h, \boldsymbol{u}_h) - \frac{C_{\mathrm{inv}}}{c_1}\tau\|\boldsymbol{s}\cdot\nabla u_h\|^2\right).
\end{aligned}$$

Using again Young's inequality and that $\tau\kappa \leq 1$ and $\tau\sigma_s \leq 1$, we get

$$\begin{aligned}
\mathcal{B}_{\mathrm{oss}}\left(u_h, v_h\right) &\geq \frac{1}{2}\|u_h\|_{\Gamma^+}^2 + \left(1 - \frac{3}{4}\alpha\right)\kappa\|u_h\|^2 + \left(1 - \frac{3}{4}\alpha\right)\left(S_\sigma u_h, u_h\right) \\
&\quad + \tau\|P_h^\perp\left(\boldsymbol{s}\cdot\nabla u_h\right)\|^2 + \frac{\alpha}{3}\tau\|P_h\left(\boldsymbol{s}\cdot\nabla u_h\right)\|^2 - \frac{C_{\mathrm{inv}}}{c_1}\alpha\tau\|\boldsymbol{s}\cdot\nabla u_h\|^2.
\end{aligned}$$

Therefore

$$\begin{aligned}\mathcal{B}_{\mathrm{oss}}\left(u_h, v_h\right) &\geq \frac{1}{2}\|u_h\|_{\Gamma^+}^2 + \left(1-\frac{3}{4}\alpha\right)\kappa\|u_h\|^2 + \left(1-\frac{3}{4}\alpha\right)\lambda_1\sigma_s\|\Pi^{\perp}u_h\|^2 \\ &\quad + \min\left\{1-\frac{\alpha C_{\mathrm{inv}}}{c_1}, \frac{\alpha}{3}-\frac{\alpha C_{\mathrm{inv}}}{c_1}\right\}\tau\|\boldsymbol{s}\cdot\nabla u_h\|^2 \\ &\geq \min\left\{1-\frac{\alpha C_{\mathrm{inv}}}{c_1}, \alpha\left(\frac{1}{3}-\frac{C_{\mathrm{inv}}}{c_1}\right), \left(1-\frac{3\alpha}{4}\right), \frac{1}{2}\right\}|||u_h|||^2. \end{aligned} \tag{5.119}$$

If we choose α such that $0 < \alpha < \min\{\frac{c_1}{C_{\mathrm{inv}}}, \frac{4}{3}\}$ we have that $\mathcal{B}_{\mathrm{oss}}\left(u_h, v_h\right) \gtrsim |||u_h|||^2$ for the discrete function v_h we have chosen, provided c_1 is large enough, for example $c_1 > 3C_{\mathrm{inv}}$.

On the other hand, using the inverse and trace inequalities (5.111) and (5.113) and condition $\tau c_1 \leq h$ we have that

$$\begin{aligned}|||v_{h,0}|||^2 &= |||\tau P_h\left(\boldsymbol{s}\cdot\nabla u_h\right)|||^2 \\ &\leq \tau^3\|\boldsymbol{s}\cdot\nabla\left(P_h\left(\boldsymbol{s}\cdot\nabla u_h\right)\right)\|^2 + \tau^2\|P_h\left(\boldsymbol{s}\cdot\nabla u_h\right)\|_{\Gamma^+}^2 \\ &\quad + \left(\kappa\tau^2 + \lambda_1\sigma_s\tau^2\right)\|P_h\left(\boldsymbol{s}\cdot\nabla u_h\right)\|^2 \\ &\leq \tau^3\frac{C_{\mathrm{inv}}^2}{h^2}\|\boldsymbol{s}\cdot\nabla u_h\|^2 + \frac{C_{\mathrm{trace}}}{h}\tau^2\|\boldsymbol{s}\cdot\nabla u_h\|^2 + 2\tau\|\boldsymbol{s}\cdot\nabla u_h\|^2 \\ &\leq \left(\frac{C_{\mathrm{inv}}^2}{c_1^2} + \frac{C_{\mathrm{trace}}}{c_1} + 2\right)\tau\|\boldsymbol{s}\cdot\nabla u_h\|^2 \\ &\lesssim |||u_h|||^2.\end{aligned}$$

Using this fact in (5.119) we have shown that for each $u_h \in \mathcal{W}_h$ there exists $v_h \in \mathcal{W}_h$ such that

$$\mathcal{B}_{\mathrm{oss}}\left(u_h, v_h\right) \gtrsim |||u_h|||\,|||v_h|||,$$

from where the inf sup condition (5.116) is verified and stability is established. ■

Lemma 5 *(Interpolation error of the OSS method) There holds*

$$\mathcal{B}_{\mathrm{oss}}\left(u - \hat{u}_h, v_h\right) \lesssim E(h)|||v_h||| \quad \forall v_h \in \mathcal{W}_h.$$

Proof. The proof is very similar to that of Lemma 3. The difference is only the treatment of the stabilization term, which in this case can be easily bounded as

$$\tau(\boldsymbol{s}\cdot\nabla(u_h - \hat{u}_h), P_h^{\perp}(\boldsymbol{s}\cdot\nabla v_h)) \leq \tau^{1/2}\|\nabla(u_h - \hat{u}_h)\|\tau^{1/2}\|\boldsymbol{s}\cdot\nabla v_h\|,$$

from where we can proceed as in Lemma 3. ■

Contrary to the Galerkin and the SUPG methods, the OSS method is not consistent (in the version we have presented it, see [20]). There is a consistency error given by the fact that

$$\mathcal{B}_{\mathrm{oss}}\left(u - u_h, v_h\right) = \tau\left(P_h^{\perp}\left(\boldsymbol{s}\cdot\nabla u\right), \boldsymbol{s}\cdot\nabla v_h\right). \tag{5.120}$$

However, this consistency error can be bounded as follows:

Lemma 6 *(Bound for the consistency error of the OSS method) Suppose that f in (5.13) belongs to the finite element space. Then, there holds*

$$\mathcal{B}_{\text{oss}}\left(u-u_h,v_h\right) \lesssim E(h)|||v_h||| \quad \forall v_h \in \mathcal{W}_h.$$

Proof. From (5.120) we have that

$$\begin{aligned}\mathcal{B}_{\text{oss}}\left(u-u_h,v_h\right) &= \tau\left(P_h^{\perp}\left(\boldsymbol{s}\cdot\nabla u\right), \boldsymbol{s}\cdot\nabla v_h\right)\\ &\leq \tau^{1/2}\|P_h^{\perp}\left(\boldsymbol{s}\cdot\nabla u\right)\|\tau^{1/2}\|\boldsymbol{s}\cdot\nabla v_h\|.\end{aligned}$$

Since $\boldsymbol{s}\cdot\nabla u = f-\kappa u - S_\sigma u$ and $P_h^{\perp}(f)=0$, we have that $P_h^{\perp}\left(\boldsymbol{s}\cdot\nabla u\right) = -P_h^{\perp}(\kappa u + S_\sigma u)$, and the results follows from the best approximation property of the projection P_h with respect to the L^2-norm and the expression of τ. ■

Remark 2 The assumption $P_h^{\perp}(f) = 0$ is not as restrictive as it might seem. Clearly, the component of f orthogonal to the finite element space vanishes when it is tested with a finite element function, and therefore the Galerkin method does not account for it, in spite of its optimal accuracy (and lack of stability). On the other hand, there would be no problem in keeping the whole residual in the definition of the subscale in (5.7.1), case in which the OSS method would be exactly consistent. □

Combining the previous results we easily get:

Theorem 7 *(Convergence of the OSS method) The solution u_h of the OSS method satisfies*

$$|||u-u_h||| \lesssim E(h).$$

5.8.4 Galerkin method

The previous analysis could be easily adapted to account for the possibility $\tau = 0$, which corresponds to the Galerkin method. Apart from the need of redefining the error function $E(h)$ given by (5.109) if $\tau = 0$, also the working norm needs to be modified, since in fact the Galerkin method provides some sort of control on the convective term, as we shall show below. More precisely, we will prove stability and convergence in the norm

$$|||v_h|||_{\text{G}}^2 := \|v_h\|_{\Gamma^+}^2 + \kappa\|v_h\|^2 + \lambda_1\sigma_s\|\Pi^{\perp}v_h\|^2 + h\|P_h(\boldsymbol{s}\cdot\nabla v_h)\|^2, \tag{5.121}$$

defined for $v_h \in \mathcal{W}_h$. This norm does not contain the whole derivative of v_h along direction $\boldsymbol{s}$, but only the projection onto the finite element space. Moreover, the factor of the last term is the mesh size h, not τ. We discuss later the implications of these facts.

Lemma 7 *(Stability of the Galerkin method) For $h(\kappa+\sigma_s) \leq C_0$, there is a constant $C > 0$ such that*

$$\inf_{u_h\in\mathcal{W}_h\setminus\{0\}} \sup_{v_h\in\mathcal{W}_h\setminus\{0\}} \frac{\mathcal{B}\left(u_h,v_h\right)}{|||u_h|||_{\text{G}}|||v_h|||_{\text{G}}} \geq C. \tag{5.122}$$

Proof. For any function $u_h \in \mathcal{W}_h$, we have

$$\mathcal{B}\left(u_h, u_h\right) = \frac{1}{2}\|u_h\|^2_{\Gamma+} + \kappa\|u_h\|^2 + \left(S_\sigma u_h, u_h\right). \tag{5.123}$$

It is obvious that $\mathcal{B}$ is not coercive in the norm (5.121). Similarly to the proof of (5.116), let us consider $v_{h,0} := hP_h\left(\boldsymbol{s}\cdot\nabla u_h\right)$. We have that

$$\begin{aligned}\mathcal{B}\left(u_h, v_{h,0}\right) &= \left(\boldsymbol{s}\cdot\nabla u_h + \kappa u_h + S_\sigma u_h, hP_h\left(\boldsymbol{s}\cdot\nabla u_h\right)\right)\\ &= h\|P_h\left(\boldsymbol{s}\cdot\nabla u_h\right)\|^2 + \kappa h\left(u_h, P_h\left(\boldsymbol{s}\cdot\nabla u_h\right)\right) + h\left(S_\sigma u_h, P_h\left(\boldsymbol{s}\cdot\nabla u_h\right)\right).\end{aligned}$$

Using Young's inequality and (5.77) we can bound this as follows:

$$\begin{aligned}\mathcal{B}\left(u_h, v_{h,0}\right) &\geq h\|P_h\left(\boldsymbol{s}\cdot\nabla u_h\right)\|^2 - \frac{3}{4}h\kappa^2\|u_h\|^2 - \frac{3}{4}h\|S_\sigma u_h\|^2 - \frac{2}{3}h\|P_h(\boldsymbol{s}\cdot\nabla u_h)\|^2\\ &\geq \frac{1}{3}h\|P_h(\boldsymbol{s}\cdot\nabla u_h)\|^2 - \frac{3}{4}h\kappa^2\|u_h\|^2 - \frac{3}{4}h\sigma_s(S_\sigma u_h, u_h).\end{aligned} \tag{5.124}$$

Thus, from (5.123) and (5.124) it follows that, for all $\alpha > 0$,

$$\begin{aligned}\mathcal{B}\left(u_h, u_h + \alpha v_{h,0}\right) \geq \frac{1}{2}\|u_h\|^2_{\Gamma+} &+ \left(1 - \frac{3}{4}h\kappa\alpha\right)\kappa\|u_h\|^2\\ &+ \left(1 - \frac{3}{4}h\sigma_s\alpha\right)\lambda_1\sigma_s\|\Pi^\perp u_h\|^2 + \frac{1}{3}\alpha h\|P_h(\boldsymbol{s}\cdot\nabla u_h)\|^2.\end{aligned}$$

From the assumption $h(\kappa + \sigma_s) \leq C_0$ it follows that we may choose α such that $\mathcal{B}(u_h, u_h + \alpha v_{h,0}) \gtrsim |||u_h|||^2_{\mathrm{G}}$. It remains only to prove that $|||v_{h,0}|||_{\mathrm{G}} \lesssim |||u_h|||_{\mathrm{G}}$, which can be done as in the proof of Lemma 4 using (5.111) and (5.113) and now condition $h(\kappa + \sigma_s) \leq C_0$:

$$\begin{aligned}|||v_{h,0}|||^2_{\mathrm{G}} &= |||hP_h\left(\boldsymbol{s}\cdot\nabla u_h\right)|||^2_{\mathrm{G}}\\ &\leq h^3\|P_h\left(\boldsymbol{s}\cdot\nabla\left(P_h\left(\boldsymbol{s}\cdot\nabla u_h\right)\right)\right)\|^2 + h^2\|P_h\left(\boldsymbol{s}\cdot\nabla u_h\right)\|^2_{\Gamma+}\\ &\quad + (\kappa h^2 + \lambda_1\sigma_s h^2)\|P_h\left(\boldsymbol{s}\cdot\nabla u_h\right)\|^2\\ &\leq h^3\frac{C^2_{\mathrm{inv}}}{h^2}\|P_h(\boldsymbol{s}\cdot\nabla u_h)\|^2 + \frac{C_{\mathrm{trace}}}{h}h^2\|P_h(\boldsymbol{s}\cdot\nabla u_h)\|^2 + h^2(\kappa + \sigma_s)\|P_h(\boldsymbol{s}\cdot\nabla u_h)\|^2\\ &\leq \left(C^2_{\mathrm{inv}} + C_{\mathrm{trace}} + h(\kappa + \sigma_s)\right)h\|P_h(\boldsymbol{s}\cdot\nabla u_h)\|^2\\ &\lesssim |||u_h|||^2_{\mathrm{G}},\end{aligned}$$

from where the result follows. ■

Remark 3 In stabilized finite element methods one is concerned not only in the asymptotic behavior $h \to 0$, but also in the limits obtained when the physical parameters vary for h fixed. Assumption $h(\kappa + \sigma_s) \leq C_0$ precludes estimate (5.122) to be valid when h is fixed and either $\kappa \to \infty$ or $\sigma_s \to \infty$. However, this is a theoretical restriction rather than a practical one in the problem we are analyzing. In particular, it does not appear in the numerical examples of Section 5.9. In fact, when κ is constant, as we assume, it can be relaxed to $h\sigma_s \leq C_0$ for stability (Lemma 7) but condition $h(\kappa + \sigma_s) \leq C_0$ will be again required for convergence

(Lemma 8 and Theorem 8). To see why $h\sigma_s \leq C_0$ is enough for stability it suffices to observe that

$$\kappa h \left(u_h, P_h \left(\boldsymbol{s} \cdot \nabla u_h\right)\right) = \kappa h \left(u_h, \boldsymbol{s} \cdot \nabla u_h\right) = \kappa h \frac{1}{2} \|u_h\|_{\Gamma^+}^2 \geq 0,$$

so that bound (5.124) is not sharp. However, the proof of Lemma 7 can be straightforwardly extended to variable coefficients if condition $h(\kappa + \sigma_s) \leq C_0$, with κ the maximum value of the absorption coefficient, is kept. □

The error function of the Galerkin method is determined by the following result:

Lemma 8 *(Interpolation error of the Galerkin method) For $h(\kappa + \sigma_s) \leq C_0$, there holds*

$$\vert\!\vert\!\vert u - \tilde{u}_h \vert\!\vert\!\vert_{\mathrm{G}} \lesssim h^{1/2} \varepsilon_1(u), \tag{5.125}$$

$$\mathcal{B}(u - \tilde{u}_h, v_h) \lesssim (\kappa^{-1/2} + h^{1/2}) \varepsilon_1(u) \vert\!\vert\!\vert v_h \vert\!\vert\!\vert_{\mathrm{G}}. \tag{5.126}$$

Proof. Estimate (5.125) is a trivial consequence of the definition of $\vert\!\vert\!\vert \cdot \vert\!\vert\!\vert_{\mathrm{G}}$ in (5.121), assumption $h(\kappa + \sigma_s) \leq C_0$, the trace inequality (5.113) and the fact that $h^{1/2}\varepsilon_1(u) = h^{-1/2}\varepsilon_0(u)$. The proof of (5.126) is as follows:

$$\begin{aligned} \mathcal{B}(u - \tilde{u}_h, v_h) &= (\boldsymbol{s} \cdot \nabla(u - \tilde{u}_h), v_h) + \kappa(u - \tilde{u}_h, v_h) + (S_\sigma(u - \tilde{u}_h), v_h) \\ &\leq \|\nabla(u - \tilde{u}_h)\| \|v_h\| + \kappa \|u - \tilde{u}_h\| \|v_h\| + \sigma_s \|u - \tilde{u}_h\| \|\Pi^\perp v_h\| \\ &\lesssim (\kappa^{-1/2}\varepsilon_1(u) + \kappa^{1/2}\varepsilon_0(u))\kappa^{1/2}\|v_h\| + \sigma_s^{1/2}\varepsilon_0(u)\sigma_s^{1/2}\|\Pi^\perp v_h\| \\ &\lesssim [\kappa^{-1/2} + (\kappa^{1/2} + \sigma_s^{1/2})h]\varepsilon_1(u) \vert\!\vert\!\vert v_h \vert\!\vert\!\vert_{\mathrm{G}}. \end{aligned} \tag{5.127}$$

The proof is complete using once again that $h(\kappa + \sigma_s) \leq C_0$. ■

Combining the results of Lemma 7 and Lemma 8 and the consistency of the Galerkin formulation it is found that

Theorem 8 *(Convergence of the Galerkin method) For $h(\kappa + \sigma_s) \leq C_0$, the solution u_h of the Galerkin method satisfies*

$$\vert\!\vert\!\vert u - u_h \vert\!\vert\!\vert_{\mathrm{G}} \lesssim (\kappa^{-1/2} + h^{1/2}) \varepsilon_1(u).$$

At this point it is interesting to compare what happens in the limit of dominant directional derivative or dominant absorption in the stabilized formulations, either SUPG or OSS, and the Galerkin method. To simplify the discussion, suppose that $\sigma_s = 0$ and let us neglect the error control obtained on the boundary Γ^+. We may write the convergence estimates as

Stabilized methods (SUPG, OSS):

$$\tau^{1/2}\|\boldsymbol{s} \cdot \nabla(u - u_h)\| + \kappa^{1/2}\|u - u_h\| \lesssim (\tau^{-1/2}h^{p+1} + \tau^{1/2}h^p)|u|_{L^2(\mathcal{S}^2;H^{p+1}(\Omega))}.$$

Galerkin method:

$$h^{1/2}\|P_h(\boldsymbol{s} \cdot \nabla(u - u_h))\| + \kappa^{1/2}\|u - u_h\| \lesssim (\kappa^{-1/2}h^p + h^{1/2}h^p)|u|_{L^2(\mathcal{S}^2;H^{p+1}(\Omega))}.$$

The behavior when $\kappa h \ll 1$ (small absorption) and when $\kappa h \gg 1$ (large absorption) is displayed in Table 5.1 (results in this table are obtained multiplying by adequate factors both sides of the corresponding error estimates). The two main conclusions that may be drawn from this table are:

Limit case	Stabilized methods	Galerkin method
$\kappa h \ll 1$	$h\\|\boldsymbol{s}\cdot\nabla(u-u_h)\\| + (\kappa h)^{1/2}\\|u-u_h\\|$ $\lesssim h^{p+1}\|u\|_{L^2(\mathcal{S}^2;H^{p+1}(\Omega))}$	$h\\|P_h(\boldsymbol{s}\cdot\nabla(u-u_h))\\| + (\kappa h)^{1/2}\\|u-u_h\\|$ $\lesssim (\kappa h)^{-1/2}h^{p+1}\|u\|_{L^2(\mathcal{S}^2;H^{p+1}(\Omega))}$
$\kappa h \gg 1$	$h\\|\boldsymbol{s}\cdot\nabla(u-u_h)\\| + \kappa h\\|u-u_h\\|$ $\lesssim (\kappa h)h^{p+1}\|u\|_{L^2(\mathcal{S}^2;H^{p+1}(\Omega))}$	$h\\|P_h(\boldsymbol{s}\cdot\nabla(u-u_h))\\| + (\kappa h)^{1/2}\\|u-u_h\\|$ $\lesssim h^{p+1}\|u\|_{L^2(\mathcal{S}^2;H^{p+1}(\Omega))}$

Table 5.1: Convergence behavior of stabilized and Galerkin methods in limiting cases

- When absorption is dominant, both stabilized methods and the Galerkin method yield optimal convergence in the $L^2(\Omega)$-norm of the error. Note however that we cannot consider h fixed and let $\kappa \to \infty$ because of the assumption $h(\kappa+\sigma_s) \leq C_0$ on which all our previous analysis relies (see also Remark 3). Thus, the estimate for $\kappa h \gg 1$ in the case of the Galerkin method has to be understood with caution, considering that κh is large but without the possibility to take the limit $\kappa h \to \infty$. It cannot be considered better than the estimate for the stabilized methods.

- When absorption is small, stabilized methods yield optimal convergence, of order h^p for the directional derivative. However, the Galerkin method fails because of the large factor $(\kappa h)^{-1/2}$ (apart from the fact that only the projection onto the finite element space of the norm of the directional derivative is controlled).

5.9 Numerical examples

To investigate and compare the accuracy and efficiency of the SUPG and OSS stabilization methods, three typical test problems with absorbing/emitting and scattering media enclosed by gray walls are considered. The directional domain $\mathcal{S}^2$ is discretized with the discrete ordinates method, using the S_N quadrature sets introduced by Lathrop and Carlson [60]. Three tests cases are selected to compare the behavior of the different methods.

After the spatial and directional discretizations have been carried out, the resulting linear system of equations is expensive and strongly coupled due to the discretization of the integral operator in the RTE (5.13). In order to save computer memory, the DOM equations are solved iteratively. If I denotes the iteration counter, the implemented iterative scheme is

$$\boldsymbol{s}\cdot\nabla u_I^\alpha + \left(\kappa + \sigma_s - \frac{\sigma_s}{4\pi}w_\alpha\phi\left(\boldsymbol{s}^\alpha,\boldsymbol{s}^\alpha\right)\right)u_I^\alpha = \frac{\sigma_s}{4\pi}\sum_{\beta=1,\beta\neq\alpha}^{N} w_\beta\phi\left(\boldsymbol{s}^\alpha,\boldsymbol{s}^\beta\right)u_{I-1}^\beta + f^\alpha, \quad (5.128)$$

with $\alpha = 1, 2, ..., N$, and where $\boldsymbol{s}^\alpha$ and w_α are the chosen sets of directions (ordinates) and weights; the unknown u_I^α is the radiative intensity propagating in direction $\boldsymbol{s}^\alpha$ evaluated at iteration I, and f^α is the source term. We have to deal with N equations that are solved independently for each direction, and that are coupled only by the right hand side. The scheme described is of Jacobi type, although a Gauss-Seidel iterative method could also be employed. The numerical examples were solved using a Gauss-Seidel iterative scheme.

In some of the cases described next, the radiative transfer equation (5.13) is subject to emissive and reflective boundary conditions of the form (5.78). As explained in subsection 5.6.2, the variational problem (5.79) needs to be discretized. In the stabilized formulation, the forms involved in the problem are modified as explained for homogeneous boundary conditions. After the DOM discretization, the new boundary conditions couple different directions through the reflective integral term. In the framework of the iterative scheme (5.128), values of u at the previous iteration can be used to evaluate the resulting right-hand-side term.

Let us consider the finite element approximation of (5.128). For each equation of this system the implementation is based on an a priori calculation of the integrals appearing in the formulation and then the construction of the matrices and right-hand-side vectors of the final algebraic systems to be solved. These matrices and these vectors can be constructed directly for each nodal point, without the need to loop over the elements, thus making the calculations much faster.

It is important to note that as $(\kappa + \sigma_s)h \to 0$ each discrete equation is dominated by the convective term. The Galerkin contribution of the convective term is a singular matrix. Therefore, as $(\kappa + \sigma_s)h \to 0$ the Galerkin method gives almost singular matrices. This causes that iterative solvers as GMRES do not converge, even when using good ILUt preconditioners. We had to use direct solvers for solving the test problems described next with the Galerkin method.

5.9.1 Gaussian shaped radiative source term between one-dimensional parallel black slabs

The first test problem that we consider, taken from [99], is known to produce Galerkin oscillations. It consists in solving the radiative transfer problem in a nonscattering medium between one-dimensional finite parallel black slab. This problem is modeled by the one dimensional RTE

$$\mu \frac{du}{dx} + \kappa u = \exp\left(-2500\,(x-0.5)^2\right), \quad x \in [0,1],$$

where μ is the cosine between direction $\boldsymbol{s}$ and the x axis.

Homogeneous boundary conditions are taken:

$$\begin{aligned} u\,(0,\mu) &= 0, \quad \mu > 0, \\ u\,(1,\mu) &= 0, \quad \mu < 0, \end{aligned}$$

The analytical solution of this problem in the case of $\mu > 0$ can be written as

$$\begin{aligned} u(x) = &-\frac{0.02\sqrt{\pi}}{2\mu} \exp\left(-\frac{\kappa}{\mu}\left(x - \frac{\kappa}{10000\mu} - 0.5\right)\right) \\ &\times \left(\operatorname{erf}\left(\frac{\kappa}{100\mu} + 50(0.5-x)\right) - \operatorname{erf}\left(\frac{\kappa}{100\mu} + 25\right)\right). \end{aligned}$$

Figure 5.1 shows the radiative intensity distribution for $\mu = 0.5773505$ and $\kappa = 1$. The Galerkin and the stabilized SUPG and OSS methods are compared against the analytical solution. We used uniform meshes, with the number of elements ranging from 20 to 400 linear elements. For coarser grids global spurious oscillations occur when the Galerkin method is used. This is because it is stable in the norm (5.121), which has poor control on the derivatives. Due to the nature of the analytical solution we found bigger oscillations for an even quantity of elements.

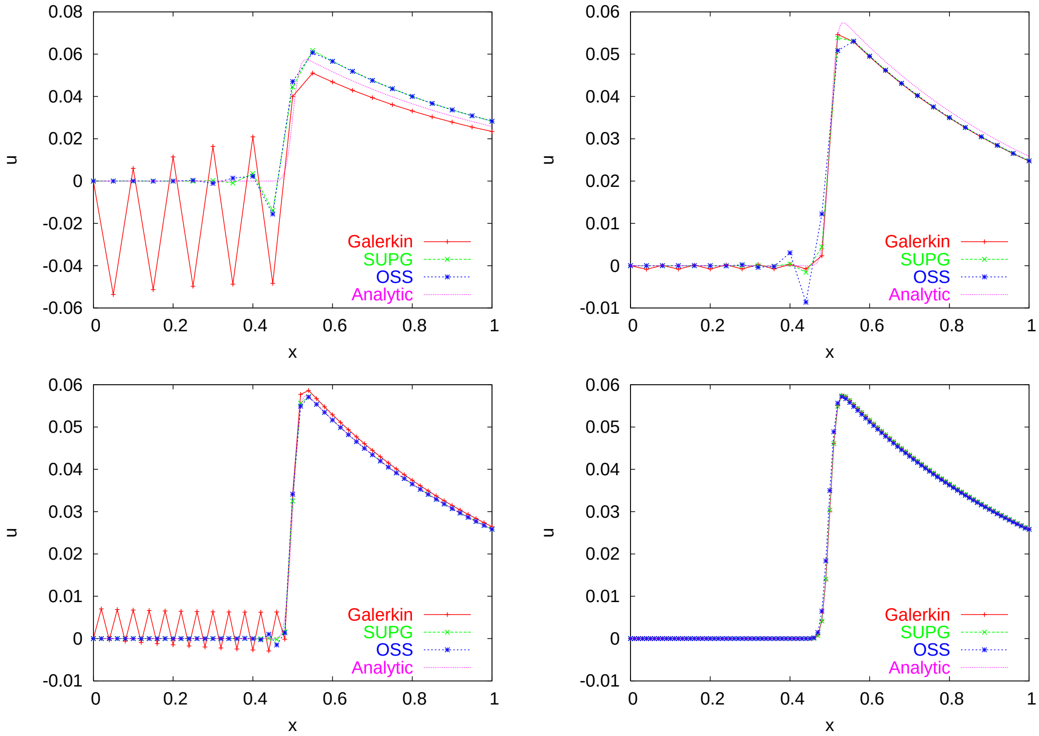

Figure 5.1: Radiative intensity distribution for a mesh with 20 (top left), 25 (top right), 50 (bottom left) and 100 (bottom right) elements.

When using stabilized formulations global oscillations are removed. For some meshes, the OSS method presents higher localized peaks than the SUPG method due to the less diffusive nature of the scheme. When using a finer grid capable of capturing the jump of the analytical solution, all oscillations are removed.

Figure 5.2 shows the L^2 error of the different methods relative to the reference solution against the mesh size h. We observe from this figure optimal convergence, that is $\|u - u_h\| \leq Ch^2$ when $h \to 0$.

5.9.2 Absorbing and anisotropic scattering in the unit square (2D problem)

The second test problem consists in solving the radiative heat transfer equation in a square domain. The medium is considered to be absorbing/emitting and with anisotropic scattering, enclosed by boundaries of length $L = 1$ m with emissivity $\epsilon = 0.8$ and reflectivity $\rho = 0.2$. From the discussion after (5.81) it follows that the maximum upper bound for η in this case is $\eta \approx 49.49$. We have chosen $\eta = 40$ with good results.

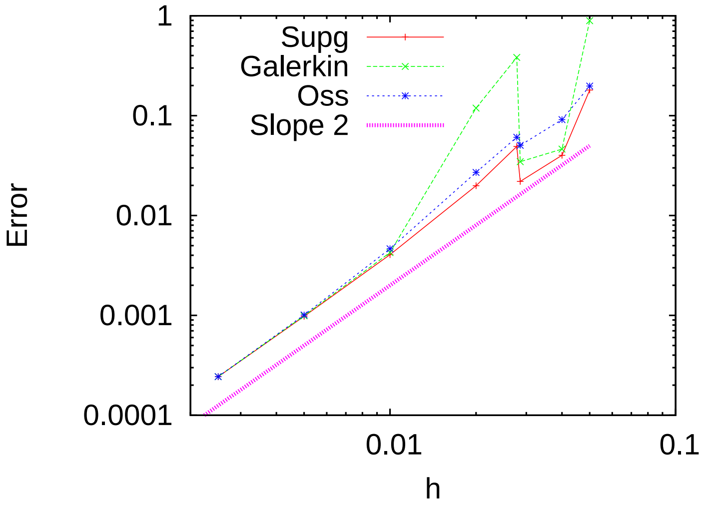

Figure 5.2: Relative error of the solutions for different methods against mesh size h.

The upper wall is maintained at a temperature $T_{\text{hot}} = 1000$ K, and all other walls at a temperature $T_{\text{cold}} = 500$ K. The medium is maintained at uniform temperature of $T_{\text{g}} = 800$ K. We consider the phase function $\phi(\boldsymbol{s}', \boldsymbol{s})$ as linearly anisotropic, of the form

$$\phi(\boldsymbol{s}', \boldsymbol{s}) = 1 + A_1 \boldsymbol{s}' \cdot \boldsymbol{s},$$

where $A_1 = 0.2$.

For the space dicretization we use bilinear rectangular elements Q_1. For discretizing the angular dependency the $SN8$ ordinates set [70] is used, consisting of 80 directions. Discretization in space goes from meshes of 20×20 to 240×240 elements.

As the RTE does not have analytical solutions for arbitrary geometries, we have compared the results of the different formulations with a reference solution, obtained using a fine grid of 480×480 elements.

We have run two cases, the first one with an optical thickness $\beta = (\kappa + \sigma_s)L = 1$, and the second one with $\beta = (\kappa + \sigma_s)L = 0.011$. In the later case the medium is quite nonparticipative. Due to the discontinuity in the boundary conditions, solutions may present sharp gradients that can activate instabilities.

Case 1 In this first case the physical properties of the medium are taken as $\kappa = 0.2$ m^{-1} and $\sigma_s = 0.8$ m^{-1}. In figure 5.3, two solutions are plotted for the radiation intensity in Ω when solving with the SUPG method and using a mesh of 240×240 elements. The picture on the left corresponds to radiation propagating from the upper hot wall, whereas in the picture on the right it propagates from the cold walls.

The solutions obtained when using Galerkin, the SUPG and the OSS methods are compared against the reference solution in figure 5.4, using meshes of 20×20, 80×80 and 240×240 linear elements. A cut of these solutions is shown. The Galerkin method shows higher numerical oscillations for finer grids. The stabilized methods OSS and SUPG give very similar results, without numerical oscillations.

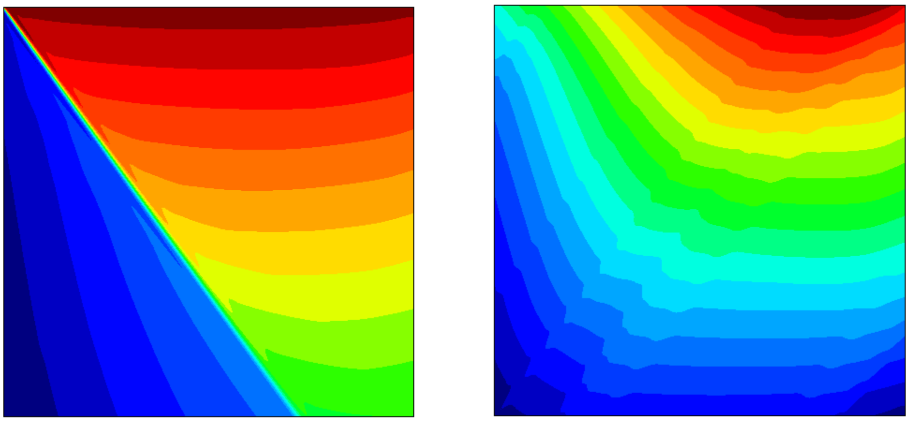

Figure 5.3: Radiative intensity solutions using the SUPG method in a mesh of 240×240 elements corresponding to case 1 ($\kappa = 0.2$ m^{-1} and $\sigma_s = 0.8$ m^{-1}). Radiation propagating from the upper hot wall (left picture) and the cold walls (right picture).

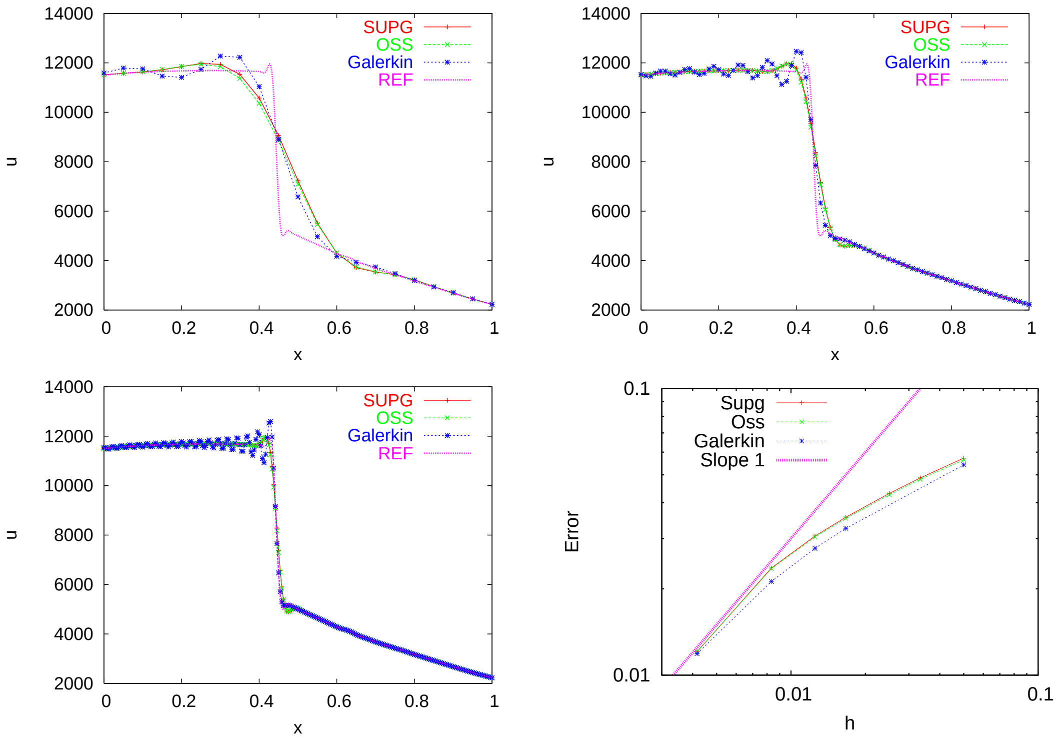

Figure 5.4: Radiative intensity cut at $x = 0.4$ m using different numerical methods on a mesh of 20×20 (top left), 80×80 (top right) and 240×240 (bottom left) elements. In all cases the reference solution computed on a mesh of 480×480 elements is also shown. Relative error of the solutions against mesh size h (bottom right). Case 1 ($\kappa = 0.2$).

The error of the different methods relative to reference solution is also plotted against mesh size h in figure 5.4 (bottom-right). This error has been computed as

$$\text{Error} = \frac{\sum_{a,\alpha} \left(u_h(\boldsymbol{x}^a, \boldsymbol{s}^\alpha) - u(\boldsymbol{x}^a, \boldsymbol{s}^\alpha)\right)^2}{\sum_{a,\alpha} \left(u(\boldsymbol{x}^a, \boldsymbol{s}^\alpha)\right)^2} \tag{5.129}$$

where a, α refers to nodes and directions, $u_h(\boldsymbol{x}^a, \boldsymbol{s}^\alpha)$ is the discrete solution at node $\boldsymbol{x}^a$ and direction $\boldsymbol{s}^\alpha$, and $u(\boldsymbol{x}^a, \boldsymbol{s}^\alpha)$ is the reference solution at this node and with this direction. For the smallest values of h a linear convergence of the error is observed. This convergence is not optimal. A possible explanation is that the analytical solution is discontinuous due to the discontinuity in the boundary conditions.

Case 2 In this case the medium has as absorption coefficient $\kappa = 0.01$ m^{-1} and as scattering coefficient $\sigma_s = 0.001$ m^{-1}. Figure 5.5 shows the solutions obtained for the radiation intensity when using the SUPG and the Galerkin methods in a mesh of 480×480 elements. In this example, the radiation intensity comes from the upper hot wall. It is observed that the Galerkin solution is polluted with global oscillations.

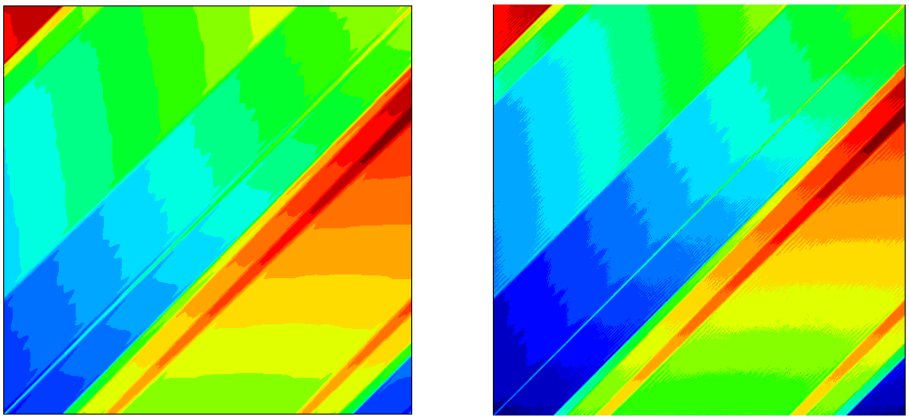

Figure 5.5: Radiative intensity solution using the SUPG (left) and the Galerkin (right) methods in a mesh of 480×480 elements. Case 2 ($\kappa = 0.01$ m^{-1} and $\sigma_s = 0.001$ m^{-1}).

In figure 5.6 different cuts of radiative intensity are shown for the stabilized and the Galerkin methods for meshes of 80×80, 240×240 and 480×480 elements. As in case 1, the Galerkin method shows higher numerical oscillations for finer grids. When using finer grids, the OSS and the SUPG methods give results similar to the reference solution, so that only this reference solution has been plotted. It is worth to note that the Galerkin oscillations are not node to node.

5.9.3 Absorbing and isotropic scattering in the unit cube (3D problem)

The third test problem consists in solving the radiative transfer equation in the unit cube $(x, y, z) \in [0, 1]^3$. The temperature of the medium is $T_\mathrm{m} = 800$ K. The boundary conditions consist of one hot wall ($z = 1$) at $T_\mathrm{h} = 1000$ K, while the other walls are maintained

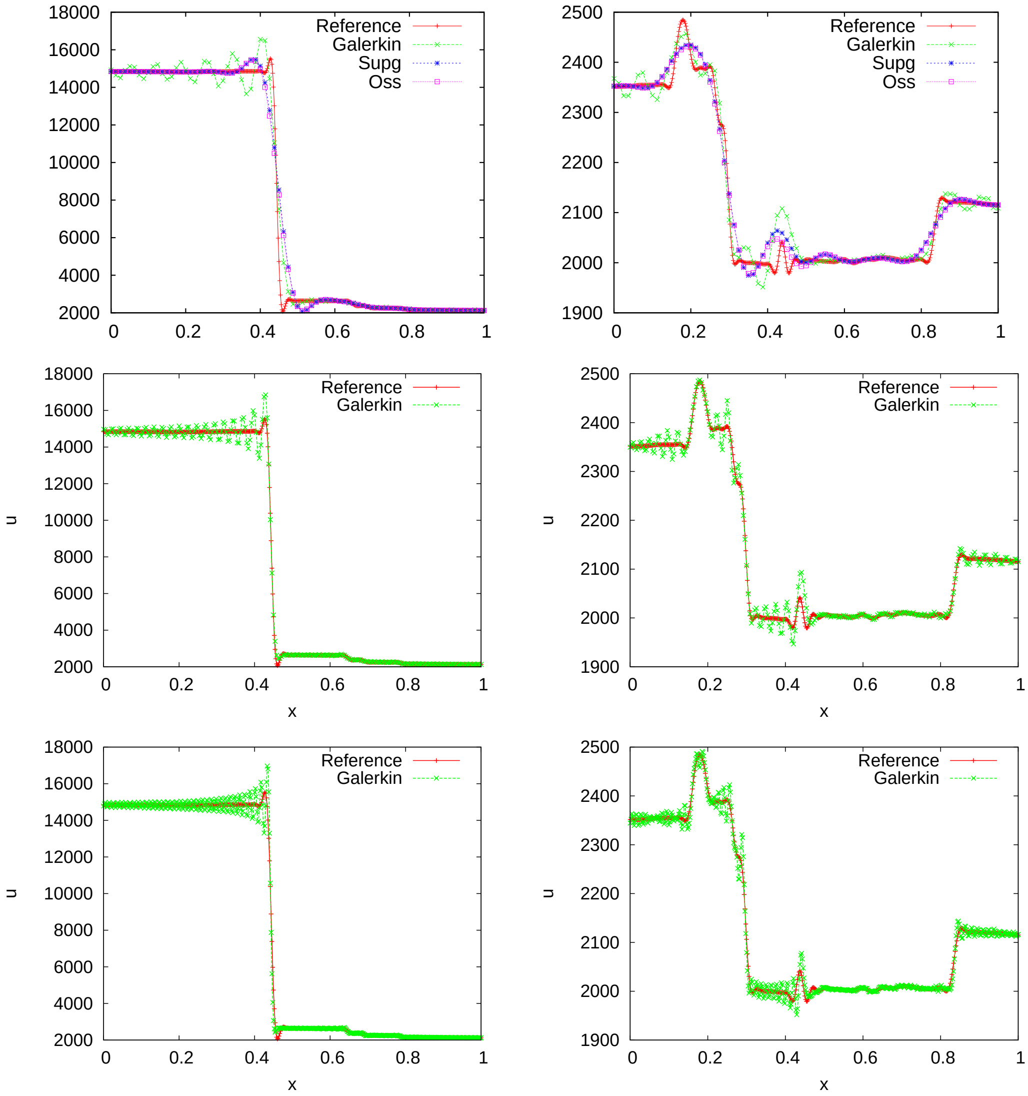

Figure 5.6: Radiative intensity cut at 0.4 m (right) and 0.6 m (left) from the hot wall for different numerical methods and reference solution in meshes of 80×80 (top) 240×240 (middle) 480×480 (bottom) elements. Case 2 ($\kappa = 0.01\ \mathrm{m}^{-1}$ and $\sigma_s = 0.001\ \mathrm{m}^{-1}$).

cold ($T_\mathrm{c} = 0$ K). The hot wall is considered opaque and non reflective ($\epsilon = 1.0$, $\rho = 0.0$). The physical absorption and scattering are $\kappa = 0.2$ and $\sigma_s = 0.3$ (SI units are assumed).

Figure 5.7 shows the solution for radiation intensity over the cubic domain coming from the upper hot wall when using the SUPG method and a mesh of $20 \times 20 \times 20$ trilinear elements. Figure 5.8 shows plots of radiative intensity cuts for the stabilized and the Galerkin methods using respectively meshes of $20 \times 20 \times 20$ and $40 \times 40 \times 40$ trilinear elements. The tests are compared to a reference solution obtained with a mesh of $80 \times 80 \times 80$ trilinear elements using the SUPG method. The obtained results using the SUPG and the OSS methods are very close. The behavior of the Galerkin method is similar to the one observed in the bidimensional problem (see figure 5.4).

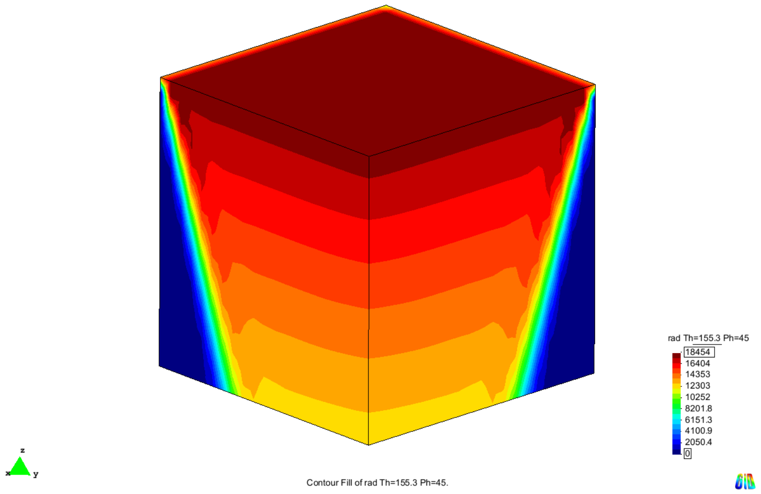

Figure 5.7: Radiative intensity solution with the SUPG method in the whole domain using a mesh of $20 \times 20 \times 20$ trilinear elements.

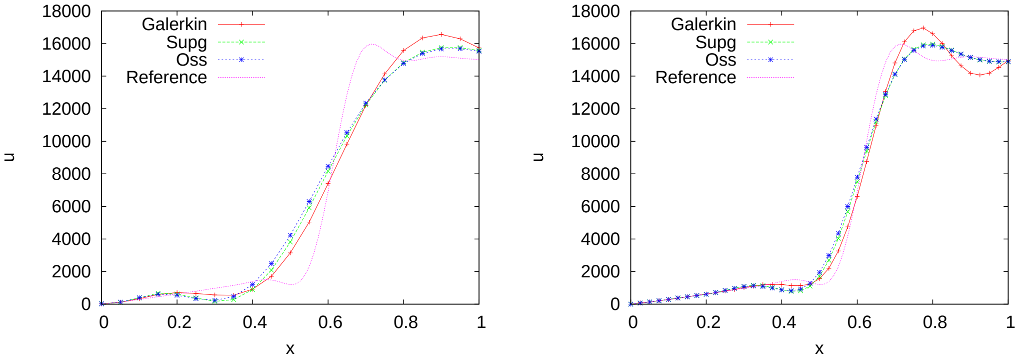

Figure 5.8: Radiative intensity cut for the SUPG, the OSS and the Galerkin methods against the reference solution in a mesh of $20 \times 20 \times 20$ (left) and $40 \times 40 \times 40$ (right) trilinear elements.

5.10 Conclusions

We have developed the radiative transfer equation, explaining radiation from a physical point of view. We have presented radiative models that come from the sphere discretization. In this chapter we have designed and analyzed stabilized finite element methods to approximate the radiative transport equation. The problem is posed in a spatial domain and in the unit sphere $\mathcal{S}^2$, and both need to be discretized. We have focused our attention to the spatial discretization, and used only the DOM in the numerical testing, although any other discretization of $\mathcal{S}^2$ could be used.

The Galerkin method for the spatial discretization suffers from numerical oscillations due to the convective term in the equation to be approximated. We have presented a non-conventional numerical analysis that shows that some control on the convective derivative can be obtained, but not enough to prevent the appearance of numerical wiggles.

In order to overcome the misbehavior of the Galerkin method, two stabilized finite element methods have been discussed, namely, the well known SUPG formulation a the OSS method. Both can be motivated within the variational multiscale framework, although some simplifying assumptions have to be added to arrive to the version of the methods analyzed here.

Both approximations, the SUPG and the OSS, are stable and optimally convergent in the same norm and with the same error function. This norm happens to be finer than the one in which the Galerkin method can be analyzed. There is full control in the convective derivative that translates into globally smooth solutions, although some local oscillations may be still encountered. As the OSS method introduces less numerical dissipation than the SUPG method, the local overshoots and undershoots are sometimes higher using the OSS method. Let us stress that the norm in which we have presented the stability and convergence results remains meaningful for all values of the physical parameters. For the SUPG method this represents a modification of well known results, whereas for the OSS method this analysis is an original contribution of this work.

Chapter 6

Subgrid approximation for thermally coupled flows with radiative heat transfer

In this chapter the low Mach number equations studied in chapter 3 are coupled with radiative equations, studied in chapter 5, to account for radiatiave heat transfer. For high temperature flows this coupling can have strong effects on temperature and velocity fields. A nonlinear stabilized finite element method has been proposed for thermally coupled incompressible flows in chapter 2 and extended for the low Mach number equations in chapter 3, obtaining stable and more accurate solutions than clasical stabilization methods. In chapter 4 it was shown that the approximation model is able to model turbulence avoiding the need of physical turbulence models. In presence of radiative heat the nonlinear coupling between temperature and radiation intensity is quite complex. The aim is to model physical subgrid coupling between temperature and radiation with the proposed nonlinear stabilization method. This coupling is very important to account to turbulence-radiation interaction models. The formulation is independent of the implemented radiative model. A subgrid modeling for the coupling terms in energy and radiation equation is proposed. The final formulation globally conserves energy if the radiative model globally conserves radiating energy, when using the same interpolation for temperature and pressure unknowns.

6.1 Introduction

Thermal radiation in gas flows has direct effects on many industrial applications, such as fires, furnaces, gas turbines, boilers, etc, where radiative transfer dominates heat transfer. Growing concern with high temperature has emphasized the need for an evaluation of the effect of radiative heat transfer. Radiation can strongly interact with convection in many situations of engineering interest and neglecting its effects may have significant consequences in the overall predictions. An accurate calculation of radiative transfer is then of crucial importance for the prediction of the thermal performance. On the other hand it is common for studies on convective flows to neglect thermal radiation, mainly because the modeling of radiative transfer increases the computational work and involves tedious mathematics.

The influence of radiation on natural convection (a common fire scenario physical mechanism) is generally stronger than that on forced convection due to the inherent coupling between temperature and flow fields.

Approximate models for radiative heat transfer have also been derived and widely used in the literature. As example for such approximation are the P_N method and the discrete ordinates method DOM. Our interest is the development of a nonlinear stabilization technique capable of solving low Mach number flows in radiating media without being focused in a specific radiative model.

Turbulence is the most common state of a fluid flow in a wide range of technologies and natural conditions. The interaction between turbulence and radiation (TRI) has been demonstrated experimentally, theoretically and numerically, and results from the highly nonlinear coupling between fluctuations of radiation intensity and fluctuations of temperature of the medium [29]. Experimental data and numerical calculations demonstrate that turbulent fluctuations may significantly increase the radiation intensity in both non-luminous and luminous flames. The net radiative power and the fraction of radiative heat loss increase due to TRI. Usually in combustion applications of LES , these interactions are either discarded altogether, or included in the computation without considering any subgrid scale model for radiation. The focus of the present chapter is on how to compute the coupling of the radiative terms in the energy equation and the thermal terms in radiative equations. We propose a stabilized finite element approximation based on the variational multiscale method, in which a decomposition of the approximating space into a coarse scale resolvable part and a fine scale subgrid part is performed. The distinctive features of our approach are to consider the subscales as transient and to keep the scale splitting in all the nonlinear terms. The first ingredient permits to obtain better stability and no restrictions on the time step size. The second ingredient permits to prove global conservation properties, gives higher accuracy to the method, and allows us to approach the problem of dealing with thermal turbulence from a strictly numerical point of view. The aim of the present work is that the stabilization terms coming from the highly nonlinear coupling between temperature and radiation, are able to model TRI subgrid effects.

The chapter is organized as follows. In Section 6.2, the Low Mach number equations with radiative coupling and their variational formulation are given. Some different coupling mechanisms between radiative and conductive heat are explained. Afterwards the VMS formulation through dynamic scale splitting is derived in Section 6.3. It is shown in Section 6.4 that this formulation provides global energy conservation when using equal interpolation spaces for the pressure and temperature equations, if the radiation model is globally conservative. The treatment of the coupling of the nonlinear terms is described in detail in Section 6.5. The dimensionless equations and important dimensionless parameters are discussed in section 6.6. The formulation is tested for both stationary and dynamic problems in Section 6.7. Conclusions are drawn in Section 6.8.

6.2 The Low Mach number problem coupled with radiative heat transfer

6.2.1 Initial and Boundary Value Problem

The low Mach number flow equations were introduced in Chapter 3. When radiative heat transfer is considered the energy equation needs to be modified adding the divergence of the total radiative heat flux term $\nabla \cdot \boldsymbol{q}_r$. The initial and boundary value problem reads as follows let $\Omega \subset \mathbb{R}^d$,with $d = 2, 3$, be the computational domain in which the flow takes place during the time interval $[0, t_{\text{end}}]$ and let $\partial\Omega$ be its boundary. Let $\mathcal{S}^2$ be the unit sphere in $\mathbb{R}^3$. The initial and boundary value problem to be considered consists in finding a velocity field $\boldsymbol{u}$, a hydrodynamic pressure field p, a temperature field T the thermodynamic pressure p^{th} , and the radiation intensity field I_λ such that

$$\begin{aligned}
\frac{\partial \rho}{\partial t} + \boldsymbol{\nabla} \cdot (\rho \boldsymbol{u}) &= 0 \quad \text{in}\, \Omega,\ t \in (0, t_{\text{end}}) \qquad (6.1)\\
\rho \frac{\partial \boldsymbol{u}}{\partial t} + \rho \boldsymbol{u} \cdot \nabla \boldsymbol{u} - \nabla \cdot \left(2\mu \boldsymbol{\varepsilon}'(\boldsymbol{u})\right) + \nabla p &= \rho \boldsymbol{g} \quad \text{in}\, \Omega,\ t \in (0, t_{\text{end}}) \qquad (6.2)\\
\rho c_p \frac{\partial T}{\partial t} + \rho c_p \boldsymbol{u} \cdot \nabla T - \nabla \cdot (k \nabla T) - \frac{dp^{\text{th}}}{dt} & \\
+ \int_0^\infty \mathrm{d}\lambda \kappa_\lambda \left(4\pi I_{b\lambda}(T) - \int_{4\pi} \mathrm{d}s I_\lambda \right) &= Q \quad \in \Omega, t \in (0, t_{\text{end}}) \qquad (6.3)\\
\boldsymbol{s} \cdot \nabla I_\lambda + (\kappa_\lambda + \sigma_{s\lambda}) I_\lambda - \frac{\sigma_{s\lambda}}{4\pi} \int_{4\pi} \mathrm{d}\boldsymbol{s}' \phi_\lambda(\boldsymbol{s}', \boldsymbol{s}) I_\lambda(\boldsymbol{s}') &= \kappa_\lambda I_{b\lambda} \quad \text{in} \Omega \times \mathcal{S}^2 \times \mathbb{R}_+ \qquad (6.4)
\end{aligned}$$

where ρ denotes the density, μ the viscosity, $\boldsymbol{\varepsilon}'(\boldsymbol{u}) = \boldsymbol{\varepsilon}(\boldsymbol{u}) - \frac{1}{3}(\boldsymbol{\nabla} \cdot \boldsymbol{u}) \boldsymbol{I}$ the deviatoric part of the rate of deformation tensor $\varepsilon(\boldsymbol{u}) = \boldsymbol{\nabla}^s \boldsymbol{u} = \frac{1}{2}\left(\boldsymbol{\nabla} \boldsymbol{u} + \boldsymbol{\nabla} \boldsymbol{u}^T\right)$, $\boldsymbol{I}$ the identity tensor, $\boldsymbol{g}$ the gravity force vector, c_p the specific heat coefficient at constant pressure, k the thermal conductivity and Q the heat source. Equations (6.1)-(6.3) represent the mass, momentum and energy conservation respectively. Equation (6.4) is the monochromatic radiative transfer equation, developed in section 5.3, and $I_\lambda(\boldsymbol{s})$ is the spectral radiative intensity at wavelength λ propagating in direction $\boldsymbol{s}$. The function $I_{b\lambda}$ is the spectral blackbody radiation at wavelength λ, depending only on the temperature T. The coefficients κ_λ and $\sigma_{s\lambda}$ are respectively the spectral absorption and scattering coefficients, and $\phi_\lambda(\boldsymbol{s}', \boldsymbol{s})$ is the scattering phase function. A detailed analysis on the radiative transfer equation (6.4) was developed in Chapter 5. Additionally the state equation for ideal gases is used to give a close the system

$$\rho = p^{\text{th}} / RT \qquad (6.5)$$

The mass, momentum and energy equations must be supplied with initial and boundary conditions. Initial conditions are

$$\begin{aligned} \boldsymbol{u} &= \boldsymbol{u}_0 \ \text{ in } \Omega,\ t=0 \\ T &= T_0 \ \text{ in } \Omega,\ t=0 \\ p^{\text{th}} &= p_0^{\text{th}} \ \text{ in } \Omega,\ t=0 \end{aligned}$$

Dirichlet and Neumann boundary conditions for Eqs. (6.1) and (6.3) are

$$\begin{aligned} \boldsymbol{u} &= \boldsymbol{0} \ \text{ in } \Gamma_D^{\boldsymbol{u}} \\ T &= 0 \ \text{ in } \Gamma_D^{T} \\ (-p\boldsymbol{I} + 2\mu\boldsymbol{\varepsilon}'(\boldsymbol{u}))\cdot\boldsymbol{n} &= \boldsymbol{t}_n \ \text{ in } \Gamma_N^{\boldsymbol{u}} \\ -k\boldsymbol{n}\cdot\nabla T &= q_n \ \text{ in } \Gamma_N^{T}. \end{aligned}$$

where $\boldsymbol{n}$ is the outer unit normal on the boundary. It is assumed that $\Gamma_D^x \cup \Gamma_N^x = \partial\Omega$, and $\Gamma_D^x \cap \Gamma_N^x = \emptyset$ for $x = T, \boldsymbol{u}$.

Due to the hyperbolic nature of the radiation equation (6.4) the intensity entering into the domain Ω needs to be imposed. The boundary $\Gamma = \partial\Omega \times \mathcal{S}^2$ of $\Omega \times \mathcal{S}^2$ is divided into the inflow Γ^- and outflow Γ^+ boundaries, defined as

$$\Gamma^- = \{(\boldsymbol{x},\boldsymbol{s}) \in \Gamma \mid \boldsymbol{s}\cdot\boldsymbol{n} < 0\}, \quad \Gamma^+ = \{(\boldsymbol{x},\boldsymbol{s}) \in \Gamma \mid \boldsymbol{s}\cdot\boldsymbol{n} \geq 0\}, \tag{6.6}$$

where $\boldsymbol{n}$ is the unit normal vector pointing outwards $\partial\Omega$ at $\boldsymbol{x}$. We shall also make use of the inflow and outflow hemispheres

$$\mathcal{S}_{\partial_x}^- := \{\boldsymbol{s} \in \mathcal{S}^2 \mid \boldsymbol{s}\cdot\boldsymbol{n} < 0\}, \quad \mathcal{S}_{\partial_x}^+ := \{\boldsymbol{s} \in \mathcal{S}^2 \mid \boldsymbol{s}\cdot\boldsymbol{n} \geq 0\}, \tag{6.7}$$

which are defined for each $\boldsymbol{x} \in \partial\Omega$.

The radiative transfer equation (6.4) is subject to emissive and reflective boundary conditions of the form

$$I_\lambda(\boldsymbol{x},\boldsymbol{s})\,|_{\mathcal{S}_{\partial_x}^-} = \epsilon_\lambda I_{b\lambda} + \frac{r_\lambda}{\pi}\int_{\mathcal{S}_{\partial_x}^+} I_\lambda(\boldsymbol{x},\boldsymbol{s})\,\boldsymbol{n}\cdot\boldsymbol{s}\,\mathrm{d}s \tag{6.8}$$

where ϵ_λ and r_λ are respectively the emission and reflective wall coefficients at wavelength λ. For opaque surfaces these coefficients are related by $r_\lambda = 1 - \epsilon_\lambda$.

6.2.2 Coupling of the radiative model

The radiative transfer equation (6.4) has six independent variables (three space coordinates, two direction coordinates and the wavelength), to discretize them is a prohibitive task. In heat transfer calculations it is only the divergence of the total radiative heat flux $\nabla\cdot\boldsymbol{q}_r$ what is of interest, affecting the energy balance equation (6.3) from which temperature will be computed. The accuracy of this term depends on how good the radiative model is. There exist several models to obtain an approximate solution to the radiation transfer equation. A usual option is to apply a directional discretization, transforming the integro-differential equation (6.4) into a set of coupled differential equations, with an arbitrary number of equations depending on the discretization level. Examples of this kind of models are the discrete ordinates method (DOM), the method of spherical harmonics (P_N-approximation), and ray tracing method, wich can be discretized in space using the finite element method, as explained in Chapter 5. The aim of the present chapter is to develop a stabilization method for the mass, momentum and energy equations, independent of the radiative model used. The radiative heat terms in the energy equation come from the divergence of the total radiative heat transfer $\nabla \cdot \boldsymbol{q}_r$, which can be expressed in terms of radiative intensity and temperature as

$$\nabla \cdot \boldsymbol{q}_r = \int_0^\infty \mathrm{d}\lambda \kappa_\lambda \left(4\pi I_{b\lambda} - G_\lambda\right) = 4\kappa_e \sigma_B T^4 - \kappa_a G(I_\lambda) \tag{6.9}$$

where G_λ and G are the spectral and total incident radiation, defined as

$$G_\lambda = \int_{4\pi} \mathrm{d}s I_\lambda \tag{6.10}$$

$$G(I_\lambda) = \int_0^\infty \mathrm{d}\lambda G_\lambda \tag{6.11}$$

whith $\mathrm{d}s$ a differential of solid angle and the subindex 4π indicates integration over all directions over the sphere. The absorption and emission coefficients κ_a and κ_e in Eq. (6.9) are spectral averages of the absorption coefficient κ_λ, weighted respectively with the radiation field G_λ and the blackbody radiation field $I_{b\lambda}$:

$$\kappa_a = \frac{\int_0^\infty \mathrm{d}\lambda \kappa_\lambda G_\lambda}{G} \tag{6.12}$$

$$\kappa_e = \frac{\pi \int_0^\infty \mathrm{d}\lambda \kappa_\lambda I_{b\lambda}}{\sigma_B T^4} \tag{6.13}$$

where σ_B is the Stephan Boltzmann constant, the constant of proportionality in the Stefan Boltzmann law, relating blackbody radiation with fourth power of temperature

$$\sigma_B T^4 = \pi \int_0^\infty \mathrm{d}\lambda I_{b\lambda}\left(T\right) \tag{6.14}$$

For a given composition and pressure, the emissive coefficient only depends the temperature. There exist expression for $\kappa_e(T)$ in terms of temperature that could be linearized in the energy equation. Although any radiation model can be used to determine radiation intensity distribution, we suppose that a general directional discretization model is applied to the radiative transfer equation, obtaining directional components of radiation intensity I_λ^d. The radiation equation of the adopted model will be denoted as $\boldsymbol{R}_M\left(I_\lambda^d, T\right) = \boldsymbol{0}$, where $\boldsymbol{R}_M$ is a partial differential operator. In the energy equation, the emission coefficient κ_e and the product of the absorption coefficient and the incident radiation $\kappa_a G$ depend on the obtained radiation intensity distribution I_λ^d, and must be given by the radiative model.

6.2.3 Coupled boundary conditions in the energy and radiation equations

Radiative heat exchange on boundaries Integrating boundary condition (6.8) over the inflow hemisphere $\mathcal{S}_{\partial_x}^-$ and omitting λ subindex we get

$$J(\boldsymbol{x}) = \epsilon \pi I_b(T) + rH(\boldsymbol{x}) \tag{6.15}$$

where the *surface irradiation* $H(\boldsymbol{x})$ is the radiative heat rate impinging into the surface at point $\boldsymbol{x}$:

$$H(\boldsymbol{x}) = \int_{S^-_{\partial_x}} I\left(\boldsymbol{x}, \boldsymbol{s}\right) \boldsymbol{s} \cdot \boldsymbol{n} ds \tag{6.16}$$

and *surface radiosity* $J(\boldsymbol{x})$ is the component of heat flux leaving the surface at location $\boldsymbol{x}$ entering into domain Ω:

$$J(\boldsymbol{x}) = \int_{S^+_{\partial_x}} I\left(\boldsymbol{x}, \boldsymbol{s}\right) |\boldsymbol{s} \cdot \boldsymbol{n}| \mathrm{d}s \tag{6.17}$$

By means of equation (6.15) the radiative heat flux over the boundary is related with radiosity J or irradiation H as

$$\begin{aligned} \boldsymbol{q}_r \cdot \boldsymbol{n} &= H - J \\ &= \frac{\left(1 - r\right) J - \epsilon \pi I_b(T)}{r} \qquad (6.18) \\ &= \left(1 - r\right) H - \epsilon \pi I_b(T) \qquad (6.19) \end{aligned}$$

Depending on the radiative model used, boundary condition (6.8) can be directly imposed, and the heat flux satisfies relations (6.19) and (6.18); this is the case for the discrete ordinates method. In some radiative models boundary condition (6.8) cannot be imposed directly; this is the case of P_1 method, where relation (6.19) or (6.18) is imposed, but not both.

Radiative boundary conditions couples radiation and temperature through I_b, it also depends on radiation intensity over the boundary through H or J, a behavior of Robin type boundary conditions.

Coupled energy boundary condition It is usual to impose a conductive heat flux as boundary condition in the energy equation. In the radiative equation is usually imposed emissive and reflective boundary condition in terms of the wall temperature and irradiation H. In some applications it is needed to have control on the complete heat transfer $\mathcal{H}$ through the boundary, coupling radiative and conductive boundary conditions as

$$-\boldsymbol{n} \cdot k \nabla T_h + \boldsymbol{q}_r \cdot \boldsymbol{n} = \mathcal{H} \tag{6.20}$$

An example is an isolated boundary where the net flux through the boundary must be null ($\mathcal{H} = 0$). This isolated wall is an emmisive and reflective wall, and needs to satisfy radiation boundary condition (6.15) depending on wall temperature and exiting radiation. The radiative boundary condition is coupled with energy equation, depending on the radiative solution through irradiation H. The total heat flux $\mathcal{H}$ is imposed in the energy boundary condition (6.20), replacing the radiative heat flux $\boldsymbol{q}_r \cdot \boldsymbol{n}$ by means of Eq. (6.19) in terms of radiosity H and wall temperature. We finally get

$$-\boldsymbol{n} \cdot k \nabla T_h - \epsilon \sigma_B T_h^4 = \mathcal{H} - (1 - r) H \tag{6.21}$$

This boundary condition is of nonlinear Robin type for the temperature, and couples radiation and temperature in the boundary.

6.2.4 Variational formulation

To obtain a variational formulation for the system (6.1)-(6.3) together with radiation model equation, let us denote by $\boldsymbol{V}, Q, W, Z$ the functional spaces where the solution is sought. The corresponding space of test functions will be denoted by $\boldsymbol{V}_0, Q_0, W_0, Z_0$

The weak form of the problem consists in finding $(\boldsymbol{u}, p, T, I_\lambda) \in (\boldsymbol{V}, Q, W, Z)$ such that

$$\left(\frac{\partial \rho}{\partial t} + \nabla \cdot (\rho \boldsymbol{u}), q\right) = 0 \qquad \forall q \in Q_0 \tag{6.22}$$

$$\left(\rho \frac{\partial \boldsymbol{u}}{\partial t} + \rho \boldsymbol{u} \cdot \nabla \boldsymbol{u}, \boldsymbol{v}\right) + \left(2\mu \boldsymbol{\varepsilon}'(\boldsymbol{u}), \boldsymbol{\varepsilon}'(\boldsymbol{v})\right) - (p, \nabla \cdot \boldsymbol{v}) = (\rho \boldsymbol{g}, \boldsymbol{v}) + (\boldsymbol{t}_n, \boldsymbol{v})_{\Gamma_N^{\boldsymbol{u}}} \qquad \forall \boldsymbol{v} \in \boldsymbol{V}_0 \tag{6.23}$$

$$\left(\rho c_p \frac{\partial T}{\partial t} + \rho c_p \boldsymbol{u} \cdot \nabla T + \kappa_e \sigma_B T^4, w\right) + (k \nabla T, \nabla w) = \left(Q + \frac{dp^{\text{th}}}{dt} + \kappa_a G(I_\lambda), w\right) + (q_n, w)_{\Gamma_N^T} \qquad \forall w \in W_0 \tag{6.24}$$

$$\left(\boldsymbol{R}_M(I_\lambda^d, T), z\right) = 0 \qquad \forall z \in Z \tag{6.25}$$

6.3 Spatial approximation of the radiation hydrodynamic equations

Let us consider a finite element partition $\{K\}$ with n_e elements of the computational domain Ω, from which we can construct finite element spaces for the velocity, pressure and temperature in the usual manner. We will denote them by $\boldsymbol{V}_h \subset \boldsymbol{V}$, $Q_h \subset Q$, $W_h \subset W$ and $Z_h \subset Z$, respectively.

Let us split the continuous space $\boldsymbol{Y} = \boldsymbol{V} \times Q \times W$ where velocity, pressure and temperature belong, as $\boldsymbol{Y} = \boldsymbol{Y}_h \oplus \widetilde{\boldsymbol{Y}}$, where $\widetilde{\boldsymbol{Y}} = \widetilde{\boldsymbol{V}} \times \widetilde{Q} \times \widetilde{W}$ is the subgrid space, that can be in principle any space to complete $\boldsymbol{Y}_h = \boldsymbol{V}_h \times Q_h \times W_h$ in $\boldsymbol{Y}$. These continuous unknowns split as

$$\boldsymbol{u} = \boldsymbol{u}_h + \widetilde{\boldsymbol{u}} \tag{6.26}$$

$$p = p_h + \widetilde{p} \tag{6.27}$$

$$T = T_h + \widetilde{T} \tag{6.28}$$

where the components with subscripts h belong to the corresponding finite element spaces, and the components with the $\widetilde{\ }$ correspond to the subgrid space. These additional components are what we will call subscales. We will not consider how the radiation intensity equation (6.4) is approximated in space, we will only focus in how the temperature T is approximated inside the radiation equation. Some finite element approximations of the discrete radiation models are described in Chapter 5.

The spatial approximation will be obtained following the same procedures and approximations done in [2] for the low Mach number equations. The same procedures are explained with deeper insight in Chapter 3. The particular approximation consists in keeping time dependency of the subscales and to keep the previous decompositions (6.26)-(6.28) in *all* the terms of the variational problem (6.22)-(6.25) even if the differential operator is approximated. It is assumed that the subscales vanish on the interelement boundaries, ∂K.

Substituting decompositions (6.26)-(6.28) in the variational problem (6.22) -(6.24), taking the tests functions in the corresponding finite element spaces and integrating some terms by parts, it is found that the solution $\left(\boldsymbol{u}_h, T_h, p_h, I^d_{\lambda h}\right) \in \boldsymbol{V}_h \times Q_h \times W_h \times Z_h$ must satisfy

$$\left(\frac{\partial \rho^h}{\partial t}, q_h\right) - \left(\rho^h \boldsymbol{u}_h, \nabla q_h\right) + \left(\rho^h \boldsymbol{n} \cdot \boldsymbol{u}_h, q_h\right)_{\partial\Omega} - \left(\rho^h \widetilde{\boldsymbol{u}}, \nabla q_h\right) = 0 \tag{6.29}$$

$$\begin{aligned}
&\left(\rho^h \frac{\partial \boldsymbol{u}_h}{\partial t} + \rho^h \left(\boldsymbol{u}_h + \widetilde{\boldsymbol{u}}\right) \cdot \nabla \boldsymbol{u}_h, \boldsymbol{v}_h\right) + \left(2\mu \boldsymbol{\varepsilon}'\left(\boldsymbol{u}_h\right), \nabla^s \boldsymbol{v}_h\right) - \left(p_h, \nabla \cdot \boldsymbol{v}_h\right) \\
&\quad - \left(\widetilde{\boldsymbol{u}}, -\frac{\partial \rho^h}{\partial t} \boldsymbol{v}_h + \rho^h \left(\boldsymbol{u}_h + \widetilde{\boldsymbol{u}}\right) \cdot \nabla \boldsymbol{v}_h + \nabla^h \cdot \left(2\mu \boldsymbol{\varepsilon}\left(\boldsymbol{v}_h\right)\right)\right) \\
&\quad + \left(\frac{\partial\left(\rho^h \widetilde{\boldsymbol{u}}\right)}{\partial t}, \boldsymbol{v}_h\right) - \left(\tilde{p}, \nabla \cdot \boldsymbol{v}_h\right) = \left(\rho^h \boldsymbol{g}, \boldsymbol{v}_h\right) + \left(\boldsymbol{t}_n, \boldsymbol{v}_h\right)_{\Gamma_N^{\boldsymbol{u}}}
\end{aligned} \tag{6.30}$$

$$\begin{aligned}
&\left(\rho^h c_p \frac{\partial T_h}{\partial t} + \rho^h c_p \left(\boldsymbol{u}_h + \widetilde{\boldsymbol{u}}\right) \cdot \nabla T_h + 4\kappa_e \sigma_B \left(T_h + \widetilde{T}\right)^4, w_h\right) \\
&- \left(\widetilde{T}, \rho^h c_p \left(\boldsymbol{u}_h + \widetilde{\boldsymbol{u}}\right) \cdot \nabla w_h - \nabla^h \cdot \left(k \nabla w_h\right)\right) + \left(c_p \frac{\partial\left(\rho^h \widetilde{T}\right)}{\partial t}, w_h\right) \\
&\quad + \left(k \nabla T_h, \nabla w_h\right) = \left(Q + \frac{dp^{\text{th}}}{dt} + \kappa_a G(I^d_{\lambda h}), w_h\right) + \left(q_n, w_h\right)_{\Gamma_N^T}
\end{aligned} \tag{6.31}$$

$$\left(\boldsymbol{R}_M \left(I^d_{\lambda h}, T_h + \widetilde{T}\right), z_h\right) = \boldsymbol{0} \tag{6.32}$$

for any test functions $\left(\boldsymbol{v}_h, q_h, w_h, z_h\right) \in \left(\boldsymbol{V}_{0,h}, Q_{0,h}, W_{0,h}, Z_{0,h}\right)$, where

$$\rho^h = \frac{p^{\text{th}}}{R\left(T_h + \widetilde{T}\right)} \tag{6.33}$$

is obtained applying the scale splitting to the state equation (6.5). The symbol ∇^h in equation (6.30) and (6.31) indicates that the integral is carried over the finite element interiors, and not over the edges, for example

$$\left(\widetilde{T}, \nabla^h \cdot \left(k \nabla w_h\right)\right) = \sum_K \left(\widetilde{T}, \nabla \cdot \left(k \nabla w_h\right)\right)_K$$

where $(\cdot, \cdot)_K$ is the $L^2(K)$ inner product.

Remark 1 The temperature has been split into $\left(T_h + \widetilde{T}\right)$ inside the radiative equation $\boldsymbol{R}_M$. In case this splitting is not carried out inside radiation equation it is convenient to introduce

$4\kappa_e\sigma_B T_h^4$ instead of $4\kappa_e\sigma_B\left(T_h+\widetilde{T}\right)^4$ in the energy equation (6.31). Otherwise energy will not be globally conserved, as it will be explained in section 6.4. □

Remark 2 It is known that the absorption coefficient κ depends strongly on temperature, being correlated with the thermal radiation emission I_b and the radiation field I. It is very important to model these correlations, specially in combustion problems because temperature is highly fluctuating in space and time. When the temperature scale splitting is taken into account inside the radiative model, the absorption and emission coefficients κ_a and κ_e are evaluated in terms of $T_h+\widetilde{T}$ through Eqs. (6.12) and (6.13). The correlations between temperature and blackbody radiation I_b, and temperature and the radiative field I are modeled when computing κ, G and I_b in terms of $(T_h+\widetilde{T})$. This is only done when introducing $T_h+\widetilde{T}$ in the radiative model. □

We have observed in numerical examples that the consideration of the temperature scale splitting $(T_h+\widetilde{T})$ in energy and radiation equations increases the radiative heat flux from hot zones, this effect is peculiar of turbulence - radiation interaction models, see for example [29].

To consider the temperature scale splitting in the radiative terms models the physical subgrid behavior that cannot be captured by the mesh, improving the obtained solutions to the equations.

In order to give a closure to system (6.29)-(6.33) we need to define how the subscales $\widetilde{\boldsymbol{u}}$, $\widetilde{p}$ and $\widetilde{T}$ are computed. In the same way the finite element equations can be understood as the projection of the original equations onto the finite element spaces, the equations for the subscales are obtained by projecting the original equations onto their corresponding spaces $\widetilde{\boldsymbol{Y}}$, taking the test functions in the subscale space in the variational problem. This yields:

$$\begin{aligned}
\rho^h\nabla\cdot\widetilde{\boldsymbol{u}}-\frac{\rho^h\left(\boldsymbol{u}_h+\widetilde{\boldsymbol{u}}\right)}{T_h+\widetilde{T}}\cdot\nabla\widetilde{T} &= R_c+p_{\text{ort}} &(6.34)\\
\frac{\partial\left(\rho^h\widetilde{\boldsymbol{u}}\right)}{\partial t}+\boldsymbol{\nabla\cdot}\left(\rho^h(\boldsymbol{u_h}+\widetilde{\boldsymbol{u}})\,\widetilde{\boldsymbol{u}}\right)-\nabla\cdot\left(2\mu\boldsymbol{\varepsilon}'\left(\widetilde{\boldsymbol{u}}\right)\right)+\nabla\widetilde{p} &= \boldsymbol{R}_m+\boldsymbol{u}_{\text{ort}} &(6.35)\\
c_p\frac{\partial\left(\rho^h\widetilde{T}\right)}{\partial t}+c_p\nabla\cdot\left(\rho^h\left(\boldsymbol{u}_h+\widetilde{\boldsymbol{u}}\right)\widetilde{T}\right)-\nabla\cdot\left(k\nabla\widetilde{T}\right) &= R_e+T_{\text{ort}} &(6.36)
\end{aligned}$$

where p_{ort}, $\boldsymbol{u}_{ort}$ and T_{ort} are functions L_2-orthogonal to the subscale space, responsible to guarantee that the subscale equations belong to the subscale spaces. The residuals of mass, momentum and energy equations are respectively

$$\begin{aligned}
R_c &= -\frac{\partial\rho^h}{\partial t}-\rho^h\nabla\cdot\boldsymbol{u}_h+\frac{\rho^h\left(\boldsymbol{u}_h+\widetilde{\boldsymbol{u}}\right)}{T_h+\widetilde{T}}\cdot\nabla T_h &(6.37)\\
\boldsymbol{R}_m &= \rho^h\boldsymbol{g}-\rho^h\frac{\partial\boldsymbol{u}_h}{\partial t}-\rho^h\left(\boldsymbol{u}_h+\widetilde{\boldsymbol{u}}\right)\cdot\nabla\boldsymbol{u}_h+\nabla\cdot\left(2\mu\boldsymbol{\varepsilon}'\left(\boldsymbol{u}_h\right)\right)-\nabla p_h &(6.38)\\
R_e &= Q+\frac{dp^{\text{th}}}{dt}-\rho^h c_p\frac{\partial T_h}{\partial t}-\rho^h c_p\left(\boldsymbol{u}_h+\widetilde{\boldsymbol{u}}\right)\boldsymbol{\cdot}\nabla T_h+\nabla\cdot\left(k\nabla T_h\right)\\
&\quad+\kappa G-4\kappa\sigma_B\left(T_h+\widetilde{T}\right)^4 &(6.39)
\end{aligned}$$

Approximation of the subscales We will approximate the subscale problem replacing the (spatial) differential operators of mass, momentum and energy equations by the algebraical operators τ_c^{-1}, τ_m^{-1} and τ_e^{-1} respectively. The approximation to the subscales equations (6.34)-(6.36) within each element of the finite element partition reads

$$\begin{aligned}
\frac{1}{\tau_c}\widetilde{p} &= R_c + p_{ort} = R_c' && (6.40)\\
\frac{\partial(\rho^h\widetilde{\boldsymbol{u}})}{\partial t} + \frac{1}{\tau_m}\widetilde{\boldsymbol{u}} &= \boldsymbol{R}_m + \boldsymbol{u}_{ort} = \boldsymbol{R}_m' && (6.41)\\
c_p\frac{\partial(\rho^h\widetilde{T})}{\partial t} + \frac{1}{\tau_e}\widetilde{T} &= R_e + T_{ort} = R_e' && (6.42)
\end{aligned}$$

The stabilization parameters τ_c, τ_m and τ_e are defined as

$$\begin{aligned}
\tau_c &= \frac{h^2}{c_1\rho^h\tau_m} = \frac{\mu}{\rho^h} + \frac{c_2}{c_1}|\boldsymbol{u}_h + \widetilde{\boldsymbol{u}}|h && (6.43)\\
\tau_m &= \left(c_1\frac{\mu}{h^2} + c_2\frac{\rho^h|\boldsymbol{u}_h + \widetilde{\boldsymbol{u}}|}{h}\right)^{-1} && (6.44)\\
\tau_e &= \left(c_1\frac{k}{h^2} + c_2\frac{\rho^h c_p|\boldsymbol{u}_h + \widetilde{\boldsymbol{u}}|}{h}\right)^{-1} && (6.45)
\end{aligned}$$

where h is the element size and c_1 and c_2 are algorithmic constants whose values for linear elements are $c_1 = 4$ and $c_2 = 2$. It is important to remark that (6.41) and (6.42) are nonlinear equations. A deep insight about the present subscale model can be found in Chapter 3, where also some linearization schemes are presented.

Remark 3 The spatial-differential operator inside the subscale equation (6.36) has been approximated to obtain Eq. (6.42). The approximation reads

$$\frac{1}{\tau_e}\widetilde{T} \approx c_p\nabla\cdot\left(\rho^h\left(\boldsymbol{u}_h + \widetilde{\boldsymbol{u}}\right)\widetilde{T}\right) - \nabla\cdot\left(k\nabla\widetilde{T}\right) \qquad (6.46)$$

Note that the nonlinear reactive term $\kappa\sigma_B\left(T_h + \widetilde{T}\right)^4$ is not approximated inside the subscale equation (6.36), and therefore stabilization parameter τ_e does not depend on $\kappa\sigma_B$. We want to remark the form of the stabilization parameter for a linear equation. In case we have a differential equation with a linear reactive term, for example

$$\rho c_p\boldsymbol{u}\cdot\nabla T - \nabla\cdot(k\nabla T) + \kappa T = f \qquad (6.47)$$

the procedure followed in this section would lead to a subscale equation of the form $\widetilde{T} = \tau R$ with a stabilization parameter expressed as $\tau^{-1} = c_1\frac{k}{h^2} + c_2\frac{\rho^h c_p|\boldsymbol{u}_h+\widetilde{\boldsymbol{u}}|}{h}$, and a residual given by

$$R = f - \rho c_p\boldsymbol{u}\cdot\nabla T_h + \nabla\cdot(k\nabla T_h) - \kappa(T_h + \widetilde{T})$$

This is equivalent to have an stabilization parameter of the form $\tau^{-1} = c_1\frac{k}{h^2} + c_2\frac{\rho^h c_p|\boldsymbol{u}_h+\widetilde{\boldsymbol{u}}|}{h} + c_3\kappa$, with the residual defined as

$$R = f - \rho c_p\boldsymbol{u}\cdot\nabla T_h + \nabla\cdot(k\nabla T_h) - \kappa T_h \qquad (6.48)$$

Now the residual does not depend on the temperature subscale, which is the classical definition when using linear subscale models. This equivalency only holds if the reactive term in τ is not affected by any constant, being $c_3 = 1$. This reasoning tells us that for a reactive linear equation of the form (6.47), with the residual defined as in (6.48), the stabilization parameter must have the dependency on κ as $\tau^{-1} = ... + \kappa$. $\square$

6.4 Global energy conservation

The aim of this section is to obtain global conservation of energy statement similar to those holding for the continuous problem, but for the problem semi-discretized in space. It has been shown in Chapter 3 that global conservation statements for mass, momentum and energy without radiative terms hold when equal interpolation is used for all variables. We shall see that energy will be globally conserved only if the radiative model $\boldsymbol{R}_M$ conserves radiation energy.

Let us integrate radiation transfer equation (6.4) over all solid angle directions, and over all the spectral domain $\lambda \in \mathbb{R}^+$ to get the zeroth moment radiative equation

$$\nabla \cdot \boldsymbol{q}_r - \kappa_a G = 4\kappa_e \sigma_B T^4$$

This equation is satisfied by most radiative models, as DOM and P_1. Integrating this equation over the spatial domain Ω one finds the following radiation conservation statement for the continuous problem

$$\int_\Omega \left(4\kappa_e \sigma_B T^4 - \kappa_a G\right) d\Omega = \int_{\partial\Omega} \boldsymbol{q}_r \cdot \boldsymbol{n} \mathrm{d}\Gamma \tag{6.49}$$

The discrete counterpart of this conservation statement is generally satisfied by the discrete approximation of radiative models (6.32). This is the case of the finite element approximation for DOM and P_1 method presented in Chapter 5, giving:

$$\int_\Omega \left(4\kappa_e \sigma_B \left(T_h + \widetilde{T}\right)^4 - \kappa_a G\right) d\Omega = \int_{\partial\Omega} \boldsymbol{q}_r \cdot \boldsymbol{n} \mathrm{d}\Gamma \tag{6.50}$$

Let us consider the finite element space for temperature equation without Dirichlet boundary conditions and an augmented problem that also contains the tractions at the Dirichlet boundaries as unknowns [48]. When using equal interpolation spaces for the temperature and pressure equations ($W_h = Q_h$), it can be shown that taking the test function $w_h = 1$ in (the augmented problem corresponding to) the finite element energy Eq. (6.31), and replacing (6.50) we get the relation

$$\int_\Omega c_p \frac{\partial}{\partial t}\left(\rho^h \left(T_h + \widetilde{T}\right)\right) d\Omega = \int_\Omega \left(Q + \frac{dp^{\mathrm{th}}}{dt}\right) d\Omega - \int_{\partial\Omega} \left(q_n + \boldsymbol{n} \cdot \left(\boldsymbol{q}_r + \boldsymbol{u}_h \rho^h c_p T_h\right)\right) d\Gamma \tag{6.51}$$

Substituting the discrete state equation $\rho^h = \frac{p^{\mathrm{th}}}{R\left(T_h + \widetilde{T}\right)}$ of ideal gases inside this equation, we obtain

$$\frac{|\Omega|}{\gamma - 1}\frac{dp^{\mathrm{th}}}{dt} + \frac{\gamma p^{\mathrm{th}}}{\gamma - 1}\int_{\partial\Omega} \boldsymbol{n} \cdot \boldsymbol{u}_h d\Gamma = \int_\Omega Q d\Omega - \int_{\partial\Omega} \left(q_n + q_{rn}\right) d\Gamma \tag{6.52}$$

which implies global energy conservation. This last equation is used in some works [90] for the tracking in time of the thermodynamic pressure p^{th} for closed flows. It is necessary that the discrete radiative model (6.32) conserves radiation energy (statement (6.50)), to satisfy energy conservation statement (6.51). The radiative equation must depend on the temperature splitting $\left(T_h + \widetilde{T}\right)$ to be consistent with the energy equation to achieve the energy conservation statement (6.50). When this splitting is ignored in the radiative model $(\left(\boldsymbol{R}_M(I^d_{\lambda h}, T_h), z_h\right) = 0)$ the radiative term in energy equation (6.31) should be introduced in the form $(4\kappa_e\sigma_B T_h^4)$ to conserve energy globally.

6.5 Linearization strategy of coupling terms bewtween radiation and temperature equations

The coupling between radiation and energy equations is extremely nonlinear, and needs to be solved iteratively in order to obtain a converged solution of the problem. Linearization schemes of mass, momentum and energy equations without considering radiative coupling were explained in detail in Chapter 3.

Linearization of radiative terms in the finite element equation We will focus on how to linearize energy equation (6.31); the radiative equation (6.32) is supposed to be solved in segregated form. The subscales are supposed to be given as we need to solve finite element problem (6.31). Linearization of radiative term $4\kappa_e\sigma_B\left(T_h + \widetilde{T}\right)^4$ in the energy equation using a Newton Rapshon scheme is always convergent, because this term never changes its concavity (second derivative sign respect to T_h remains unchanged). If temperature T_h is known at iteration k, the nonlinear term is approximated at iteration $k+1$ in terms of T_h^{k+1} as

$$4\kappa_e\sigma_B\left(T_h^{k+1} + \widetilde{T}\right)^4 \approx 4\kappa_e\sigma_B\left(T_h^{k} + \widetilde{T}\right)^3\left(4T_h^{k+1} - 3T_h^{k} + \widetilde{T}\right) \tag{6.53}$$

Other linearization strategies were used, like fixed point iteration

$$4\kappa_e\sigma_B\left(T_h^{k+1} + \widetilde{T}\right)^4 \approx 4\kappa_e\sigma_B\left(T_h^{k} + \widetilde{T}\right)^3\left(T_h^{k+1} + \widetilde{T}\right)$$

or

$$4\kappa_e\sigma_B\left(T_h^{k+1} + \widetilde{T}\right)^4 \approx 4\kappa_e\sigma_B\left(T_h^{k} + \widetilde{T}\right)^3\left(2T_h^{k+1} - T_h^{k} + \widetilde{T}\right)$$

but convergence was always faster when using Newton Raphson scheme (6.53). Convergence was always achieved when applying Newton Raphson. The fixed point iteration did not converge in many examples. We obtained faster convergence applying sobrerelaxation schemes for the coupling between radiation and temperature equations.

Linearization of radiative terms in the subscale equation The subscale equations form a nonlinear system of equations that must be linearized. Linearization schemes for the subscale equations without considering radiation coupling are detailed in Chapter 3, where it was shown that the Newton Raphson scheme applied to the monolithically coupled system of equations was the most efficient one. Radiative transfer introduces a nonlinear term $4\kappa\sigma_B\left(T_h+\widetilde{T}\right)^4$ affecting the temperature subscale $\widetilde{T}$ in the subscale energy Eq. (6.36). We will focus on linearization of this radiative term inside subscale energy Eq. (6.36) equation. We have observed that the Newton Raphson scheme is unconditionally convergent because the function does not change its concavity. The finite element unknowns are assumed to be given as we need to solve the subscale problem. If the temperature subscale is known at iteration k, the approximation of the nonlinear reactive term respect to $\widetilde{T}^{k+1}$ at iteration $k+1$ is

$$4\kappa_e\sigma_B\left(T_h+\widetilde{T}^{k+1}\right)^4 \approx 4\kappa_e\sigma_B\left(T_h+\widetilde{T}^{k}\right)^3\left(T_h+4\widetilde{T}^{k+1}-3\widetilde{T}^{k}\right) \tag{6.54}$$

Linearization of the coupled energy boundary condition When we want to impose an amount of conductive plus radiative heat flux, we need to apply the nonlinear boundary condition (6.21) to energy equation (6.31). This condition couples energy and radiation unknowns on the boundary, being very important for optically thin problems where $\kappa_a L < 1$, where L is a characteristic length of the problem. We have found in the numerical experiments that this boundary condition needs to be linearized properly. The most efficient method was to apply a Newton Raphson scheme. Although it is always convergent, the solution converged extremely slowly when solving optically thin problems. When applying simpler linearization schemes the solution does not converge. Assuming a known temperature at iteration k, boundary condition (6.21) is linearized to approximate temperature at iteration $k+1$ as

$$-\boldsymbol{n}\cdot k\nabla T_h^{k+1} - \epsilon\sigma_B\left(T_h^k\right)^3\left(4T_h^{k+1}-3T_h^k\right) = \mathcal{H} - (1-r)H \tag{6.55}$$

being implemented as a boundary condition of Robin Type.

6.6 Relevant dimensionless parameters

The aim of this section is to present the relevant dimensionless parameters measuring the relative importance of radiative, conductive and convective heat transfer into the energy equation (6.3). In order to obtain a dimensionless energy equation, we take the following dimensionless variables

$$\begin{aligned}
\boldsymbol{u}^* &= \frac{\boldsymbol{u}}{U_0}, & T^* &= \frac{T-T_0}{\Delta T}, & \boldsymbol{x}^* &= \frac{\boldsymbol{x}}{L}\\
t^* &= t\frac{U_0}{L}, & \rho^* &= \frac{\rho}{\rho_0}, & \kappa^* &= \frac{\kappa}{\kappa_0}\\
k^* &= \frac{k}{k_0}, & G^* &= \frac{G}{\sigma_B T_0^4}, & S^* &= \frac{S}{S_0}
\end{aligned}$$

where L_0, U_0, T_0, ΔT, ρ_0, κ_0, k_0, S_0 are the scales of length, velocity, temperature, temperature variation, density, absorption, conductivity and external heat respectively. We define the optical length scale as $\tau = \kappa_0 L_0$, and the temperature variation coefficient as $\varepsilon = \Delta T/T_0$.

For simplicity, we will neglect time derivative of thermodynamical pressure. Replacing into energy equation (6.3) all the variables in term of the dimensionless ones, we arrive to the following dimensionless equations (omitting symbol *):

$$\rho\left(\frac{\partial T}{\partial t}+\rho\boldsymbol{u}\cdot\nabla T\right)-\frac{1}{\mathrm{Pe}}\left(\nabla\cdot(k\nabla T)+\frac{\tau}{\mathrm{Pl}}\left(4\kappa_e\left(1+\varepsilon T\right)^4-\kappa_a G(I_\lambda)\right)\right)=Q$$

where, τ, Pe, Pl and ε are respectively the optical thickness of the medium, Peclet, Planck and temperature variation numbers, defined as

$$\begin{aligned}\tau &= L\kappa, \qquad \mathrm{Pe}=\frac{\rho c_p U_0 L}{k}\\ \mathrm{Pl} &= \frac{k\Delta T}{L\sigma_B T_0^4}, \qquad \varepsilon=\frac{\Delta T}{T_0}\end{aligned}$$

For Low Mach number flows with large temperature variation it is usual to consider a temperature variation number $\varepsilon=1$. The relation between conductive to radiative heat transfer is given by Pl/τ. For optically thick mediums it is usual to take $L_0=1/\kappa$, i.e. $\tau=1$. And therefore the Planck number can be determined as $\mathrm{Pl}=\frac{k\kappa}{\sigma_B T_0^3}=N$, where N is known as the radiation to conduction parameter, commonly introduced in text books [70]. When the medium is optically thin $\tau \ll 1$, radiative heat transfer does not depend on local properties and therefore Pl/τ does not give a good estimate for the relation of conductive to radiative heat transfer. In the case of high Reynolds number flows, the relation of interest is between radiative to convective heat transfer, given by $PlPe/\tau$. When $PlPe/\tau \lesssim 10$ radiative heat transfer needs to be considered for high Reynolds number flows and not optically thin medium.

6.7 Numerical examples

6.7.1 Fire in a 3D room with an open door

This test example is a fire compartment similar to that considered in Chapter 3, but now simulating the effect of radiative heat transfer, and increasing the power of the source that models the fire, in order to the obtain higher temperatures to increase the importance of radiative heat transfer effects.

The problem domain is $\Omega=[0,L]\times[0,L]\times[0,H]$ where $L=2.8$ m and $H=2.18$ m. The compartment has an open door on the side wall of the room ($x=L$) whose dimension is 0.7×1.853 m^2. An scheme of the problem domain is shown in Fig. 6.1. The fire is modeled by an uniform heat source of 30 kW, located at the center of the room just over the floor, with dimensions $0.84\times 0.84\times 0.218$ m^3. Adiabatic boundary conditions are imposed on all the walls. Non slip boundary conditions for velocity are imposed on all the boundaries except the door, where atmospheric boundary condition is imposed, that is, a traction $\boldsymbol{t}_n=(-\rho|\boldsymbol{g}|z,0,0)$. As the flow is open $((\Gamma_N^{\boldsymbol{u}}\neq\emptyset))$, the thermodynamic pressure is set constant in time to $p^{\mathrm{th}}=101325$ Pa. The initial temperature and velocity values are $T_0=300$ K and $\boldsymbol{u}_0=\boldsymbol{0}$ over all domain Ω. Furthermore, the viscosity is $\mu=0.0094\ \frac{\mathrm{kg}}{\mathrm{m\,s}}$ and $\mathrm{Pr}=0.71$. The gravity is set to $\boldsymbol{g}=(0,0,-9.8)$ m/s^2. The medium was treated as gray, with homogeneous absorption and emissive coefficientes $\kappa_a=\kappa_e=10$ m^{-1}, and a zero scattering coefficient.

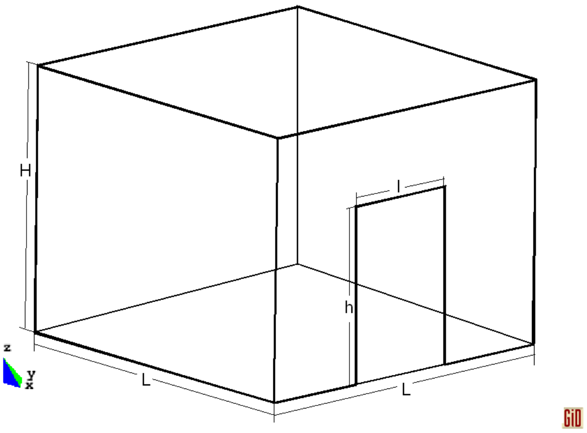

Figure 6.1: Problem domain of the room with an open door

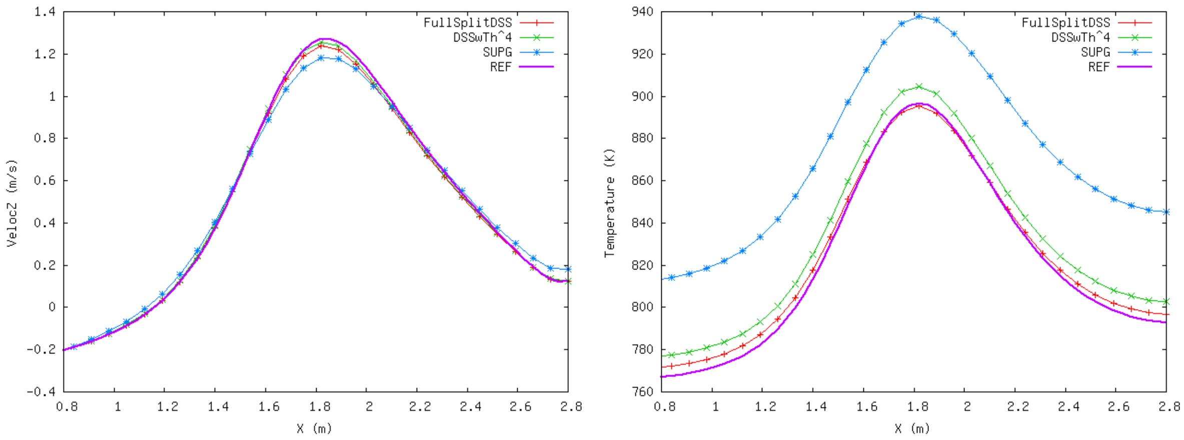

Figure 6.2: Temperature and vertical velocity distributions along x direction

The radiative field was obtained using the P_1 approximation to radiation transport equation, explained in section 5.5. This is a valid approximation model, since the radiative intensity is not too directionally anisotropic.

The compartment was meshed using a grid of $40 \times 40 \times 40$ uniform trilinear elements Q_1. We solved the problem using a time step size of $\Delta t = 1.0$ s. We compare the obtained solutions with three different stabilization methods, the classical SUPG method, and the dynamical and nonlinear subscale method presented in this chapter with and without temperature scale splitting of the radiative term $4\kappa\sigma_B T^4$. When temperature scale splitting is (not) considerer in energy equation, then it is also (neither) considered as radiative source in radiation equation. The obtained results are compared against a reference solution obtained using the SUPG method over a fine mesh of $80 \times 80 \times 80$ uniform elements, and a time step size of $\Delta t = 0.5$ s. The computation is advanced until $t_{\text{end}} = 180.0$ s using the second order time integration scheme BDF2. The tolerance for the nonlinear iterations was set to $5 \cdot 10^{-4}$ in the relative norm of the difference between two iterates.

In Figs. 6.2, 6.3 and 6.4 the temperature and vertical velocity distributions along the x, y and z directions using the DSS and ASGS methods at $t = t_{\text{end}}$ are shown. The DSS method is labeled as FullSplitDSS when temperature splitting is labeled in all terms, and is

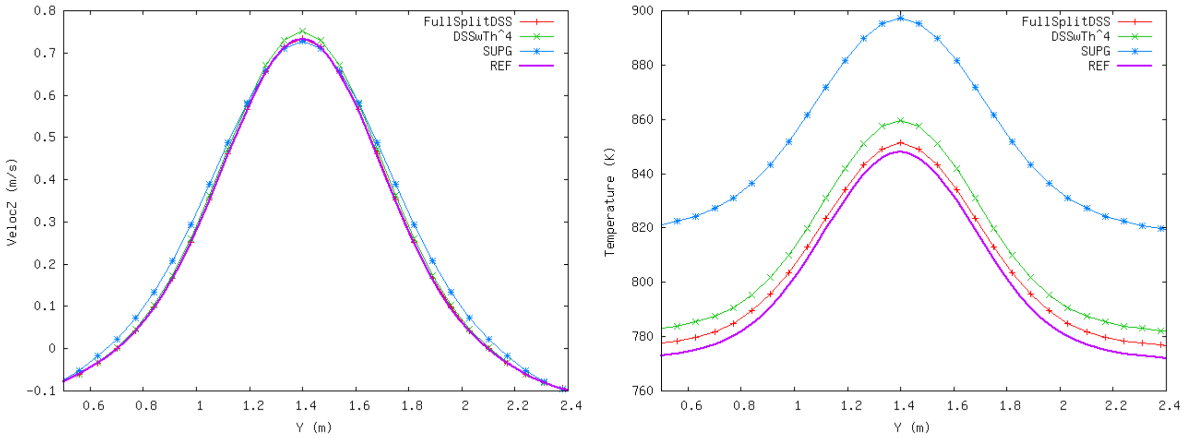

Figure 6.3: Temperature and vertical velocity distributions along y direction

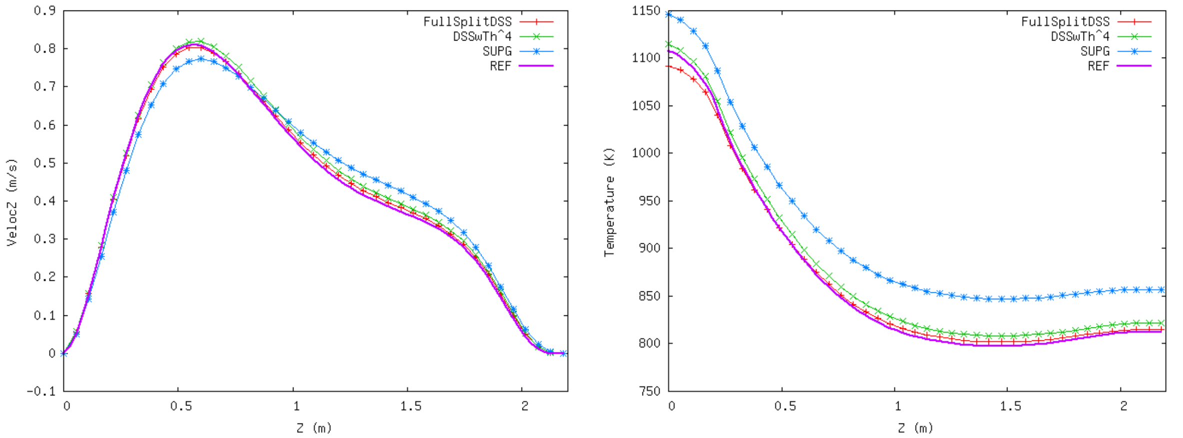

Figure 6.4: Temperature and vertical velocity distributions along z direction

labeled as DSSwThˆ 4 when temperature splitting is not taken into account in radiative term. In all those figures the greater similarity of the results respect to the reference solution when using the DSS method against SUPG method is clearly observed. The same observation was done in Chapter 3. We can observe that to perform temperature scale splitting in radiative term has the effect of decreasing the obtained temperature, obtaining temperature results more similar to the reference solution. The effect of temperature splitting is more noticeable in the temperature solution, vertical velocity is less affected, and is difficult to conclude if there exists an improvement.

The time evolution of temperature and vertical velocity (along the z direction) at points $(1.55, 1.4, 0.55)$ m , $(1.3, 1.3, 0.2)$ m and $(1.4, 1.4, 1.0)$ m are compared in Figs. 6.5, 6.6, 6.7. It is observed that when using the ASGS method the solution differs much more from the reference solution than when using the DSS method. It is difficult to observe the difference in the solutions when splitting or not the temperature in radiative term, and more difficult is to confirm if there exist any improvement. However, observing temperature cuts at time t_{end} it is seen that exists an improvement on temperature field.

In Fig. 6.8 the distribution of the temperature subscale over plane $y = L/2$ when $t = t_{\text{end}}$

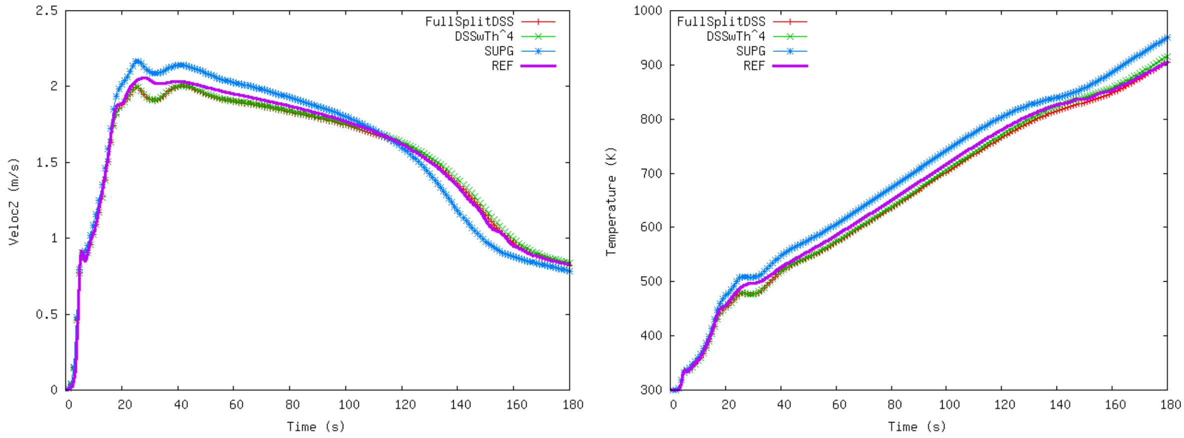

Figure 6.5: Time evolution of temperature and vertical velocity (i.e. u_z) at point $(1.55, 1.4, 0.55)$m

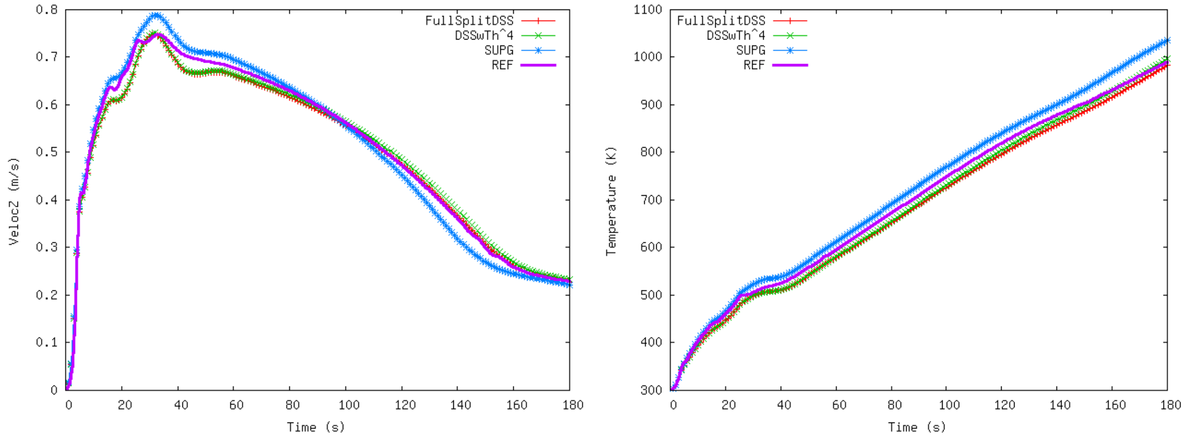

Figure 6.6: Time evolution of temperature and vertical velocity (i.e. u_z) at point $(1.55, 1.4, 0.55)$m

is shown. It is seen that the maximum subscale values are located over the source term is located, contributing to a raise of radiation source when adding the temperature subscale. We would like to mention that to consider a spatial subscale distribution over the source with zero mean and zero skewnes, then the subscale would contribute to a positive raise of the radiative source. In Fig. 6.9 the temperature distribution over plane $y = L/2$ at time $t = t_{\text{end}}$ when considering and not considering temperature splitting in radiative term of energy equation is shown. It is seen a temperature decrease when considering scale splitting, a similar effect of radiation-turbulence interaction models. Fig. 6.9 showns the radiative heat distribution over plane $y = L/2$ at time $t = t_{\text{end}}$ when considering and not considering temperature splitting in radiative term of energy equation. It is seen that the radiative heat flux decreases when considering the temperature splitting, this is due to the decrease of temperature over the fire. The effect of considering temperature scale splitting in term $4\kappa\sigma_B(T_h + \widetilde{T})^4$ enhances the obtained results increasing the radiative heat flux from hot zones, this is the expected turbulent effect of modeling a subgrid temperature. We believe that the difference on the results when considering temperature scale splitting in radiative term will be more noticeable in turbulent flames. The effect of modeling $4\kappa\sigma_B(T_h + \widetilde{T})^4$ in a purely numerical form, supplies the effect

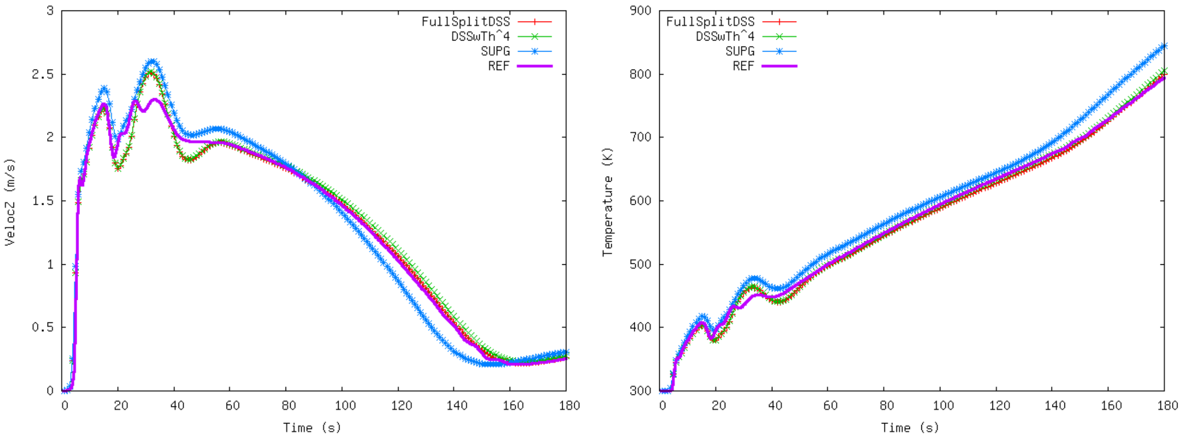

Figure 6.7: Time evolution of temperature and vertical velocity (i.e. u_z) at point $(1.3, 1.3, 1.2)$m

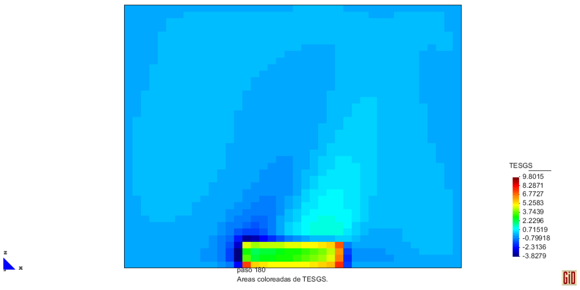

Figure 6.8: Temperature subscale distribution on the plane $y = L/2)$

of using a LES method to model turbulent radiation interaction.

Performance of the methods The total number of nonlinear iterations needed to solve the problem (i.e. the sum of the nonlinear iterations performed in all time steps) and the total cpu time are indicated in Table 6.1. The cpu time spent for assembly of the Low Mach equations (which includes numerical integration and solution of the subscale problem, i.e. operations involving a loop over integration points) and cpu time spent in (linear) solver procedures are also indicated. The cpu time spent solving the radiation equation is also indicated.

The total number of nonlinear iterations over the low Mach equations is 5% lower using DSS method. However, the use of DSS method increases the cpu time of assembly operations per iterarion, therefore the total cpu time is 6.5% higher using DSS method, but the obtained solution is much better. The same behavior was observed in the same problem in chapter 3, without radiation, using a smaller fire source, using the same mesh with the same time step. The method is observed to be very competitive. The cpu time spent solving radiation equations does not differ more than 1% using the different methods in Low Mach equations. The cpu time of DSS method does not change when taking into account the temperature splitting on radiative term. The cpu solver time is a little lower using ASGS method, that is, the system is a little better conditioned. We think this is due to the discontinuities of the subscales. The little extra cpu-time occurs at expenses of obtaining a much better solution.

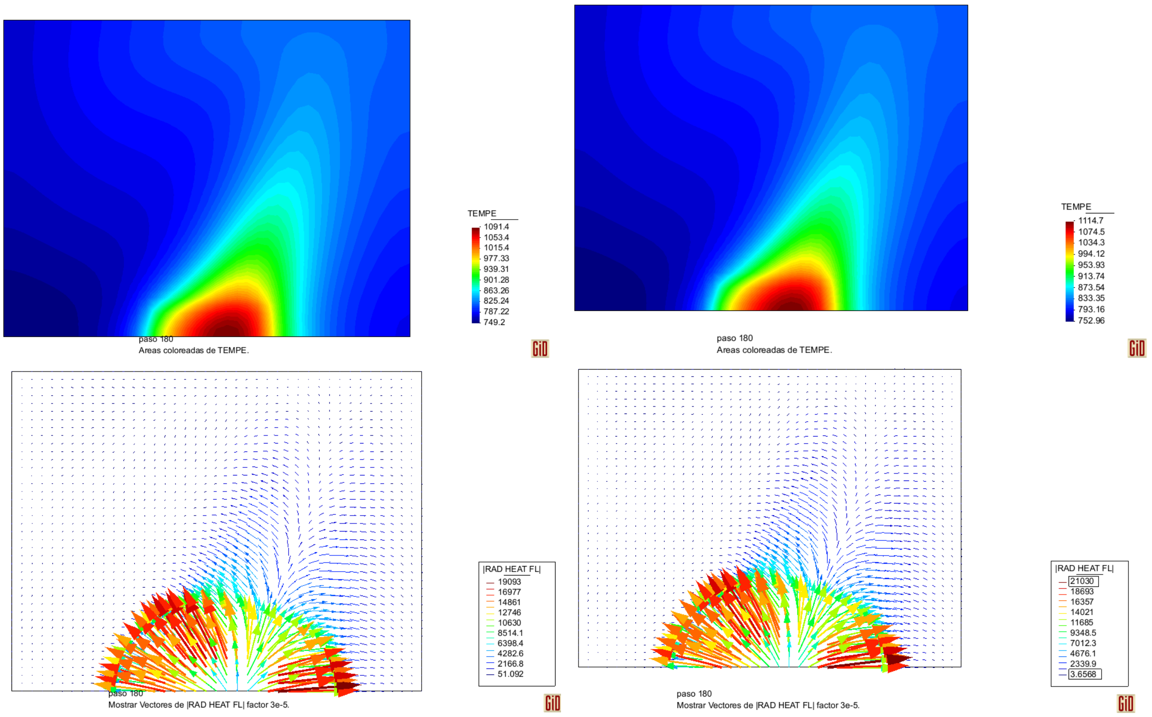

Figure 6.9: Temperature distribution and radiative heat flux distribution over plane $y = L/2$ when splitting radiative term as $4\kappa\sigma_B(T_h + \widetilde{T})^4$ (left) and not splitting $4\kappa\sigma_B T_h^4$ (right))

	# iters.	total cpu(s)	cpu LM(s)	cpu Rad(s)	cpu assem LM(s)	cpu solv LM(s)
ASGS	3579	82563	66182	16341	24159	42023
DSSwTh4	3438	88105	71896	16144	28359	43537
DSSFULL	3406	88103	71985	16054	28549	43436

Table 6.1: Comparison of the total number of iterations and the required cpu time for the different methods.

6.7.2 Fire in a vehicular tunnel

This problem was solved without taking radiative heat transfer into account in [78]. In this section we will solve and compare the obtained results when radiative heat transfer is modeled or not.

A fire is a complex phenomenon whose detailed simulation involves many different aspects that we are not considering in this work. Here we have used a simple model that considers the fire as a source of heat, without taking into account the exact reactive mechanism, as it would imply a precise knowledge of the chemical components of the fuel. The heat released during a fire, which is between 1 MW and 100 MW, is partially dissipated by the flow and partially transported towards the concrete structure where it is finally dissipated. As the fire temperature increases, radiative heat transfer becomes a more important mechanism of heat transfer, decreasing the temperature of fire, affecting bouyant effects and velocity field. Thus, in this problem we will solve a fire in a vehicular tunnel, and we will compare the results when radiative heat transfer is modeled or not.

We solved the radiative problem using the P_1 approximation to the radiative heat transfer equation. This is a very simple and a valid model when radiation field can be approximated as linearly anisotropic.

The high Reynolds number of the problem implies the need of taking turbulence into account. Since the meshes we will use are relatively coarse to capture all the scales of the model proposed in Chapter 4 we do this introducing a Smagorinsky eddy viscosity, which is defined by

$$\mu^t = \rho^h c_s h^2 \left(\boldsymbol{\varepsilon}'(\boldsymbol{u}) : \boldsymbol{\varepsilon}'(\boldsymbol{u})\right)^{1/2} \tag{6.56}$$

where c_s is an empirical constant, h is the characteristic length, taken as the mesh size, and $\boldsymbol{\varepsilon}'(\boldsymbol{u})$ is the deviatoric part of the rate of deformation tensor. A subgrid thermal conductivity is also added. It is defined in terms of the subgrid viscosity as

$$k^t = \frac{\mu^t c_p}{\mathrm{Pr}^t} \tag{6.57}$$

where Pr^t is the turbulent Prandtl number, which is assumed to be constant (and taken to be 0.5). Two simulations were carried out, considering and not considering a radiative participating media. The medium is assumed as gray with an uniform absorption coefficient $\kappa_a = \kappa_e = 20\ \mathrm{m}^{-1}$ and scattering coefficient $\sigma_s = 0.1\ \mathrm{m}^{-1}$, modeling smoke as uniformly distributed along the tunnel.

We solve the problem using a mesh of 55000 Q_1 elements. The heat source is of 18 MW, which corresponds to a small size fire (a car for example) distributed in a volume of 12 m^3. A preliminary calculation was performed to reproduce the initial state of a wind flowing through the tunnel which was obtained applying a pressure difference between the tunnel inlet and outlet, in order to give an approximate velocity of 0.5 m/s. On the tunnel walls Neumann boundary conditions based on universal profiles were applied (wall laws). Boundary conditions for temperature were defined to reproduce the real situation as close as possible. On the tunnel walls, a Robin type condition was applied using a convection coefficient $h_c = 36$ suggested by laboratory experiments. The temperature of the concrete walls was fixed to $T_w = 297$ K. In both calculations we used a time step $\Delta t = 1.0$ s. On the entrance and exit of the tunnel, zero Neumann boundary conditions were considered. Radiative boundary conditions were imposed assuming an opaque and gray surface with emissivity and reflectivity coefficients $\epsilon = r = 0.5$.

The physics of the flow is quite complex and the temporal evolution is chaotic. When the heating starts, strong bouyancy forces determine the formation of a plume and recirculating zones that are fully tridimensional and of complex structure. In order to have a comparison between the non radiating and radiating problem, we display in Figure 6.10 the velocity field at 180 s after the starting of the heating, and in Figure 6.11 the corresponding temperature distribution is shown. Both figures show a detail of the fire zone introducing cutting planes that intersect the fire zone. The heat source generates the plume that can be clearly observed in in Figure 6.10, where an expansion of the flow is also apparent. This expansion is better shown in Figure 6.12 where contour lines of divergence of the velocity are shown.

The effect of radiation is to transport heat from the source to colder regions, being absorbed within the medium. The flame temperature is decreased in the source, and temperature gradients are weakened in closer regions. Time evolution for temperature and vertical velocity at two points, over the source and above the source, are compared in Figure 6.13 for radiating and non radiating problem. It is observed that during the first 60s of simulation after the starting of the heating, the effect of radiation is very small, decreasing slightly the maximum temperature over the source. Both solutions are very similar over the first period, but the difference between both solutions increases over time. After 110 s the chaotic nature of the flow is observed. The flame temperature is lower over all simulation time using a radiating model. However, temperature evolution above the source is lower with a radiative model only during the first 110 s. After that time, temperature evolution is chaotic and is difficult to make a comparison at a given point outside the source. It is observed that maximum temperatures are lower with a radiative medium. Vertical velocity is a measure of the convection caused by the fire. It is seen that vertical velocity is lower over the first 110 s. After that time it is difficult to get a conclusion comparing velocities due to the chaotic flow.

The nonlinear equations describing the flow are solved using two nested loops, an external global loop and internal loops for the low Mach number equations and radiation equations. A maximum number of 6 iterations in the external loop were performed with a convergence tolerance of $10^{-3}\%$ for the velocity and temperature. The linear system has been solved using a GMRES method preconditioned using an ILUT strategy.

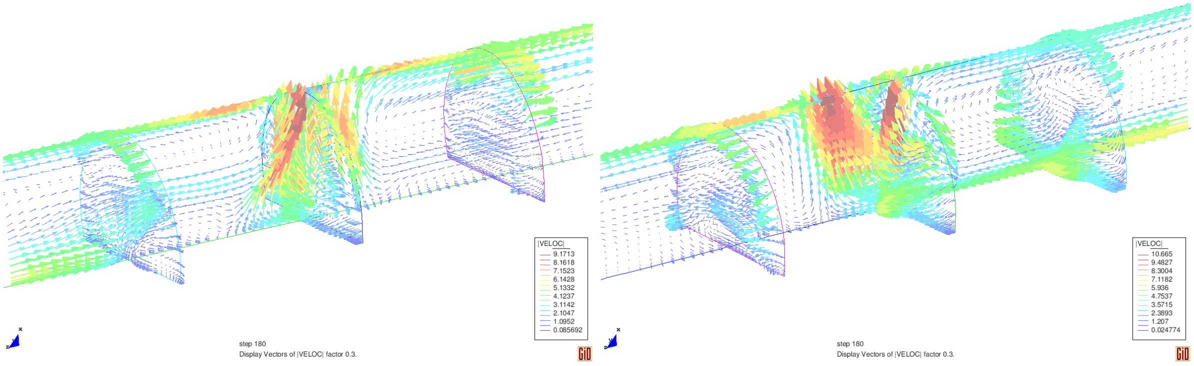

Figure 6.10: Velocity field at t=180 s using (left) and not using (right) a radiative model

6.8 Conclusions

In this chapter a finite element approximation of the low Mach number equations coupled with a radiative heat transfer model based on a splitting of the unknowns into finite element and unresolvable components has been developed. The main ingredients of the formulation are:

- To consider time dependent subscales.
- To keep the subscale components in all the nonlinear terms.

The effect of considering time dependent subscales is well known [27] and our experience with the low Mach number equations confirms the properties known for incompressible flows.

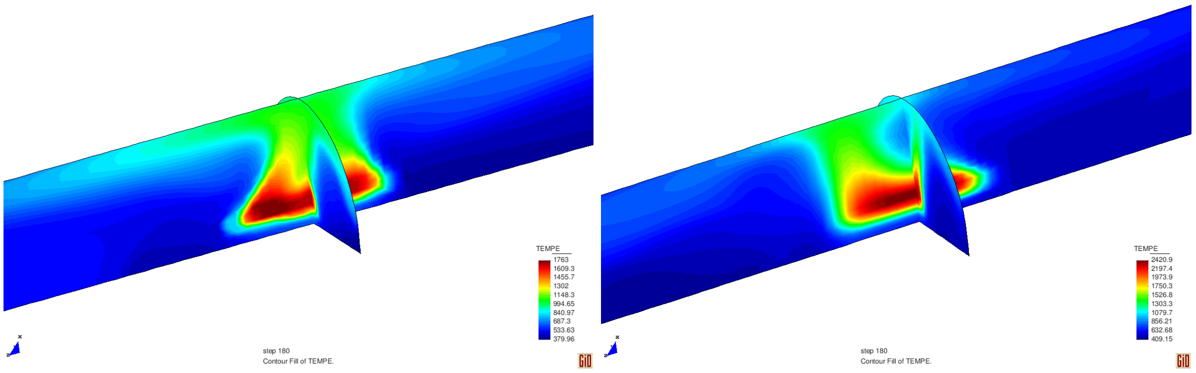

Figure 6.11: Temperature field at t=180 s using (left) and not using (right) a radiative model

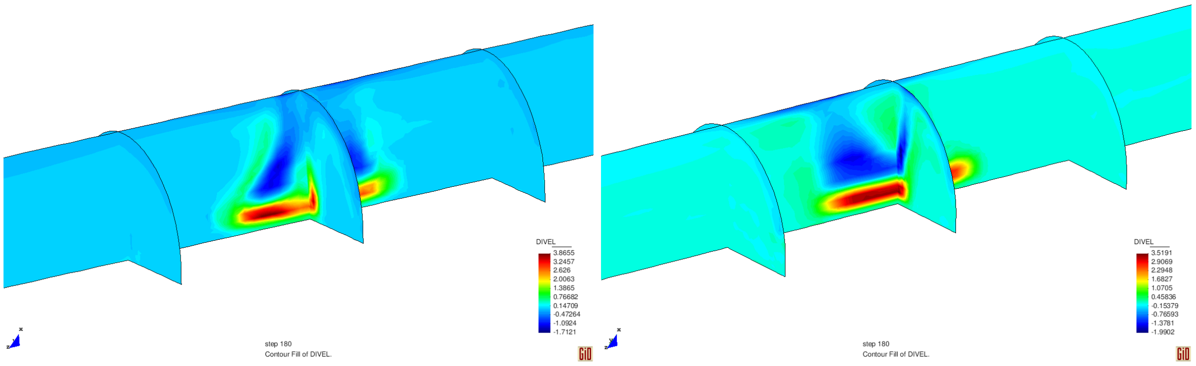

Figure 6.12: Divergence of the velocity field at t=180 s with (left) and without (right) a radiative model

The effect of considering the splitting of the unknowns in all the terms leads to a more accurate solution than classical stabilization methods and provides global mass, momentum and energy conservation when using equal interpolation spaces for the velocity, pressure and temperature equations. An improvement in the quality of the solution is obtained when considering the spliting of the radiation terms in the temperature equation.

We would like to stress, once again, that we keep the splitting of the unknowns in all terms *also in the subscale equations*, and we have numerically verified that this makes a difference in the accuracy of the scheme.

This nonlinear and transient treatment of the subscales *also in the subscale equations* has a computational cost, in memory requirements and very little in the cpu-(and will be usually dominated by the memory needed to solve the linear system)time. Nevertheless, the extra amount of memory needed only grows linearly with the number of nodes (and will be usually dominated by the memory needed to solve the linear system).

The formulation intrinsically contains cross- and Reynolds- stress terms, and TRI terms that try to model the unsolved eddies and subgrid interaction between radiation and temperature, presenting an open door to turbulence modeling. The present method remains unchanged irrespective of whether laminar, transitional and turbulent situations are present.

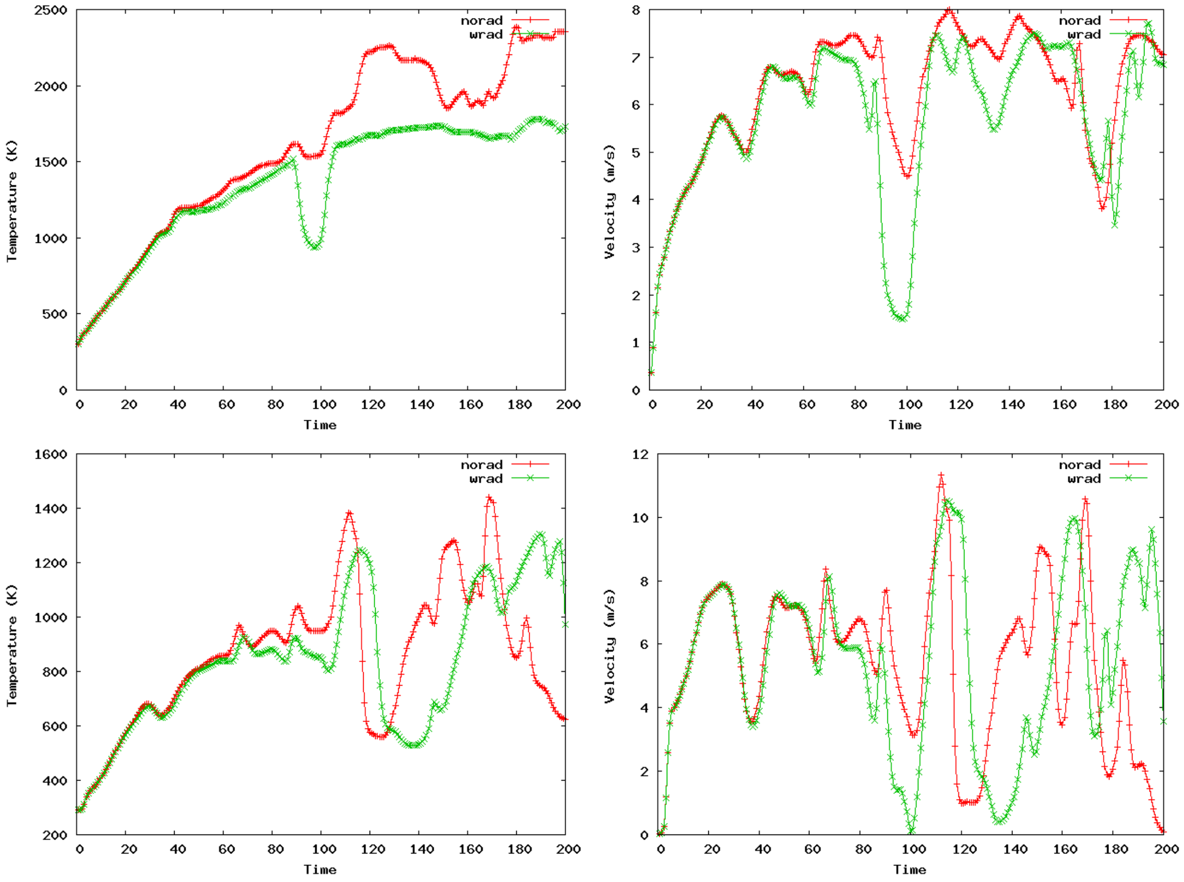

Figure 6.13: Time evolution of velocity and temperature at point $(1.6, 0.66, 40.0)$m (top) and $(4.7, 0.51, 40.0)$m (bottom) with (wrad) and without (norad) the use of a radiative model

We have emphasized the advantages of the temperature splitting ($T_h + \widetilde{T}$) inside the radiative model and the radiative terms in the energy equation. When performing this splitting more accurate solutions were found in the numerical examples.

It is known that the absorption coefficient κ depends strongly on temperature, being correlated with the thermal radiation emission I_b and radiation field I. It is very important to model these correlations, specially in combustion problems, because temperature is highly fluctuating in space and time. The formulation presented in this chapter introduces subgrid terms that model these correlations when the temperature scale splitting is taken into account inside the radiative model equations, through the dependence of κ, G and I_b in $T_h + \widetilde{T}$.

Chapter 7

Conclusions

In this chapter we present the conclusions and the possible research lines that could be followed starting from this thesis.

7.1 Achievements

The objective of this work, to develop a finite element dynamical nonlinear subgrid scale approximation for nonlinear system of equations that describe the behavior of thermally coupled flows, has been achieved. The proposed nonlinear subgrid modeling, derived through a scale splitting in the variational multiscale context, provides a stable and very accurate formulation for this kind nonlinear problems. This method involves a nonlinear modelling of the subgrid scales, that has been shown to be capable of modeling the involved subgrid physical mechanisms appearing in highly variable density flows and radiative heat coupling at low and high Reynolds number. We have started with the incompressible Boussinesq approximation for thermally coupled flows, and we arrived to the variable density low Mach approximation coupled with radiative heat transfer. The main conclusions are the following

- In chapter 2 a variational multiscale finite element approximation for thermally coupled incompressible flows is described. The subscales were considered as transient and orthogonal, keeping the effect of the subscales both in the nonlinear convective terms of the momentum and energy equations. This strategy allows us to simulate thermally coupled turbulent flows. The dissipative structure of the formulation is analyzed, identifying the energy transfer terms and the possibility to have scale separation and to model backscatter when considering orthogonal subscales.

- In chapter 3 a variational multiscale finite element approximation for thermally coupled variable density flows at low Mach number was developed. The subscales are considered as transient, and the subscale components are kept in all the nonlinear terms (including the state equation), and we have numerically verified that this makes a substantial difference in the accuracy of the scheme. An orthogonal subscale scheme was also proposed, leading to a simplified formulation and more accurate solutions.

- In chapter 4 it is shown that the method proposed in chapter 3 is adequate for the simulation of turbulent flows without the use of a physical model for the turbulence effects. The nonlinear model of the subscales can be understood as a LES modeling of the Reynolds Stress tensor. The dissipative structure is analyzed identifying the main dissipative mechanisms of the formulation, and the influence of the numerical parameters on the total dissipation. An skew symmetric formulation was developed, avoiding non physical dissipation mechanisms.

- In chapter 5 the contribution is the design and analysis of stabilized finite element methods to approximate the radiative transport equation, motivated within the variational multiscale framework. As the radiative equations are linear, the subgrid numerical modelling was also linear. It is shown that the SUPG and the multiscale formulations are stable and optimally convergent. A non-conventional numerical analysis of the Galerkin method was presented.

- In chapter 6 a closure is given to the thesis, extending the stabilization methods proposed in previous chapters when radiative heat transfer mechanisms are present in low Mach number flows. The stabilized method was extended accounting for the nonlinear coupling between temperature and radiation. Numerical results show the accuracy of the scheme.

As mentioned in the introduction, the work developed during this thesis is the base for the following publications:

- Chapter 2: “Finite element approximation of turbulent thermally coupled incompressible flows with numerical sub-grid scale modelling”, R. Codina, J. Principe and M. Avila. International Journal of Numerical Methods for Heat & Fluid Flow. Vol. 20 No. 5 (2010) 492-516

- Chapter 3: “A finite element dynamical nonlinear subscale approximation for the low Mach number flow equations”, M. Avila, R. Codina and J. Principe. Journal of Computational Physics Vol. 230 (2011) 7988–8009.

- Chapter 4: “Large eddy simulation of low Mach number flows using a dynamical and nonlinear finite element subgrid scale model”, M. Avila, J. Principe and R. Codina. Submitted.

- Chapter 5: “Spatial approximation of the radiation transport equation using a subgrid-scale finite element method”, M. Avila, J. Principe and R. Codina. Computer Methods in Applied Mechanics and Engineering, 2011, vol. 200: 425-438.

- Chapter 6: “Subgrid finite element approximation for thermally coupled flows with radiative heat transfer”, M. Avila, J. Principe and R. Codina. In preparation.

7.2 Future Work

We describe here the open lines of research:

- As the proposed formulation gives very accurate results when solving nonlinear system of equations, a future research line is to implement the nonlinear M1 method for the radiative equations [33]. This is a very accurate model involving a system of only 4 equations, being therefore much cheaper than DOM approximation. The future research line is to approximate the M1 radiation model with the nonlinear subscale approximation developed in this thesis, aiming to obtain accurate results when dealing with the nonlinear subgrid mechanisms.

- The modeling of temperature radiation interaction of the proposed stabilization method needs further research, and results are difficult to be validated. An open line of research is to account for the dependency of the radiation properties on temperature, increasing radiation and temperature interaction. It is known that when combustion processes are involved, stronger fluctuations of temperature, radiation and velocity fields are generated, getting stronger turbulence radiation interaction. An interesting research line would be to design an extension of the stabilization method proposed in this thesis when a combustion model is coupled to radiation and Navier Stokes equations, accounting for the dependence of radiation properties with temperature. This is a more realistic problem where numerical results could be validated against experiments, giving insight to the subgrid scale models. The coupling between chemical reaction rate, temperature, and radiation is highly nonlinear and subgrid physical models need to be added when solving this equations. May be it is optimistic to model this physical subgrid processes with the sole use of nonlinear numerical models (avoiding physical models), but we believe that this modeling would enhance the accuracy of the obtained results. The nonlinear subgrid equations need to be designed for all these coupling, and then to be validated, giving an interesting insight to the dynamical and nonlinear numerical subscale concept.

Bibliography

[1] M. Asadzadeh. A finite element method for the neutron transport equation in an infinite cylindrical domain. *SIAM Journal on Numerical Analysis*, 35:1299–1314, 1998.

[2] M. Avila, J. Principe, and R. Codina. A finite element dynamical nonlinear subscale approximation for the low mach number flow equations. *Journal of Computational Physics*, 230:7988–8009, 2011.

[3] S. Badia and R. Codina. On a multiscale approach to the transient Stokes problem. Transient subscales and anisotropic space-time discretization. *Applied Mathematics and Computation*, 207:415–433, 2009.

[4] S. Badia, R. Codina, and J.V. Gutiérrez-Santacreu. Long term stability estimates and existence of global attractors in a finite element approximation of the Navier-Stokes equations with numerical sub-grid scale modeling. *SIAM Journal on Numerical Analysis*, 48:1013–1037, 2010.

[5] Y. Bazilevs, V. M.Calo, J. A. Cottrell, T. J. R. Hughes, A. Reali, and G. Scovazzi. Variational multiscale residual-based turbulence modeling for large eddy simulation of incompressible flows. *Computer Methods in Applied Mechanics and Engineering*, 197:173–201, 2007.

[6] A. Beccantini, E. Studer, S. Gounand, J. P. Magnaud, and T. Kloczko. Numerical simulations of a transient injection flow at low Mach number regime. *International Journal for Numerical Methods in Engineering*, 76:662–696, 2008.

[7] P.B. Bochev, M.D. Gunzburger, and R.B. Lehoucq. On stabilized finite element methods for the Stokes problem in the small time-step limit. *International Journal for Numerical Methods in Fluids*, 53:573–597, 2007.

[8] J. P. Boris, F. F. Grinstein, E.S. Oran, and R. L. Kolbe. New insights into large eddy simulation. *Fluid Dynamics Research*, 10(4-6):199, 1992.

[9] J.P. Boris, F.F. Grinstein, E.S. Oran, and R.L. Kolbe. New insights into large eddy simulation. *Fluid Dyn. Res.*, 10:199–228, 1992.

[10] J. Boussinesq. *Théorie analytique de la chaleur*, volume 2. GauthierVillars, 1903.

[11] A. N. Brooks and T. J. R. Hughes. Streamline upwind/petrov-galerkin formulations for convection dominated flows with particular emphasis on the incompresible Navier-Stokes equations. *Computer Methods in Applied Mechanics and Engineering*, 32:199–259, 1982.

[12] S. Chandrasekhar. *Radiative Transfer*. Dover Publications, 1960.

[13] P. Cheng. *Study of the flow of a radiating gas by a differential approximation*. PhD thesis, Standford University, 1965.

[14] P. Cheng. Dynamics of a radiating gas with application to flow over a wavy wall. *AIAA Journal*, 4:238–245, 1966.

[15] M.A. Christon, P.M. Gresho, and S.B. Sutton. Computational predictability of natural convection flows in enclosures. *International Journal for Numerical Methods in Fluids*, 40:953–980, 2002.

[16] R. Codina. Comparison of some finite element methods for solving the diffusion-convection-reaction equations. *Computer Methods in Applied Mechanics and Engineering*, 156:185–210, 1998.

[17] R. Codina. Stabilization of incompressibility and convection through orthogonal subscales in finite element methods. *Computer Methods in Applied Mechanics and Engineering*, 190(13-14):1579–1599, Dec 2000.

[18] R. Codina. A stabilized finite element method for generalized stationary incompressible flows. *Computer Methods in Applied Mechanics and Engineering*, 190(20–21):2681–706, 2001.

[19] R. Codina. Stabilized finite element approximation of transient incompressible flows using orthogonal subscales. *Comput. Methods Appl. Mech. Engrg.*, 191:4295–4321, 2002.

[20] R. Codina. Analysis of a stabilized finite element approximation of the oseen equations using orthogonal subscales. *Applied Numerical Mathematics*, 58:264–283, 2008.

[21] R. Codina. Finite element approximation of the hyperbolic wave equation in mixed form. *Computer Methods in Applied Mechanics and Engineering*, 197:1305–1322, 2008.

[22] R. Codina. Finite element approximation of the three field formulation of the stokes problem using arbitrary interpolations. *SIAM Journal on Numerical Analysis*, 47:699–718, 2009.

[23] R. Codina, J.M. González-Ondina, G. Díaz-Hernández, and J. Principe. Finite element approximation of the modified Boussinesq equations using a stabilized formulation. *International Journal for Numerical Methods in Fluids*, 57:1305–1322, 2008.

[24] R. Codina and J. Principe. Dynamic subscales in the finite element approximation of thermally coupled incompressible flows. *International Journal of Numerical Methods in Fluids*, 54:707–730, 2007.

[25] R. Codina, J. Principe, and M. Avila. Finite element approximation of turbulent thermally coupled incompressible flows with numerical sub-grid scale modelling. *International Journal of Numerical Methods for Heat and Fluid Flow*, 20(5):492–516, 2010.

[26] R. Codina, J. Principe, and J. Baiges. Subscales on the element boundaries in the variational two-scale finite element method. *Computer Methods in Applied Mechanics and Engineering*, 198:838–852, 2009.

[27] R. Codina, J. Principe, O.Guasch, and S.Badia. Time dependent subscales in the stabilized finite element approximation of incompressible flow problems. *Computer Methods in Applied Mechanics and Engineering*, 196:2413–2430, 2007.

[28] R. Codina and O.C. Zienkiewicz. CBS versus GLS stabilization of the incompressible Navier-Stokes equations and the role of the time step as stabilization parameter. *Communications in Numerical Methods in Engineering*, 18:99–112, 2002.

[29] P.J. Coelho. Numerical simulation of the interaction between turbulence and radiation in reactive flows. *Progress in Energy and Combustion Science*, 33(4):311 – 383, 2007.

[30] B. Davison. *Neutron Transport Theory*. Oxford University Press, London, 1958.

[31] P.A.B. de Sampaio, P.H. Hallak, A.L.G.A. Coutinho, and M.S. Pfeil. A stabilized finite element procedure for turbulent fluid-structure interaction using adaptive time-space refinement. *International Journal for Numerical Methods in Fluids*, 44:673–693, 2004.

[32] J. Douglas and J. Wang. An absolutely stabilized finite element method for the Stokes problem. *Mathematics of computation*, 52:495–508, 1989.

[33] B. Dubroca and J.L. Feugeas. Etude thorique et numrique d'une hirarchie de modles aux moments pour le transfert radiatif. *Comptes Rendus de l'Acadmie des Sciences - Series I - Mathematics*, 329(10):915 – 920, 1999.

[34] A. Ern and J.L. Guermond. Discontinuous Galerkin methods for Friedrichs's systems: I. general theory. *SIAM Journal on Numerical Analysis*, 44:753–778, 2006.

[35] D. Marini F. Brezzi and E. Süli. Residual-free bubbles for advection-diffusion problems: the general error analysis. *Numerische Mathematik*, 85:31–47, 2000.

[36] W.A. Fiveland. A discrete ordinates method for predicting radiative heat transfer in axysimmetric enclosures. *ASME Paper 82-HT-20*, 1982.

[37] W.A. Fiveland. Discrete ordinates methods for radiative heat transfer in isotropically and anisotropically scattering media. *ASME Journal of Heat Transfer*, 109:809–812, 1987.

[38] W.A. Fiveland. Finite element formulation of the discrete ordinates method for multidimensional geometries. *J Thermophys. Heat transfer*, 8:426–433, 1994.

[39] V. Gravemeier and W. A. Wall. An algebraic variational multiscale-multigrid method for large-eddy simulation of turbulent variable-density flow at low Mach number. *Journal of Computational Physics*, 229:6047–6070, 2010.

[40] V. Gravemeier and W. A. Wall. Residual-based variational multiscale methods for laminar transitional and turbulent variable-density flow at low Mach number. *International Journal for Numerical Methods in Fluids*, 65:12601278, 2011.

[41] O. Guasch and R. Codina. A heuristic argument for the sole use of numerical stabilization with no physical les modelling in the simulation of incompressible turbulent flows. *Submitted*, 2010.

[42] I. Harari and T.J.R. Hughes. What are c and h?: Inequalities for the analysis and design of finite element methods. *Computer Methods in Applied Mechanics and Engineering*, 97(2):157 – 192, 1992.

[43] V. Heuveline. On higher- order mixed fem for low Mach number flows: Applications to a natural convection benchmark problem. *International Journal for Numerical Methods in Fluids*, 41:1339–1356, 2003.

[44] J.O. Hinze. *Turbulence*. McGraw-Hill, 1975.

[45] J. Hoffman and C. Johnson. A new approach to computational turbulence modeling. *Computer Methods in Applied Mechanics and Engineering*, 195:2865–2880, 2006.

[46] P. Houston and E. Sli. Stabilised hp-finite element approximation of partial differential equations with nonnegative characteristic form. *Computing*, 66:99–119, 2001. 10.1007/s006070170030.

[47] G. Houzeaux and J. Principe. A variational subgrid scale model for transient incompressible flows. *International Journal of Computational Fluid Dynamics*, 22:135–152, 2008.

[48] T. J. R. Hughes, G. Emgel, L. Mazzei, and M. G. Larson. The continuous Galerkin method is locally conservative. *Journal of Computational Physics*, 163:467–488, 2000.

[49] T. J. R. Hughes, G. R. Feijóo, L. Mazzei, and J.B. Quincy. The variational multiscale method–a paradigm for computational mechanics. *Computer Methods in Applied Mechanics and Engineering*, 166:3–24, 1998.

[50] T. J. R. Hughes, L. P. Franca, and M. Balestra. A new finite element formulation for computational fluid dynamics: V. Circumventing the Babuška-Brezzi condition: a stable Petrov Galerkin formulation of the stokes problem accomodating equal order interpolations. *Computer Methods in Applied Mechanics and Engineering*, 59(1):85–99, 1986.

[51] T. J. R. Hughes, L. Mazzei, and K. E. Jansen. Large eddy simulation and the variational multiscale method. *Computing and Visualization in Science*, 3:47–59, 2000.

[52] T. J. R. Hughes, L. Mazzei, and A. A. Oberai. The multiscale formulation of large eddy simulation: Decay of homogeneous isotropic turbulence. *Physics of fluids*, 13(2):505–512, February 2001.

[53] T. J. R. Hughes, A. A. Oberai, and L. Mazzei. Large eddy simulation of turbulent channel flows by the variational multiscale method. *Physics of fluids*, 13(6):1784–1799, June 2001.

[54] T. J. R. Hughes, G. Scovazzi, and L. P. Franca. Multiscale and stabilized methods. In T.J.R Hughes E. Stein, R. de Borst, editor, *Enciclopedia of Computational Mechanics*. Willey: Chichester, 2004.

[55] T.J.R. Hughes. Multiscale phenomena: Green's function, the Dirichlet-to-Neumann formulation, subgrid scale models, bubbles and the origins of stabilized formulations. *Computer Methods in Applied Mechanics and Engineering*, 127:387–401, 1995.

[56] T.J.R. Hughes and G.N. Wells. Conservation properties for the Galerkin and stabilised forms of the advection-diffusion and incompressible Navier-Stokes equations. *Computer Methods in Applied Mechanics and Engineering*, 194:1141–1159, 2005.

[57] J.H. Jeans. The equations of radiative transfer of energy. *Monthly Notices Royal Astronomical Society*, 78:28–36, 1917.

[58] G. Kanschat. Robust finite element discretization for radiative transfer problems with scattering. *East-West Journal of Numerical Mathematics*, 6(4):265–272, 1998.

[59] V. Kourganoff. *Basic Methods in Transfer Problems*. Dover Publications, New York, 1963.

[60] K.D. Lathrop and B.G. Carlson. *Discrete-ordinates angular quadrature of the neutron transport equation*. Technical Information Series Report LASL-3186, Los Alamos Scientific Laboratory, 1965.

[61] B. Lessani and M. V. Papalexandris. Time-accurate calculation of variable density flows with strong temperature gradients and combustion. *Journal of Computational Physics*, 212(1):218–246, 2006.

[62] D.K. Lilly. The representation of small-scale turbulence theory in numerical simulation experiments. In H.H. Goldstine, editor, *Proc. IBM Scientific Computing Symp. on Environmental Sciences*, 1967.

[63] P.L. Lions. *Mathematical Topics in Fluid Dynamics, Volume 1. Inompressible Models*. Oxford University Press, 1996.

[64] P.L. Lions. *Mathematical Topics in Fluid Dynamics, Volume 2. Compressible Models*. Oxford University Press, 1998.

[65] W. Liu and G. Makhviladze. An implicit finite element solution of thermal flows at low Mach number. *Journal of Computational Physics*, 227:2743–2757, 2008.

[66] G. Lube and G. Rapin. Residual-based stabilized higher-order fem for advection-dominated problems. *Computer Methods in Applied Mechanics and Engineering*, 195(3336):4124 – 4138, 2006.

[67] A. Majda and J. Sethian. The derivation and numerical solution of the equations for zero Mach number combustion. *Combustion Science and Technology*, 42:185–205, 1985.

[68] M.J. Martinez and D.K. Gartling. A finite element method for low-speed compressible flows. *Computer Methods in Applied Mechanics and Engineering*, 193(21-22):1959–1979, May 2004.

[69] M.F. Modest. Photon-gas formulation of the differential approximation in radiative transfer. *Letters in Heat and Mass Transfer*, 3:111–116, 1976.

[70] M.F. Modest. *Radiative heat transfer*. Academic Press, 2003.

[71] R. D. Moser, J. Kim, and N. N. Mansour. Direct numerical simulation of turbulent channel flow up to re[sub tau] = 590. *Physics of Fluids*, 11(4):943–945, 1999.

[72] R. L. Murray. *Nuclear Reactor Physics*. Prentice Hall, Englewood Cliffs, NJ, 1957.

[73] F. Nicoud. Numerical study of a channel flow with variable properties. In *Annual Resear Briefs, Center for Turbulence Research*. 1998.

[74] F. Nicoud. Conservative high-order finite-difference schemes for low-mach number flows. *Journal of Computational Physics*, 158:71–97, 2000.

[75] F. Nicoud and T. Poinsot. Dns of a channel flow with variable properties. In Eaton Editors, editor, *First International Symposium on Turbulence and Shear Flow Phenomena*. Santa Barbara, USA, 1999.

[76] J.A. Nitsche. Uber ein variationsprinzip zur lösung von dirichlet-problemen bei verwendung von teilräumen, die keinen randbedingungen unterworfen sind. *Abhandlungen aus dem Mathematischen Seminar der Universität Hamburg*, 36:9–15, 1971.

[77] S.B. Pope. *Turbulent Flows*. Cambridge University Press, 2000.

[78] J. Principe. *Subgrid scale stabilised finite elements for low speed flows*. PhD thesis, Universitat Politecnica de Catalunya, 2008.

[79] J. Principe and R. Codina. A stabilized finite element approximation of low speed thermally coupled flows. *International Journal of Numerical Methods for Heat and Fluid Flow*, 18:835–867, 2007.

[80] J. Principe and R. Codina. Mathematical models for thermally coupled low speed flows. *Advances in Theoretical and Applied Mechanics*, 2:93–112, 2009.

[81] J. Principe, R. Codina, and F. Henke. The dissipative structure of variational multiscale methods for incompressible flows. *Computer Methods in Applied Mechanics and Engineering*, 199:791–801, 2010.

[82] P. Le Quere, C. Weisman, H. Paillere, J. Vierendeels, E. Dick, R. Becker, M. Braack, and J. Locke. Modelling of natural convection flows with large temperature differences: A benchmark problem for low Mach number solvers. Part 1. Reference solutions. *ESAIM: Mathematical Modelling and Numerical Analysis*, 39(3):609–616, 2005.

[83] M.M. Razzaque, D.E. Klein, and J.R. Howell. Finite element solution of radiative heat transfer in two dimensional rectangular enclosure with gray participating media. *J Heat Transfer*, 105:933–936, 1983.

[84] J.N. Reddy and D.K. Gartling. *The finite element method in heat transfer and fluid dynamics*. CRC Press, 1994.

[85] S. Richling, E.Meinköhn, N.Kryzhevoi, and G.Kanschat. Radiative transfer with finite elements. *Astronomy Astrophysics*, 380:776–788, 2001.

[86] P. Sagaut. *Large Eddy Simulation for Incompressible Flows*. Scientific Computing, Springer, 2001.

[87] R. Sevilla, S. Fernández-Méndez, and A. Huerta. NURBS-enhanced finite element method for Euler equations. *0271-2091*, 57(9):1051–1069, 2008.

[88] F. Shakib and T.J.R. Hughes. A new finite element formulation for computational fluid dynamics: IX. Fourier analysis of space-time Galerkin/least-squares algorithms. *Computer Methods in Applied Mechanics and Engineering*, 87:35–58, 1991.

[89] A. E. Tejada-Martinez and K. E. Jansen. On the interaction between dynamic model dissipation and numerical dissipation due to streamline upwind/petrovgalerkin stabilization. *Computer Methods in Applied Mechanics and Engineering*, 194(911):1225 – 1248, 2005.

[90] I. Teleaga, M. Sead, I. Gasser, Axel Klar, and J.Struckmeier. Radiation models for thermal flows at low mach number. *Journal of Computational Physics*, 215:506–525, 2006.

[91] T. Tezduyar and S. Sathe. Stabilization parameters in SUPG and PSPG formulations. *Journal of Computational and Applied Mechanics*, 4:71–88, 2003.

[92] A. V. Trofimova, A. E. Tejada-Martnez, K. E. Jansen, and R. T. Lahey Jr. Direct numerical simulation of turbulent channel flows using a stabilized finite element method. *Computers & Fluids*, 38(4):924 – 938, 2009.

[93] J. Truelove. Discrete-ordinate solution of the radiation transport equation. *ASME Journal of Heat Transfer*, 109:1048–1051, 1987.

[94] J. Truelove. Three-dimensional radiation in absorbing-emitting-scattering media using the discrete ordinates approximation. *J. Quant. Spectrosc. Radiat. Tranfer*, 39:27–31, 1988.

[95] R. Viskanta. Heat transfer by conduction and radiation in absorbing and scattering materials. *J Heat Transfer*, 143:143–150, 1965.

[96] W.P. Wang and R. H. Pletcher. On the large eddy simulation of a turbulent channel flow with significant heat transfer. *Physics of Fluids*, 8(12):3354–3366, 1996.

[97] D.C. Wilcox. *Turbulence modeling for CFD*. DCW Industries, Inc. La Cañada, California, 1993.

[98] K. Yosida. *Functional Analysis*. Springer, 1980.

[99] J.M. Zhao and L.H. Liu. Second order radiative transfer equation and its properties of numerical solution using the finite element method. *Numerical Heat Transfer, Part B*, 51:391–409, 2007.